Dynamic effects of harnessing cables on distributed parameter systems for space applications: Analytical modeling and experimental validation

by

Pranav Agrawal

A thesis
presented to the University of Waterloo
in fulfillment of the
thesis requirement for the degree of
Doctor of Philosophy
in
Mechanical and Mechatronics Engineering

Waterloo, Ontario, Canada, 2020

Examining Committee Membership

The following served on the Examining Committee for this thesis. The decision of the Examining Committee is by majority vote.

External Examiner:	Luc Mongeau Professor Dept. of Mechanical Engineering McGill University
Supervisor(s):	Armaghan Salehian Associate Professor Dept. of Mechanical and Mechatronics Engineering University of Waterloo
Internal Member:	Fue-Sang Lien Professor Dept. of Mechanical and Mechatronics Engineering University of Waterloo
Internal Member:	Stewart McLachlin Assistant Professor Dept. of Mechanical and Mechatronics Engineering University of Waterloo
Internal-External Member:	Sriram Narasimhan Professor Dept. of Civil and Environmental Engineering University of Waterloo

Author's Declaration

I hereby declare that I am the sole author of this thesis. This is a true copy of the thesis, including any required final revisions, as accepted by my examiners.

I understand that my thesis may be made electronically available to the public.

Abstract

Power and data signal cables constitute a major component of lightweight spacecraft and satellite structures. These cables can account for up to as high as 30% of the structural mass and hence significantly impact the structural dynamics. Until the last decade, these cables were primarily modeled using ad hoc techniques that considered cables as non-structural mass elements and neglected their stiffness and damping effects. However, in the last decade, accurate modeling of *cable-harnessed structures* has come into the spotlight by incorporating cable dynamics that are governed by cable's stiffness and damping in addition to its mass. Accuracy of these lightweight space structure models are important because the control systems heavily rely on them for their robust performance. Hence, the primary goal of this research is to create simple analytical models that can predict the accurate dynamic behavior of cable-harnessed structures. The beauty of analytical models lie in the fact that they result in low-order high-fidelity governing partial differential equations (PDE) and hence are advantageous over the numerical methods, such as finite element method. A reliable low-order PDE of a dynamical system ensures the robustness of the control algorithms. Additionally, analytical models provide deeper insights into the system due to the possibility of obtaining closed-form solutions and ease of conducting parametric analysis.

The current research can be classified into solving the following two broad problems: 1. modeling the damping mechanisms in cable-harnessed beam structures, 2. modeling the accurate stiffness and inertia effects in cable-harnessed two-dimensional structures.

The first problem addresses accurate modeling of material damping in the cable-harnessed beam system which was identified as a major gap in the present literature. The system consists of the cables wrapped around the beam in specific periodic geometry. In the presented research, the energy loss mechanisms in the system was incorporated by using the Kelvin-Voigt and hysteresis damping models. Applying an energy-equivalent homogenization method, the proposed technique modeled the cable-harnessed beam as an equivalent continuum (beam-like) structure. In order to validate the model, cable damping was first characterized using dynamic testing methods and relevant loss factors were obtained for both the models. In the next step, experimental modal testing was performed on the fabricated cable-harnessed beams to obtain the modal characteristics of the system such as natural frequencies and frequency response functions. These experimentally obtained characteristics were compared with those using the proposed model and were found to be in a good agreement.

The second problem constitutes the major contribution of this thesis. It is worth mentioning that in the past, no analytical models have been developed that consider *two-*

dimensional plate-like host structures to model the cable-harnessed system. Researchers have generally considered *one-dimensional beam-like* host structures for modeling purpose as it simplifies the mathematical formulation. In this research, analytical modeling based on a homogenization approach is proposed to develop an equivalent continuum model of cable-harnessed plates. This modeling problem is further broken down into the following sub-problems depending on the way the cables are harnessed to the host plates: 1. cables harnessed parallel to a plate's edge, and 2. cables wrapped across the plate in a defined pattern. For both these cases, separate mathematical derivations were carried out to obtain governing PDEs that represent the dynamic behavior of these structures. The proposed models are experimentally validated using modal testing of the fabricated cable-harnessed plates. Comparisons of natural frequencies, mode shapes and frequency response functions provided confidence in the correctness of the proposed model. In addition to providing accuracy for low order control algorithms, the proposed models can be further used to obtain optimal cable placement strategies such that the dynamic effects of the cable harness are minimized.

Acknowledgements

First and foremost, I would like to thank my advisor Dr. Armaghan Salehian for supporting my dream of pursuing a PhD in the area of vibrations. I am grateful to her for a high-quality technical guidance and feedbacks during my entire PhD. In addition, I acknowledge the planning skills that I have learnt during my PhD research and I give full credit to Dr. Salehian as she consistently motivated me to make achievable short-term and long-term plans. I'm sure the gained technical expertise in the area of structural dynamics and meticulous planning skills will assist me in the future throughout my career.

I would like to further thank Dr. Luc Mongeau for accepting to hold the external examiner position for my PhD defence examination. I am also thankful to my committee members Dr. Fue Sang Lien, Dr. Sriram Narasimhan and Dr. Stewart McLachlin for agreeing to be in my PhD committee.

I would also like to specially mention my *guru* Dr. Shakti Gupta at IIT Kanpur for igniting a passion of research within me that has propelled my academic journey so far. I am thankful to him for our regular discussions during my PhD on both professional and personal fronts.

I'd like to further acknowledge my ex-labmates Dr. Blake Martin and Dr. Karthik Yerrapragadha who answered my several technical questions during my PhD. They were very kind to give a prompt response to my queries even after their graduation. I would also like to thank Jeffrey Sixt for reading my journal manuscripts and providing editorial feedbacks.

Last but not the least, a big shout out to my friends and family members for their constant support and encouragement. I have had a great time at Waterloo because of some amazing people who I have had a chance to share my apartment with. I would like to thank my ex-roommates - Abhisek, Ajay, Nalin, Karthik, Prashanth, Rohit, Shivesh, Souvik, and my current roommates - Abhinav, Naman and Yash. These friends have been like a family away from home.

My research was funded by The Natural Sciences and Engineering Research Council of Canada (NSERC) for which I'm highly grateful. I also received the International Doctoral Student Award (IDSA) for which I convey my thanks to the University of Waterloo. I am also thankful to the Vice-President, Academic and Provost, and Graduate Studies and Postdoctoral Affairs (GSPA) for the Doctoral Thesis Completion Award.

Dedicated to my parents

Table of Contents

List of Figures

List of Tables

List of Symbols

Chapter 2

(x, y, z) = global Cartesian coordinates

(ξ, y, z) = local Cartesian coordinates

A_b = beam cross sectional area

A_c = cable cross-sectional area

b = beam width

$\bar{b} = \frac{b}{2} + r_c$

B_1, B_2, B_3 = strain energy coefficients for Kelvin-Voigt damped system

B_1^* = complex coefficient in strain energy of hysteretically damped system

B_1', B_1'' = real and imaginary parts ofB_1^*, respectively

C_b = Kelvin-Voigt coefficient of beam internal damping

C_c = Kelvin-Voigt coefficient of cable internal damping

D_1 = coefficient of Rayleigh dissipation function for Kelvin-Voigt damped system

E_b = beam Youngs modulus

E_c = cable Youngs modulus

E_b^*, E_b', E_b'' = complex modulus, storage modulus and loss modulus of beam, respectively

E_c^*, E_c', E_c'' = complex modulus, storage modulus and loss modulus of cable, respectively

$F(x, s)$ = state space matrix in DTFM

$f_e(\xi, t)$ = transverse external force on a fundamental element

$G(x, \kappa, s), H(x, s)$ = transfer functions and boundary influence functions in DTFM

h = beam thickness

$\bar{h} = \dfrac{h}{2} + r_c$

I_b = beam second moment of area about y axis ($I_b = bh^3/12$)

K_1 = coefficient for the kinetic energy of the equivalent homogenized system

L_e = length of the fundamental element

l = length of the beam

m_e = mass of the fundamental element

m_{node} = lumped cable mass at the end of the fundamental element for diagonal pattern

Q_D = non-conservative damping force

r_c = cable radius

s = Laplace operator

R_b = beam Rayleigh dissipation function

R_c = cable Rayleigh dissipation function

R_e = fundamental element Rayleigh dissipation function

R_{tot} = total Rayleigh dissipation function in cable-harnessed system

T = cable tension

T_e = fundamental element kinetic energy

T_{tot} = kinetic energy in cable-harnessed system

U_e = fundamental element strain energy

U_{tot} = total strain energy of cable-harnessed system

U^* = complex strain energy

u_x, u_y, u_z = global displacement field

V_b = 3-dimensional volumetric domain for beam within the fundamental element

V_c = 3-dimensional volumetric domain for cable within the fundamental element

$w(x,t)$ = transverse displacement of cable-harnessed system

z_c = z coordinate for the center of the cable

ε_{ij} = Green-Lagrange strain tensor

ε_b = longitudinal normal strain in beam

ε_c = axial normal strain in cable

δW_d = virtual work due to internal damping

$\gamma(s)$ = inhomogeneity in the boundary conditions in DTFM

η_{kb} = beam Kelvin-Voigt damping proportionality constant

η_{kc} = cable Kelvin-Voigt damping proportionality constant

η_{hb} = beam hysteretic loss factor

η_{hc} = cable hysteretic loss factor

η_{CH} = effective hysteretic loss factor in cable-harnessed system

ϕ = fundamental matrix in DTFM

ρ_b = beam density

ρ_c = cable density

θ = cable wrapping angle

Θ = objective function

σ_b = longitudinal normal stress in beam

σ_c = axial normal stress in cable

κ = coordinate of the excitation location in x-direction in DTFM

$\Psi(x, s)$ = solution vector in Laplace domain in DTFM

Chapter 3

(x, y, z) = global Cartesian coordinates

A_b = beam cross sectional area

A_c = cable cross-sectional area

b = beam width

$\bar{b} = \frac{b}{2} + r_c$

B_1 = stiffness coefficient for Kelvin-Voigt damped equation

B_1^* = complex stiffness coefficient for hysteretic damped equation

B_1', B_1'' = real and imaginary parts ofB_1^*, respectively

C_b = Kelvin-Voigt coefficient of beam internal damping

C_c = Kelvin-Voigt coefficient of cable internal damping

D_1 = coefficient of Rayleigh dissipation function for Kelvin-Voigt damped system

D_{ak}, D_{ah} = air damping coefficient

E_b = beam Youngs modulus

E_c = cable Youngs modulus

E_b^*, E_b', E_b'' = complex modulus, storage modulus and loss modulus of beam, respectively

E_c^*, E_c', E_c'' = complex modulus, storage modulus and loss modulus of cable, respectively

f = frequency of excitation of the elastomer test system

g_f = dimensionless acceleration factor

g = acceleration due to gravity

h = beam thickness

$\bar{h} = \dfrac{h}{2} + r_c$

H_{FRF} = analytical expression of the FRF

I_b = beam second moment of area about y axis ($I_b = bh^3/12$)

j = square root of -1

K_1 = mass per unit length of the equivalent homogenized system

K^* = complex dynamic stiffness

K' = storage stiffness

L_e = length of the fundamental element

l_c = length of the cable clamped in the elastomer machine

n = number of cables

r_c = cable radius

T = cable tension

$w(x,t)$ = transverse displacement of cable-harnessed system

x_{sen} = x coordinate of the sensing location

$y(x,t)$ = transformed displacement variable

α_h = air damping constant in hysteretic damping model

α_k = air damping constant in Kelvin-Voigt damping model

η_{kb} = beam Kelvin-Voigt damping proportionality constant

η_{kc} = cable Kelvin-Voigt damping proportionality constant

η_{hb} = beam hysteretic loss factor

η_{hc} = cable hysteretic loss factor

η_{CH} = effective hysteretic loss factor in cable-harnessed system

ρ_b = beam density

ρ_c = cable density

θ = cable wrapping angle

ω_s = shaker excitation frequency

ϕ_n = nth mode shape function

β_n = nth solution of the characteristic equation of a clamped-free beam

A_n = Mass normalized coefficient of the mode shape ϕ_n

ω_n = natural frequency of the cable-harnessed system

Γ_n = nth temporal variable in the series solution of $y(x,t)$

ζ_k = kth modal damping ratio

$\mu\,(x,t)$ = a function used for transforming the displacement variable w to y

(t) = sinusoidal displacement of the elastomer test system

A_e = amplitude of the excitation in the elastomer test system

δ = delta function

Chapter 4

a = plate length (along x-direction)

A_c = cable cross-sectional area

b = plate width (along y-direction)

C_1, C_2 = coefficients in the total strain energy

C_{11}, C_{22} = constants in the equilibrium solution S(x,y)

D = flexural rigidity of the plate

$D_{11}, D_{12}, D_{66}, D_{22}$ = coefficients in the equation of motion of the homogenized system

E_c = cable Youngs modulus

E_p = plate Youngs modulus

E_k = total kinetic energy within the fundamental element

$E_{k,sys}$ = total kinetic energy of the system

h = plate thickness

K_1 = coefficient in the kinetic energy expression of the homogenized system

L_1 = length of the fundamental element (along x-direction)

L_2 = width of the fundamental element (along y-direction)

M_x^H = moment per unit length of homogenized system at the edge $x = a$

N_x = distributive compressive load on the plate per unit length in x direction

P_x = higher order stress resultant obtained at the edge $x = a$

r_c = cable radius

$S(x, y)$ = equilibrium solution

T = pretension in the cable

t = time

u_x, u_y, u_z = displacement field

U_{cable} = strain energy of the cable within the fundamental element

U_{plate} = strain energy of the plate within the fundamental element

U_{sys} = total strain energy of the system

U_{tot} = total strain energy within a fundamental element

$w(x, y, t)$ = transverse displacement in z-direction

$\bar{w}(x, y, t)$ = variable introduced to eliminate the inhomogeneous boundary condition terms

z_c = z coordinate of plate-cable interface, $z_c = h/2$

$\varepsilon_{ij}^{(2)}$ = second order strain tensor

ε_c = axial strain in cable

ρ_c = cable density

ρ_p = plate density

ν = poissons ratio

σ_{xx} = normal bending or axial stress in plate or cable per unit length, respectively

(η, ξ, z) = local coordinate system

(x, y, z) = global coordinate system

Chapter 5

A_c = cable cross-sectional area

a = plate length along the x-direction

b = plate width along the y-direction

C_i = cable strain energy coefficients for zigzag and diagonal pattern

C_i' = additional cable strain energy coefficients for diagonal pattern

$\bar{C}_i$ = the Cable segments in the fundamental element

D = flexural rigidity of the plate

E_p = plate Youngs modulus

E_c = cable Youngs modulus

H_i = coefficients in the expression of the systems total strain energy

h = plate thickness

K_1 = coefficient in the systems total kinetic energy expression

L_1, L_2 = planar dimensions of a fundamental element

L_1' = length variable to denote cable segment $\bar{C}_1$ along the η axis

m = number of fundamental elements in a pattern in each row

n = number of rows of repeating fundamental elements

N_x = uniformly distributed compressive load per unit length in the x-direction

N_y = uniformly distributed compressive load per unit length in the y-direction

N_{xy} = uniformly distributed shear load per unit length in the xy plane

T = cable pre-tension

T_p = plate kinetic energy within a fundamental element

T_c = cable kinetic energy within a fundamental element

T_{el} = total kinetic energy within a fundamental element

T_{sys} = total kinetic energy of the system

t = time

U_c = total cable strain energy within a fundamental element

$(U_c)^{\bar{C}_1}, (U_c)^{\bar{C}_3}$ = cable strain energy in the cable segments $\bar{C}_1$ and $\bar{C}_3$

U_{el} = total strain energy within a fundamental element due to plate and cable

U_p = strain energy due to plate within a fundamental element

$U_p^{(1)}, U_p^{(2)}, U_p^{(3)}$ = three components of plate strain energy

U_{sys} = total strain energy of the system

u_x, u_y, u_z = displacement field

w = transverse displacement

(x, y, z) = global coordinate system

x', x'' = coordinates along the cable direction

(η, ξ, z) = local coordinate system

z_c = z coordinate of the plate-cabled interface

$\varepsilon_{ij}^{(2)}$ = green-Lagrange strain tensor

$\varepsilon_{\eta\eta}, \varepsilon_{\xi\xi}, \varepsilon_{\eta\xi}$ = non-zero strain tensor components in local coordinates

$\varepsilon_{x'x'}, \varepsilon_{x''x''}$ = transformed strain along the $x\prime, x\prime\prime$ directions

$\varepsilon_{c\prime}, \varepsilon_{c\prime\prime}$ = total strain within the cable along the $x\prime, x\prime\prime$ directions

$\varepsilon'_x,\ \varepsilon'_y,\ \gamma'_{xy}$ = bending normal and shear strains in the plate

$\mathcal{L}$ = Lagrangian

ρ_p = plate mass density

ρ_c = cable mass density

θ = cable wrapping angle

ν = Poissons ratio

ω_{BP} = natural frequency of the bare plate

ω_{CP} = natural frequency of the cabled plate

Chapter 6

All the symbols used in this chapter were defined for Chapter 5.

Chapter 7

A_d, B_d, C_d = coefficients in a characteristic equation $f_d(\lambda) = 0$

A_c = cable cross-sectional area

D = flexural rigidity of the host plate

$D_{11}, D_{12}, D_{22}, D_{66}$ = coefficients of equation of motion of a parallel cable-harnessed plate

$D^o_{11}, D^o_{12}, D^o_{22}, D^o_{66}$ = coefficients of equation of motion of a specially orthotropic laminated plate

E_c = cable Youngs modulus

E_1, E_2, G_{12} = Youngs moduli and shear modulus of an orthotropic plate

E_p = host plates Youngs modulus

$f_d(\lambda)$ = characteristic equation of eigenvalues obtained for system with diagonal pattern

h_o = thickness of a specially orthotropic laminated plate

h = thickness of the host plate in a cable-harnessed plate

H_2, H_3, H_4, H_{13} = coefficients in equation of motion for cabled plate with diagonal/zigzag pattern

H_{10}, H_{11} = additional coefficients in equation of motion for diagonal pattern cabled plate

K_{diag} = stiffness matrix for a diagonal pattern cabled plate system

K_1 = homogenized mass per unit area of a cable-harnessed plate

L_2 = width of the fundamental element of a cable-harnessed plate

N_x = distributed compressive load on the plate per unit length in x direction

$(N_x)_{cr}$ = maximum value of N_x

n = number of parallel cables in a parallel cable-harnessed plate

P_{cr} = critical buckling load

T = cable tension

T_{max} = maximum tension to be applied for a stable system

U_{twist} = twist strain energy of the homogenized cabled plate system

w = transverse displacement

z_c = $z$coordinate of the plate-cable interface

ρ_p, ρ_c = mass density of the host plate and cable, respectively

ρ^o_p = mass density of a specially orthotropic laminated plate

λ = eigenvalue

θ = wrapping angle

ν = Poissons ratio of the host plate

ν_{12}, ν_{21} = Poissons ratio for 1-2 axis for an orthotropic plate

Chapter 8

A_c = cable cross-sectional area

A, B, C = undetermined coefficients in the solution of displacement vector

E_c = cable Youngs modulus

E = Youngs modulus of the cylindrical shell

h = cylindrical shell thickness

k = dimension-less constant defined as $h^2/(12R^2)$

K_0, K_1, K_2 = coefficient in the characteristic equation of non-dimensional frequency

l = length of a cylindrical shell

L = length of the host cylinder of the cable-harnessed shell

L_e = length of a fundamental element in cable-harnessed shell

$[L]$ = a matrix differential operator

$[L_{D-M}]$ = matrix differential operator for Donnell-Mushtari shell theory

$[L_{MOD}]$ = a modified matrix differential operator

m = axial wave number

M_x = longitudinal bending moment

M_1 = homogenized mass per unit area of the cable-harnessed system

n = circumferential wave number

N_c = number of parallel cables attached on a cable-harnessed cylindrical shell

N_x = distributed compressive force acting on the shell per unit length

P_x = axial membrane force

R = radius of the cylindrical shell

s = non-dimensional value of x

$\bar{s}$ = non-dimensional parameter defined for $\bar{x}$

t = time

T = cable tension

u_i = displacement vector

(u, v, w) = components of the displacement vector u_i

$(\bar{u}, \bar{v}, \bar{w})$ = displacement vector defined for a fundamental element

U = total strain energy of a cylindrical shell with no external loading

U_c = cable strain energy within a fundamental element

U_s = strain energy of a cylindrical shell within the fundamental element

U_{tot} = total strain energy within a fundamental element of cable-harnessed system

(x, r, θ) = global coordinate system of the cylindrical shell

$(\bar{x},\ \bar{r},\ \bar{\theta})$ = local coordinate system defined for the fundamental element

z = coordinate of a point in cylinder measured from mid-surface normal to radius

$(\alpha,\ \beta)$ = in-plane coordinate system of a general shell element

$(\varepsilon_\alpha, \varepsilon_\beta)$ = normal strain in the α and β directions, respectively in a general shell element

$\varepsilon^i_{\bar{x}}$ = second order initial strain in a compressed cylindrical shell in the x direction

$\gamma_{\alpha\beta}$ = shear strain in the $\alpha - \beta$ plane in a general shell element

$(\sigma_\alpha,\ \sigma_\beta)$ = normal stress in the α and β directions, respectively in a general shell element

$\sigma^i_{\bar{x}}$ = initial longitudinal stress on the cylinder due to distributed compressive loading

$\sigma_{\alpha\beta}$ = shear stress in the $\alpha - \beta$ plane in a general shell element

∇^2 = Laplacian

ρ = mass density of the cylindrical shell

ρ_c = cable mass density

ϕ_e = angle subtended by a fundamental element at the center of the cylinder

$\lambda = m\pi R/l$

ω = natural frequency in rad/s

Ω = non-dimensional frequency parameter

Chapter 1

Introduction

1.1 Motivation

Since the advent of electrical transmission, cables have played a significant role in human evolution, especially in the last century. With applications varying from data and signal transfer in electrical systems to load carrying structural elements in civil and marine structures, cables have become an essential part of human surroundings. Cables are generally attached to other structures in two ways: 1. fixed at both ends, in which cables undergo standalone motion (like guitar strings or suspended cables on bridge structures as shown in Fig. 1.1), or 2. harnessed to a host structure such that it is attached at multiple locations and both, cables and host structure, move together. Some examples of the second case are the cables harnessed to spacecraft or automotive panels as shown in Fig. 1.2. Since such panels are connected to cables at multiple locations, the panel's dynamic characteristics under an external excitation are sensitive to how the cables are harnessed/connected to the structure. Hence, for lightweight spacecraft structures, it is important to accurately model the cable dynamics. The motivation of the current work originates from the second case and lies in the fact that the accurate dynamic models of these lightweight structures play an important role in building robust control algorithms, which are essential for successful space programs. The low accuracy of these dynamic models can lead to controller overshoot which can result in failure of sensitive devices on-board. Because very few studies have been conducted on understanding the dynamic behavior of lightweight cable-harnessed structures, the current research work would play an important role in the aerospace industry. The paucity in literature (as discussed in the following section) is evident that this area of research has much scope for exploration.

Figure 1.1: Cable-stayed bridge with cables attached at its ends (Picture Information: Signature Bridge, New Delhi retrieved online from [1])

In the last five decades, the innovations in materials science have resulted in spacecraft structures and their components with increasing stiffness to weight ratio. Decreasing the mass of a structure without compromising on the strength has always been on a top priority for the designer of such structures. However, as the weight of these structures was plummeting, the increased use of data and signal transfer (for power and control applications of the spacecraft) was increasing the weight due to the use of cables. It has been reported that in the modern spacecraft, these cables account for 6-7% of the total mass and can be as high as 30% for some structural components as reported in Ref. [5]. Since it is required to have the accurate dynamic models for these lightweight structures (especially for robust control algorithms), accounting the cable dynamics plays a vital role in deciding the system's accuracy. Furthermore, due to the large size of space structures, the ground testing of the assembled structure is often complicated as discussed in Ref. [6], and hence, the accurate models of these structures are essential.

Motivated by this fact, the primary goal of this research was to develop simple analytical models that can predict accurate dynamic characteristics of the entire cable harnessed structure. Analytical models provide an essential tool for deconstructing the mechanisms underlying complex structures, helps in analyzing the behavior observed in the laboratory experiments, and making essential conclusions. Additionally, analytical models can provide a set of mathematical relations between 'system characteristics' and 'system parameters' that provides deeper insights into the system.

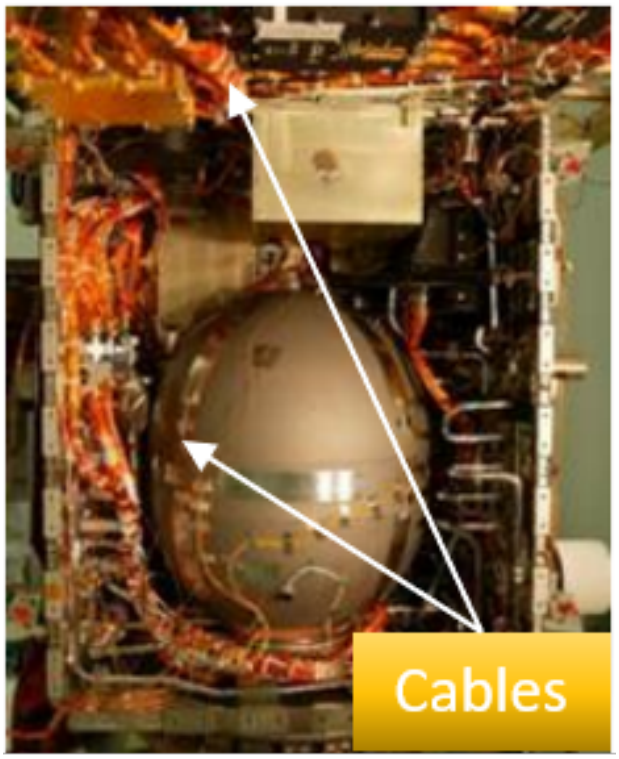

Figure 1.2: Cable-harnessed fuel propellant tank within a spacecraft structure with cables attached at multiple locations. Picture courtesy: Ardelean et al. [7]; reprinted by permission of the American Institute of Aeronautics and Astronautics, Inc.

1.2 Literature Review

In this section, a detailed overview of the literature related to this work has been presented. Although, the research related to the impact of cable dynamics on the lightweight space structures came into the spotlight in the previous decade only, the modeling approach used in this research have been used in the past as well. This starts with a literature survey on the dynamics of cable-harnessed space structures, followed by the works on the homogenization approach for modeling. Later on, few works on structural damping are presented to discuss energy loss mechanisms in distributed parameter systems. A brief overview of studies on cable-harnessed structures, which are aimed towards applications other than the space industry is presented. Finally, for the sake of completeness, some relevant differential equations in structural dynamics are presented that would be referred throughout the thesis for comparison with the proposed work.

1.2.1 Cable-Harnessed Space Structures

A series of studies carried out by the United States Air Force Research Laboratory, Space vehicle component branch (AFRL/VSSV) reported the preliminary studies on cable harnessing effects, refer [8, 9, 7]. For instance, the results presented in Ref. [8] highlighted the importance of modeling the cable dynamics that was previously ignored, as cables were predominantly modeled using non-structural mass elements at the cable attachment locations. In [9], the authors studied the frequency response of a free-free beam with and without cable harness mounted in the longitudinal and serpentine configuration as shown in Fig. 1.3. The cable harness used in this study followed the spacecraft integration standards and the cables were attached to the host beam using cable ties. It was observed that at low frequencies, the effect of cable mass was dominant; however, at high frequencies, cable damping played an important role. Additionally, the authors developed experimental procedures to determine the physical properties of cables in Ref. [7] for the accurate modeling of the cable harnesses.

Using the methods described in Ref. [7], key modeling parameters of a cable under lateral excitation were determined in Refs. [10, 11] using unique signal processing and analysis techniques. The spacecraft cables were also reported to behave *beam-like* lending credibility for using beam modeling to predict the dynamics of cable-harnessed structures. The details of problems encountered while testing these cables have been elaborated in Ref. [12] that includes tangents, rat holes, and dead ends. Finally, based on the testing methods, a database of cable properties (such as the equivalent extensional modulus, damping ratios,

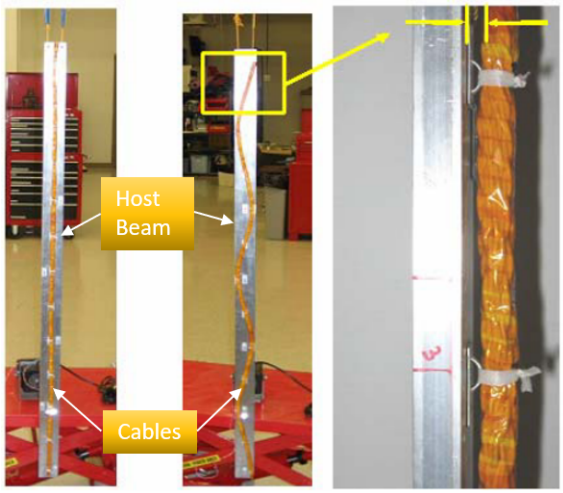

Figure 1.3: Cable harness mounting details (a) straight configuration, (b) serpentine configuration, and (c) side view of attachment. Picture courtesy: Goodding et al. [9]; reprinted by permission of the American Institute of Aeronautics and Astronautics, Inc.

area moment of inertia, and shear rigidity in cables) for the finite element (FE) modeling was developed in Ref. [13]. Once this characterization of cable properties was completed, the research on cable dynamics branched into two streams. The first stream dealt with modeling of standalone cables especially by characterizing the cable damping effects, as discussed in references [14, 15, 16, 17, 18, 19, 20, 21, 22]. Whereas, the second stream was focused on modeling and experiments of cable harness attached to a host structure, refer [6, 5, 23, 24, 25, 26, 27, 28, 29, 30, 31, 32, 33, 34, 35, 36, 2].

The next two paragraphs outlines the research conducted in the first stream. As mentioned earlier, damping in the cable plays a vital role in predicting the accurate dynamics of the lightweight cabled structure. To obtain frequency-independent modal damping for flexural structures, the authors in Refs. [14, 15] presented a concept of geometric rotation-based viscous damping model in which an internal resisting shear force of a beam is proportional to the time rate of change of the slope. The primary objective of these works was to obtain models based on the Euler-Bernoulli formulation that exhibits frequency-independent modal damping. This research was further extended in Refs. [16, 17, 18], assuming the spacecraft wiring harness cable as a shear and Timoshenko beam model. In all these works mentioned above, the authors modeled the *standalone cables* as damped beams and did not consider the damping in a cable-harnessed structure as a whole.

The study in Ref. [19] presents an excellent review of the damping models of helical

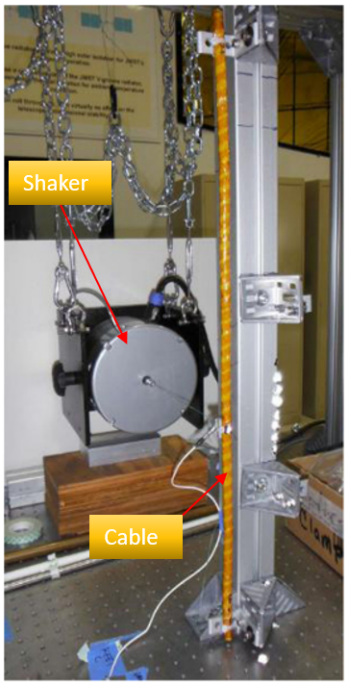

Figure 1.4: Cable test setup: A standalone cable is attached at two ends and is excited laterally using a shaker. Picture courtesy: Spak et al. [22]; reprinted by permission of the Springer Nature BV

cable behavior. The focus of this work was to examine the internal damping in the cables and exploring various energy loss mechanisms such as inter-wire friction, variable bending stiffness, and internal and viscoelastic dissipation. It was observed that in order to develop a realistic cable model, the effects of friction forces, viscoelasticity, and bending stiffness should be considered as a function of cable curvature and wire properties. Later on, this research group investigated the dynamic response of standalone space flight cables using the Euler-Bernoulli and Timoshenko beam models and considering proportional viscous and time hysteresis damping mechanisms for dissipative effects [20]. Empirical investigations of the spacecraft bundle cables to determine factors that affect the dynamics of the cables were performed in Ref. [21]. It was emphasized that cable must remain in tension to obtain a linear model since a slack cable would introduce nonlinearities in the system. Furthermore, the cables' characteristics, such as density, area, bending stiffness, and modulus of rigidity were determined to predict the natural frequencies of the cable in Ref. [22]. The test setup to measure these cable parameters has been shown in Fig. 1.4. Note that these works focused on studying standalone cables without attaching them to a host structures.

The second stream, as mentioned above, considers the effects of cables when they are harnessed to a host structure. Related to this, the AFRL research group studied the harnessed cables in two different ways: 1. the cables were attached to a host beam (one-dimensional structure) in Ref. [6] similar to that shown in Fig. 1.3 (a), and 2. the cables were attached to a host panel (two-dimensional structure) [5], similar to shown in Fig. 1.5. The cable properties summarized in Ref. [13] were used to model the cable as a shear beam element in a FE framework. The damping in the cables was included by assigning an experimentally determined element structural damping factor to the cable's finite elements. The resulting model matched very well with the experiments.

Further, the spectral element method was used to model the cable-harnessed beam structure as a double beam model and the results were found more efficient and accurate that the FE method [23, 24]. The authors in Ref. [25] used Distributed Transfer Function Method (DTFM) to model the cabled beam structure. This model included shear effects, tension and hysteretic damping for modeling the helically stranded cables. It was found to be in a better agreement with experiments compared to the cables being modeled as non-structural mass elements. The experimental setup of the cabled beam tested in Ref. [25] has been shown in Fig. 1.6. Note that in the above mentioned references [6, 5, 23, 24, 25], the authors have modeled the attached cables in a straight configuration to their respective host structures on its one surface. However, in reality, these cables are harnessed in a very complicated pattern and hence, to answer the question "*How would the dynamics of a structure change if the cables are wrapped around it?*", further research was conducted on wrapped cable-harnessed structures. The current thesis also contributes to answering the above question.

The research on the effects of a complex attachment of the cables on a host beam has been described in various studies [26, 27, 28, 29, 30, 31, 32, 33]. It is also important to note that these works were among the first to develop analytical solutions of the cable-harnessed beam structures. In the initial works, the cable was modeled as a pre-tensioned bar member that can not undergo compression [26, 27]. However, later, it was found that the cable tension did not play any effect in the analytical model and hence, the cable was modeled as a taut string element with a constant tension [28]. To further increase the model accuracy, a variable tension model, and a higher-order Green-Lagrange strain tensor was used in Ref. [29]. Additionally, pre-compression in the beam due to cable tension was also considered while modeling. One of the major assumptions made in these models was that the string was assumed to be in perfect contact with the beam structures implying no-slip condition. These assumptions resulted in a linear analytical model that was simple to analyze. The authors also studied two wrapping patterns that were periodic in geometry and were coined as *zigzag* and *diagonal* patterns as shown

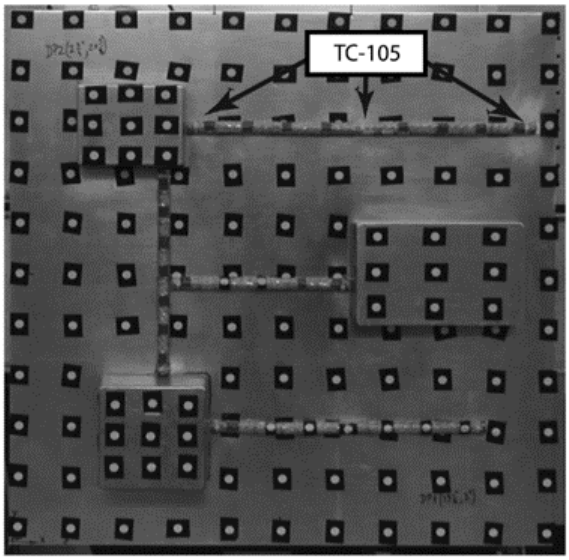

Figure 1.5: Test Panel with cables and electronic boxes. Picture courtesy: Coombs et al. [5]; reprinted by permission of the American Institute of Aeronautics and Astronautics, Inc.

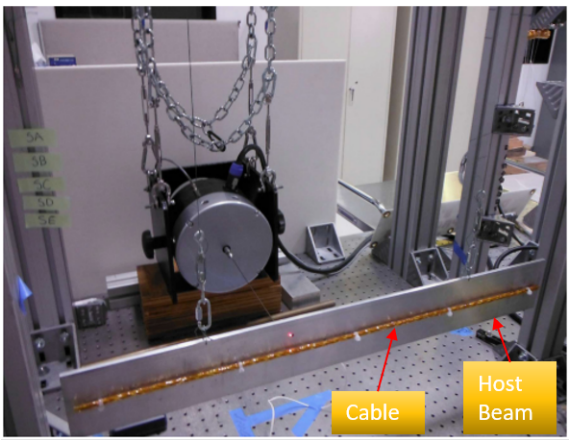

Figure 1.6: Cabled beam test set-up; cable attached to beam with cable ties and beam suspended for free end condition simulation. Picture courtesy: Spak et al. [25]; reprinted by permission of the Elsevier Science & Technology Journals

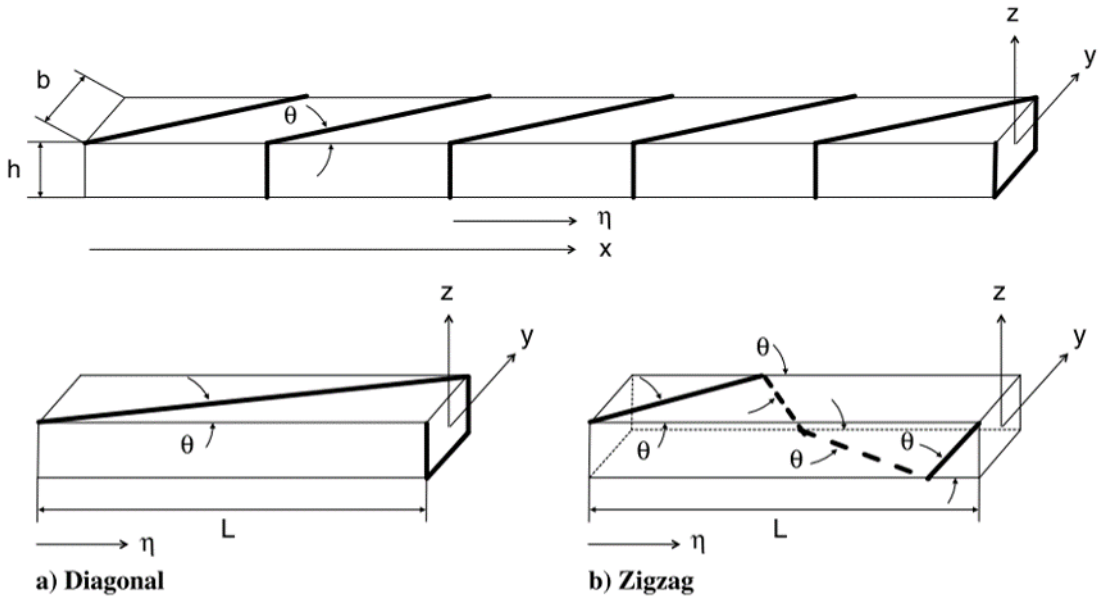

Figure 1.7: Top: Cable-harnessed beam structure with a periodically wrapped pattern; Bottom: Fundamental elements of the periodic structure. Picture courtesy: Martin et al. [31]; reprinted by permission of the American Institute of Aeronautics and Astronautics, Inc.

in Fig. 1.7. A homogenization technique was used to obtain analytical solutions to the problem. Further, the dynamic behavior of the system was validated in ANSYS in Ref. [31] along with a detailed discussion on parametric analysis. The experimental validation of periodically wrapped cabled beams, using frequency response functions, was presented in Ref. [30] for several structures wrapped in the zigzag pattern. The dynamic effects of cables that are non-periodically wrapped around the beam for a more general case have been studied in Ref. [33]. In this study, the Lindstedt - Poincare method was used to solve the spatially dependent partial differential equations (PDEs) for response functions that were also experimentally validated. However, these studies on wrapped cable-harnessed structures did not consider damping mechanisms in their models, resulting in a major gap in the literature. The study presented in the current work is heavily based on these works as the author used similar model assumptions to fill the gap in the literature.

Some recently published studies also modeled cables using string theory assumptions. The studies shown in Refs. [34, 35, 36, 2] consider coupling effects between different coordinates of motion due to a straight cable harnessed at an offset to the beam centerline as

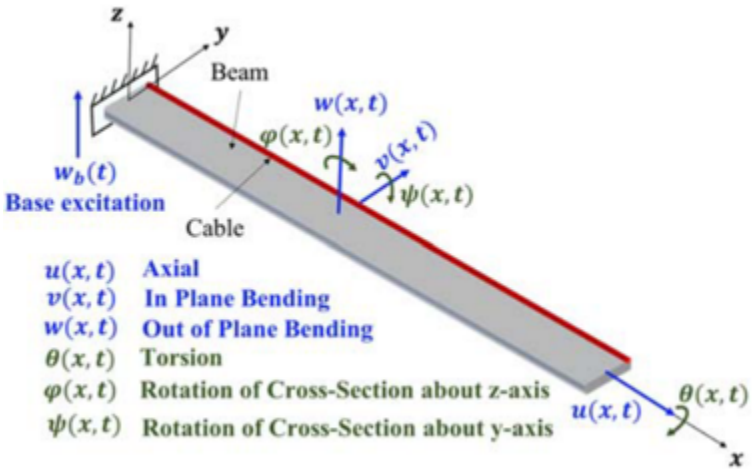

Figure 1.8: Schematic of the cable-harnessed beam cable present at an offset to beam centreline. Picture courtesy: Yerrapragada et al. [2]

shown in Fig. 1.8. These works also used similar model assumptions as Ref. [31] and validated the results experimentally. However, the damping effects were still not considered in these studies.

Another recent work based on the periodically wrapped cable-harnessed beam systems deals with the optimal placement of the cables such that there is minimal impact on the dynamics of the host structure [37]. In this work, the authors have used the formulations developed by Martin et al. [31] and applied optimization techniques to minimize the difference between the natural frequencies of the cabled beam and bare beam. This resulted in the optimal number of fundamental elements for the zigzag and diagonal patterns. The developed formulation is also experimentally validated in the paper.

This thesis is a result of conducting research on cabled structures that aims to: 1. investigate and fill gaps present in the literature on modeling damping mechanisms, and 2. develop and formulate new analytical solutions that are more realistic to the industrial applications. The cabled structures find a lot of applications in space and automotive industry and hence, these models can be applied during the design phase for a accurate model. In this effort, it was identified that modeling the damping mechanisms in previously studied works on *periodically wrapped cable-harnessed beams* [30, 31] was by far the most significant gap to be filled. Since cable damping effects are difficult to characterize, these effects were not considered in the previous works. However, it has been repeatedly mentioned in the literature that modeling the cable damping effects is essential to predict

the accurate dynamic behavior of the cabled structures.

Further, it should be noted that the analytical solutions in literature have been presented only for *beam-like* host structures. Although, *plate-like* two-dimensional host structures are more realistic than beam-like structures, no analytical solutions have been presented for cable-harnessed plates as per the author's best knowledge. A few numerical studies have been published [5, 38] that consider cables harnessed to flat panels, but no analytical solutions were proposed in these works. Therefore, in this thesis, new PDEs that govern the dynamics of cable-harnessed plate structures are developed, followed by experimental validation, thereby constituting the significant contribution of this research.

1.2.2 Homogenization technique

Complicated structures are often modeled using the FE framework, in which the system is discretized into many finite elements. However, this method becomes computationally expensive when high accuracy is required, mainly when vibrations or buckling problems need to be solved. Moreover, for the systems with a periodic geometry, such as lattice-like or truss structures, the FE method does not utilize any advantage of the periodicity. Due to these drawbacks, researchers use other methods to simplify system modeling using periodicity conditions and obtain an *equivalent continuum structure* that can analyze the complex structure efficiently. The continuum modeling techniques for repetitive lattice structures are reviewed in Ref. [39]. There are typically three approaches, also known as homogenization techniques, to obtain the equivalent continuum structures that are studied in the literature:

- use of a discrete field method to obtain difference equations, which are further converted to differential equations using Taylor's series expansion (refer [40, 41, 42])
- application of multi-scale asymptotic expansion (refer [43, 44, 45])
- use of energy-equivalence method (refer [46, 47, 48, 49, 50, 51, 52, 53, 54, 55, 56, 57])

In this thesis, the energy equivalence homogenization technique is used to obtain the analytical models of different cable-harnessed structures. This technique has been widely used in the past to obtain the dynamic behavior of various lattice-like systems. Some of the applications include the modeling of net and cloth dynamics [47], gridwork dynamics [48], a micropolar continuum [46]. In these works, the lattice structures are simplified by modeling them as an equivalent homogenized continuum thus expressing the model as a

partial differential equation in space and time. Similarly, this technique has been widely used for modeling complicated truss structures as equivalent continuum beams that are simple to solve and analyze. Note that the truss structures find significant applications in spacecraft and satellite systems [49, 39, 51, 52, 53, 54, 55, 56, 57].

The energy-equivalence homogenization technique for modeling periodic truss structures is based on defining an equivalent continuum beam such that the latter has approximately the same kinetic and strain energy upon applying the same displacement field as in the original structure. This approximation yields accurate results when the number of periodic fundamental elements in the structures are large in number. In this technique, the kinetic and strain energy of the fundamental element is first calculated using the exact displacement field. In the next step, the displacement is expanded as a Taylor's series to determine an approximation of total energy expressions which are then divided by the length of fundamental element in order to obtain energy densities. These densities are integrated over the domain to obtain the total strain and kinetic energy of the continuum system. Further, Hamilton's principle is applied to obtain a PDE of the homogenized continuum in one-dimensional space and time that was initially a complex structure.

As discussed in the previous paragraphs and the past works, the energy-homogenization technique helps to obtain simplistic analytical models of complicated systems. Hence, this method is used in the current study to model the cable-harnessed beam-like and plate-like structures where the cable harness generates inhomogeneity in the system. For the cable-harnessed beam systems, this method has been used for undamped structures in the past [31] which was also experimentally validated in Ref. [30]. However, the current work extended the work done in Ref. [31] to model the damping mechanisms and validating it using a numerical and experimental approach. In addition, the energy-equivalence homogenization technique was applied to model the dynamics of the *plate-like cable-harnessed structures* for the first time which also yielded promising results.

1.2.3 Structural damping

Incorporating accurate damping models in distributed parameter systems is often a difficult task to accomplish due to the presence of various factors contributing to energy loss. The passive damping in the structures has been studied since the 1800s with one of the oldest treatises on this topic by Lord Rayleigh [58] and it is still one of the mystery. Lord Rayleigh proposed 'dissipation function', a quadratic function for energy dissipation rate which remains one of the most extensively used damping mechanisms in the structures. He proposed the idea of a 'damping matrix' as a linear combination of 'stiffness matrix'

and 'mass matrix' (*proportional damping*). This idea has further benefited many scientists and modal analysts who wish to incorporate damping in their models. In the case of proportionally damped systems, the procedure of modal analysis can be similarly applied as in the case of undamped systems which provides considerable simplifications in the modeling of damped systems.

The damping in a continuum structure can be studied by either discretization into a lumped parameter model (represented in the form of coupled ordinary differential equations) or as a distributed parameter model (represented in the form of a PDE). The analytical models developed in the present thesis are based on distributed parameter models because having a reliable low-order high fidelity PDE is advantageous for implementing control algorithms. However, for a vibrating continuum, for example, a beam can have energy loss due to several mechanisms making it difficult to model the exact loss in the system. One of them is material (internal) damping, which is generally low for metals and high for polymer or composite materials. Another mechanism is the external damping in which one of the major source is the air damping (interaction of the beam with surrounding medium). Some other sources of external damping includes the energy loss at boundaries (if the system is not free at all its ends), or the presence of accelerometer wax/cables attached to the structure (if non-contact measurement techniques are not used). Although, few loss mechanisms can be easily quantified and included in the modeling technique, there are always some qualitative loss mechanisms which have to be either ignored due to the modeling complexity (like the loss at boundaries) or must be reduced (like using a laser Doppler vibrometer instead of an accelerometer). Hence, based on the loss mechanisms, relevant damping models are used for modeling purpose.

Different modeling techniques for lumped parameter systems that include single degree-of-freedom systems and multiple degree-of-systems has been discussed in a dissertation by Adhikari [59]. Since the focus of the current thesis is based on damping in the distributed parameter system, four practical models are presented here as discussed in Ref. [60]. These damping models were presented for a Euler-Bernoulli beam structure, however, they can be used for any other distributed parameter system as well.

1. **Viscous damping**:

   The PDE for the vibration of an Euler-Bernoulli beam in transverse direction with viscous damping can be written as:

$$\frac{\partial^2}{\partial x^2}\left(E_b I_b(x)\frac{\partial^2 w(x,t)}{\partial x^2}\right) + \rho_b A_b \frac{\partial^2 w(x,t)}{\partial t^2} + \gamma \frac{\partial w(x,t)}{\partial t} = 0 \tag{1.1}$$

where γ is the viscous damping constant of proportionality, $w(x,t)$ is the transverse displacement of the beam, $E_bI_b(x)$ is the spatially dependent flexural rigidity of the beam, ρ_b is the constant mass density and A_b is the beam cross-sectional area. The physical basis of including this damping is the air resistance that causes a resistance force proportional to the velocity $\frac{\partial w(x,t)}{\partial t}$.

2. **Strain-rate damping**:

   The PDE for the vibration of an Euler-Bernoulli beam in transverse direction with strain-rate damping can be written as:

$$\frac{\partial^2}{\partial x^2}\left(E_bI_b(x)\frac{\partial^2 w(x,t)}{\partial x^2}\right)+\rho_bA_b\frac{\partial^2 w(x,t)}{\partial t^2}+\beta I_b\frac{\partial^5 w(x,t)}{\partial x^4\partial t}=0 \tag{1.2}$$

   where β is the strain-rate dependent damping constant. In this 'strain-rate' damping model, the stress is proportional to strain as well as strain rate in the constitutive relationship. This damping model is also known as *viscoelastic* or *Kelvin-Voigt* damping model and has been later discussed in this work in mode detail.

3. **Time hysteresis damping**:

   The PDE for the vibration of an Euler-Bernoulli beam in transverse direction with the time hysteresis damping can be written as:

$$\frac{\partial^2}{\partial x^2}\left(E_bI_b(x)\frac{\partial^2 w(x,t)}{\partial x^2}-\int_{-r}^{0}g\left(s\right)\frac{\partial^2}{\partial x^2}w\left(x,t+s\right)ds\right)+\rho_bA_b\frac{\partial^2 w(x,t)}{\partial t^2}=0 \tag{1.3}$$

   where the damping is introduced by assuming stress-strain relationship in which stress is proportional to strain in addition to the past history of the strain. The history kernel $g(s)$ is defined as

$$g\left(s\right)=\frac{\alpha}{\sqrt{-s}}\exp\left(\beta s\right) \tag{1.4}$$

   where α and β are constants.

4. **Spatial hysteresis damping**:

   The PDE for the vibration of an Euler-Bernoulli beam in transverse direction with the spatial hysteresis damping can be written as:

$$\frac{\partial^2}{\partial x^2}\left(E_b I_b(x)\frac{\partial^2 w(x,t)}{\partial x^2} - \frac{\partial}{\partial x}\left[\int_0^l h\left(x,\xi\right)\left\{\frac{\partial^2 w\left(x,t\right)}{\partial x \partial t} - \frac{\partial^2 w\left(\xi,t\right)}{\partial x \partial t}\right\} d\xi\right]\right) + \rho_b A_b \frac{\partial^2 w(x,t)}{\partial t^2} = 0 \quad (1.5)$$

where the kernel function is defined as

$$h\left(x,\xi\right) = \frac{a}{b\sqrt{2\,\pi}} \exp\left(-\frac{\left(x-\xi\right)^2}{2b^2}\right) \quad (1.6)$$

where a and b are constants.

The spatial hysteretic damping is based on interpreting the energy lost in the beam as resulting from differential rates of rotation of neighboring beam sections causing internal friction.

There are several other models proposed for more complicated nonlinear damping and non-viscously damped systems; however, the scope of the current research would include only linear viscous, viscoelastic and hysteretic damping models.

1.2.4 Other applications of cabled structures

The cable-harnessed structures can have applications other than space structures. It was mentioned in section 1.1 that cables are generally attached to the structures in two ways: 1) either fixed to the host at two ends, or 2) harnessed to a host structure at multiple points.

The study of the first method was mainly discussed in the applications that include, but are not limited to, civil or marine structures. In civil structures, the effect of cable dynamics in cable-stayed bridges has been discussed in detail, primarily by considering nonlinear vibrations in Refs. [61, 62, 63, 64, 65]. Moreover, for the marine structures as well, nonlinear vibration analysis was done in the works [66, 65] where the cable is assumed to have a tension-slack configuration. More applications of this attachment method include the dynamics of the overhead power transmission lines where propagation of shock waves is studied in another nonlinear model proposed in Ref. [67]. It is important to note that these are possible applications of cabled structures where cable dynamics impact the host

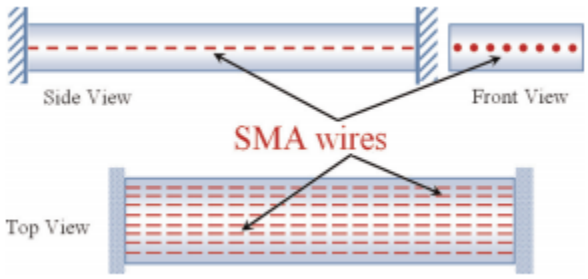

Figure 1.9: A schematic of the shape memory alloy (SMA)-reinforced beam. Picture courtesy: Rezaei et al. [70]. Permission to reuse this picture is pre-approved as per SAGE publishing.

structure dynamics. However, the scope of the current study is focused on the second method of cable attachment.

With respect to the second method, in addition to the applications on space structures, there are other works, that are worth mentioning. One of the applications of modeling cable-harnessed structure lies in optical fiber coupler used in telecommunications. A simplified model developed in Ref. [68] presents the modeling of the substrate as a beam and the optical fiber as a taut string. The string is connected to the substrate at multiple points using an adhesive material, vibrating together and resulting in a coupled equation of motion. In the present work as well, the cable is modeled as a taut string. In another application [69], a cable is used to suppress the vibrations in a cantilever beam when attached at finite locations. An interesting application caters to the structures that have embedded shape memory alloy (SMA) wires. In Ref. [70], the SMA wires are embedded in a clamped-clamped beam as shown in Fig. 1.9. In the formulated mathematical model, the wires and beam are assumed to be in perfect no-slip contact. In addition, the effect of the pre-strain of the SMA wires on the beam structure is taken into consideration. These two assumptions are also used while modeling the cable-harnessed structures in the current thesis. Experimental studies on the shift in dynamics of the host structure due to embedded SMA wires was presented in Ref. [71].

There is no analytical model present in the literature that considers the cable-harnessed structures with plates as the substrate (host). In this study, the host structures were modeled as two-dimensional plate-like structures and cables as taut strings. The proposed linear models are simple to analyze, have high accuracy and can be easily implemented in control algorithms.

1.2.5 Standard differential equations in structural dynamics

In this thesis, the equivalent continuum models are developed for cable-harnessed structures. These models are represented in form of PDEs, which are shown to have a similarity with some standard PDEs that are studied in the field of structural dynamics. The relevant PDEs are presented in this section to help in making a comparison while analyzing the PDEs of the cable-harnessed structures in later chapters by referring to this section. Following are the differential equations of different structures under free vibration in transverse direction:

1. Euler-Bernoulli beam (undamped) [72]

$$E_b I_b \frac{\partial^4 w(x,t)}{\partial x^4} + \rho_b A_b \frac{\partial^2 w(x,t)}{\partial t^2} = 0 \tag{1.7}$$

   In this equation, $w(x,t)$ represents the transverse displacement of a Euler beam. In addition, the Young's Modulus E_b and mass density ρ_b are assumed to be constant across the length of the beam. The area of cross-section A_b is also uniform and the I_b represents the second moment of area of the beam's cross-section.

2. Euler-Bernoulli beam with air and Kelvin-Voigt damping [72]

$$E_b I_b \frac{\partial^4 w(x,t)}{\partial x^4} + \rho_b A_b \frac{\partial^2 w(x,t)}{\partial t^2} + \gamma \frac{\partial w(x,t)}{\partial t} + \beta I_b \frac{\partial^5 w(x,t)}{\partial x^4 \partial t} = 0 \tag{1.8}$$

   In this equation, in addition to the terms in Eq. 1.7, the third term represents the viscous or air damping and the fourth term corresponds to the strain-rate damping, also called as Kelvin-Voigt damping. γ and β are the damping constants.

3. Euler-Bernoulli beam with hysteretic damping [73]

$$E_b^* I_b \frac{\partial^4 w(x,t)}{\partial x^4} + \rho_b A_b \frac{\partial^2 w(x,t)}{\partial t^2} = 0 \tag{1.9}$$

   The hysteretic damping in an Euler beam is included by using a complex Young's modulus E_b^*. The real part of this term is called the storage modulus and corresponds to the stiffness in the system, whereas the imaginary part is called the loss modulus that corresponds to damping.

4. Kirchhoff's thin rectangular plate [74]

$$D\left(\frac{\partial^4 w(x,y,t)}{\partial x^4}+2\frac{\partial^4 w(x,y,t)}{\partial x^2\partial y^2}+\frac{\partial^4 w(x,y,t)}{\partial y^4}\right)+\rho_p h\frac{\partial^2 w(x,y,t)}{\partial t^2}=0 \qquad (1.10)$$

This equation represents the governing motion in the transverse direction of a thin rectangular plate. The transverse displacement at a point (x, y) within the plate at time t is defined as $w(x, y, t)$. D represents the flexural stiffness of the plate, ρ_p is plate's mass density, and h is the thickness.

Moreover, the first term, $D\frac{\partial^4 w(x,y,t)}{\partial x^4}$, corresponds to the bending stiffness in the x-direction; the second term, $2D\frac{\partial^4 w(x,y,t)}{\partial x^2\partial y^2}$ corresponds to the twisting and coupled-bending stiffness; and the third term $\frac{\partial^4 w(x,y,t)}{\partial y^4}$ corresponds to the bending stiffness in the y-direction. Additionally, the last term represents the inertia effect in the system.

5. Specially orthotropic laminated plate [3]

$$D^o_{11}\frac{\partial^4 w(x,y,t)}{\partial x^4}+2(D^o_{12}+2D^o_{66})\frac{\partial^4 w(x,y,t)}{\partial x^2\partial y^2}+D^o_{22}\frac{\partial^4 w(x,y,t)}{\partial y^4}+\rho^o_p h\frac{\partial^2 w(x,y,t)}{\partial t^2}=0 \qquad (1.11)$$

The Eqs. 1.11 and 1.12 are generally discussed under the umbrella of 'mechanics of composite materials'. A *specially orthotropic lamina* has principal material axes (direction of fiber alignment) aligned with the natural body axes. In a specially orthotopic laminated plate, there is either a single layer of a specially orthotropic material or multiple specially orthotropic layers that are symmetrically arranged about the laminate middle surface.

The equation 1.11 has similar derivative terms as that of Kirchhoff's plate; however, due to presence of fibers, the material constants are different in a specially orthotropic laminated plate. D^o_{11} and D^o_{22} corresponds to the flexural rigidity in the x and y direction, respectively. On the other hand, D^o_{12} and D^o_{22} corresponds to the stiffness in the coupled-bending and twist motion, respectively. The subscript o is used to differentiate these coefficients, corresponding to specially **o**rthotropic plate, with those developed in the current research work, As it is seen later in the Chapters 4 and 5, the governing PDEs of the equivalent continuum structure of some cable-harnessed structures are of same form as Eq. 1.11 and the coefficients would be used without the subscript o.

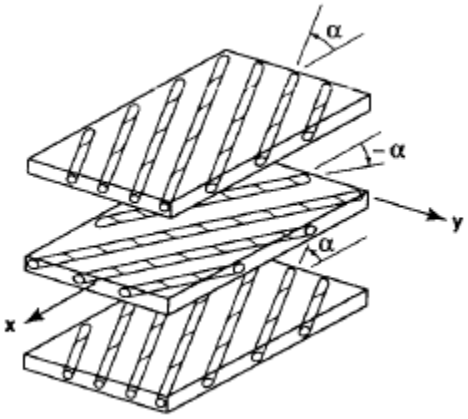

Figure 1.10: Unbonded view of a three-layered regular symmetric angle ply laminate. Picture courtesy: R. M. Jones [3]

6. Symmetric angle-ply laminated plate [3]

$$D_{11}^{SAP}\frac{\partial^4 w(x,y,t)}{\partial x^4} + 4D_{16}^{SAP}\frac{\partial^4 w(x,y,t)}{\partial x^3 \partial y} + 2(D_{12}^{SAP} + 2D_{66}^{SAP})\frac{\partial^4 w(x,y,t)}{\partial x^2 \partial y^2} + 4D_{26}^{SAP}\frac{\partial^4 w(x,y,t)}{\partial x \partial y^3} + D_{22}^{SAP}\frac{\partial^4 w(x,y,t)}{\partial y^4} + \rho_p^{SAP} h\frac{\partial^2 w(x,y,t)}{\partial t^2} = 0 \tag{1.12}$$

A symmetric angle-ply laminate falls under a sub-class of symmetric composite laminates which has adjacent lamina at an angle $+\alpha$ and $-\alpha$ to the axial direction of the laminate as shown in Fig. 1.10. Such laminates have orthotropic laminae of equal thicknesses. In addition to the terms shown in Eq. 1.11, there are two additional terms in the PDE of a symmetric angle-ply laminate corresponding to D_{16}^{SAP} and D_{26}^{SAP} that represents the bend-twist coupling in the laminated plate. The governing PDE of the equivalent continuum model of a diagonal pattern cable-harnessed structure studied in Chapter 5 was found similar to that of a symmetric angle-ply laminated plate.

1.3 Thesis Objectives

The overall objective of this thesis is towards creating accurate analytical models for cable-harnessed structures. To start with, the modeling technique to include damping in the

cable-harnessed beam structures is developed for the cables wrapped in zigzag and diagonal manner. In order to complete the analytical model, the damping characterization of cable material is done followed by the experimental modal testing of the fabricated cable-harnessed beam structures for validation purpose. As a next step towards the major contribution of the thesis, analytical modeling of the dynamics of cable-harnessed plate structures when cables are attached in a complex wrapped pattern with a periodic fundamental element is developed. The numerical verification of this study is presented by comparing the results with finite element simulations. The proposed analytical models are also experimentally validated for multiple cable-harnessed plate structures with parallel, zigzag and diagonal patterns.

1.4 Organization of thesis

In this section, the outline of the thesis is presented.

In Chapter 2, mathematical modeling is developed to incorporate damping mechanisms in cable-harnessed beam structures. Two energy loss mechanisms, namely Kelvin-Voigt and hysteretic damping models, have been considered for modeling purpose. The verification of the model is done by comparing results with DTFM. Finally, a detailed parametric analysis to study the effect of various system parameters on overall damping has been discussed.

In Chapter 3, the material damping in different cables were characterized to get the best fit for Kelvin-Voigt and hysteretic damping model using the characterization curves. The experimental modal analysis on the fabricated cable-harnessed beam setups was then conducted, and the dynamic characteristics of the system were obtained. A comparison with the analytical model and the relevant discussion is then presented.

In Chapter 4, an analytical modeling technique has been proposed for the cable-harnessed plate structure with cables attached in a straight configuration parallel to each other. Experimental validation is further presented for this model by comparing the natural frequencies, FRFs and mode shapes of different fabricated cable-harnessed structures.

In Chapter 5, an analytical modeling technique has been proposed for the cable-harnessed plate structure with cables attached in complex wrapping patterns. The governing equations of motion are derived for two different wrapping patterns, namely diagonal and zigzag. The model results were analyzed using frequency response functions and compared using FE simulations for different boundary conditions. Finally, a detailed parametric analysis is presented by varying system parameters and discussing their effects on change in system dynamics.

In Chapter 6, the modal testing experiments are conducted on the cable-harnessed structures with cables wrapped in periodic patterns and the obtained results are used to validate the analytical model proposed in Chapter 5. The novelty of the proposed model is also highlighted by comparing it with an existing cable-harnessed beam model.

In Chapter 7, the stability of the governing partial differential equations obtained in Chapters 4 and 5 for cable-harnessed plates are discussed.

In Chapter 8, a preliminary investigation on cable-harnessed cylindrical shell structure was examined. A homogenized equivalent continuum model was developed for a structure with multiple cables attached to a cylindrical shell in a parallel configuration. The results obtained from the proposed analytical model are verified using FE simulations.

In Chapter 9, the major conclusions and contributions of the current thesis are presented. In addition, the future improvements and further possible developments based on the current work has also been presented.

Chapter 2

Modeling of Damping Mechanisms in Cable-Harnessed Beam Structures

In this chapter, an analytical model is developed based on the mathematical formulation of damping mechanisms in cable-harnessed beam structures[1]. This research work was conducted to further build on the work of the undamped model proposed by Martin et al. [31, 30] and fill a significant gap in the literature. The present study was conducted by incorporating two energy loss mechanisms namely Kelvin-Voigt and hysteretic damping models.

The chapter 2 is organized as follows: the cable-harnessed beam system is first described and all the model assumptions are listed. To obtain the equivalent continuum model of the structure, the expressions of kinetic energy and the strain energy are calculated for the system that contains the contributions from both the beam and cable. As mentioned above, to include the damping in the system, two models were considered. For the Kelvin-Voigt damping model, to obtain the total energy loss in the system, the total Rayleigh dissipation function was calculated. Whereas for the hysteretic damping model, the energy loss mechanism was accounted in the expression of complex strain energy. The PDEs for the equivalent continuum model of the structure were then obtained using the homogenization method and Hamilton's principle. Next, in order to present the numerical verification for the proposed analytical model, a Distributed Transfer Function Method (DTFM) was used. (DTFM has also been used earlier by Spak et al. [25] for modeling the damping in the cables that are harnessed to the beam in a longitudinal configuration. However, in the

[1]The work presented in this chapter has been published as a research article in the *ASME Journal of Vibration and Acoustics* [75].

present work, the systems with cables that are wrapped around the beam structure are studied.) Next, a detailed parametric analysis is presented followed by the comparisons between the two damping models.

2.1 Mathematical modeling

The homogenization method is a useful approach that helps simplify mathematical modeling for structures of repeated patterns. Periodicity condition constitutes a major criterion for the validity of this approach in dynamic modelling of structures. In this regard, the energy-equivalence homogenization method, as discussed in the chapter 1, is one of the most common approaches in which kinetic and strain energies and Rayleigh dissipation functions for a fundamental repeated element are found in terms of the displacement components evaluated at the element center. It is then assumed that for a structure with a sufficiently large number of fundamental elements, the local effects within an element are negligible and, therefore, the energy expressions of the fundamental element divided by the elements length are good representatives for the energy per unit length of the entire system. These energy per unit lengths are then used along with the Hamilton's principle to obtain the equations of motion for the entire system.

2.1.1 System description and model assumptions

The system consists of a uniform rectangular cross-section beam, made of homogeneous and isotropic material, wrapped by cables in repeated patterns as shown in Figs. 2.1 and 2.2. Two wrapping patterns are considered namely zigzag and diagonal pattern, and their respective fundamental elements are also shown in these figures. The cable is assumed to be under a pre-tension in the equilibrium position and remains in tension during vibration. The pre-compression in the beam element, as a result of the cable tension, has also been accounted for. The attached cable has a circular cross-section (radius $= r_c$) and is wrapped around the beam structures in a periodic pattern. The length of the host beam structure is denoted by l and that of fundamental repeated element is L_e. The width and thickness of the host beam is denoted by b and h, respectively. The local coordinate system (ξ, y, z) is defined for the fundamental element, whereas the global coordinate system (x, y, z) caters to the entire beam system.

The effects due to the initial twist due to the pre-tensioned wrapping has been shown to be negligible [31] and, therefore, is ignored in the present mathematical model. Further,

the cable is assumed to stay in perfect contact with the host beam during vibration. This assumption enables the model to assume a single degree of freedom for both the beam and cable structure, which makes the model simplistic in nature compared to the case when two different degrees of freedom (DOF) are considered. Further complexity is introduced in the two DOF model as the connection element would also have to be modeled separately. In addition, this perfect contact assumption is reasonable because in the earlier studies on cable-harnessed beam structures, refer [31, 30, 33], it has been seen that when the cables are wrapped around the host beam in tension, the system dynamics observed in the experiments can be well predicted using this modeling assumption.

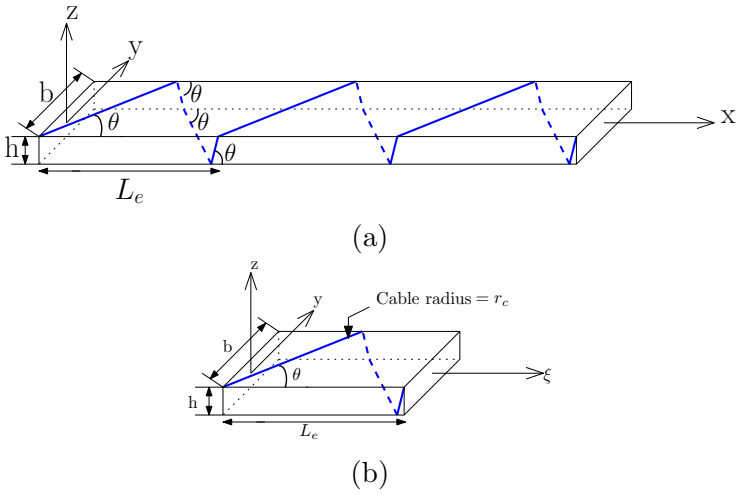

Figure 2.1: (a) Schematic of a cable-harnessed beam with the zigzag pattern, (b) Fundamental element of the zigzag pattern

In the presented homogenized model, Euler-Bernoulli beam assumptions are used to model the host beam characteristics. Hence, as a starting point, a linearized displacement field is assumed:

$$\begin{aligned} u_x(x,z,t) &= -z\, w'(x,t) \\ u_y(x,z,t) &= 0 \\ u_z(x,z,t) &= w(x,t) \end{aligned} \tag{2.1}$$

where $w(x,t)$ is the transverse displacement of a coordinate x of the beam and w' indicates the partial derivative of w with respect to x. This displacement field is then used to find the kinetic energy, strain energy and energy lost due to damping for a fundamental element in terms of the spatial and time derivatives for these displacement components that

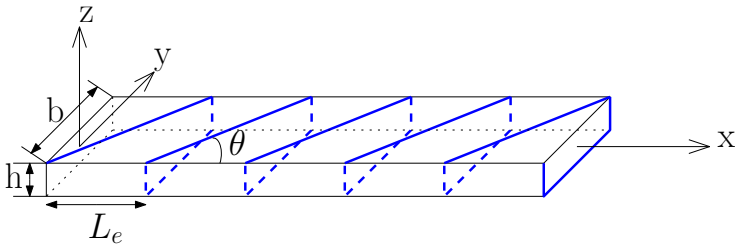

(a)

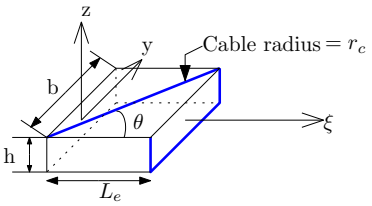

(b)

Figure 2.2: (a) Schematic of a cable-harnessed beam with the diagonal pattern, (b) Fundamental element of the diagonal pattern

are evaluated at the center of the fundamental element as will be shown in the following sections.

2.1.2 Kinetic energy

Neglecting the rotary inertia, the kinetic energy of the fundamental element can be found using the mass of the element and the transverse velocity evaluated at the center of the element (assuming $\frac{\partial w(\xi,t)}{\partial t}\Big|_{\xi=L_e/2} = \dot{w^*}$) as [31]:

$$T_e = \frac{1}{2} m_e \left(\dot{w^*}\right)^2 \tag{2.2}$$

where the fundamental element mass for each of the two patterns shown in Figs. 2.1 and 2.2 can be found using the detailed derivations shown in Appendix section A.1 as

$$\begin{aligned} m_{e-zigzag} &= \left(\rho_b A_b + \frac{\rho_c A_c}{\cos\theta}\right) \frac{(4\bar{b} + 4\bar{h})}{\tan\theta} \\ m_{e-diagonal} &= \left(\rho_b A_b + \frac{\rho_c A_c \tan\theta}{\bar{b}} \left[\frac{\bar{b}}{\sin\theta} + 2\bar{h} + \bar{b}\right]\right) \frac{2\bar{b}}{\tan\theta} \end{aligned} \tag{2.3}$$

Here, ρ_b, ρ_c, A_b, A_c represent the beam and cable's mass densities and cross-sectional areas, respectively. Also, $\bar{b} = b/2 + r_c$, and $\bar{h} = h/2 + r_c$. The cable wrapping angle, θ, is assumed to be constant along the length of the beam as shown in Figs. 2.1 and 2.2. Using Eq. 2.3, the kinetic energy for each of the two fundamental elements shown in the figure may be found as

$$\begin{aligned} T_{e-zigzag} &= \frac{1}{2} m_{e-zigzag} \left(\dot{w}^*\right)^2 \\ T_{e-diagonal} &= \frac{1}{2} m_{e-diagonal} \left(\dot{w}^*\right)^2 \end{aligned} \tag{2.4}$$

As shown in Appendix section A.1, the length of the fundamental element for the two patterns can be written in terms of host beam and cable parameters, and wrapping angle as

$$\begin{aligned} L_{e-zigzag} &= (4\bar{b} + 4\bar{h})/\tan\theta \\ L_{e-diagonal} &= \frac{2\bar{b}}{\tan\theta} \end{aligned} \tag{2.5}$$

Now, the kinetic energy expressions in Eq. 2.4 are used to find the kinetic energy per unit length for the structure as follows:

$$\begin{aligned} \frac{T_{e-zigzag}}{L_{e-zigzag}} &= \frac{1}{2}\left(\rho_b A_b + \frac{\rho_c A_c}{\cos\theta}\right)\left(\dot{w}^*\right)^2 \\ \frac{T_{e-diagonal}}{L_{e-diagonal}} &= \frac{1}{2}\left(\rho_b A_b + \frac{\rho_c A_c \tan\theta}{\bar{b}}\left[\frac{\bar{b}}{\sin\theta} + 2\bar{h} + \bar{b}\right]\right)\left(\dot{w}^*\right)^2 \end{aligned} \tag{2.6}$$

It should be noted that a major assumption for the homogenization approach pertains to these energy per unit length remaining constant along the overall length of the structure. Therefore, using Eq. 2.6, the differential kinetic energy of the overall system can be found as

$$\begin{aligned} dT_{zigzag} &= \frac{1}{2}\left(\rho_b A_b + \frac{\rho_c A_c}{\cos\theta}\right)\left(\dot{w}^*\right)^2 \, dx \\ dT_{diagonal} &= \frac{1}{2}\left(\rho_b A_b + \frac{\rho_c A_c \tan\theta}{\bar{b}}\left[\frac{\bar{b}}{\sin\theta} + 2\bar{h} + \bar{b}\right]\right)\left(\dot{w}^*\right)^2 \, dx \end{aligned} \tag{2.7}$$

Integrating the given differential kinetic energy terms over the total length l of the beam, the total kinetic energy of the entire cabled beam system is obtained as [31]

$$T_{tot} = \int_0^l \frac{1}{2} K_1 \left(\dot{w}\right)^2 dx \tag{2.8}$$

where $\dot{w}$ represents $\frac{\partial w(x,t)}{\partial t}$ and K_1 for the two patterns are given by

$$\begin{aligned} K_{1-zigzag} &= \rho_b A_b + \frac{\rho_c A_c}{\cos\theta} \\ K_{1-diagonal} &= \rho_b A_b + \frac{\rho_c A_c \tan\theta}{\bar{b}} \left[\frac{\bar{b}}{\sin\theta} + 2\bar{h} + \bar{b} \right] \end{aligned} \tag{2.9}$$

It should be noted that Eq. 2.9 represents the homogenized mass per unit length for both the wrapping patterns. For similar wrapping angle, the diagonal pattern would have a higher mass per unit length than the zigzag pattern.

2.1.3 Strain energy

Obtaining the strain energy of the fundamental element is another necessary step in finding the equivalent continuum model for a structure of given repeated patterns. For this purpose, similarly, the strain energy of the cable and beam within the fundamental element is first obtained [31]. The Green-Lagrange strain tensor is used to find the strain-displacement relationship as

$$\varepsilon_{ij} = \frac{1}{2} \left(u_{i,j} + u_{j,i} + \sum_{k=\{x,y,z\}} u_{k,i} u_{k,j} \right) \text{ where } \quad i,j = \{x,y,z\} \tag{2.10}$$

Substituting Eq. 2.1 in 2.10, the only non-zero component of the strain tensor is,

$$\varepsilon_{xx} = -zw'' + \frac{z^2}{2}\left(w''\right)^2 + \frac{1}{2}\left(w'\right)^2 \tag{2.11}$$

This expression denotes the longitudinal normal strain in the x-direction. However, the net longitudinal strain in the beam within a fundamental element will be calculated after considering the effect of pre-compression due to the string pre-tension. Assuming T as the pre-tension in the cable, the pre-strain in the cable can be written as $T/E_c A_c$. Also, the cable pre-tension is responsible for an initial compressive strain in the beam given by $-T\cos(\theta)/E_b A_b$. E_c and E_b denote the Young's modulus of the cable and beam, respectively. To formulate the following equations within the fundamental element, the local coordinate ξ corresponding to the longitudinal direction of the fundamental element

is used. Hence, the longitudinal strain for the beam within the fundamental element during vibrations can be written as

$$\varepsilon_b(\xi,t) = -\frac{T\cos(\theta)}{E_b A_b} + \varepsilon_{\xi\xi} \tag{2.12}$$

Similarly, the total strain in the cable comprises of the pre-tension strain and strain during bending vibrations. The bending strain component along the cable is found using a tensor transformation as $\varepsilon_{\xi\xi}\cos^2(\theta)$. This strain is assumed to be the same across the cable cross-section A_c. Therefore, the total strain is evaluated at the center of the cable at any time t as

$$\varepsilon_c(\xi,t) = \frac{T}{E_c A_c} + \varepsilon_{\xi\xi}|_{z=z_c(\xi)}\cos^2(\theta) \tag{2.13}$$

where $z_c(\xi)$ is assumed to be the z coordinate of the center of the cable at location ξ. Once the net strains are calculated, the next step is to calculate the total strain energy for a fundamental element. This is defined by the sum of the individual energy components for the beam and cable within the elements shown in Figs. 2.1 and 2.2. The strain energy of the beam part within an arbitrary fundamental element is given as

$$U_{e,beam} = \iiint_{V_b} \frac{1}{2} E_b \left(\varepsilon_b(\xi,t)\right)^2 dV \tag{2.14}$$

where V_b denotes the volume of beam fundamental element. Similarly, the strain energy in the cable part within an arbitrary fundamental element is found as

$$U_{e,cable} = \iiint_{V_c} \frac{1}{2} E_c \left(\varepsilon_c(\xi,\ t)\right)^2 dV \tag{2.15}$$

where V_c denotes the volume of cable fundamental element. Using Eqs. 2.11, 2.12, 2.13, 2.14, 2.15, the total strain energy for a fundamental element can be found as

$$U_e \approx \int_0^{L_e} \left(\frac{1}{2}\left[E_b I_b + E_c A_c z_c^2 \cos^3\theta + T z_c^2 \cos\theta - \frac{T\cos\theta I_b}{A_b}\right]\left(\frac{\partial^2 w}{\partial\xi^2}\right)^2 \right.$$
$$\left. - T z_c \cos\theta \frac{\partial^2 w}{\partial\xi^2} + \frac{T^2\ \cos^2\theta}{2E_b A_b} + \frac{T^2}{2E_c A_c\cos\theta}\right) d\xi \tag{2.16}$$

The approximation symbol is used because the terms higher than second-degree of displacement $w(\xi,t)$ and its derivatives are ignored as shown in Appendix section A.2.

Further, the Taylor series expansion up to the second order of the displacement $w(\xi, t)$ about the fundamental element center is substituted in Eq. 2.16 and integrated over the fundamental element length to obtain the total element strain energy, U_e, details of which are presented in the Appendix. The z_c coordinate values for the cables center at which the cable strain is evaluated are listed in Appendix section A.2 in Eqs. A.18 and A.25.

$$U_{e-zigzag} = \frac{1}{2}\Bigg(E_b I_b \frac{\left(4\bar{b}+4\bar{h}\right)}{\tan\theta} + \frac{4E_c A_c \bar{h}^2 \cos^3\theta}{\tan\theta}\left(\bar{b}+\frac{\bar{h}}{3}\right) + \frac{4T\bar{h}^2\cos\theta}{\tan\theta}\left(\bar{b}+\frac{\bar{h}}{3}\right) - T\cos\theta\frac{I_b}{A_b}\frac{\left(4\bar{b}+4\bar{h}\right)}{\tan\theta}\Bigg)\left[\frac{\partial^2 w}{\partial\xi^2}\left(\frac{L_e}{2},t\right)\right]^2 + \frac{T^2 L_e\cos^2\theta}{2E_b A_b} + \frac{T^2 L_e}{2E_c A_c\cos\theta} \tag{2.17}$$

$$U_{e-diagonal} = \frac{1}{2}\left(\frac{2\bar{b}}{\tan\theta}\right)\left(E_b I_b + E_c A_c \bar{h}^2\cos^3\theta + T\cos\theta\left(\bar{h}^2 - \frac{I_b}{A_b}\right)\right)\left[\frac{\partial^2 w}{\partial\xi^2}\left(\frac{L_e}{2},t\right)\right]^2 - T\bar{h}L_e\cos\theta\frac{\partial^2 w}{\partial\xi^2}\left(\frac{L_e}{2},t\right) + \frac{T^2 L_e\cos^2\theta}{2E_b A_b} + \frac{T^2 L_e}{2E_c A_c\cos\theta} \tag{2.18}$$

On the right-hand side of both the above expressions, L_e represents the fundamental element length corresponding to the wrapping pattern. The element length from Eq. 2.5 and strain energy expressions in Eqs. 2.17 and 2.18 are then used to find the strain energy per unit length of the structure as follows:

$$\frac{U_{e-zigzag}}{L_{e-zigzag}} = \frac{1}{2}\Bigg(E_b I_b + E_c A_c \bar{h}^2\cos^3\theta\left(\frac{\bar{b}+\frac{\bar{h}}{3}}{\bar{b}+\bar{h}}\right) + T\cos\theta\left(\frac{\bar{h}^2\left(\bar{b}+\frac{\bar{h}}{3}\right)}{\bar{b}+\bar{h}} - \frac{I_b}{A_b}\right)\Bigg)\left[\frac{\partial^2 w}{\partial\xi^2}\left(\frac{L_e}{2},t\right)\right]^2 + \frac{T^2\cos^2\theta}{2E_b A_b} + \frac{T^2}{2E_c A_c\cos\theta} \tag{2.19}$$

$$\frac{U_{e-diagonal}}{L_{e-diagonal}} = \frac{1}{2}\left(E_b I_b + E_c A_c \bar{h}^2\cos^3\theta + T\cos\theta\left(\bar{h}^2 - \frac{I_b}{A_b}\right)\right)\left[\frac{\partial^2 w}{\partial\xi^2}\left(\frac{L_e}{2},t\right)\right]^2 - T\bar{h}\cos\theta\frac{\partial^2 w}{\partial\xi^2}\left(\frac{L_e}{2},t\right) + \frac{T^2\cos^2\theta}{2E_b A_b} + \frac{T^2}{2E_c A_c\cos\theta} \tag{2.20}$$

Similar to the kinetic energy case, these expressions are assumed to remain constant across the entire length of the equivalent homogenized structure. This is a valid assumption when a structure's ratio of overall length to the fundamental element length is sufficiently large indicating the fundamental element is sufficiently small compared to the entire structure. Using this assumption, the differential energy expressions for an equivalent continuum model for the strain energy are found as

$$dU_{zigzag} = \left(\frac{1}{2}\left[E_bI_b + E_cA_c\bar{h}^2\cos^3\theta\left(\frac{\bar{b}+\frac{\bar{h}}{3}}{\bar{b}+\bar{h}}\right) + T\cos\theta\left(\frac{\bar{h}^2\left(\bar{b}+\frac{\bar{h}}{3}\right)}{\bar{b}+\bar{h}} - \frac{I_b}{A_b}\right)\right]\left[\frac{\partial^2 w}{\partial x^2}(x,t)\right]^2 + \frac{T^2\cos^2\theta}{2E_bA_b} + \frac{T^2}{2E_cA_c\cos\theta}\right)dx \quad (2.21)$$

$$dU_{diagonal} = \left(\frac{1}{2}\left[E_bI_b + E_cA_c\bar{h}^2\cos^3\theta + T\cos\theta\left(\bar{h}^2 - \frac{I_b}{A_b}\right)\right]\left[\frac{\partial^2 w}{\partial x^2}(x,t)\right]^2 - T\bar{h}\cos\theta\frac{\partial^2 w}{\partial x^2}(x,t) + \frac{T^2\cos^2\theta}{2E_bA_b} + \frac{T^2}{2E_cA_c\cos\theta}\right)dx \quad (2.22)$$

Integrating the given differential strain energy terms over the total length of the beam, the strain energy of the entire cabled beam system is obtained as [31],

$$U_{tot} = \int_0^l \left(\frac{1}{2}B_1\left(\frac{\partial^2 w}{\partial x^2}\right)^2 + B_2\frac{\partial^2 w}{\partial x^2} + B_3\right)dx \quad (2.23)$$

This expression represents the homogenized strain energy of an equivalent continuum structure where, B_1, B_2 and B_3 for each of the two patterns are given as

$$B_{1-zigzag} = E_bI_b + E_cA_c\bar{h}^2\cos^3\theta\left(\frac{\bar{b}+\frac{\bar{h}}{3}}{\bar{b}+\bar{h}}\right) + T\cos\theta\left(\frac{\bar{h}^2\left(\bar{b}+\frac{\bar{h}}{3}\right)}{\bar{b}+\bar{h}} - \frac{I_b}{A_b}\right) \quad (2.24a)$$

$$B_{2-zigzag} = 0 \quad (2.24b)$$

$$B_{3-zigzag} = \frac{T^2\cos^2\theta}{2E_bA_b} + \frac{T^2}{2E_cA_c\cos\theta} \quad (2.24c)$$

$$B_{1-diagonal} = E_b I_b + E_c A_c \bar{h}^2 \cos^3\theta + T\cos\theta\left(\bar{h}^2 - \frac{I_b}{A_b}\right) \tag{2.25a}$$

$$B_{2-diagonal} = -T\bar{h}\cos(\theta) \tag{2.25b}$$

$$B_{3-diagonal} = \frac{T^2\cos^2\theta}{2E_bA_b} + \frac{T^2\tan\theta}{2\ E_cA_c\bar{b}}\left[\frac{\bar{b}}{\sin\theta} + 2\bar{h} + \bar{b}\right] \tag{2.25c}$$

2.1.4 Energy lost due to damping

The next step in finding an equivalent homogenized model is to incorporate the damping effects. Both Kelvin-Voigt and hysteretic damping models are used to represent the damping effects from the cables. The damping in the host beam is also included in each damping model.

Kelvin-Voigt damping

The stress-strain constitutive relations for the Kelvin-Voigt model can be written as

$$\sigma_b = E_b\varepsilon_b + C_b\dot{\varepsilon}_b = E_b\left(\varepsilon_b + \eta_{kb}\dot{\varepsilon}_b\right) \tag{2.26}$$

$$\sigma_c = E_c\varepsilon_c + C_c\dot{\varepsilon}_c = E_c\left(\varepsilon_c + \eta_{kc}\dot{\varepsilon}_c\right) \tag{2.27}$$

where σ_b and ε_b are the longitudinal normal bending stress and strain in the beam, and σ_c and ε_c represent the axial stress and strain in the cable, respectively. Also, C_b and C_c represent the damping coefficients in $N - s/m^2$, and η_{kb}, η_{kc} are the proportionality constants in s for the beam and cable damping, respectively. The overdot indicates the derivative taken with respect to time. The Rayleigh dissipation function of the beam within an arbitrary fundamental element can then be found using the time derivative of its strain as [76]

$$R_b = \int_0^{L_e}\int_{A_b}\frac{1}{2}C_b\left(\dot{\varepsilon}_b\right)^2 dV \tag{2.28}$$

On substitution of Eq. 2.12 in Eq. 2.28, the dissipation function for the beam material in a fundamental element can be written as

$$R_b = \int_0^{L_e}\int_{A_b}\frac{1}{2}C_b\left(\frac{\partial}{\partial t}\left(-\frac{T\cos\theta}{E_bA_b} - z\frac{\partial^2 w}{\partial\xi^2} + \frac{z^2}{2}\left(\frac{\partial^2 w}{\partial\xi^2}\right)^2 + \frac{1}{2}\left(\frac{\partial w}{\partial\xi}\right)^2\right)\right)^2 dA\,d\xi \tag{2.29}$$

Performing the above integration and ignoring the higher order and nonlinear terms as shown in appendix section A.3,

$$R_b \approx \int_0^{L_e} \int_{A_b} \frac{1}{2} C_b z^2 \left(\frac{\partial^3 w}{\partial t \ \partial \xi^2} \right)^2 dA d\xi \tag{2.30}$$

This can be further simplified as

$$R_b = \int_0^{L_e} \frac{1}{2} C_b I_b \left(\frac{\partial^3 w}{\partial t \ \partial \xi^2} \right)^2 d\xi \tag{2.31}$$

The total energy loss rate for the fundamental element will also include the loss due to damping in the cables within the element. As an example, this rate can be found for the diagonal element shown in Fig. 2.2 as

$$R_c = \int_0^{L_e/\cos\theta} \int_{A_c} \frac{1}{2} C_c \left(\dot{\varepsilon}_c \right)^2 \Big|_{z=z_c(\xi)} dA \ dl \tag{2.32}$$

Note that the cables on the side and bottom sections for this pattern do not contribute to the energy loss for the diagonal pattern as they will not strain during bending vibrations. Using Eq. 2.13, the dissipation function for the cable is expanded as

$$\begin{aligned} R_c = \int_0^{L_e} \Bigg[\int_{A_c} \Bigg[\frac{1}{2} C_c \Bigg(\frac{\partial}{\partial t} \Bigg(\frac{T}{E_c A_c} \\ + \left(-z_c \frac{\partial^2 w}{\partial \xi^2} + \frac{z_c^2}{2} \left(\frac{\partial^2 w}{\partial \xi^2} \right)^2 + \frac{1}{2} \left(\frac{\partial w}{\partial \xi} \right)^2 \right) \cos^2(\theta) \Bigg) \Bigg)^2 \Bigg] dA \Bigg] \left(\frac{d\xi}{\cos(\theta)} \right) \end{aligned} \tag{2.33}$$

Similarly, ignoring the higher order and nonlinear terms will result in

$$R_c \approx \int_0^{L_e} \frac{1}{2} C_c A_c z_c^2 \cos^3\theta \left(\frac{\partial^3 w}{\partial t \ \partial \xi^2} \right)^2 d\xi \tag{2.34}$$

It can be easily shown that the Rayleigh dissipation function for the cables within the zigzag fundamental element results in the same expression shown above. Further details for this derivation are presented in appendix section A.3. Finally, the Rayleigh dissipation

function for the entire fundamental element consisting of both cable and beam components for either the zigzag or diagonal wrapping patterns can be found as

$$R_e = R_b + R_c = \int_0^{L_e} \frac{1}{2} \left(C_b I_b + C_c A_c z_c^2 \cos^3 \theta \right) \left(\frac{\partial^3 w}{\partial t \, \partial \xi^2} \right)^2 d\xi \tag{2.35}$$

Using the Taylor's series expansion for $\dot{w}(\xi, t)$ as shown in appendix section A.3, the Rayleigh dissipation function for the fundamental element of both wrapping patterns can be found as

$$R_{e-zigzag} = \frac{1}{2} \left[C_b I_b \frac{\left(4\bar{b} + 4\bar{h}\right)}{\tan\theta} + \frac{4 C_c A_c \bar{h}^2 \cos^3\theta}{\tan\theta} \left(\bar{b} + \frac{\bar{h}}{3} \right) \right] \left[\frac{\partial^3 w}{\partial t \, \partial \xi^2} \left(\frac{L_e}{2}, t \right) \right]^2 \tag{2.36}$$

$$R_{e-diagonal} = \frac{1}{2} \left(\frac{2\bar{b}}{\tan\theta} \right) \left[C_b I_b + C_c A_c \bar{h}^2 \cos^3\theta \right] \left[\frac{\partial^3 w}{\partial t \, \partial \xi^2} \left(\frac{L_e}{2}, t \right) \right]^2 \tag{2.37}$$

Dividing the above energy loss rate expression by the respective length of the fundamental element,

$$\frac{R_{e-zigzag}}{L_{e-zigzag}} = \frac{1}{2} \left[C_b I_b + C_c A_c \bar{h}^2 \cos^3\theta \left(\frac{\bar{b} + \frac{\bar{h}}{3}}{\bar{b} + \bar{h}} \right) \right] \left[\frac{\partial^3 w}{\partial t \, \partial \xi^2} \left(\frac{L_e}{2}, t \right) \right]^2 \tag{2.38}$$

$$\frac{R_{e-diagonal}}{L_{e-diagonal}} = \frac{1}{2} \left[C_b I_b + C_c A_c \bar{h}^2 \cos^3\theta \right] \left[\frac{\partial^3 w}{\partial t \, \partial \xi^2} \left(\frac{L_e}{2}, t \right) \right]^2 \tag{2.39}$$

On the right hand side of both the above expressions, L_e represents the length of fundamental element corresponding to the wrapping pattern.

Once again, the conditions for the periodicity and having sufficiently large number of fundamental elements over the span of the structure are used. Hence, the ratios in Eqs. 2.38 and 2.39 are assumed constant across the entire length of the equivalent homogenized structure and the differential of the Rayleigh dissipation function is found as

$$dR_{zigzag} = \frac{1}{2} \left[C_b I_b + C_c A_c \bar{h}^2 \cos^3\theta \left(\frac{\bar{b} + \frac{\bar{h}}{3}}{\bar{b} + \bar{h}} \right) \right] \left[\frac{\partial^3 w}{\partial t \, \partial x^2} (x, t) \right]^2 dx \tag{2.40}$$

$$dR_{diagonal} = \frac{1}{2} \left[C_b I_b + C_c A_c \bar{h}^2 \cos^3\theta \right] \left[\frac{\partial^3 w}{\partial t \, \partial x^2} (x, t) \right]^2 dx \tag{2.41}$$

Integrating the above expressions over the total beam length, the total dissipation function is obtained in the following form:

$$R_{tot} = \int_0^l \frac{1}{2} D_1 \left(\dot{w}''\right)^2 dx \tag{2.42}$$

where, the coefficient D_1 depends on the wrapping pattern and system parameters and is found as

$$D_{1-zigzag} = C_b I_b + C_c A_c \bar{h}^2 \cos^3\theta \left(\frac{\bar{b} + \bar{h}/3}{\bar{b} + \bar{h}}\right) \tag{2.43}$$

$$D_{1-diagonal} = C_b I_b + C_c A_c \bar{h}^2 \cos^3\theta \tag{2.44}$$

Hysteretic damping

In the hysteretic damping model, the complex modulus is used to obtain the constitutive relationship of the material. Complex modulus consists of a real and imaginary part which represents the storage and loss modulus, respectively. It includes the information on elastic modulus and damping [73] and is written as

$$E_b^* = E_b' \left(1 + j\eta_{hb}\right) = E_b' + jE_b'' \tag{2.45a}$$

$$E_c^* = E_c' \left(1 + j\eta_{hc}\right) = E_c' + jE_c'' \tag{2.45b}$$

where $j = \sqrt{-1}$ and the subscripts b and c denote beam and cable, respectively. The storage and loss modulus are denoted by E' and E'', respectively. The storage modulus relates to the material's ability to store the energy elastically; whereas, the loss modulus is related to the material's ability to dissipate stress through heat. The dimensionless loss factors, η_{hb} and η_{hc}, represent the ratios of loss modulus to storage modulus for the beam and cable, respectively. The constitutive relationship between stress and strain is then written as

$$\sigma_b\left(t\right) = E_b^* \ \varepsilon_b\left(t\right) \tag{2.46a}$$

$$\sigma_c\left(t\right) = E_c^* \ \varepsilon_c\left(t\right) \tag{2.46b}$$

Using the relations in Eq. 2.46, the complex strain energy within a fundamental element of the beam and cable system is written as

$$U_{e,beam}^* = \iiint_{V_b} \frac{1}{2} E_b^* \left(\varepsilon_b\left(\xi, t\right)\right)^2 dV \tag{2.47a}$$

$$U^*_{e,cable} = \iiint_{V_c} \frac{1}{2} E^*_c \left(\varepsilon_c \left(\xi,\ t\right)\right)^2 dV \tag{2.47b}$$

Adding these two equations and using the similar methodology to derive the total strain energy as followed earlier in Eqs. 2.14 − 2.25, the total complex strain energy is obtained for a hysteretically damped system as

$$U^*_{tot} = \int_0^l \left(\frac{1}{2} B^*_1 \left(\frac{\partial^2 w}{\partial x^2} \right)^2 + B_2 \frac{\partial^2 w}{\partial x^2} + B_3 \right) dx \tag{2.48}$$

where, B_2 and B_3 are the same as mentioned in Eqs. 2.24 and 2.25, and B^*_1 for each of the two patterns is given as

$$B^*_{1-zigzag} = E^*_b I_b + E^*_c A_c \bar{h}^2 \cos^3\theta \left(\frac{\bar{b} + \frac{\bar{h}}{3}}{\bar{b} + \bar{h}} \right) + T \cos\theta \left(\frac{\bar{h}^2 \left(\bar{b} + \frac{\bar{h}}{3} \right)}{\bar{b} + \bar{h}} - \frac{I_b}{A_b} \right) \tag{2.49a}$$

$$B^*_{1-diagonal} = E^*_b I_b + E^*_c A_c \bar{h}^2 \cos^3\theta + T \cos\theta \left(\bar{h}^2 - \frac{I_b}{A_b} \right) \tag{2.49b}$$

2.1.5 Equation of motion

In this section, the governing equations of motion for transverse vibrations of the cable-harnessed beam system are derived for both damping models.

Kelvin-Voigt damping

Application of Hamilton's principle for the damped system results in,

$$\delta \int_{t_0}^{t_1} \mathcal{L} dt = \int_{t_0}^{t_1} \left(\delta T_{tot} - \delta U_{tot} + \delta W_d \right) dt = 0 \tag{2.50}$$

where T_{tot}, U_{tot} and W_d denote the kinetic and strain energies and energy loss due to damping, respectively and δ is the variation. The energy loss variations due to the Kelvin-Voigt damping [77] is found using

$$\delta W_d = Q_D \delta w = -\frac{\partial R_{tot}}{\partial \dot{w}} \delta w \tag{2.51}$$

Here, Q_D is the non-conservative damping force and is obtained by differentiating the Rayleigh dissipation function with respect to velocity $\dot{w}$. Using equations 2.8, 2.23, 2.42,

2.50, and 2.51, and applying Hamilton's principle, the governing equation of motion for the transverse vibrations and associated boundary conditions are found as

$$K_1\ddot{w} + B_1 w'''' + D_1 \dot{w}'''' = 0 \tag{2.52}$$

$$w(x,t) = 0|_{x=0 \text{ or } l} \tag{2.53a}$$
$$w\prime(x,t) = 0|_{x=0 \text{ or } l} \tag{2.53b}$$
$$B_1 w''(x,t) + D_1 \dot{w}''(x,t) = -B_2|_{x=0 \text{ or } l} \tag{2.53c}$$
$$B_1 w'''(x,t) + D_1 \dot{w}'''(x,t) = 0|_{x=0 \text{ or } l} \tag{2.53d}$$

Further details of applying the Hamilton's principle are shown in appendix section A.4. It should be noted that the PDE in Eq. 2.52 resembles in form to the equation of motion of a *Euler beam with Kelvin-Voigt damping* as also shown in Eq. 1.2. Hence, the governing PDE of the cable-harnessed structure can be represented as an equivalent Kelvin-Voigt damped Euler beam with equivalent stiffness and inertia coefficient as B_1 and K_1, respectively. Additionally, D_1 represents the equivalent damping coefficient of the homogenized structure.

Also, note that the coefficient B_3 disappears in the equation of motion because it is a constant term in the strain energy expressions, and on applying the variation in Hamilton's principle, it vanishes. The coefficient B_2 disappears for the zigzag pattern, whereas it is a non-zero constant for the diagonal pattern. Hence, for the case of diagonal pattern, the moment boundary condition can be transformed to a homogeneous equation as described in [31] and further solved for natural frequencies and damping ratios.

The solution procedure to obtain the frequency response function for the homogenized Kelvin-Voigt damped system is elaborated in Appendix A.5.

Hysteretic damping

Similar to the previous case, the equations of motion for the cable-harnessed system with hysteretic damping can be found. Here, the total strain energy U^*_{tot} is found in Eq. 2.48 using the dynamic moduli E^*_b and E^*_c that also include the dissipation factors due to damping. Therefore, the governing equation of motion for the hysteretically damped system can be written as

$$K_1\ddot{w} + B_1^* w'''' = 0 \tag{2.54}$$

where the coefficients K_1 and B_1^* are evaluated for different wrapping patterns in Eq. 2.9 and Eq. 2.49, respectively. The coefficient B_1^* is also referred to as the equivalent

complex flexural stiffness of the system [78]. It contains the information of stiffness and damping for both the cable and beam structure.

Substituting Eq. 2.45 in Eq. 2.49, B_1^* can be written by separating real and imaginary values as $B_1^* = B_1' + jB_1''$. Therefore, the effective loss factor of the cable-harnessed system can be written as $\eta_{CH} = B_1''/B_1'$. The η_{CH} values for each of the zigzag and diagonal patterns can be found as

$$(\eta_{CH})_{zigzag} = \frac{\left(E_b'' I_b + \frac{E_c'' A_c \bar{h}^2 \cos^3\theta \left(\bar{b}+\frac{\bar{h}}{3}\right)}{\bar{b}+\bar{h}} \right)}{\left(E_b' I_b + \frac{E_c' A_c \bar{h}^2 \cos^3\theta \left(\bar{b}+\frac{\bar{h}}{3}\right)}{\bar{b}+\bar{h}} + T\cos\theta \left(\frac{\bar{h}^2\left(\bar{b}+\frac{\bar{h}}{3}\right)}{\bar{b}+\bar{h}} - \frac{I_b}{A_b} \right) \right)} \tag{2.55a}$$

$$(\eta_{CH})_{diagonal} = \frac{\left(E_b'' I_b + E_c'' A_c \bar{h}^2 \cos^3\theta \right)}{\left(E_b' I_b + E_c' A_c \bar{h}^2 \cos^3\theta + T\cos\theta \left(\bar{h}^2 - \frac{I_b}{A_b} \right) \right)} \tag{2.55b}$$

These effective loss factors signify the overall hysteretic damping loss in the cable-harnessed system. The numerator signifies the imaginary part for the equivalent complex bending stiffness and corresponds to the overall energy loss in the structure. Conversely, the denominator is the real part and represents the system strain energy.

It is also worth mentioning that contrary to the case of the cables moving freely as studied in Ref. [79], the assumptions of the presented work pertain to linear models for the cable and, therefore, the cubic nonlinearities occurring due to the mid-plane stretching are absent in the PDE. The same assumptions are made for previous cable-harnessed structures discussed in Refs. [25, 28, 29, 31]. Therefore, the major goal for the presented work is to incorporate damping in the previously studied cable-harnessed structures using the same assumptions.

The solution procedure to obtain the frequency response function for the homogenized Kelvin-Voigt damped system is elaborated in Appendix A.6.

2.1.6 Special case: cables attached in a longitudinal pattern

In addition to the two wrapping patterns considered in the previous sections, a special case of the longitudinal pattern shown in Fig. 2.3 is also considered in this part. In this pattern, the cable is attached above the centerline on the top surface of the beam. The

related coefficients of the governing equation of motion for both the damping models for the longitudinal pattern can be easily obtained as

$$K_1 = \rho_b A_b + \rho_c A_c \tag{2.56a}$$

$$B_1 = E_b I_b + E_c A_c \bar{h}^2 + T\left(\bar{h}^2 - \frac{I_b}{A_b}\right) \tag{2.56b}$$

$$B_2 = -T\bar{h} \tag{2.56c}$$

$$B_3 = \frac{T^2}{2E_b A_b} + \frac{T^2}{2\ E_c A_c} \tag{2.56d}$$

$$D_1 = C_b I_b + C_c A_c \bar{h}^2 \tag{2.56e}$$

$$B_1^* = E_b^* I_b + E_c^* A_c \bar{h}^2 + T\left(\bar{h}^2 - \frac{I_b}{A_b}\right) \tag{2.56f}$$

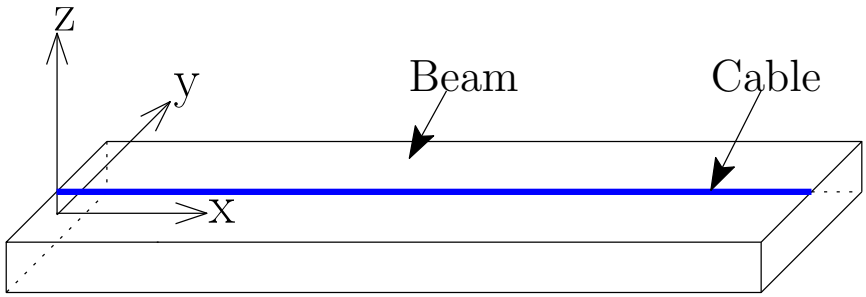

Figure 2.3: Special case of cable-harnessed beam with cable attached in a straight line on the top surface above the centerline (Longitudinal pattern)

2.2 Distributed Transfer Function Method

In this section, the formulation for the DTFM is developed in order to verify the proposed analytical model for the damped cable-harnessed structures with the two wrapping patterns presented in the previous section. The DTFM was initially developed by Yang et al. [80] to obtain the closed-form transfer functions of a one-dimensional distributed parameter system. In short, this method transforms the systems equations in the Laplace domain which are then cast into a matrix form. After formulating the fundamental matrix of the system, the transfer function is evaluated.

For a diagonal wrapping pattern, DTFM would predict an exact closed-form transfer function as the system can be separated into multiple uniform sub-systems with a cable lumped mass present on each sub-system node. Comparatively, for a zigzag wrapped pattern, DTFM predicts an approximate solution of the transfer function, as the section of cable on the beam face parallel to $x-z$ plane introduces a non-uniformity in the system that can not be exactly solved. The cause of this non-uniformity is the variation of the $z-$coodinate of the center of cable as a function of x; hence, the transfer function for a zigzag pattern cannot be obtained in an exact form. However, the sections of the system where the cable is present on the beam face parallel to the $x-y$ plane can be treated as uniform sub-systems.

For the non-uniformly distributed parameter systems, Yang et al. [81] proposed a step-function approximation method within the DTFM framework. For the current research, this method is applied to obtain closed form transfer functions of zigzag and diagonal wrapped patterns.

2.2.1 Formulation for the zigzag pattern

Figure 2.4(a) shows the front view of multiple fundamental elements of the zigzag wrapped cable-harness beam and Fig. 2.4(b) shows a magnified single fundamental element. The single element has been further divided into four sections/sub-systems namely S-1—S-4. Sections S1 and S3 have the cable attached diagonally on the top and bottom surfaces of the beam, respectively, whereas in the sections S-2 and S-4, the cable is present on the beam face parallel to the $x-z$ plane.

Assuming Kelvin-Voigt damping in the beam and cable, the equation of motion for the standalone sub-systems, S-1—S-4, can be written in local coordinates as

$$B_1 w'''' (\xi,t) + K_1 \ddot{w} (\xi,t) + D_1 \dot{w}'''' (\xi,t) = f_e(\xi,t) \tag{2.57}$$

where $f_e(\xi,t)$ is an external force. The PDE coefficients B_1, K_1, and D_1 are dissimilar for different sets of sub-systems. For the sub-systems, S-1 and S-3, the coefficients are constant and are written as $B_1 = E_b I_b + E_c A_c \bar{h}^2 \cos^3\theta + T\bar{h}^2 \cos\theta - T\cos\theta I_b/A_b$, $K_1 = \rho_b A_b + \rho_c A_c/\cos\theta$, and $D_1 = C_b I_b + C_c A_c \bar{h}^2 \cos^3\theta$. Since the coefficients are not a function of ξ, the sub-systems S-1 and S-3 can be distinguished as uniformly distributed parameter systems in the fundamental element. However, for the sub-systems S-2 and S-4, the coefficients are listed as $B_1 = E_b I_b + E_c A_c z_c^2(\xi) \cos^3\theta + T z_c^2(\xi)\cos\theta - T\cos\theta I_b/A_b$, $K_1 = \rho_b A_b + \rho_c A_c/\cos\theta$, and $D_1 = C_b I_b + C_c A_c z_c^2(\xi)\cos^3\theta$. Clearly, the coefficients B_1 and

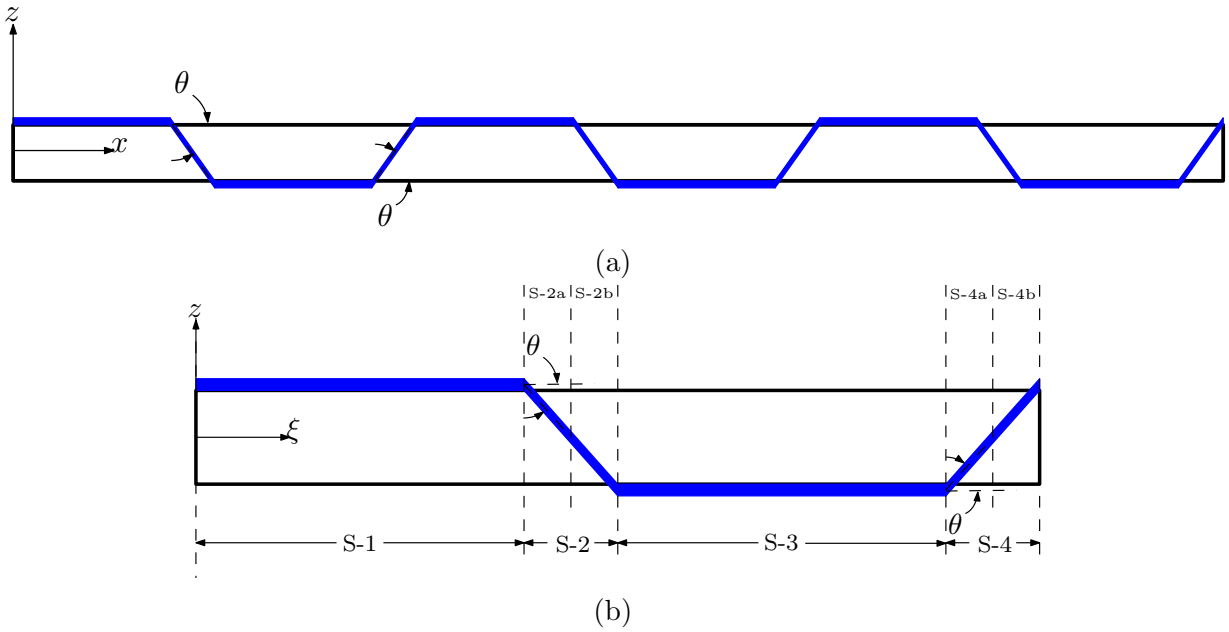

Figure 2.4: (a) Front view of a cable-harnessed beam with the zigzag wrapping pattern, (b) Fundamental element and the sub-systems (front view)

D_1 are the function of coordinate ξ for S-2 and S-4. Also, the values of $z_c(\xi)$ for the zigzag pattern are listed in Eq. A.18. Hence, the sub-systems S-2 and S-4 are distinguished as non-uniformly distributed in the fundamental element.

Next, considering the cable-harnessed system composed of numerous sub-systems along multiple fundamental elements as shown in Fig. 2.4(a), Eq. 2.57 can be written on a sub-system level in generalized form for the global coordinate system (x, y, z). After taking the Laplace transform, the equation can be written as

$$\bar{w}''''(x,s) = -\frac{K_1 s^2}{B_1 + D_1 s}\bar{w}(x,s) + \frac{f_e(x,s)}{B_1 + D_1 s}, \quad x \in (0,1) \tag{2.58}$$

where $\bar{w}(x,s)$, $f_e(x,s)$ are the Laplace transform of $w(x,t)$, $f_e(x,t)$, respectively, and s is the complex parameter. For DTFM, the domain of x is made $(0,1)$ by non-dimensionalizing it over the length of the entire cable-harnessed beam. To obtain a closed-form transfer function of the system, the above equation is represented in a matrix form as

$$\frac{\partial}{\partial x}\Psi(x,s) = F(x,s)\,\Psi(x,s) + \nu(x,s) \tag{2.59}$$

where $\Psi(x,s) = \{\bar{w}(x,s), \bar{w}'(x,s), \bar{w}''(x,s), \bar{w}'''(x,s)\}^T$ is the solution vector in Laplace domain, and $\nu(x,s) = \left\{0, 0, 0, \frac{f_e(x,s)}{B_1+D_1 s}\right\}^T$ corresponds to the force vector where $\{.\}^T$ is the transpose of the vector. This representation in matrix form is similar to the state-space representation and hence, $F(x,s)$ is also called the state space matrix. The matrix $F(x,s)$ forms the core of the DTFM approach as all the properties of cable and beam are embedded in the single matrix. $F(x,s)$ for the current set of sub-systems is written as

$$F(x,s) = \begin{bmatrix} 0 & 1 & 0 & 0 \\ 0 & 0 & 1 & 0 \\ 0 & 0 & 0 & 1 \\ -\frac{K_1 s^2}{B_1+D_1 s} & 0 & 0 & 0 \end{bmatrix} \tag{2.60}$$

Clearly, $F(x,s)$ is independent of x for the sub-systems S-1 and S-3 and is a function of x for the sub-systems S-2 and S-4 across all the fundamental elements. The boundary conditions can also be expressed using matrix form as

$$M(s)\Psi(0,s) + N(s)\Psi(1,s) = \gamma(s), \quad x \in (0,1) \tag{2.61}$$

where $\gamma(s)$ represents the inhomogeneity present in the boundary conditions. $M(s)$ and $N(s)$ are called the boundary condition matrices.

For the boundary value problem represented by Eq. 2.59 and Eq. 2.61, there exists a unique solution which is represented as [80]

$$\Psi(x,s) = \int_0^1 G(x,\kappa,s)\nu(\kappa,s)d\kappa + H(x,s)\gamma(s), \quad x \in (0,1) \tag{2.62}$$

where

$$G(x,\kappa,s) = \begin{cases} H(x,s)M(s)\phi^{-1}(\kappa,s), & \kappa < x \\ -H(x,s)N(s)\phi(1,s)\phi^{-1}(\kappa,s), & \kappa > x \end{cases} \tag{2.63}$$

and

$$H(x,s) = \phi(x,s)\left[M(s) + N(s)\phi(1,s)\right]^{-1} \tag{2.64}$$

where $\phi(x,s)$ is the fundamental matrix of Eq. 2.59 satisfying

$$\frac{\partial}{\partial x}\phi(x,s) = F(x,s)\phi(x,s), \phi(0,s) = I. \tag{2.65}$$

$G(x, \kappa, s)$ and $H(x, s)$ are the transfer function and boundary influence function of the system, respectively. Also, the variables x, κ signify the sensing and actuation location, respectively, while determining the transfer function $G(x, \kappa, s)$.

The fundamental matrix $\phi(x, s)$ is the key to transfer function analysis. $G(x, \kappa, s)$ and $H(x, s)$ are calculated once the fundamental matrix is known. It is of primary importance to know that the exact $\phi(x, s)$ can be calculated in the closed-form for the uniformly distributed systems or sub-systems. However, for non-uniformly distributed systems, the exact closed form is not available in general [81]. Hence, in case of non-uniform sub-systems, the step-function approximation method is used where the non-uniform sub-systems are divided into a sequence of uniform sub-domains.

In Fig. 2.4(b), the non-uniform sub-system, S-2 is divided into S-2a and S-2b, and similarly S-4 is divided into S-4a and S-4b. Since the thickness of the beam is small compared to the width, only two sub-domains are considered to divide the non-uniform sub-systems. It was seen that there was no major impact on the system dynamics on further dividing these non-uniform sub-systems; however, the computational cost increased significantly. Using the step-function approximation method, the matrix $F(x, s)$ can be approximated for non-uniform sub-domains as $F(s) \approx F(\Delta x/2, s)$, where Δx is the length of sub-domain. Once the spatially independent matrix $F(s)$ is obtained for all the sub-systems, the fundamental matrix $\phi(x, s)$ can be easily calculated for the cable-harnessed beam [81]. It should be noted that the cable inertia effects are properly captured while applying step-function approximation method. However, the stiffness effects, in general, are marginally over-estimated due to presence of finite steps in non-uniform sub-domains.

In order to obtain transfer function for the hysteretically damped system using DTFM, the same procedure is followed as mentioned in Eqs. 2.60 —2.65 but with the modified $F(x, s)$ matrix which can be obtained by taking the Laplace transform of Eq. 2.54 (after including an external force) as

$$F(x, s) = \begin{bmatrix} 0 & 1 & 0 & 0 \\ 0 & 0 & 1 & 0 \\ 0 & 0 & 0 & 1 \\ -\frac{K_1 s^2}{B_1^*} & 0 & 0 & 0 \end{bmatrix} \tag{2.66}$$

The knowledge of $F(x, s)$ for the hysteretically damped system enables us to formulate $\phi(x, s)$ which is further used to obtain the transfer function $G(x, \kappa, s)$ for hysteretically damped systems.

2.2.2 Formulation for the diagonal pattern

A schematic of the front view of the diagonally wrapped cable-harnessed beam is shown in Fig. 2.5. There are N fundamental elements in the system, also referred to as sub-systems. Each sub-system has a diagonally passing cable on the top surface of the beam, which is a uniformly distributed parameter system governed by the PDE mentioned in Eq. 2.57. At the node of each sub-system, the cable section is present on a plane parallel to the $y-z$ plane along the three faces of the beam. This section of the cable can be assumed as a lumped mass at the node and written as $m_{node} = \rho_c A_c \left(2\bar{b} + 4\bar{h}\right)$. Hence, the whole system can be considered as a discretized, uniformly distributed parameter system with equal lumped mass at each node. Using DTFM, an exact transfer function of this system can be found. These cable elements are called lumped mass because it was assumed that they do not undergo deformation during bending vibrations in the transverse direction and hence there is no strain energy stored in these elements. In the following equations, important mathematical steps to obtain the exact transfer function of the given problem using DTFM are presented.

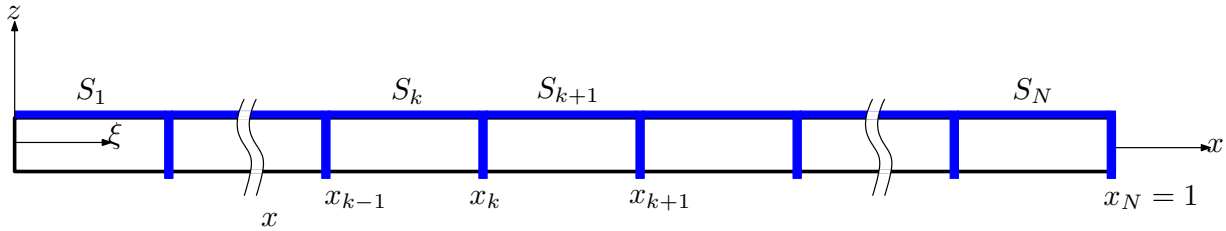

Figure 2.5: Multiple fundamental elements in the diagonal pattern of cable-harnessed beam

Since the fundamental matrix $\phi(x,s)$ is independent of boundary condition, consider the problem

$$\frac{\partial}{\partial x}\Psi(x,s) = F(x,s)\,\Psi(x,s), \quad \Psi(0,s) = \varrho, \qquad x \in (0,1) \tag{2.67}$$

where ϱ is an arbitrary complex 4×1 vector and $F(x,s)$ contains the coefficients of PDE of the system. The solution of Eq. 2.67 is of the form [81]

$$\Psi(x,s) = \phi(x,s)\,\varrho \tag{2.68}$$

Divide the non-dimensional length domain $(0,1)$ into N sub-domains (x_{k-1}, x_k), $k = 1,2,\ldots,N$, where $0 = x_0 < x_1 < \ldots < x_N = 1$. Clearly, in sub-domain $(x_{k-1}, x_k) \in S_k$

(say), the distributed parameter system is uniform. Since this sub-domain is similar to the uniform sub-domain of the zigzag pattern, the Laplace transform of homogeneous system in Eq. 2.57 can be used. The equation for any sub-domain S_k can be written as

$$\frac{\partial}{\partial x}\Psi_k(x,s) = F_k(s)\,\Psi_k(x,s), x \in (x_{k-1}, x_k) \tag{2.69}$$

where $F_k(s)$ is a constant and can be written either from Eq. 2.60 or Eq. 2.66 for the Kelvin-Voigt or hysteretic damping, respectively. The solution of Eq. (61) is written as [81]

$$\Psi_k(x,s) = e^{F_k(s)(x-x_{k-1})}\Psi_k(x_{k-1},s) \tag{2.70}$$

Next, in order to apply the displacement continuity and force balance at the node of the sub-systems, the column matrix $\Psi_k(x,s)$ is written by augmenting two column matrices $u_k(x,\ s)$ and $\epsilon_k(x,s)$, named as displacement and strain vectors, respectively. In addition, internal force vector $\sigma_k(x,s)$ relates to the strain vector using a constitutive relation as shown for the sub-domain S_k,

$$\Psi_k(x,s) = \begin{pmatrix} u_k(x,s) \\ \epsilon_k(x,s) \end{pmatrix} \quad , \quad \sigma_k(x,s) = E_k(s)\,\epsilon_k(x,s) \tag{2.71}$$

The vectors are described as $u_k(x,\ s) = \left\{\bar{w}(x,s), \bar{w}^{(1)}(x,s)\right\}^T$, and $\epsilon_k(x,s) = \left\{\bar{w}^{(2)}(x,s), \bar{w}^{(3)}(x,s)\right\}^T$, $\sigma_k(x,s) = \{M_b(x,s),\ V_b(x,s)\}^T$, where $M_b(x,s)$ and $V_b(x,s)$ are the bending moment and shear force, respectively. $E_k(s) \in C^{2\times 2}$ is the constitutive matrix.

The subsystems S_k and S_{k+1} are interconnected at the node x_k. Displacement continuity and force balance at x_k requires $u_k(x_k,s) = u_{k+1}(x_k,s)$ and $\sigma_k(x_k,s) = \sigma_{k+1}(x_k,s)$ respectively, or equivalently using Eq. 2.71,

$$\Psi_{k+1}(x_k,s) = T_k(s)\,\Psi_k(x_k,s), \quad T_k(s) \in C^{4\times 4} \tag{2.72}$$

where

$$T_k(s) = \begin{bmatrix} 1 & 0 & 0 & 0 \\ 0 & 1 & 0 & 0 \\ 0 & 0 & 1 & 0 \\ -m_{node}s^2/B_1 & 0 & 0 & 1 \end{bmatrix} \tag{2.73}$$

Here, the matrix $T_k(s)$ inherits both the conditions imposing displacement continuity and force balance. Note that the inertia of the cable elements at the node has been

accounted for while balancing the shear force at the nodes. The boundary condition in Eq. 2.67 is satisfied by subsystem S_1 i.e.

$$w(x,s) = e^{F_1(s)x}\gamma, \ \forall \ x \in (0, x_1) \tag{2.74}$$

Hence, using Eqs. 2.70, 2.72, and 2.74, the fundamental matrix for the system can be written as

$$\phi(x,s) = e^{F_{k+1}(s)(x-x_k)} T_k(s)\, e^{F_k(s)(x_k-x_{k-1})} \ldots T_1(s)\, e^{F_1(s)x_1} \tag{2.75}$$

Since, the fundamental elements length is same across the beam due to periodicity, $x_1 = x_2 - x_1 = \ldots = x_k - x_{k-1} = L_e$. In addition, uniformity in the fundamental element across the structure and same lumped mass promises the following relations: $F_1(s) = F_2(s) = \ldots = F_N(s)$, and $T_1(s) = T_2(s) = \ldots = T_N(s)$. Once the fundamental matrix is obtained from Eq. 2.75, the transfer function for a diagonal pattern can be evaluated in closed form by using Eq. 2.63 for both damping models.

In summary, for the zigzag pattern, the cable inertia effects are predicted to be exactly the same for both the homogenization method and DTFM. The cable stiffness effects, in general, are over-predicted in DTFM due to the use of step-function approximation method, whereas in the homogenization method, the total strain energy of the cable segments are accounted for and homogenized, yielding a better approximation. In contrast, for the diagonal pattern, the cable stiffness effects are predicted to be the same for both methods whereas the cable inertia effects are predicted differently; DTFM predicts the exact inertial effects whereas the homogenization method assumes that the lumped mass present on the $y-z$ plane is averaged over the fundamental element. Since diagonal pattern is a uniformly distributed parameter system for prediction of vibration characteristics in transverse bending direction, DTFM is able to predict an exact frequency response in this case.

2.3 Model Verification

In order to visualize the dynamic characteristics of a system, *frequency response functions* (FRFs) are generally utilized. Using FRFs, natural frequencies of a system can be visualized through its peaks. And roughly speaking, damping in the system can be interpreted through the width of those peaks, i.e. for a highly damped systems, the FRF peaks will be lower and broader. Further, the partial differential equations in Eq. 2.52 and 2.54 are in standard forms for damped beam mechanisms as shown in Refs. [72] and [82], respectively. Hence, the FRFs for each of the two systems can be found using the separation of

variables method. It should be noted that for a Kelvin-Voigt damped system, the obtained analytical form of damping ratio is frequency-dependent and given as $\zeta_n = D_1\omega_n/(2B_1)$ where ω_n is the n^{th} natural frequency. Whereas, for a hysteretically damped system, the damping ratio is frequency-independent and found as, $\zeta_n = \eta_{CH}/2$.

The system parameters shown in Table 2.1 are used in this work for model verification. To model the Kelvin-Voigt and hysteretic damping in the cables, cables with different geometric and material properties are chosen that best exhibit the characteristics of respective models. In the case of the host beam, the material damping was considered for Aluminum-6061 in both Kelvin-Voigt and hysteretic damping models of cable-harnessed systems to build a generalized model. The air damping is neglected in this chapter. The cable parameters chosen in this simulation study has been obtained from the realistic cables which were used for the experiments and are detailed in the next chapter. The damping factors shown in Table 2.1 have been obtained from the material characterization of the cables which are also explained in the next chapter. It should be further noted that although the effect of these cables may seem insignificant, as discussed in the next section on comparison of FRFs, these small changes in dynamics of the space structures is of a big concern. The accurate dynamic model help in building a robust vibration control algorithm used in the spacecraft structures. Hence, in these studies, we model the small changes in the dynamics of the host structure when the cables are attached and validate them using experiments in the next chapter.

It is also worth mentioning that the pretension in the cables result in pre-compression of the beam. Since the equivalent homogenized model considers the beam and cable as a whole, this compression is an internal force to the system and, therefore, any buckling analysis due to cable tension is beyond the scope of this work. In other words, upon application of the homogenization approach to obtain a beam model with equivalent EI and ρA for the cable-harnessed structure, the information pertaining to the buckling of the host beam as a sub-component is lost. To be more specific, when the strain energy expressions of beam and cable within the fundamental elements in Eqs. A.12 and A.16 are summed up to obtain the total strain energy, the term $\frac{1}{2}T\cos\theta\left(\frac{\partial w}{\partial \xi}\right)^2$ vanishes, due to which the buckling phenomenon for the host beam is no longer predicted by the homogenized model. It should be noted that the values for the cable tension were chosen to avoid beam buckling for the current study. It is also worth mentioning that the critical buckling load due to an external compressive load applied to the cable-harnessed system are different than the host beam structure and the equivalent homogenized model can predict this.

Table 2.1: Material and geometric properties of beams and cables

Beam	
width, mm	6
thickness, mm	0.97
length, m	0.25
Mass density, Kg/m^3	2700
Youngs modulus, GPa	68.9
η_{kb}, s	1.06×10^{-6}
η_{hb}	0.002

Kelvin-Voigt damped Cable	
Youngs modulus, GPa	1.18
Cross sectional diameter, mm	1.2
Mass density, Kg/m^3	1196
η_{kc}, s	1.2722×10^{-4}
Pretension, N	1

Hysteretically damped Cable	
Storage modulus, GPa	63.93
Cross sectional diameter,mm	0.7
Mass density, kg/m^3	1400
η_{hc}	0.035
Pretension, N	1

Wrapping pattern properties	
Number of fundamental elements for the zigzag pattern	3
Number of fundamental elements for the diagonal pattern	3, 6

2.3.1 Comparison of FRFs

In this section, the FRFs obtained using the equivalent homogenized model of cable-harness beam structures and DTFM are compared. The driving point frequency response functions are obtained for actuation and sensing locations at $x = l/10$ as per the global coordinate system. This location is carefully chosen to avoid nodes for the first five modes of interest at least. Further, the three zigzag, diagonal and longitudinal periodic patterns are used along with two damping models, Kelvin-Voigt and hysteretic damping as shown in Figs. 2.6 —2.11. A clamped-free (CF) boundary condition has been considered in the current study. Both damped and undamped cases are shown for comparison. In these FRFs, the response is shown for the first six modes. The zoomed-in figures of the highest mode of interest are also shown. Moreover, the natural frequencies from the two methods are listed in Tables 2.2 and 2.3 for Kelvin-Voigt and hysteretic damping models, respectively, for both wrapping patterns. The frequency data is shown for the first ten modes. In these tables, 'Hom' is used as a short form to represent the homogenization method in these tables. The FRF figures and frequency tables are shown for cable-harnessed structures with 3 fundamental elements for the zigzag pattern and 6 fundamental elements for the diagonal pattern in order to maintain a similar wrapping angle. This makes it easier to compare between the two wrapping patterns.

Figures 2.6, 2.7, and 2.8 show the comparison between the FRFs obtained from the homogenization and DTFM methods for both undamped and Kelvin-Voigt damped systems, using the system parameters in Table 2.1. Clearly, the homogenization method and DTFM are in a very good agreement.

For the diagonal pattern shown in Fig. 2.7, the higher modal frequencies seem to be overestimated by the homogenization method compared to the other two patterns shown in Figs. 2.6 and 2.8. This is due to the lumped mass of the cable segment present on the plane parallel to $y-z$ plane in the diagonal pattern being averaged over the fundamental element in the homogenization method. In contrast, they are modeled as an exact lumped mass in DTFM. Due to the cables low Young's modulus in the Kelvin-Voigt damping model, the mass effects of this cable are dominant over the stiffness effects in predicting the system dynamics. Hence, the lumped cable mass averaging acts as a source for the larger error between the two methods. For the zigzag pattern in Fig. 2.6, the results are in a better agreement because the mass per unit length in the homogenized and DTFM model is equal for this pattern. It is also shown that the best match between all three FRFs corresponds to the longitudinal pattern in 2.8 as both the homogenization and DTFM predict an exact solution for this pattern. These figures additionally highlight the significance of including damping in the models.

Table 2.2: Natural frequencies (in Hz) of beam harnessed with zigzag and diagonally wrapped cables having Kelvin-Voigt damping under CF boundary; 'Hom' represents homogenization method

	Zigzag pattern (3 fundamental elements)						Diagonal pattern (6 fundamental elements)					
	Hom		DTFM		Relative error in HOM		Hom		DTFM		Relative error in HOM	
Mode	Undamped	Damped	Undamped	Damped	Undamped	Damped	Undamped	Damped	Undamped	Damped	Undamped	Damped
1	12.38	12.38	12.38	12.38	0.00%	0.00%	12.30	12.29	12.25	12.25	0.41%	0.33%
2	77.56	77.56	77.56	77.56	0.00%	0.00%	77.07	77.07	76.73	76.73	0.44%	0.44%
3	217.17	217.17	217.16	217.15	0.00%	0.01%	215.8	215.8	214.71	214.71	0.51%	0.51%
4	425.57	425.56	425.49	425.48	0.02%	0.02%	422.9	422.87	420.44	420.42	0.59%	0.58%
5	703.51	703.43	703.22	703.16	0.04%	0.04%	699.07	698.99	694.18	694.12	0.70%	0.70%
6	1050.93	1050.67	1049.61	1049.46	0.13%	0.12%	1044.29	1044.03	1032.25	1032.06	1.17%	1.16%
7	1467.82	1467.12	1469.26	1468.66	-0.10%	-0.10%	1458.55	1457.84	1461.41	1460.76	-0.20%	-0.20%
8	1954.50	1952.55	1954.47	1953.20	0.00%	-0.03%	1941.86	1940.18	1936.10	1934.68	0.30%	0.28%
9	2510.06	2506.56	2509.87	2507.26	0.01%	-0.03%	2494.21	2490.65	2483.62	2480.68	0.43%	0.40%
10	3135.41	3128.57	3134.75	3129.89	0.02%	-0.04%	3115.61	3108.66	3099.58	3093.87	0.52%	0.48%

Another aspect to analyze these figures is the natural frequencies comparison between the three different wrapping patterns. It is shown that the highest natural frequencies correspond to the longitudinal pattern because this pattern creates the lowest mass effect and highest stiffening effect from the cables. For the diagonal and zigzag patterns, cables are wrapped around the beam and hence, the added cable mass due to wrapping is larger. Whereas, the added stiffness is smaller due to the presence of a component of cable stiffness along the longitudinal axis. Regarding the comparison of natural frequencies for the zigzag and diagonal pattern (as also listed in Table 2.2), the zigzag pattern exhibits higher natural frequencies for every mode. This is true for both damped and undamped models. The reason is based on the combination of the cable's material properties, the cable stiffness effects, and the cable mass effects added in each pattern. As mentioned earlier, the Kelvin-Voigt damped cable mass effects are dominant over its stiffness effects. As a result, the zigzag pattern, which according to Eq. 2.9 has a smaller mass per unit length, tends to exhibit higher natural frequencies compared to the diagonal pattern. It is important to mention that the natural frequencies of these wrapping patterns highly depend on the choice of cable material. As also seen later, in contrast to the above-mentioned case, the diagonal pattern would have a higher natural frequency than the zigzag pattern for cable chosen in the hysteretically damped model.

The results from the hysteretic damping model is now discussed. Figures 2.9, 2.10, and 2.11 show the comparison between FRFs obtained from the homogenization and DTFM methods for both undamped and hysteretically damped systems under CF boundary, given the set of system parameters in Table 2.1. Clearly, the two models, homogenized and DTFM, are in very good agreement for both undamped and hysteretically damping system.

For the given system parameters, the zigzag pattern FRF shown in Fig. 2.9 exhibits

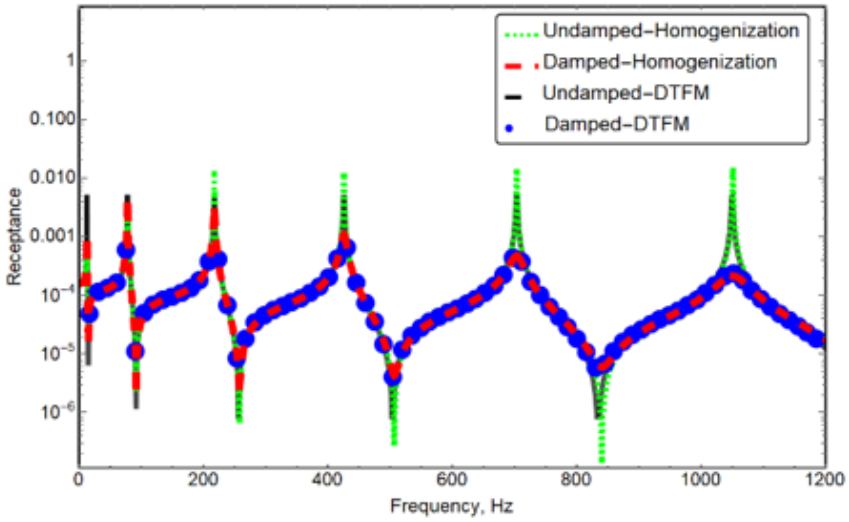

(a)

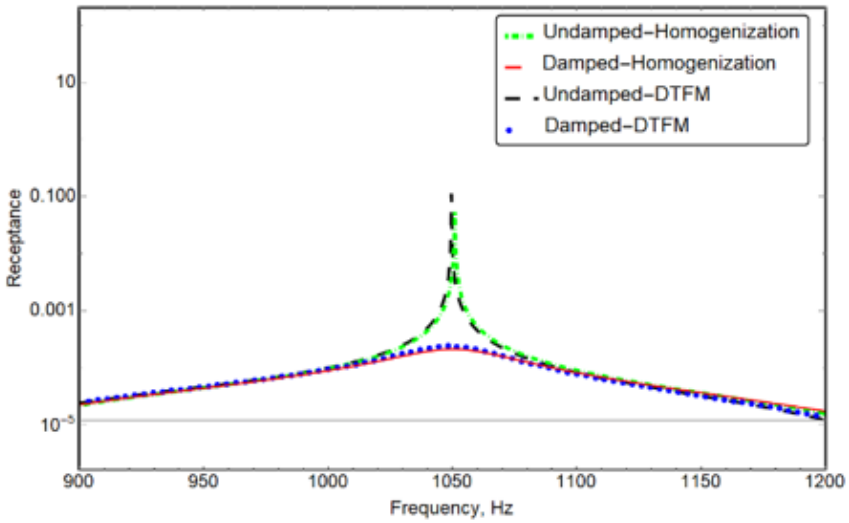

(b)

Figure 2.6: (a) Homogenization method and DTFM comparison of receptance (m/N) FRFs for undamped and **Kelvin-Voigt** damped system under CF boundary for the **zigzag pattern** (b) zoomed-in plots for the highest mode

a larger difference between the homogenization method and DTFM amongst all three patterns. This can also be seen from a comparison of natural frequencies in Table 2.3, where

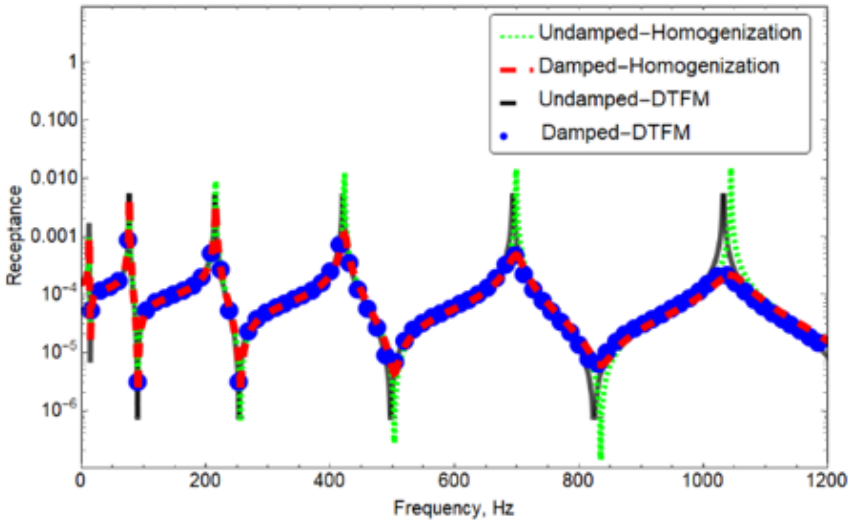

(a)

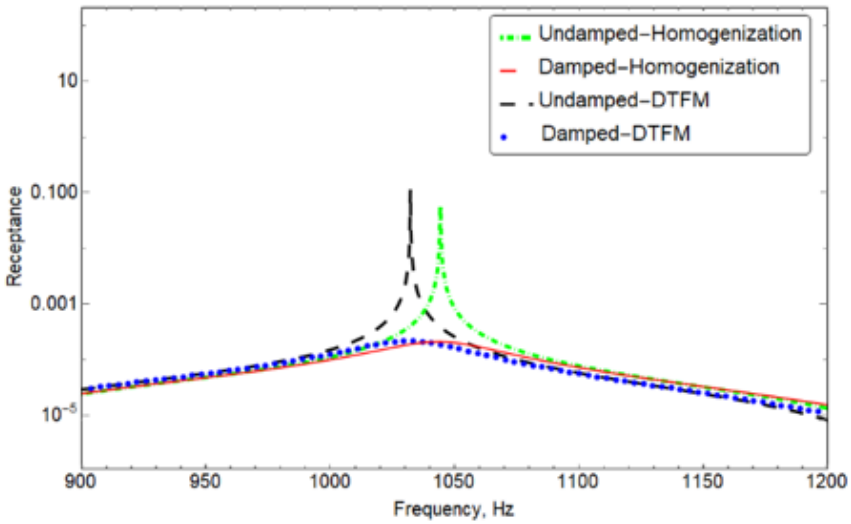

(b)

Figure 2.7: (a) Homogenization method and DTFM comparison of receptance (m/N) FRFs for undamped and **Kelvin-Voigt** damped system under CF boundary for the **diagonal** pattern (b) zoomed-in plots for the highest mode

natural frequencies for the zigzag pattern have a higher relative error in the homogenization method. This is in contrast to the Kelvin-Voigt damping model presented earlier, where

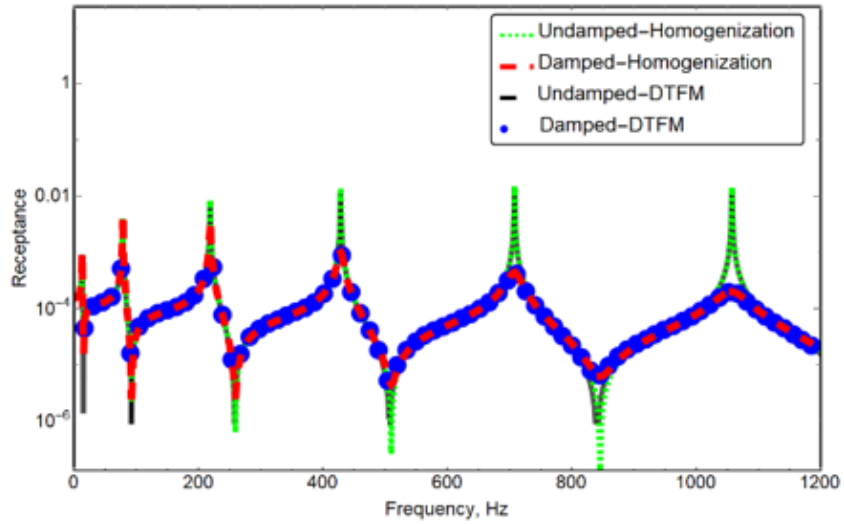

(a)

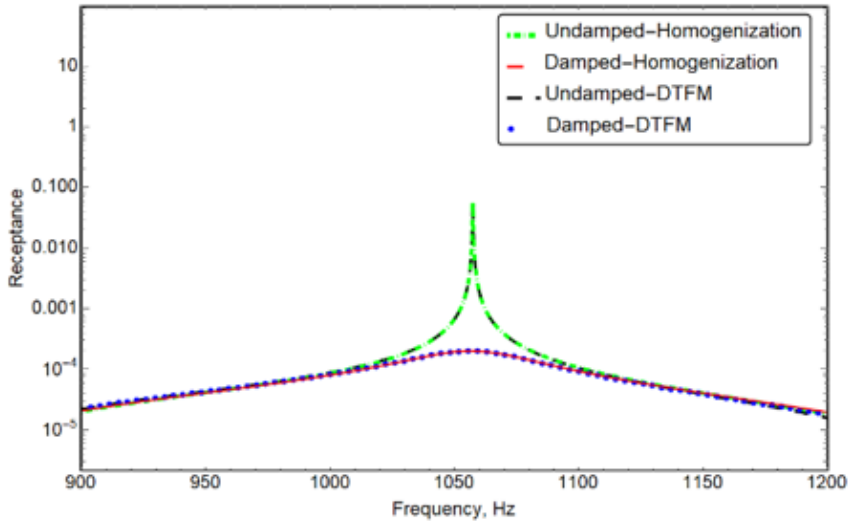

(b)

Figure 2.8: (a) Homogenization method and DTFM comparison of receptance (m/N) FRFs for undamped and **Kelvin-Voigt** damped system under CF boundary for the **longitudinal** pattern (b) zoomed-in plots for the highest mode

natural frequencies in the diagonal pattern showed higher error compared to the zigzag pattern. The larger error in the zigzag pattern is due to the high cable stiffness used in

the hysteretically damped model. Hence, the difference in stiffness predictions by DTFM results in higher error for natural frequencies. Recall, that for the zigzag pattern, the added cable inertia effects are predicted to be the same in both DTFM and homogenization model. However, the cable stiffness effects are marginally over-estimated in DTFM due to the use of the step-function approximation method. Moreover, for the homogenization method, since the strain energy of all cable elements is considered, the cable stiffness effect is a better approximation. This is the reason why natural frequencies predicted by the homogenization method have a larger error for zigzag pattern. For the diagonal wrapping pattern in 2.10, the stiffening effects are estimated to be the same by both methods, and hence the FRFs are a better match between the two methods. This can be also seen by comparing the natural frequencies from Table 2.3. Comparing the FRFs of different patterns in Figs. 2.9, 2.10, and 2.11, the longitudinal pattern yields the most-consistent result, as both the homogenization and DTFM predict an exact solution for this pattern. These FRF figures additionally highlight the significance of including damping in the models. Also, comparisons between the two damping models for a similar set of system parameters are presented later.

An interesting point to note from Tables 2.2 and 2.3 is that there is an abrupt change in the trend of frequency error observed in Mode-6 for both patterns. For the CF boundary, the Mode-6 peaks for the zigzag wrapped structure are located near the cable sections present on the beam face parallel to the $x - z$ plane. Recall, these sections are non-uniformly distributed systems in DTFM. Because the beam curvature is maximum at the modes peak, the stiffening effect predicted by DTFM is lower and hence, the Mode-6 natural frequency is observed to be higher for the homogenization method. The frequencies for other modes are however smaller for the homogenization method, following the reasoning given in the previous paragraph. Similarly, for the diagonal pattern, Mode-6 peaks are near the cable sections, which are in the plane parallel to $y - z$ plane and assumed as lumped mass. However, since the velocities are higher for the peaks in this case, the homogenization method results in a greater under-estimation of the kinetic energy for this mode. This is because the homogenization method assumes the averaging of lumped mass over the entire fundamental element.

Also, the diagonal pattern natural frequencies predicted by both methods are higher than the zigzag pattern for CF boundary shown in Table 2.3. This is due to the difference in cable stiffness added in each pattern. Also, since the cable Youngs modulus is significantly high in hysteretically damped system, the cable stiffness effects are dominant over the mass effects in determining the system dynamics. Besides, it is seen from Eq. 2.54 that the real part of B_1^* is the equivalent flexural stiffness for the homogenized model and according to Eq. 2.49, the real part of B_1^* for diagonal pattern would always be larger than the zigzag

Table 2.3: Natural frequencies (in Hz) of beam harnessed with zigzag and diagonally wrapped cables having hysteretic damping under CF boundary; 'Hom' represents homogenization method

	Zigzag pattern (3 fundamental elements)						Diagonal pattern (6 fundamental elements)					
	Hom		DTFM		Relative error in HOM		Hom		DTFM		Relative error in HOM	
Mode	Undamped	Damped	Undamped	Damped	Undamped	Damped	Undamped	Damped	Undamped	Damped	Undamped	Damped
1	14.97	14.96	15.08	15.08	-0.73%	-0.80%	15.31	15.31	15.30	15.30	0.07%	-0.07%
2	93.81	93.79	94.47	94.45	-0.70%	-0.70%	95.98	95.95	95.85	95.83	0.14%	-0.13%
3	262.68	262.62	264.32	264.28	-0.62%	-0.63%	268.73	268.68	268.33	268.28	0.15%	-0.15%
4	514.76	514.65	517.44	517.37	-0.52%	-0.53%	526.61	526.52	525.69	525.60	0.18%	-0.18%
5	850.93	850.79	853.79	853.70	-0.33%	-0.34%	870.53	870.43	868.64	868.53	0.22%	-0.22%
6	1271.14	1271.01	1266.43	1266.35	0.37%	0.37%	1300.42	1300.38	1295.48	1295.41	0.38%	-0.38%
7	1775.40	1775.38	1803.00	1802.87	-1.53%	-1.52%	1816.42	1816.44	1817.75	1817.82	-0.07%	0.08%
8	2363.70	2364.01	2384.22	2384.00	-0.86%	-0.84%	2418.29	2418.75	2416.01	2416.45	0.09%	-0.10%
9	3036.04	3037.27	3056.72	3055.40	-0.68%	-0.59%	3105.96	3107.78	3101.86	3102.96	0.13%	-0.16%
10	3792.42	3795.33	3814.18	3804.51	-0.57%	-0.24%	3879.77	3883.53	3874.73	3875.98	0.13%	-0.19%

pattern for a similar wrapping angle. The higher stiffening effects in the diagonal pattern results in the higher natural frequencies as compared to a zigzag pattern.

Also, comparing the Kelvin-Voigt and hysteretically damped system, it becomes evident that the frequencies for the later are noticeably larger than the former. This is due to the significantly higher cable Young's modulus used for the hysteretically damped system compared to the one that is best modeled using the Kelvin-Voigt damping model. Moreover, the FRFs in Figs. 2.6, 2.7, and 2.8 obtained from the Kelvin-Voigt model show an increase in modal damping ratios for higher frequencies; in comparison, the hysteretic model exhibits a constant modal damping ratio in Figs. 2.9, 2.10, and 2.11. This is because the modal damping ratios are directly proportional to the natural frequencies in the Kelvin-Voigt model; whereas for the hysteretic model, they are frequency-independent as also discussed in the beginning of this section.

It should be further noted that the FRF figures show the first six modes only to avoid the clutter in the plot. However, it has been shown in the Tables 2.2 and 2.3 that the homogenization model has a capability of predicting the accurate natural frequencies in the high frequency range as well.

A major advantage of using the homogenization method is the significantly reduced computational time over the DTFM. As an example, the computations for the FRF for the hysteretically damped zigzag cable-harnessed beam shown in Fig. 2.9 was found to be around 2,020 times faster when comparing homogenization to the DTFM. This ratio becomes amplified for the more complex and realistic geometries of space structures.

Further, a comparison between the three different patterns can be made by plotting their FRFs in the same plot. To amplify the differences between various wrapping patterns

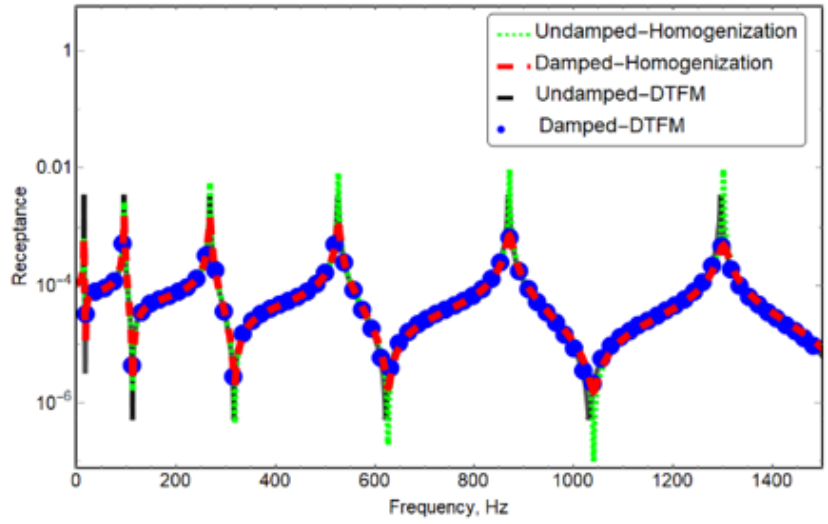

(a)

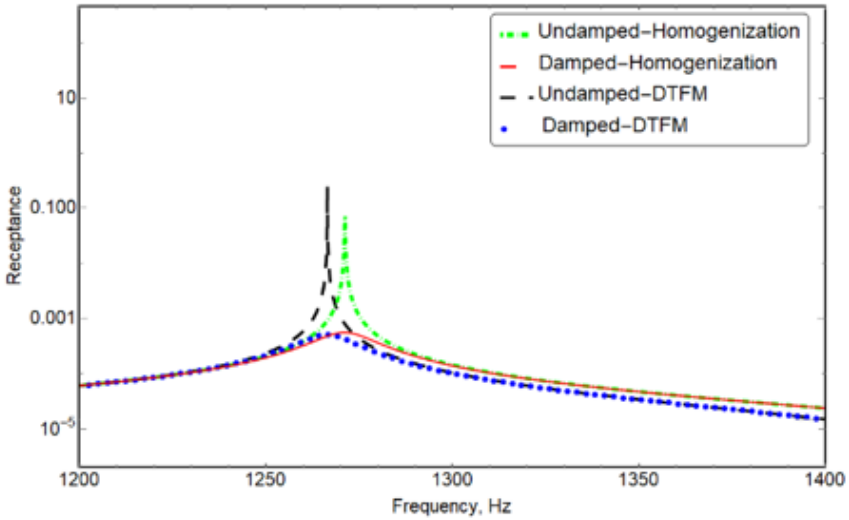

(b)

Figure 2.9: (a) Homogenization method and DTFM comparison of receptance (m/N) FRFs for undamped and **hysteretically** damped system under CF boundary for the **zigzag** pattern (b) zoomed-in plots for the highest mode

for each model, a larger beam width of 0.03 m was chosen. Other system parameters used remain the same as what was previously listed for each damping model. Also, only the CF

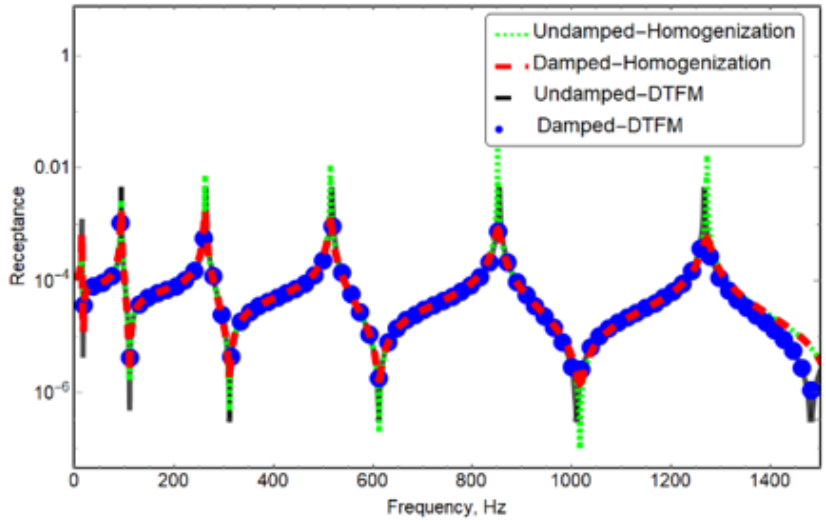

(a)

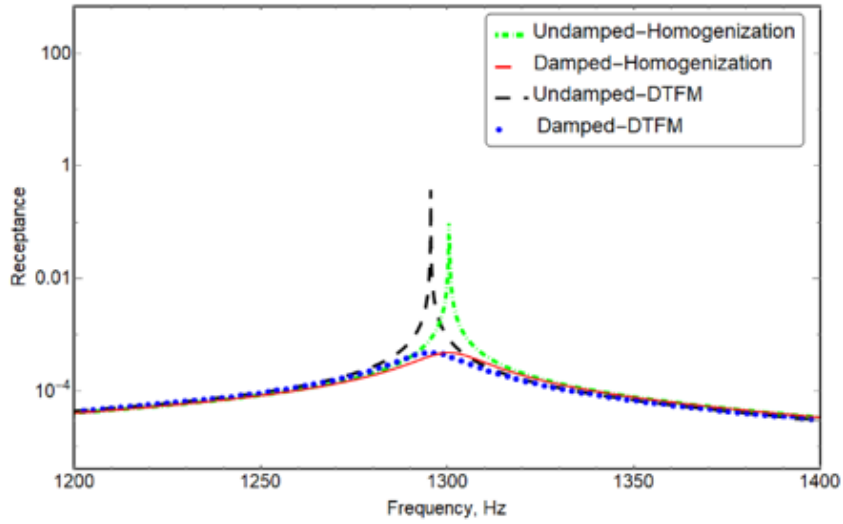

(b)

Figure 2.10: (a) Homogenization method and DTFM comparison of receptance (m/N) FRFs for undamped and **hysteretically** damped system under CF boundary for the **diagonal** pattern (b) zoomed-in plots for the highest mode

boundary condition is used as an example. The results are shown in Fig. 2.12. Clearly, the longitudinal pattern exhibits higher damping as compared to the diagonal and zigzag

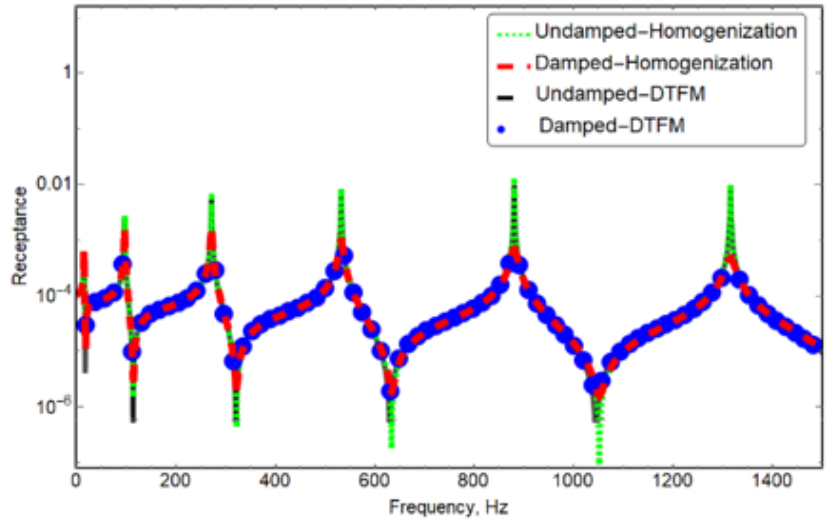

(a)

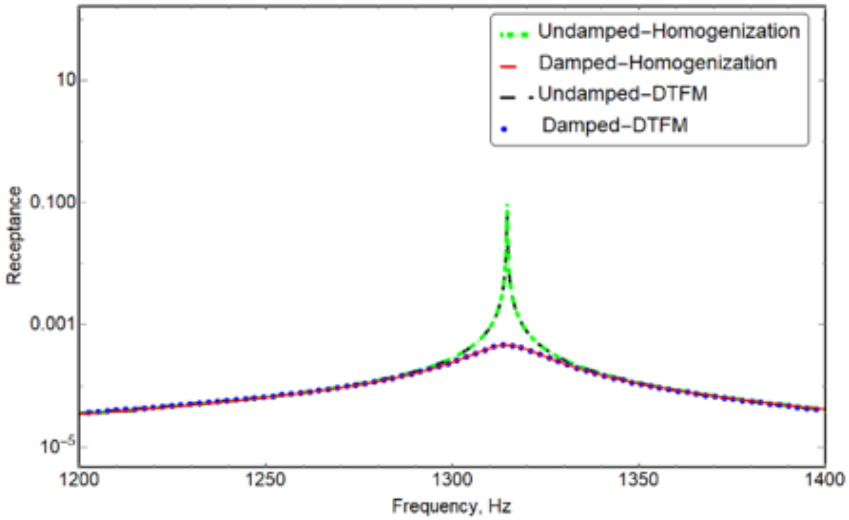

(b)

Figure 2.11: (a) Homogenization method and DTFM comparison of receptance (m/N) FRFs for undamped and **hysteretically** damped system under CF boundary for the **longitudinal** pattern (b) zoomed-in plots for the highest mode

patterns for both damping models. This is because the effective damping induced due to cable addition for diagonal and zigzag patterns is related to the wrapping angle over which

the damping force from the cable is projected. Therefore, for the case of the longitudinal pattern, the damping effects are maximized due to the zero angle with the horizontal axis.

The larger difference between frequencies for the longitudinal and other two patterns for the given system parameters of the hysteretically damped system is due to the larger cable Young's modulus. This further signifies the cable stiffening effects for the longitudinal pattern. This pattern has shown to have a larger stiffening effect compared to the other two patterns for the out-of-plane bending frequencies [36, 2].

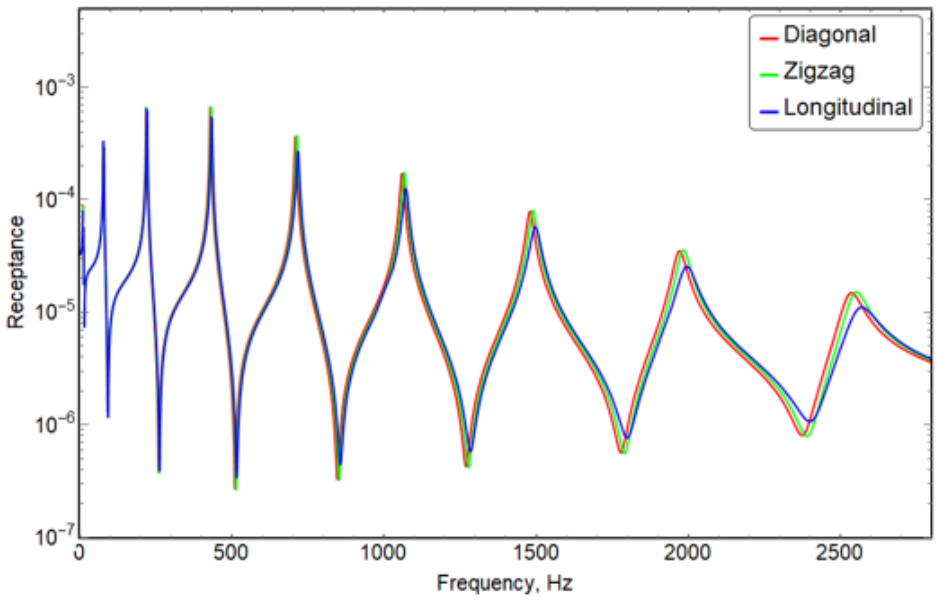

(a)

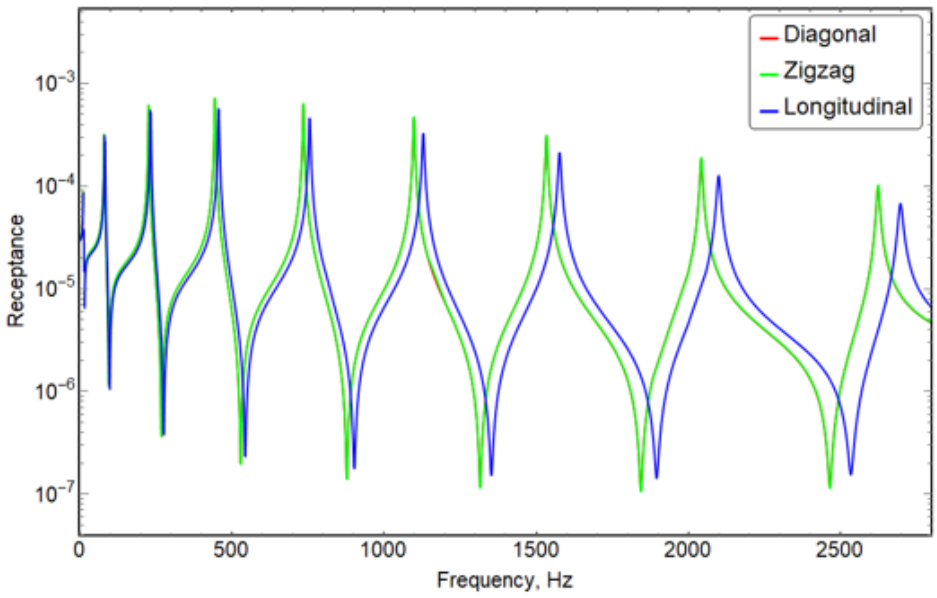

(b)

Figure 2.12: FRF comparison to exhibit damping effects among different wrapping pattern for (a) Kelvin-Voigt damped model, $b = 0.03m$, and (b) Hysteretically damped model, $b = 0.03m$

2.4 Parametric Analysis

In this section, the effects of several structural parameters such as cable radius, beam width, and fundamental element number on the overall damping of the cable-harnessed beams are discussed. This study is carried out for a CF boundary condition with $x = 0$ edge being clamped. The damping ratios are analytically obtained for Kelvin-Voigt model and hysteresis model as $\zeta_n = D_1\omega_n/(2B_1)$ and $\zeta_n = \eta_{CH}/2$, respectively. The half power bandwidth method presented in [72] is used to estimate the modal damping ratios for the DTFM.

Also, two different numbers of fundamental elements are chosen for the diagonal pattern to allow a fair comparison to the zigzag system as shown in Table 2.1. One case uses to the same number of elements for both patterns, and the other results in a similar wrapping angle. Also, while varying one system parameter, the other parameters are held constant as shown in the Table 2.1.

2.4.1 Effect of cable radius

Figures 2.13 and 2.14 compare the modal damping ratios for both damping models as a function of the cable radius. The term 'Hom' in the legends refers to the homogenization method. As expected, the damping ratios increase with the cable radius for all patterns and both damping models. Also, the damping ratios increase for the higher modes of the Kelvin-Voigt model, as they are directly proportional to the natural frequencies of the corresponding modes as shown in the equations above.

Moreover, as the cable radius becomes large, the difference between damping ratio estimations for the two methods increases. The difference is attributed to the averaging assumptions within a fundamental element for the homogenization method, and its reliance on the system periodicity. As the cables become a dominant part of the structure, the non-homogeneity within an element increases, and this method starts to show its limitations.

Additionally, for the Kelvin-Voigt model shown in Fig. 2.13, the differences between the two methods estimations are smallest for the fundamental modes, and increases with the mode number. This larger difference for the higher modes is because of the smaller number of fundamental elements per wavelength of the frequency of interest for the higher modes.

For the diagonally wrapped Kelvin-Voigt model, the damping ratio differences are smaller for the smaller number of fundamental elements as seen in Figs. 2.13(b) and 2.13(c).

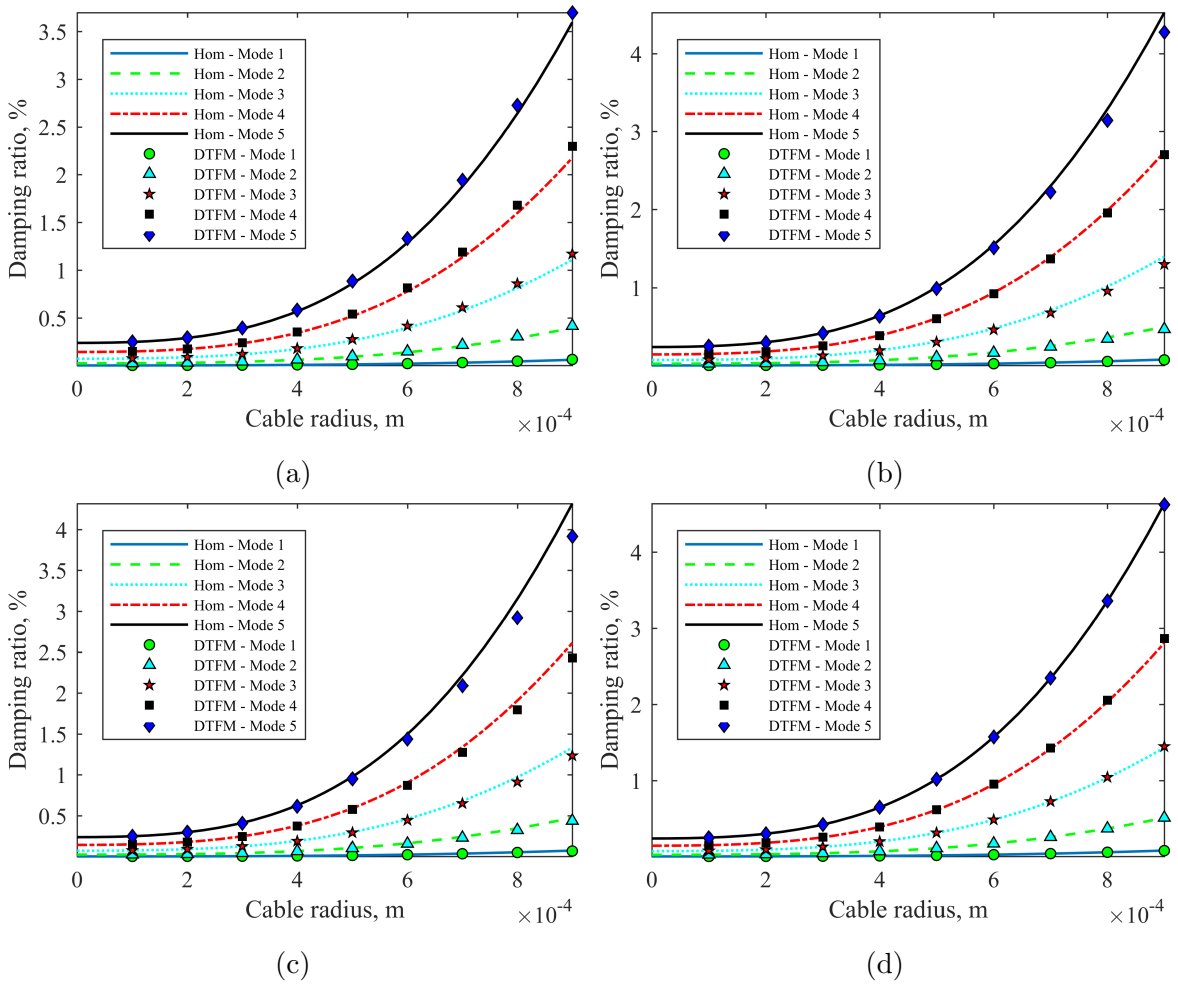

Figure 2.13: Damping effects for variable **cable radius** in a **Kelvin-Voigt** damped system for (a) zigzag, 3 fundamental elements, (b) diagonal, 3 fundamental elements, (c) diagonal, 6 fundamental elements and (d) longitudinal pattern

Recall that the cable parameters used in the Kelvin-Voigt model had a mass-dominant effect on the host structure dynamics. Also recall that for diagonal pattern, the difference in DTFM and homogenization method occur only due to cable inertia. Hence, when a smaller number of fundamental elements are used in diagonal patterns, the cable inertia effects are lower, leading to a smaller difference between the methods damping ratio predictions.

Amongst every pattern, the diagonal structure shows the greatest error between the two models' damping ratios; whereas the longitudinally wrapped beam demonstrates the

smallest error due to the homogenization being an exact solution for this case. This is directly related to the difference in natural frequencies predicted by both methods. As explained previously for the cable properties chosen for Kelvin-Voigt material, the diagonal patterns show higher error in frequencies due to difference in the estimation of cable inertia effects. Since the damping ratios are proportional to frequencies in this model, their errors are higher for the diagonal pattern.

The damping ratio comparisons for the hysteretically damped models as a function of the cable radius are shown in Fig. 2.14. It should be noted that for the hysteretic damping model, the modal damping ratios are constant across all modes. Therefore, only the first modal damping ratio is considered for comparison. For the homogenization method, this ratio is obtained using Eq. 2.55 and $\zeta_n = \eta_{CH}/2$. Also, expressions similar to Eq. 2.55 are obtained for the longitudinal pattern. Finally, the DTFM damping ratios are obtained by using the half-power bandwidth method from the FRFs.

As shown in Fig. 2.14, the homogenized model is in very good agreement with the DTFM for all the zigzag, diagonal and longitudinal patterns. Also, similar to the Kelvin-Voigt model, the damping ratios increase as the cable radius increases for every pattern, eventually reaching an asymptote for very large radii. The initial damping ratio increase is due to the attachment of a high damping cable to the weakly-damped host structure. However, as the cable radius becomes large, the cable becomes a dominant part of the equivalent homogenized system. In the limiting case, the damping ratio of the system saturates because it cannot be larger than the constant damping ratio of the hysteretically damped cable.

Another interesting observation in these hysteretic damping plots is the presence of a point of inflection, for which the corresponding cable radius could be numerically obtained. Before the point of inflection, the damping in the system has a higher sensitivity to change in cable radius. It was also observed for the diagonal pattern that when the number of fundamental elements was decreased, the error in the homogenization method increased; at higher cable radii this error is particularly significant.

Since the hysteretic damping ratios are independent of natural frequencies, the difference between damping ratios obtained from homogenization and DTFM in Figs. 2.14(a) and (c) are significantly less than what is observed for the Kelvin-Voigt damping case in Figs. 2.13(a) and (c).

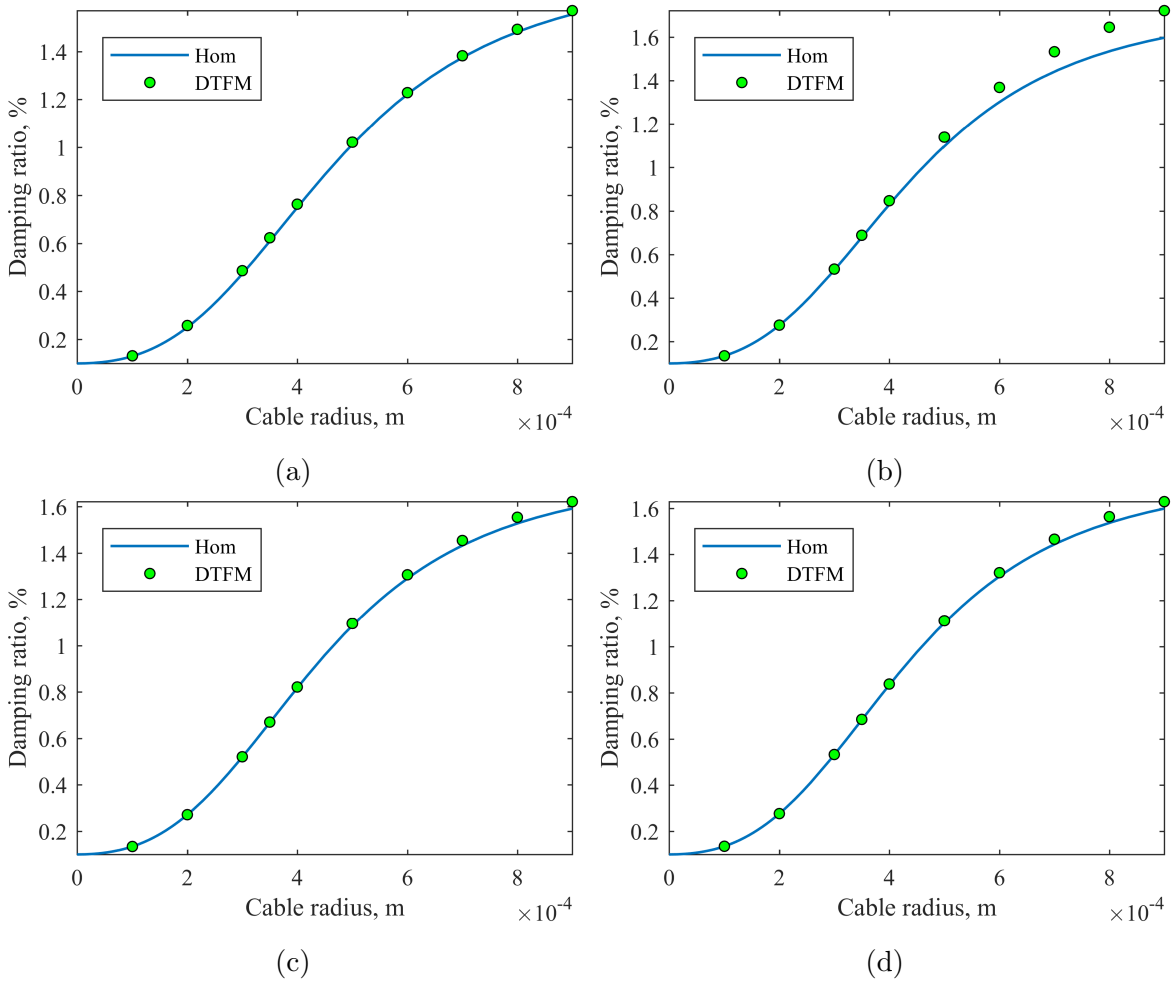

Figure 2.14: Damping effects for variable **cable radius** in a **hysteretically** damped system for (a) zigzag, 3 fundamental elements, (b) diagonal, 3 fundamental elements, (c) diagonal, 6 fundamental elements and (d) longitudinal pattern

2.4.2 Effect of beam width

Figure 2.15 shows the Kelvin-Voigt modal damping ratio variations for each wrapping pattern as a function of beam width. As shown in these figures, the overall damping ratio decreases as the beam width increases. This is expected as the cable damping effects diminish for a larger beam volume. Also, all figures show very good agreement between the two methods with the best agreement shown for the longitudinal pattern. This is expected,

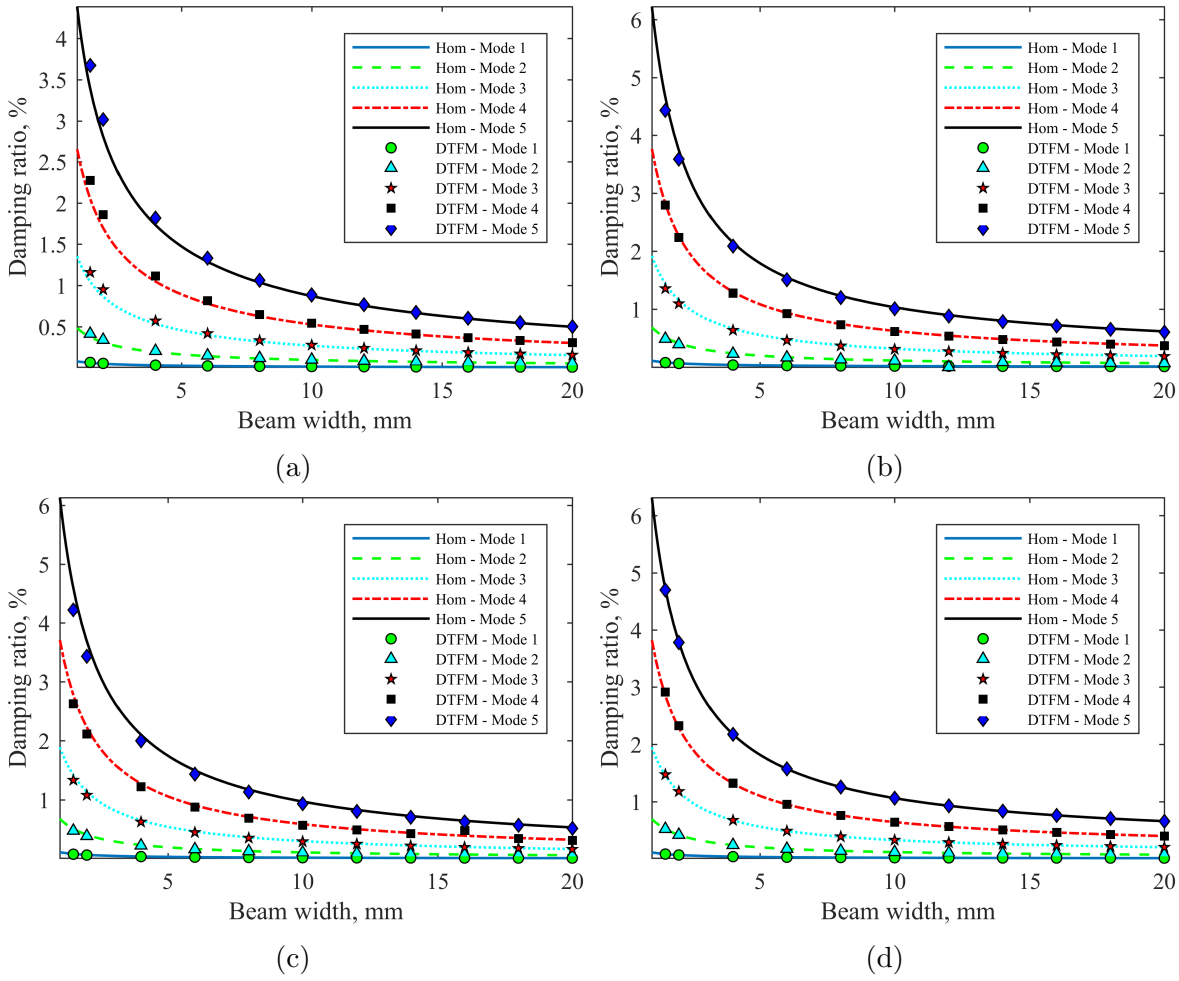

Figure 2.15: Damping effects for variable beam width in a Kelvin-Voigt damped system for (a) zigzag, 3 fundamental elements, (b) diagonal, 3 fundamental elements, (c) diagonal, 6 fundamental elements and (d) longitudinal pattern

as the errors associated with the homogenization assumptions for periodicity are minimal because the average strain energy for a discretized element is exact. It is also shown that the errors are particularly larger for zigzag and diagonal patterns for smaller beam widths. This is because smaller widths increase the cable effects, causing the errors associated with the pattern periodicity in the homogenization approach to increase.

It is also observed that for the zigzag pattern in Fig. 2.15(a), the damping ratios predicted by the homogenization method are marginally lower, whereas for the diagonal

pattern in Figs. 2.15(b) and 2.15(c), the ratios are slightly higher. This is particularly true for smaller beam widths, and is due to the over-estimation of stiffness by the DTFM. This leads to higher natural frequency predictions, and since damping ratios are directly proportional to the frequencies, the ratios are higher for DTFM. Conversely, the reason for the higher damping ratio in the diagonal pattern is the under-estimation of the cable inertia effects by the homogenization method. This leads to higher natural frequencies and hence higher damping ratios predicted by the homogenization method.

Additionally, the damping ratios seem to converge to a value for higher beam widths. This is because as the beam width increases, the overall damping effects of the cables become negligible. Mathematically, it is explained as follows: the saturation in modal damping ratios, $\zeta_n = D_1\omega_n/(2B_1)$, is related to the natural frequencies of the system. Since the governing PDE in Eq. 2.52 is similar to the Kelvin-Voigt damped beam formulation, ω_n is proportional to $\sqrt{B_1/K_1}$. For both the patterns, the values for K_1 are listed in Eqs. 2.9, and that of B_1 in Eqs. 2.24 and 2.25. It can be calculated that at large values of beam width, the cable effects diminish and the values of the coefficients K_1 and B_1 tend to limit $\rho_b A_b$ and $E_b I_b$, respectively. Since the ratio $E_b I_b/\rho_b A_b$ is independent of beam width, $\sqrt{B_1/K_1}$ tends to become independent of beam width. This results in saturation of the natural frequencies at high beam width. In addition, $D_1/2B_1$ was calculated and seen to be independent of the beam width for wide beams; therefore, the damping ratio saturates at large beam width as per the expression for ζ_n mentioned above. It should also be noted that the modal damping ratios saturate at different values corresponding to their natural frequencies.

Similarly, the modal damping ratios for the hysteretic damping model with respect to the beam width are presented in Fig. 2.16. Similar to the Kelvin-Voigt model, these ratios are found to decrease for the larger beam width as expected. Also, the longitudinal pattern shows the best match between the two models and the zigzag shows smaller accuracy for the smaller beam width values. The higher error for the zigzag pattern at low beam width can again be attributed to the error in DTFM where the step-function approximation method fails to predict the exact damping ratio when beam width becomes the same order as beam thickness.

In addition, as the beam width increase, the contribution of the cable in the homogenized continuum structure starts to decrease and in the limiting cases of wide beams, the wrapping angle becomes very large and hence, the damping contribution of the cable becomes negligible. As a result, the beam becomes the dominant component of the homogenized structure and since it is a hysteretically damped material, the constant loss factor of the beam results in a constant damping ratio for higher beam width. Mathematically, it can be seen from Eq. 2.55 that as beam width increase, η_{CH} saturates for wide beams

and the saturated value is given by loss factor of the beam $\eta_{hb} = E_b''/E_b' = 0.002$. The corresponding saturation value of damping ratio in Fig. 2.16 is $\zeta = 0.1\%$.

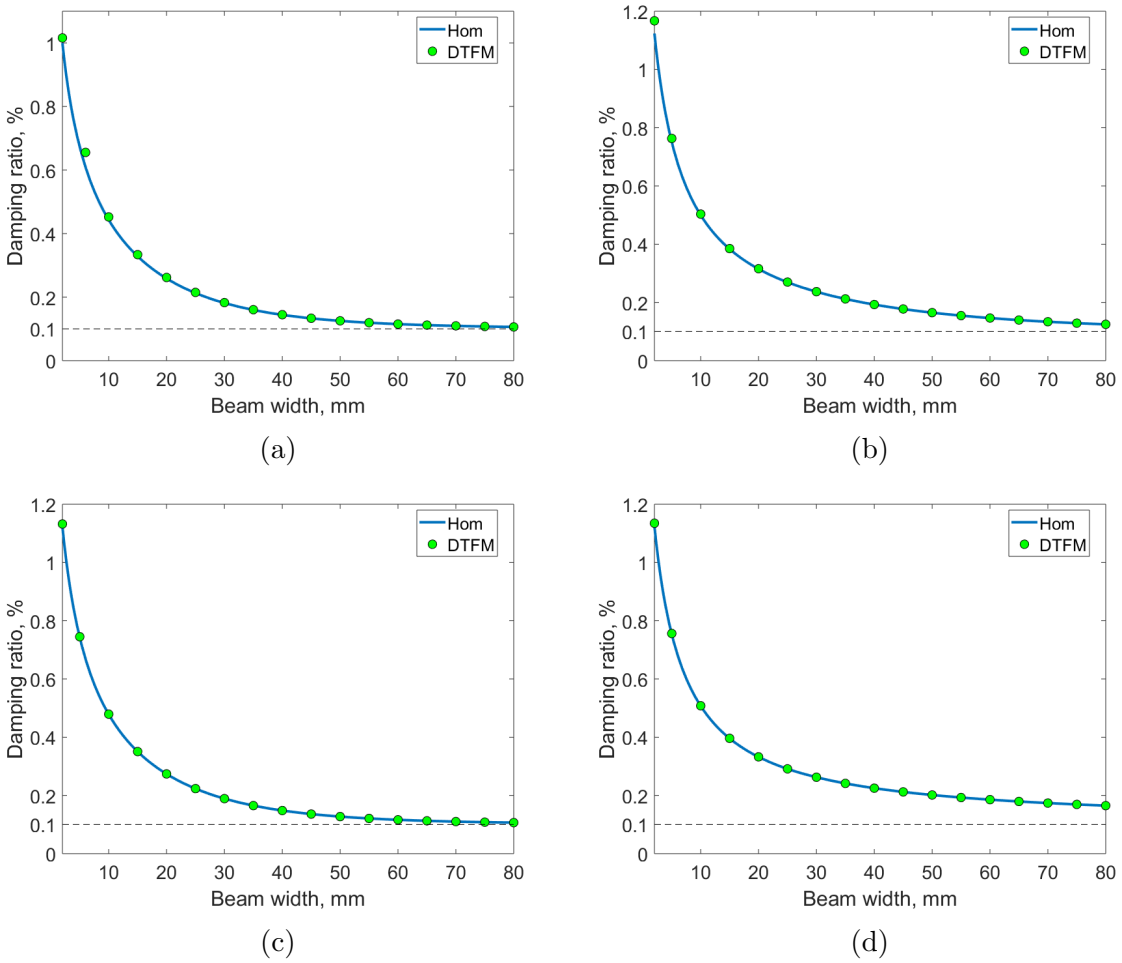

Figure 2.16: Damping effects for variable beam width in a hysteretically damped system for (a) zigzag, 3 fundamental elements, (b) diagonal, 3 fundamental elements, (c) diagonal, 6 fundamental elements and (d) longitudinal pattern

2.4.3 Effect of number of fundamental elements

Finally, the comparisons between the modal damping ratios for a various number of fundamental elements are shown in Fig. 2.17 for Kelvin-Voigt damping model. It is observed

for both wrapping patterns that the modal damping ratios decrease as the number of fundamental elements increases. This is expected, as the larger number of elements results in a tighter wrapping which further implies a larger wrapping angle, as shown in Figs. 2.1 and 2.2. This reduces the damping effects of the cables due to a smaller projection of their damping forces along the beam length. Therefore, for a single fundamental element system, the resultant damping will be the largest. Mathematically, this could also be understood using the expression of Kelvin-Voigt model damping ratios, $\zeta_n = D_1\omega_n/(2B_1)$. Clearly, the damping ratios depend on both the frequencies and coefficient ratio D_1/B_1. Since a larger number of fundamental elements result in a larger wrapping angle, this reduces the stiffening effects of the cables due to a smaller projection of their strain along the beam axis resulting in smaller frequencies. Additionally, this tighter wrapping increases the overall cable mass, further reducing these frequencies. Moreover, the ratio D_1/B_1 decreases with increasing number of fundamental elements. Therefore, since both the coefficient ratio and natural frequencies decrease for a larger number of fundamental elements, using the equation shown above one can see that the damping ratios become smaller.

The wrapping angle for the zigzag pattern is larger than the diagonal pattern given the same number of fundamental elements. This results in overall smaller damping for the zigzag pattern compared to the diagonal. This tighter wrapping pattern for the zigzag system also results in a much faster decay of the damping effects with increasing number of elements. Hence, the modal damping ratios seem to converge faster to their final values as shown in Fig. 2.17(a).

As expected, the higher modes exhibit larger damping ratios as well as larger errors between the two models. This error is due to the smaller number of fundamental elements per wavelength of the frequency of interest for the higher modes in the homogenization method.

It is also observed for the zigzag pattern in Fig. 2.17(a) that the damping ratios predicted by the homogenization method are marginally lower. In contrast, the ratios for the diagonal pattern in Fig. 2.17(b) are higher, particularly for a smaller number of fundamental elements. For fewer fundamental elements, the non-uniformly distributed sections in the zigzag pattern would be longer and hence, DTFM predicts higher frequencies. This leads to higher damping ratios as compared to the homogenization method. In comparison, the homogenization method for the diagonal pattern with few fundamental elements yields a greater inaccuracy in predicting the cable inertia effects. This is due to lumped cable mass being averaged over a much larger domain. As a result, under-prediction of the system's kinetic energy in homogenization method translates to higher frequencies and hence, higher damping ratios.

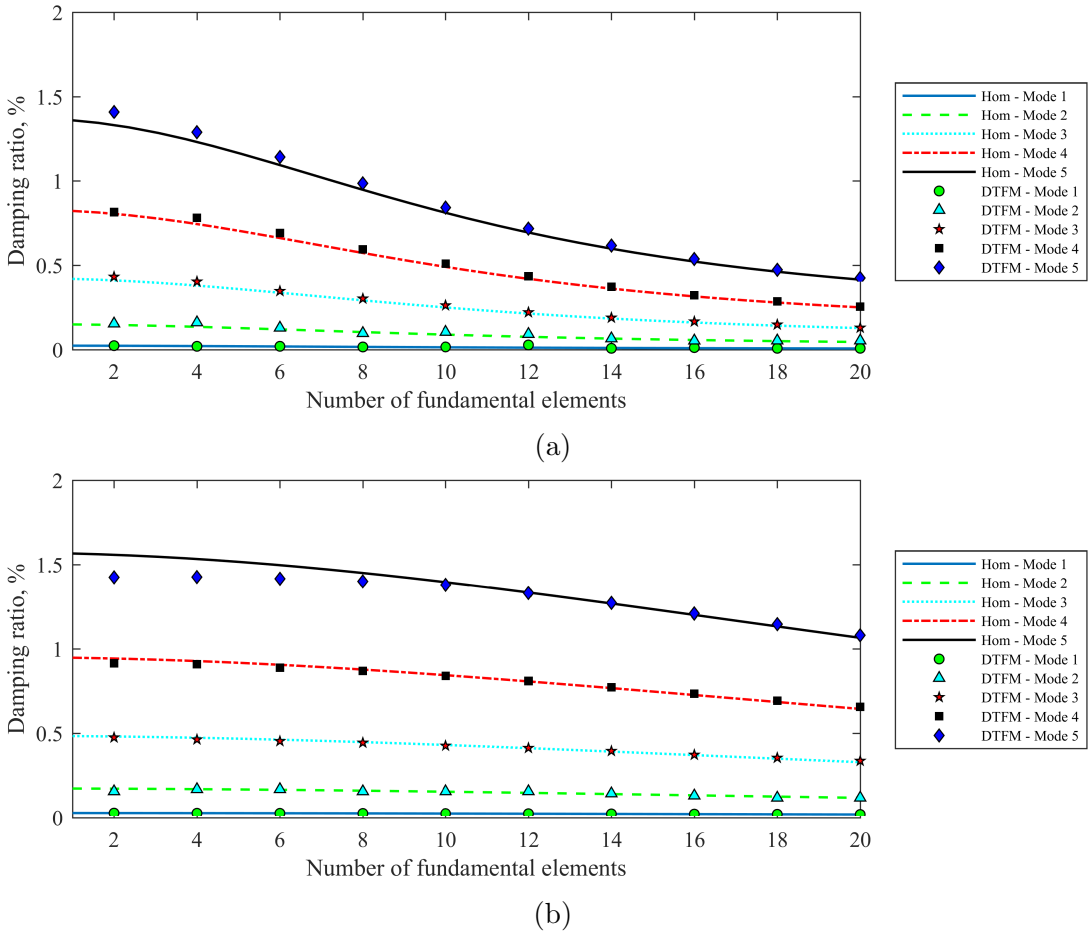

Figure 2.17: Effects of number of fundamental elements in a Kelvin-Voigt damped system for (a) zigzag and (b) diagonal pattern

Similarly, the modal damping ratios for a hysteretically damped system are presented across a range of number of fundamental elements in Fig. 2.18. Also, these figures show that the damping ratios decrease for a larger number of elements due to larger wrapping angles. This is further supported by Eq. 2.55. Similar to the previous cases, the two models are in better agreement for the diagonal pattern. As well, for increasing number of fundamental elements, the error between the homogenization method and DTFM decreases due to the assumptions for the periodicity in the homogenization method being more valid.

It should also be noted that as the number of fundamental elements decrease, or the ratio (L_e/l) increase, the homogenization model starts to show its limitations and becomes

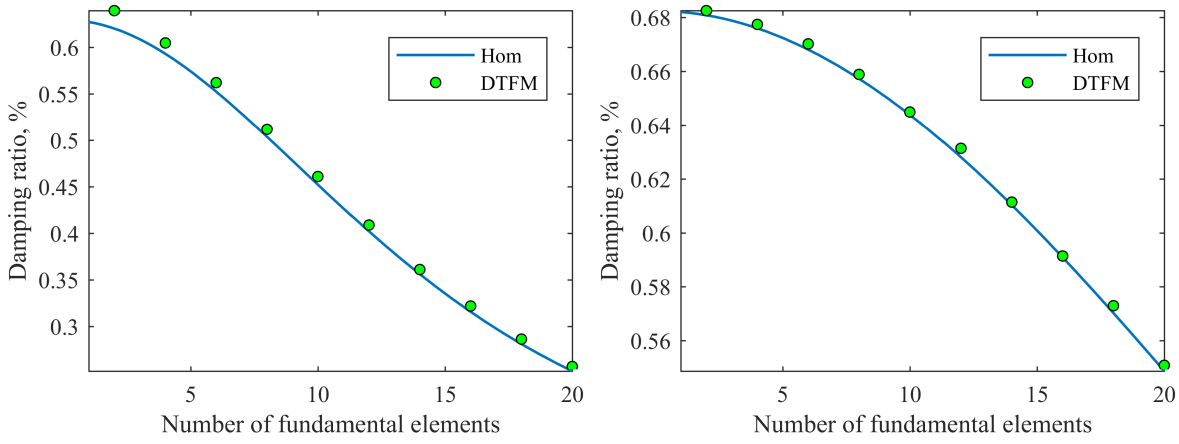

Figure 2.18: Effects of number of fundamental elements in a hysteretically damped system for (a) zigzag and (b) diagonal pattern

inaccurate even for lower vibration modes. Hence, when fewer number of elements are present, the model becomes sensitive to small variations in the length of a fundamental element.

2.5 Comparison between the two damping models

So far, the results for the two damping models were presented and discussed separately. It should be noted that it is difficult to use both models for the same material and hence, a choice of model has to be made based on the material characteristics. In previous sections, the geometric and material parameters of the cable were chosen differently. In this section, the two damping models are compared by assuming similar geometric and material properties of beam and cable with an aim to predict a similar damping behavior. However, it should be noted that it is not possible to predict similar damping behavior from both the models for a large number of modes.

To have a coherence between the two models, it is assumed that the cable energy loss per vibration cycle is consistent for each model. Assuming a standing waveform of a cable as $A\cos(kx)\sin(\omega t)$, the total energy dissipated in one cable vibration cycle (modeled as a string) from the two damping models is calculated as (see Appendix A.7):

$$W_{KV} = \pi^2 \eta_{kc} T A^2 \omega k \tag{2.76a}$$

$$W_H = \pi^2 \eta_{hc} T A^2 k \tag{2.76b}$$

As it is assumed that this loss in energy is equal for both models, it results in the relation $\eta_{hc} = \eta_{kc}\omega$, where ω is the frequency of vibration. This relation would not hold for a frequency bandwidth of interest as it relates the two coefficients at only one frequency. Hence, η_{hc} is considered to remain constant and η_{kc} is calculated such that both the models predict similar damping behavior in the initial few modes. This exercise is divided into three cases where η_{kc} is calculated in order to have the best match between the two damping models for 1) first mode, 2) first and the second mode, 3) first three modes. To start with, an objective function, $\Theta(\eta_{kc}) = \sum_i (\eta_{hc} - \eta_{kc}\omega_i)^2$ is proposed, where ω_i is the i^{th} natural frequency of the system. This function is minimized with respect to η_{kc} that results in the evaluation of η_{kc} for the three cases:

$$(\eta_{kc})_I = \eta_{hc}/(\omega_1) \tag{2.77a}$$

$$(\eta_{kc})_{I,II} = \eta_{hc}(\omega_1 + \omega_2)/(\omega_1^2 + \omega_2^2) \tag{2.77b}$$

$$(\eta_{kc})_{I,II,III} = \eta_{hc}(\omega_1 + \omega_2 + \omega_3)/(\omega_1^2 + \omega_2^2 + \omega_3^2) \tag{2.77c}$$

In order to compare the damping behavior of both models, simulations are performed using the homogenization method for a cable-harnessed structure wrapped in diagonal pattern with 6 fundamental elements under a CF boundary. It is assumed that the beam is undamped for this analysis and the remaining beam properties are assumed to remain unchanged as mentioned in Table 2.1: $b = 6\ mm$, $h = 0.97\ mm$, $l = 0.25\ m$, $\rho_b = 2700\ Kg/m^3, E_b = 68.9\ GPa$. The cable properties used in the hysteretically damped system are also chosen to be the same as mentioned in Table 2.1. $E_c = 63.93 \times 10^9\ GPa, \rho_c = 1400\ Kg/m^3, r_c = 0.35\ mm, \eta_{hc} = 0.035, T = 1\ N$. It should be noted that the cable chosen for the Kelvin-Voigt damping has same material and geometric properties, except η_{kc}, and is determined using Eq. 2.77 for the three cases.

Figure 2.19 shows the comparison between the FRF obtained for both the damping models. Figs. 2.19(a)-(c) are each dedicated to the three cases of similar damping behavior for initial modes. In Case-1 shown in Fig. 2.19(a), the damping ratio is equal for the first mode; hence, both models predict the same system response near the first mode. However, as frequency increases, the Kelvin-Voigt model starts to predict higher damping. The difference can be highlighted in the sixth mode where the damping ratio predicted by the Kelvin-Voigt model is 33.6%, while the hysteretic damping model predicts the ratio as

0.60 %. The FRFs for Case-2 are obtained by minimizing the least square error between damping ratios of the first two modes and, hence, it is shown in Fig. 2.19(b), the models damping are well-matched for the first two modes. With increasing frequency, however, the error between models becomes significant. Similarly, FRFs for Case-3 (see Fig. 2.19(c)), are obtained by minimizing the least square error between damping ratios of the first three modes. Likewise, the models have a good match for the initial three modes. Afterwards, the Kelvin-Voigt model starts to predict higher damping at greater frequencies and the difference in response becomes worse. Also, it can be shown that as an attempt is made for a good match between the larger numbers of modes, the accuracy in prediction on damping in fundamental modes will be compromised. Hence, upon examination of the 3 cases shown above, it is seen that the best match between a smaller number of modes for the two models results in the Kelvin-Voigt model predicting much smaller energy contribution to the overall response for the higher modes.

After conducting this study, it is observed that the two models, although upon using the same system parameters such as geometric and material properties and energy loss per unit vibrations cycle, can predict an overall different damping behavior. Hence, it is important to consider the correct damping model that corresponds to the material characteristics of the cable and host structure, and predict accurate system dynamics. In summary, Kelvin-Voigt damping is most suitable when higher modes exhibit more highly damped behavior. Alternatively, for a system with fairly similar damping ratios across the fundamental modes the hysteretic damping would be more appropriate.

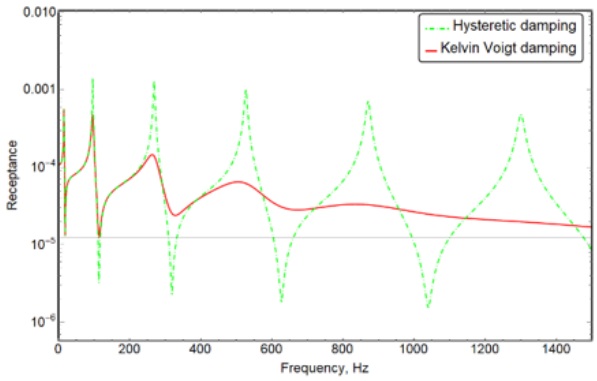

(a)

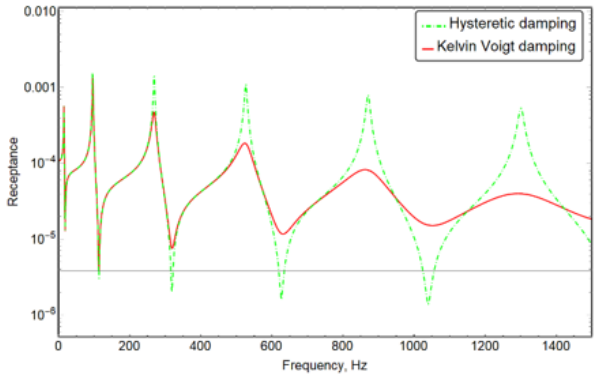

(b)

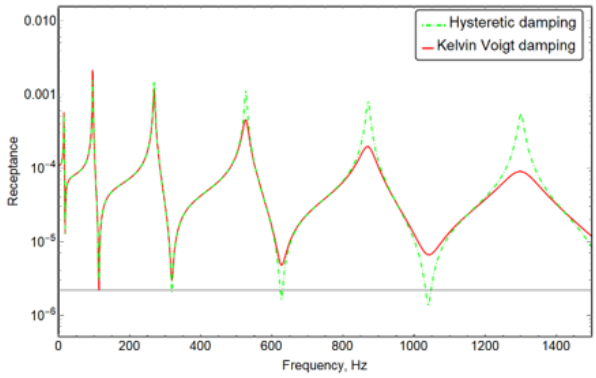

(c)

Figure 2.19: Comparison of Receptance (m/N) FRFs for hysteretic damping and Kelvin-Voigt damping for (a) Case-1, (b) Case-2 and (c) Case-3

2.6 Summary of the chapter

Obtaining low-order and high-fidelity dynamic models represented by simple partial differential equations as shown in the current chapter are of great advantage in studying the dynamic behavior of structures motivated by aerospace applications which are difficult to be ground tested prior to their launch. One of the major aspects of these modeling efforts includes the damping effects of power and signal cables on a host structure. In this regard, an analytical method for analyzing damping in cable-harnessed beam structures using a homogenization mathematical technique was presented. The proposed analytical models provide simple tools for studying the dynamics of these complex structures and are aimed at ultimately helping with the optimal cable patterns and their placements to help minimally impact the dynamics of the major components and payloads.

The presented work used an energy-based homogenization approach to obtain an equivalent damped continuum model for cable-harnessed beams. Two damping models namely, Kelvin-Voigt and hysteretic models are used to present the energy loss in the structure. Using the Green-Lagrange strain tensor to develop the strain energy and the Rayleigh dissipation function for the system, the governing equations were obtained for both the damping models. These equations were found to be similar in form to a damped Euler-Bernoulli beam. In addition, a distributed transfer function method is used as a method for comparison. The FRF results from the homogenization and DTFM are shown to match very well for both damping models. A big advantage of using homogenization technique was the significantly reduced computational time as compared to DTFM and FEM. Finally, a parametric analysis was performed to show the effects of different structural parameters on the overall damping behavior of the system. The findings from the analysis can be summarized as follows:

1. With an increase in cable radius, the damping in the system monotonically increases for Kelvin-Voigt damping model. Whereas, for the hysteretically damped model, the damping initially increases and then it levels off.

2. With an increase in the beam width, the damping in the system decreases for both the damping models.

3. As the number of fundamental elements increases, the damping in the system decreases. It was shown that for the zigzag pattern, the rate of the decrease was higher compared to the diagonal pattern for a given number of fundamental elements.

4. Kelvin-Voigt damping model was most suitable for cable-harnessed structure when higher modes are found to exhibit highly damped behavior.

5. A cable-harnessed system with fairly similar damping ratio across the modes is better modeled using the hysteretic damping model.

These findings can be applied during the design process of a cable-harnessed system to determine the appropriate cable parameters as well as wrapping pattern to optimize the dynamic behavior of the host structure. An optimal cable wrapping pattern can be obtained to minimize the cable dynamic effects on the host structure. In addition to the aerospace applications, these findings can be useful for marine and civil applications where cables are used widely.

Chapter 3

Experimental Validation of Damping Mechanisms in Cable-Harnessed Beam Structures

The analytical model of the cable-harnessed beam structures by incorporating damping mechanism was proposed in the previous chapter. In the current chapter, an experimental approach is used to validate the results obtained from the equivalent continuum model for the two damping models. [1]

It should be noted that only material damping was considered in the previous chapter, however, in the current chapter, an additional air damping factor is considered. The air damping has been included for a better accuracy in the model. Hence, the equation of motion is revisited in this chapter and an additional air damping term has been incorporated. Also, in the modeling section, a formulation for determining frequency response function (FRF) has been discussed for the sinusoidal base excitation of the structures.

Further, in order to conduct the experimental validation, the damping in the cables used for fabricating cable-harnessed systems were first characterized. The characterization yields the damping coefficients for both the damping models: Kelvin-Voigt and hysteresis. Thereafter, the air damping and beam's material damping constants were calculated. The acquisition of these damping parameters is necessary for finding the unknown parameters in the analytical model. To obtain the modal characteristics of the cable-harnessed beams, modal testing experiments were conducted. The experiments were conducted for zigzag

[1] The research work presented in this chapter has been published in *ASME Journal of Vibration and Acoustics* [83].

wrapping patterns and longitudinal pattern. The obtained response functions and natural frequencies are then compared with the model data for a successful model validation.

3.1 Analytical Model

In this section, a brief description is presented for analytical modeling of the cable-harnessed beam structure studied comprehensively in the Chapter 2. The main reason for the re-iteration of the model in this chapter is the inclusion of the damping term in the governing equation of motion which was absent in the Eqs. 2.52 and 2.54. Hence, the PDEs have an additional damping term which is briefly discussed in this section. Also, in the current chapter, the validation is presented for the zigzag wrapped cable pattern as shown in Fig. 3.1(a) and the special case of longitudinal pattern shown in Fig. 3.1(b).

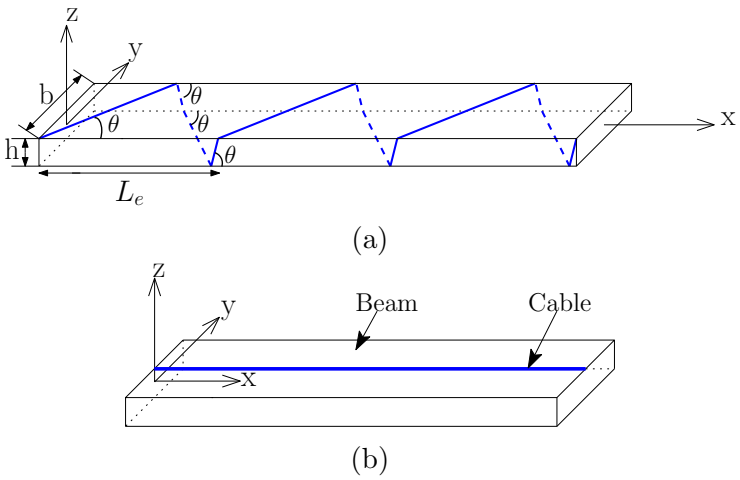

Figure 3.1: (a) Schematic of a cable-harnessed beam showing (a) zigzag pattern and (b) longitudinal pattern

3.1.1 Equation of motion for Kelvin-Voigt damping

The governing equation of motion (EOM) for the Kelvin-Voigt damped system can be written as (by including the additional air damping effects in Eq. 2.52):

$$K_1\ddot{w} + B_1 w'''' + D_1 \dot{w}'''' + D_{ak}\dot{w} \ = 0 \tag{3.1}$$

where the coefficients for the zigzag pattern can be written as

$$K_1 = \rho_b A_b + \frac{\rho_c A_c}{\cos\theta} \tag{3.2a}$$

$$B_1 = E_b I_b + E_c A_c \bar{h}^2 \cos^3\theta \left(\frac{\bar{b} + \frac{\bar{h}}{3}}{\bar{b} + \bar{h}}\right) + T\cos\theta \left(\frac{\bar{h}^2\left(\bar{b} + \frac{\bar{h}}{3}\right)}{\bar{b} + \bar{h}} - \frac{I_b}{A_b}\right) \tag{3.2b}$$

$$D_1 = C_b I_b + C_c A_c \bar{h}^2 \cos^3\theta \left(\frac{\bar{b} + \bar{h}/3}{\bar{b} + \bar{h}}\right) \tag{3.2c}$$

$$D_{ak} = \alpha_k(\rho_b A_b) \tag{3.2d}$$

where α_k is the air damping constant. Although air damping would be small in the space applications, it is necessary to consider it in the current modeling because of its contribution in the energy loss in the lab-scale experiments. It should be noted that the viscoelastic damping coefficients are related to respective elastic modulus as $C_b = \eta_{kb} E_b$ and $C_c = \eta_{kc} E_c$ where η_{kb}, η_{kc} are the proportionality constants in (s) for the beam and cable damping, respectively. Also, the energy dissipation due to the air damping effect is also considered by including a velocity proportional term, $D_{ak}\dot{w}$ in the governing PDE. This energy loss occurs due to the interaction of the beam with the surrounding air. Whereas, the air damping effect due to attached cable is neglected in the current study. Segregating the losses from the air damping and material damping of the cable is an arduous task, which is another reason why the entire energy loss in the cable is assumed as the internal (material) damping loss.

3.1.2 Equation of motion for hysteretic damping

The governing EOM for the hysteretically damped system is written as (by including air damping in Eq. 2.54)

$$K_1\ddot{w} + B_1^* w'''' + D_{ah}\dot{w} = 0 \tag{3.3}$$

where the air damping coefficient, D_{ah} is assumed to be dependent only on beam parameters. The coefficients are expanded for the zigzag pattern as

$$B_1^* = E_b^* I_b + E_c^* A_c \bar{h}^2 \cos^3\theta \left(\frac{\bar{b} + \frac{\bar{h}}{3}}{\bar{b} + \bar{h}}\right) + T\cos\theta \left(\frac{\bar{h}^2\left(\bar{b} + \frac{\bar{h}}{3}\right)}{\bar{b} + \bar{h}} - \frac{I_b}{A_b}\right) \tag{3.4a}$$

$$D_{ah} = \alpha_h(\rho_b A_b) \tag{3.4b}$$

The corresponding coefficients for the longitudinal pattern can be seen from Eq. 2.56. Further, B_1^* can be written as $B_1^* = B_1' + jB_1''$ where B_1' can be considered as an effective storage modulus of the homogenized system and B_1'' as an effective loss modulus. Also, the hysteretic damping loss factors for the beam and cable are defined as $\eta_{hb} = E_b''/E_b'$ and $\eta_{hc} = E_c''/E_c'$, respectively. These loss factors would be used later during the characterization of hysteretic damping in beams and cables. Also, the storage modulus of beam and cable, E_b' and E_c' used in the hysteretic damping model can be assumed to be equal to the respective elastic modulus E_b and E_c used in the Kelvin-Voigt model [84]. These values are however not equal in the real world because of the different tests through which they are acquired. The storage modulus is calculated using a dynamic test in which the material oscillates whereas to obtain the elastic modulus, the material is constantly stretched in the stress-strain test.

It is also important to note that the air damping coefficient, D_{ah} is considered different from D_{ak}. This is because of the presence of different damping mechanisms of beam material present in each equation. In the current work, the acquisition of material damping constants of the beam along with the air damping constants for both damping models is based on the modal testing experiment results of the bare beam. Due to different damping mechanisms in both the models, the obtained air damping coefficients are dissimilar and hence are considered different for both formulations.

3.1.3 Theoretical frequency response function

Kelvin-Voigt damping

The experimental validation of the damping behavior in the system is done through comparison of the FRFs. The experimental results, as explained later, are obtained using modal testing by clamping the cable-harnessed beams' left end with a fixture mounted on an electrodynamic shaker (as described in the next section). The shaker provides the sinusoidal excitation to the structure and sweeps through a pre-set frequency range. This excitation results in a non-homogenous BC because the displacement of the left edge would have a non-zero sinusoidal displacement and the BC becomes, for $\omega_s \neq 0$,

$$w\left(0,t\right) = \frac{gg_f}{\omega_s^2}\sin\left(\omega_s t\right) \tag{3.5a}$$

$$w'\left(0,t\right) = 0 \tag{3.5b}$$

$$B_1 w''(l,t) + D_1 \dot{w}''(l,t) = 0 \tag{3.5c}$$

$$B_1 w'''(l,t) + D_1 \dot{w}'''(l,t) = 0 \tag{3.5d}$$

and the EOM for transverse vibrations remains the same as Eq. 3.1. In Eq. 3.5(a), g is the acceleration due to gravity, g_f is a dimensionless acceleration factor, and ω_s is the excitation frequency of shaker.

To transform the displacement BC into a homogeneous equation, a function, $\mu(x,t)$, satisfying all the BCs is introduced similar to [30] where $\mu(x,t) = \left(g g_f/\omega_s^2\right)\sin(\omega_s t)$. Using a transformation, $y(x,t) = w(x,t) - \mu(x,t)$, the governing PDE can be written in terms of $y(x,t)$ as:

$$K_1\ddot{y} + B_1 y'''' + D_1 \dot{y}'''' + D_{ak}\dot{y} = K_1 g g_f \sin(\omega_s t) - \left(\frac{D_{ak} g g_f}{\omega_s}\right)\cos(\omega_s t) \tag{3.6}$$

and the new BCs of the transformed PDE become homogeneous as

$$y(0,t) = 0 \tag{3.7a}$$

$$y\prime(0,t) = 0 \tag{3.7b}$$

$$B_1 y''(l,t) + D_1 \dot{y}''(l,t) = 0 \tag{3.7c}$$

$$B_1 y'''(l,t) + D_1 \dot{y}'''(l,t) = 0 \tag{3.7d}$$

It is important to note that since Kelvin-Voigt damping is a proportionally damped system, the mode shapes remains identical to the undamped system. For a clamped-free system, the mode shapes are given as [72]

$$\phi_n(x) = A_n\left\{\cos(\beta_n x) - \cosh(\beta_n x) - \frac{\cos(\beta_n l) + \cosh(\beta_n l)}{\sin(\beta_n l) + \sinh(\beta_n l)}\left[\sin(\beta_n x) - \sinh(\beta_n x)\right]\right\} \tag{3.8}$$

where β_n is the n^{th} solution obtained from the characteristic equation of the clamped-free system $\cos(\beta l)\cosh(\beta l) = -1$, A_n are the mass-normalized coefficients of the mode shapes. Also, the undamped natural frequencies can be found using [30]

$$\omega_n = \beta_n^2\sqrt{\frac{B_1}{K_1}} \tag{3.9}$$

When the series solution, $y(x,t) = \sum_{n=1}^{\infty} \phi_n(x)\,\Gamma_n(t)$ is substituted in Eq. 3.6 and simplified after multiplying by $\phi_k(x)$ along with the orthogonality condition of the mode shapes, we obtain

$$\begin{aligned}\ddot{\Gamma}_k(t) + 2\zeta_k\omega_k\dot{\Gamma}_k(t) + \omega_k^2\Gamma_k(t) &= gg_f\left(K_1\int_0^l \phi_k(x)\,dx\right)\sin(\omega_s t) \\ &\quad - gg_f\left(D_{ak}\int_0^l \phi_k(x)\,dx\right)\cos(\omega_s t) \\ &= gg_f\bar{\phi}_k\sin(\omega_s t) - gg_f\bar{\phi'}_k\cos(\omega_s t) \quad (3.10)\end{aligned}$$

where $\bar{\phi}_k$ and $\bar{\phi'}_k$ are written as a means of simplification of the terms within the respective brackets. Also, in this case, $\bar{\phi'}_k$, does not imply the derivative of $\bar{\phi}_k$. Further, in the process of obtaining Eq. 3.10, following orthogonality conditions were used:

$$\int_0^l K_1\phi_k(x)\,\phi_n(x)\,dx = \delta_{kn} \quad (3.11a)$$

$$\int_0^l B_1\phi_k(x)\,\phi_n''''(x)\,dx = \omega_k^2\delta_{kn} \quad (3.11b)$$

Also, in the Eq. 3.10, the modal damping ratio of the system was defined as

$$\zeta_k = \frac{D_1\omega_k}{2B_1} + \frac{D_{ak}}{2K_1\omega_k} \quad (3.12)$$

Finally, evaluating the steady state solution of Eq. 3.10, the analytical expression of the FRF for the base excitation $(m/(m/s^2))$ can be obtained as

$$H_{FRF}(x_{sen},\omega_s) = \left|\frac{1}{\omega_s^2} + \sum_{k=1}^{\infty}\frac{\phi_k(x_{sen})\left(\bar{\phi}_k - j\frac{\bar{\phi'}_k}{\omega_s}\right)}{\omega_k^2 + j\,(2\,\zeta_k\omega_k\omega_s) - \omega_s^2}\right| \quad (3.13)$$

where $j = \sqrt{-1}$, and x_{sen} is the distance of the sensing location for calculating FRF measured from clamped end, $x = 0$.

Hysteretic damping

The theoretical FRF derivation is carried out similarly for the hysteretic damping model. The sinusoidal shaker excitation introduces a non-homogeneous term in the displacement BC at the clamped end. Following the procedure analogous to the calculation of theoretical FRF for the Kelvin-Voigt damping, the non-homogeneous terms can be removed by introducing a function and transforming the governing PDE. Also, for the constant hysteretic damping model, the mode shapes remain identical to the undamped model. Using the orthogonality of the mode shapes, the temporal equation for the hysteretic damping model can be obtained similar to Eq. 3.10,

$$\ddot{\Gamma}_k(t) + D_{ah}\dot{\Gamma}_k(t) + \left(1 + j\frac{B_1''}{B_1'}\right)\omega_k^2\Gamma_k(t) = gg_f\bar{\phi}_k\sin(\omega_s t) - gg_f\bar{\phi'}_k\cos(\omega_s t) \tag{3.14}$$

Here, the natural frequencies are calculated using $\omega_k = \beta_k^2\left(\sqrt{\frac{K_1}{B_1'}}\right)$. Further, evaluating the steady state solution of Eq. 3.14, the analytical expression of the FRF $(m/(m/s^2))$ is obtained as

$$H_{FRF}(x_{sen},\omega_s) = \left|\frac{1}{\omega_s^2} + \sum_{k=1}^{\infty}\frac{\phi_k(x_{sen})\left(\bar{\phi}_k - j\frac{\bar{\phi\prime}_k}{\omega_s}\right)}{\omega_k^2 + j\left(\frac{B_1''}{B_1'} + \frac{D_{ah}\omega_s}{\omega_k^2}\right)\omega_k^2 - \omega_s^2}\right| \tag{3.15}$$

3.2 Experimental Setup

In this section, the setup for characterizing the cable damping are discussed. Then, the experimental setup to obtain the modal characteristics of the cable-harnessed beams is presented.

3.2.1 Material Characterization

To quantify the material damping in the cables, the dynamic characterization of cables is done using an MTS 831 elastomer test system [85]. It is designed to measure different dynamic properties of a material by applying an oscillating load over a frequency range. In this study, the focus is on obtaining tan delta for the cable, which provides a means of quantifying the material damping. Tan delta $(\tan\delta)$ is a dissipation factor and can be understood as the ratio of energy lost to energy stored. It expresses the out-of-phase time relationship between an impact force and the resultant force that is transmitted to the supporting body. The higher value of the tan delta would imply a larger damping

coefficient. In addition, the elastic stiffness for the cable is also acquired to determine the cable's elastic modulus.

Figure 3.2 shows the elastomer test system with cable specimen clamped in it. The cable specimen is held between the clamp fixtures with help of mini line crimps in order to prevent cable slipping during tests. The line crimps provide better support to the cables at the ends compared to tying a knot. A mean load of 15 N is specified in the machine which results in the pre-tension in the cable. Further, a sinusoidal amplitude $X(t) = A_e sin(2\pi f)t$ is applied in the axial direction from 10 to 400 Hz in the interval of 10 Hz increments under amplitude A_e, where f is the excitation frequency. The amplitudes were chosen based on each cable's stiffness and the testing feasibility.

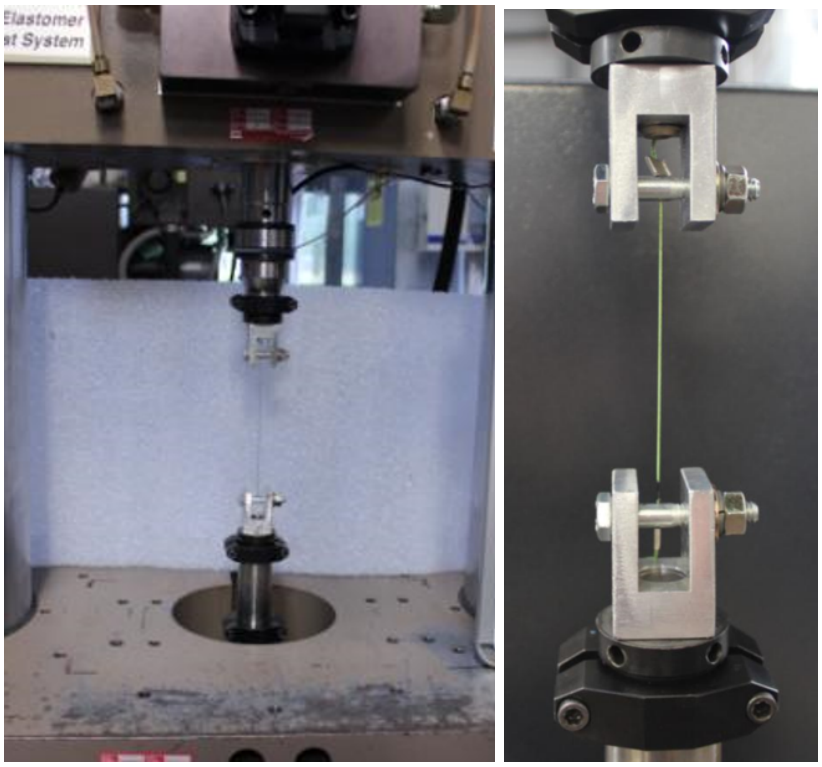

(a) (b)

Figure 3.2: (a) Front view of Elastomer Test System with a cable sample between the clamps, (b) close up of a cable sample C-1 clamped for testing

The elastomer test system measures the elastic stiffness K' and the phase δ between the load and displacement at a given excitation frequency. The dynamic stiffness is then

calculated using $K^* = K'(1 + j \tan\delta)$. The acquisition of tan delta over the frequency range enables the use of both Kelvin-Voigt and hysteretic damping models for the cable. The damping constants and other material properties for these cables are shown in the Sec. 3.3.1.

It should also be noted that the longitudinal excitation in the damping characterization of cables was preferred over a lateral excitation method. This is because in the latter case, the effect of air drag plays a significant role in loss mechanism. Hence, it becomes difficult to quantify and segregate the effect of internal damping due to cable material. Whereas in the longitudinal excitation, the air damping effects can be neglected as the motion is in the axial direction.

3.2.2 Modal Analysis Setup

Figure 3.3 shows the experimental setup for the modal testing of the cable-harnessed beam structure. The figure also shows the zoomed-in fabricated setup of zigzag wrapped and longitudinally attached cable-harnessed beams. The structure is excited using the base excitation method by clamping it on a fixture attached to Modal Shop 2075E dual purpose electrodynamic shaker as shown in Fig. 3.3(a). The shaker is controlled by a Siemens LMS 05 Mobile SCADAS data acquisition unit. Using a Modal Shop 2050E09 power amplifier and a PCB Piezotronics 352A24 accelerometer for the feedback control loop, a sinusoidal base excitation of the desired acceleration profile is generated and swept in the pre-set frequency range. It is worth mentioning that to increase the accuracy for capturing the response near the resonance, a low sweep rate of 0.01 Hz/s was used. For the displacement sensing on the vibrating structure, a Polytec OFV-505 laser vibrometer and Polytec OFV-5000 controller is used. The Sine Control module of LMS TestLab is used in the PC for measurement and analysis purposes.

Figure 3.3(b) shows the cable wrapped periodically around the beam in a zigzag pattern and Fig. 3.3(c) shows the cable attached longitudinally to the top surface along the center-line. The cable is under a constant pre-tension which is applied during fabrication using a hanging mass of known weight. For fabrication of the zigzag pattern, one end of the cable is tied to a small hole located on a corner of the beam free end, and the other cable end is tied to a hanging mass. The cable is then carefully wrapped around the beam such that the hanging mass remains stationary and its steady gravity force ensures a constant cable tension during the whole wrapping process. The constant cable tension is retained after wrapping the beam, as the other end of the cable is held between the clamps. Additionally, in some fabricated setups, multiple cables were wrapped around the structure. This was

done by applying tension to all the cables together which were then twisted to form a cable bundle before wrapping. This was done to maintain the tension in all the cables because in other case some cables might lose tension during the process of wrapping. This cable bundle was then wrapped around the beam in the similar manner described above.

Similarly, the cable is attached longitudinally in Fig. 3.3(c), however, the process is easier compared to wrapping. One end of the cable is tied to the hole located along the center-line near the beam free edge and the other end is tied to the known hanging mass. The taut cable is passed through the clamp which is tightened after ensuring that the cable is along the beam centerline. Finally, a small square piece of reflective tape is attached at the sensing location on these structures for an adequate laser beam reflection.

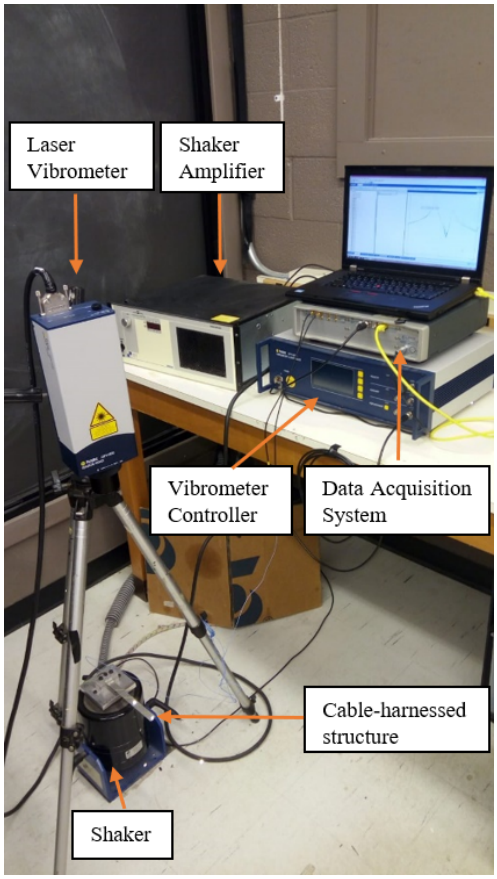

(a)

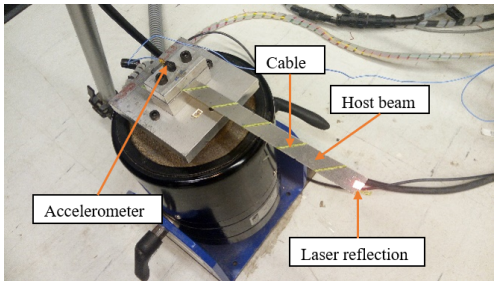

(b) (c)

Figure 3.3: (a) Experimental setup of the cable-harnessed system under base excitation, (b) beam wrapped with cable in a zigzag pattern, (c) cable attached in a longitudinal manner

3.3 Experimental validation

To validate the homogenization method, the FRFs obtained from the modal testing of the fabricated cable-harnessed beams are compared with the two damping models. As far as the nature of the homogenization method is concerned, there should be a consistency in choosing a damping model that is suitable for the entire cable-harnessed system. Therefore, the same damping model was chosen for both the substrate and cable corresponding to each test. As previously stated, damping parameters for the beam were determined separately for both damping models to provide a good match between the test and model for the bare beam.

To obtain the damping constants for the host beam, an inverse approach is utilized using the modal damping ratios from the modal tests of the unwrapped beam. For the cables damping properties, as seen previously, a direct method that involves material characterizations using an Elastomer test system is used. Since a major contribution of this study is to investigate the damping effects of the cables on the host beam structure, any model updating or inverse approach for the cable damping characterization would defy the purpose of the analytical model validation. Therefore, a direct approach was used to perform the cable damping characterization. The acquisition of the cable and beam parameters are further explained in more details in the following section.

3.3.1 System parameters

In this sub-section, the parameters obtained from the material characterization of the cable are firstly discussed followed by the air damping parameters from modal testing of the bare beam. Further, the details of fabricated cable-harnessed structures for the modal testing experiments are presented.

Cable Parameters

Recall, the storage stiffness, K' and tan delta were measured for the four cables using the elastomer test system. To obtain the storage modulus of the cable, the average value of measured storage stiffness over the frequency range of interest is calculated and transformed using $E'_c = K'(l_c/A_c)$, where l_c is the length of the cable clamped in the elastomer machine and A_c is the cable's cross-sectional area.

The dynamic testing was carried out for the four cables listed in Table 3.1. Cables of different diameters were used varying from 0.4 mm to 1.24 mm. The damping constants for the cables are calculated based on the measured tan delta from the dynamic testing

discussed in 3.2.1. Fig. 3.4 shows the plot of tan delta against frequency for the four cables which is used to characterize the cable damping with both damping models. According to the hysteretic damping model, the constant loss factor of the cable, η_{hc} is independent of the frequency. Recall, it was defined as the ratio of the loss modulus to the storage modulus. Hence, the hysteretic loss factor is equal to a constant value of tan delta i.e. $\eta_{hc} = \tan\delta$ and is obtained by calculating an average of the tan delta values in the entire frequency bandwidth for each cable. The calculated loss factor of the cables is further listed in Table 3.1.

The variation of tan delta in Fig. 3.4 are also interpreted such that the damping behavior of the cable can be modeled using Kelvin-Voigt damping. For this damping model, the dynamic modulus for the cable is written using $E_c^*(\omega) = E_c + j\ C_c\omega$. Comparing it with the dynamic modulus obtained from the test, $E_c^* = E_c'(1 + j\tan\delta)$, the relations, $\tan\delta = C_c\omega/E_c$ and $E_c = E_c'$ are obtained. According to this model, tan delta is a linear function of ω. This is used to calculate C_c from Fig. 3.4 by finding the slope of the line of best fit using the least-squares method provided the storage modulus is already calculated. Here, it should be noted that ω is circular frequency expressed in rad/s. The Kelvin-Voigt damping coefficient, C_c for all the four cables, is then reported in Table 3.1. Additionally, the cable storage modulus and the mass density are also reported.

Table 3.1: Geometric and material properties of the cables used for testing

Cable	Cable Name	Diameter (mm)	η_{hc}	$C_c(Pa-s)$	$E_c(GPa)$	ρ_c (Kg/m^3)
C-1	Power Pro Fishing line	0.4	0.035	1,335,614.69	63.93	1400
C-2	Technifiber Xone Tennis string	1.18	0.12	150,125.09	1.18	1196
C-3	BG 65 Titanium Badminton string	0.73	0.14	290,986.74	3.16	1021
C-4	Volkl V-Pro 18	1.24	0.025	305,242.40	4.46	1385

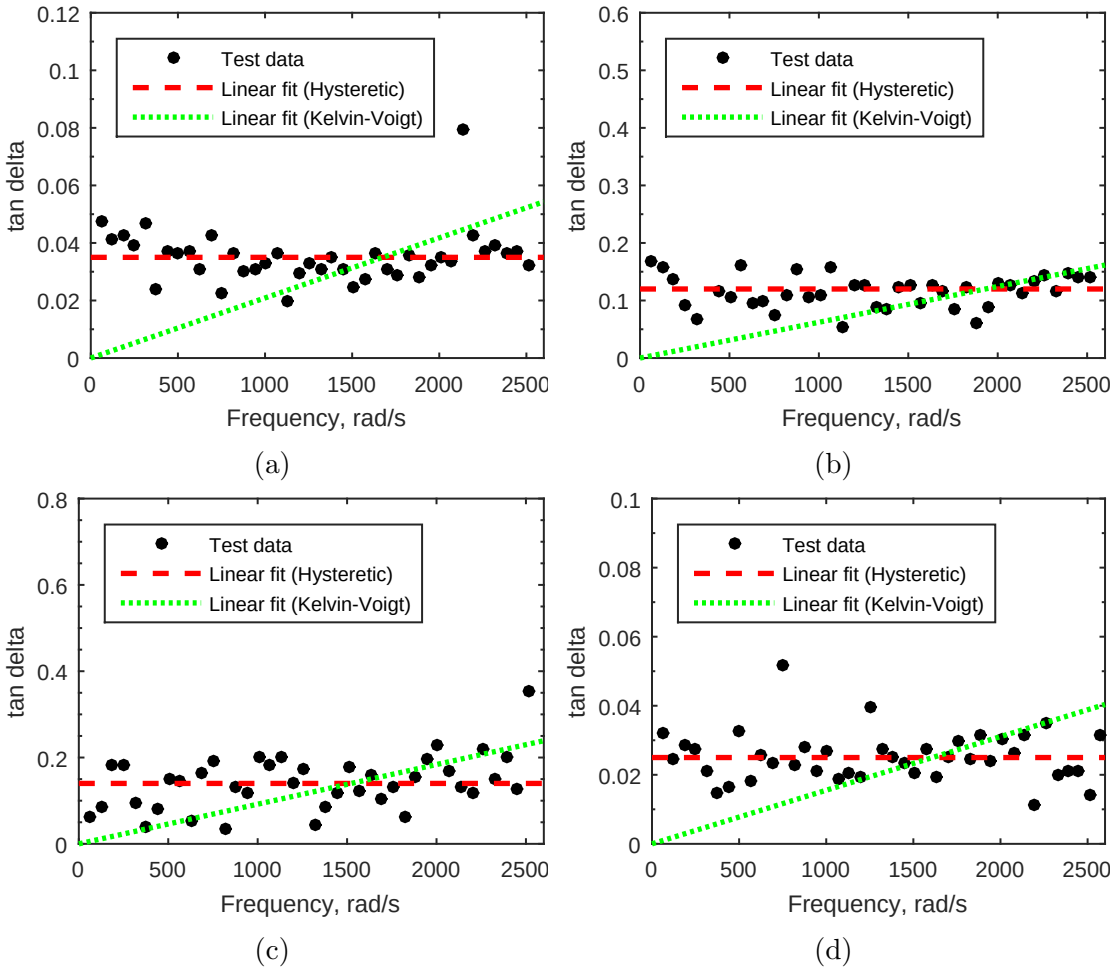

Figure 3.4: Material characterization data and linear curve fit of hysteretic and Kelvin-Voigt damping models for the four cables: (a) Cable C-1, (b) Cable C-2, (c) Cable C-3, (d) Cable C-4

Beam parameters and air damping coefficients

Three different beams made of Aluminum-6061 were used as host structures to study the effects of beam parameters on the overall damping of the system. The dimensions of the beams are listed in Table 3.2. Beam B-1 was chosen as a benchmark beam and other beams were chosen with respect to the dimensions of this beam. For example, B-2 is a thinner and shorter beam. The Beam B-3 was chosen to be a narrower beam as compared to B-1. The length of these beams was chosen such that their fundamental frequencies are close

to each other. The material properties for the chosen beam material are: $E_b = 68.9\ GPa$, $\rho_b = 2768\ Kg/m^3$.

Table 3.2: Geometric and damping parameters of the three host beams used for testing

Beam	Length (cm)	Width (mm)	Thickness (mm)	Kelvin-Voigt damping		Hysteresis damping	
				η_{kb}	α_k	η_{hb}	α_h
B-1	26	16	0.97	1.06×10^{-6}	1.21	0.0020	0.75
B-2	17	15.6	0.41	1.59×10^{-6}	1.37	0.0018	0.91
B-3	26	6	0.97	9.59×10^{-7}	1.00	0.0015	0.63

Although Aluminum is a weakly damped material, the damping in the beam is modeled to increase the accuracy of the model. For both the damping models, the beam damping parameters are chosen separately to provide a good match between the test and model for the three bare beams. Also, separate air damping effects are included in both damping models. In order to calculate these parameters, the modal testing of the three bare beams listed in Table 3.2 was conducted and natural frequencies and modal damping ratios were obtained. To predict the beam Kelvin-Voigt damping constant η_{kb} and corresponding air damping constant α_k, the analytical expressions of the modal damping ratios are first obtained. Applying the least square error method [60] to minimize the difference between the analytical and experimental damping ratio for the first five modes results in the damping constants mentioned in Table 3.2. A similar exercise was performed to obtain the beam hysteretic damping constant η_{hb} and the corresponding air damping constant α_h.

Using the geometric and material parameters listed in Table 3.2, the analytical model FRF for the three bare beams are compared with those obtained from the modal testing and are shown in Fig. 3.5 for both the damping models. As expected, the FRFs from both the damping models match very well with the test results due to the inclusion of accurately calculated beam damping parameters.

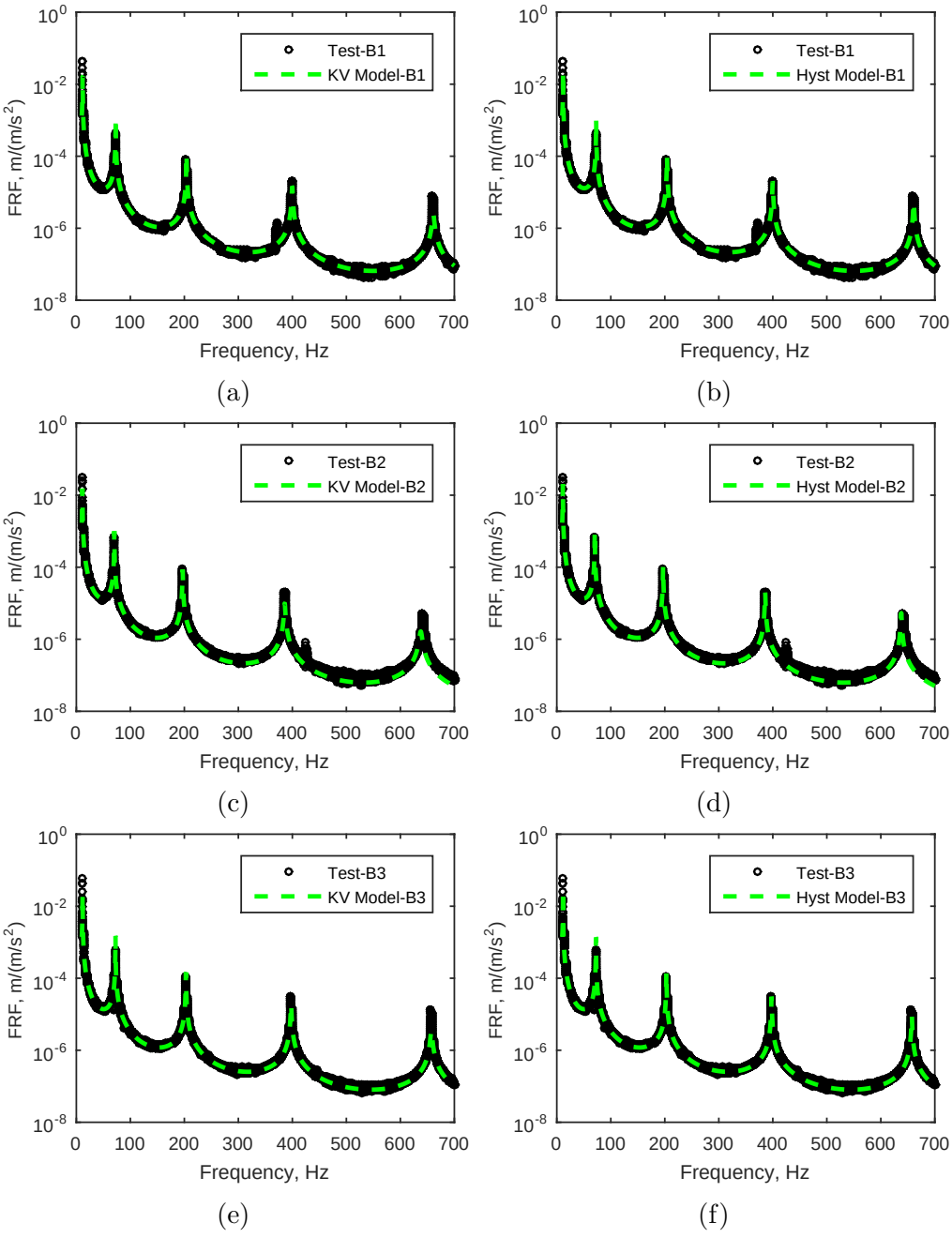

Figure 3.5: Comparison between model and test for the bare beams; Kelvin Voigt models are shown for beams B-1 —B-3 in (a), (c), (e), respectively. Hysteretic models are shown for beams B-1 —B-3 in (b), (d), (f), respectively.

Cable harnessed beam parameters

Next, the characterized beams and cables are used to fabricate different cable-harnessed structures listed in Table 3.3. In this study, modal testing experiments are performed on the 7 test structures altering system parameters such as cable material, beam geometrical properties, and/or cable wrapping patterns. The tests 1-4 have the zigzag pattern whereas tests 5-7 have the longitudinal attached cable-harnessed beam. A clamped-free boundary was used during the shaker excitation of each test. As well, the values of cable tension for the cable-harnessed beams were chosen to avoid the buckling in the beam.

Table 3.3: Different cases of cable-harnessed system tested with a clamped-free boundary

Test #	Beam[2]	Cable[3]	Number of cables attached	Pattern	Cable Tension (N)	Number of fundamental elements	Sensing location, x_{sen}, cm
1	B-1	C-1	3	Zigzag	3	5	25.5
2	B-1	C-1	5	Zigzag	3	5	25.5
3	B-2	C-1	1	Zigzag	1	5	16.5
4	B-1	C-3	3	Zigzag	3	5	25.5
5	B-1	C-2	1	Longitudinal	3	-	25.5
6	B-1	C-4	1	Longitudinal	3	-	25.5
7	B-3	C-2	1	Longitudinal	1	-	25.8

Tests 1, 2 and 4 use beam B-1 as the host structure with the zigzag wrapping pattern where the tests 1 and 2 have different number of cable C-1 wrapped to the host beam, whereas the test 4 has the cables C-3 wrapped. When multiple cables are attached to the host structure in form of a bundle, it increases the cable radius effectively. This effective radius is considered as $\sqrt{n}r_c$, where n is the number of cables attached [2]. This expression can be derived after equating the total area of the attached cables to the area of a cable bundles effective radius. The test 3 uses the beam B-2 wrapped with the cable C-1. In this manner, different system parameters are used with an aim to validate the proposed model of damping in periodically wrapped cable-harnessed beams.

As mentioned earlier, various material and geometrical properties for cables as well as wrapping patterns are considered for validation purposes. However, the wrapping pattern was chosen based on its feasibility regarding cable dimensions. For instance, the thicker cables C2 and C4 could not be used to wrap in a zigzag pattern and therefore, only longitudinal patterns were considered as seen for tests 5-7 in Table 3.3. Also, it would be

[2]Properties of the beams are listed in Table 3.2

[3]Properties of the cables are listed in Table 3.1

shown later that a comparison between the effects of the two patterns can be established between tests 4 and 5 because of the similar geometric and damping properties of the harnessed cables on the same host beam.

3.3.2 Experimental cable-harnessed and bare beam FRFs

Figures 3.6 and 3.7 show the experimental FRFs of cabled and bare beams from all the seven tests listed in Table 3.3. It is obvious from the comparison of the FRFs that the cable attachment has a noticeable damping effect on all the vibration modes and hence, modeling the damping mechanism can not be ignored. Also, in certain test cases the damping effects due to cable attachment are very high. Amongst all the tests, a high cable damping effect is seen in tests 2, 6 and 7. Hence, the following discussion is based on these three tests.

The cabled beam FRF in Fig. 3.6(b) corresponds to the test 2 which has zigzag wrapping of five C-1 cables to the host beam B-1. The higher damping of cabled beam structures is primarily attributed to the multiple cables attached to the host. Recall, the higher number of cables effectively increases the cable radius thereby increasing the cable damping effects. It should be noted that the damping effects are more profound in the higher vibration modes. In addition, an increase in the natural frequency of the cabled beams resulting from the stiffening effect due to the wrapped cables is observed. This stiffness effect was observed and discussed in [30], however, the comparison was done with the undamped model only. The experimental data shown here additionally highlights the importance of modeling damping in the cabled beam structures.

The FRFs plotted for tests 6 and 7 in Figs. 3.7(b) and 3.7(c), respectively, compares different longitudinally attached cable-harnessed beams with corresponding bare beams. The FRFs of the cabled beams show significant damping in the system. This is in contrast to the damping exhibited by the bare beam which has sharper peaks; hence the cable damping becomes important while modeling the dynamic behavior of cabled beams. Since the damping is found to be prominent at the higher modes, it becomes essential for designers to incorporate accurate cable damping in the models for higher frequency bandwidth falling in critical zones of the structure.

It is also interesting to see the overall mass and stiffening effects due to cable attachment in Figs. 3.6(b), 3.7(b) and 3.7(c). This can be done by comparing the natural frequency peaks of cabled beam against the bare beam. In Fig. 3.7(b), the natural frequencies of the cabled beam are almost equal to that of the bare beam. This infers that the inertia effect of cable C-4 neutralizes the added stiffening effect when attached to the host B-1. Interestingly, when the cable C-1 is attached to the same host B-1 in test 2, as shown

in Fig. 3.6(b), an overall cable stiffening effect is observed resulting in increase of natural frequencies. Mathematically, this can be interpreted by comparing the two ratios: $\sqrt{B_1/K_1}$ and $\sqrt{E_b I_b/(\rho_b A_b)}$ [30]. The natural frequencies of the cabled beam and the bare beam are directly proportional to the respective ratios. In the case of test 1, the ratio $\sqrt{B_1/K_1}$ exceeds $\sqrt{E_b I_b/(\rho_b A_b)}$ due to strong stiffening effect of cable C-1 and hence, the natural frequencies increase. Notably, Fig. 3.7(c) shows an overall mass effect when the cable C-2 is attached to the narrower beam. This is due to the low elastic modulus of the cable C-2 resulting in a lower value of $\sqrt{B_1/K_1}$ compared to $\sqrt{E_b I_b/(\rho_b A_b)}$ for the corresponding bare beam. Hence, the natural frequencies decrease on attaching the cable for test 7.

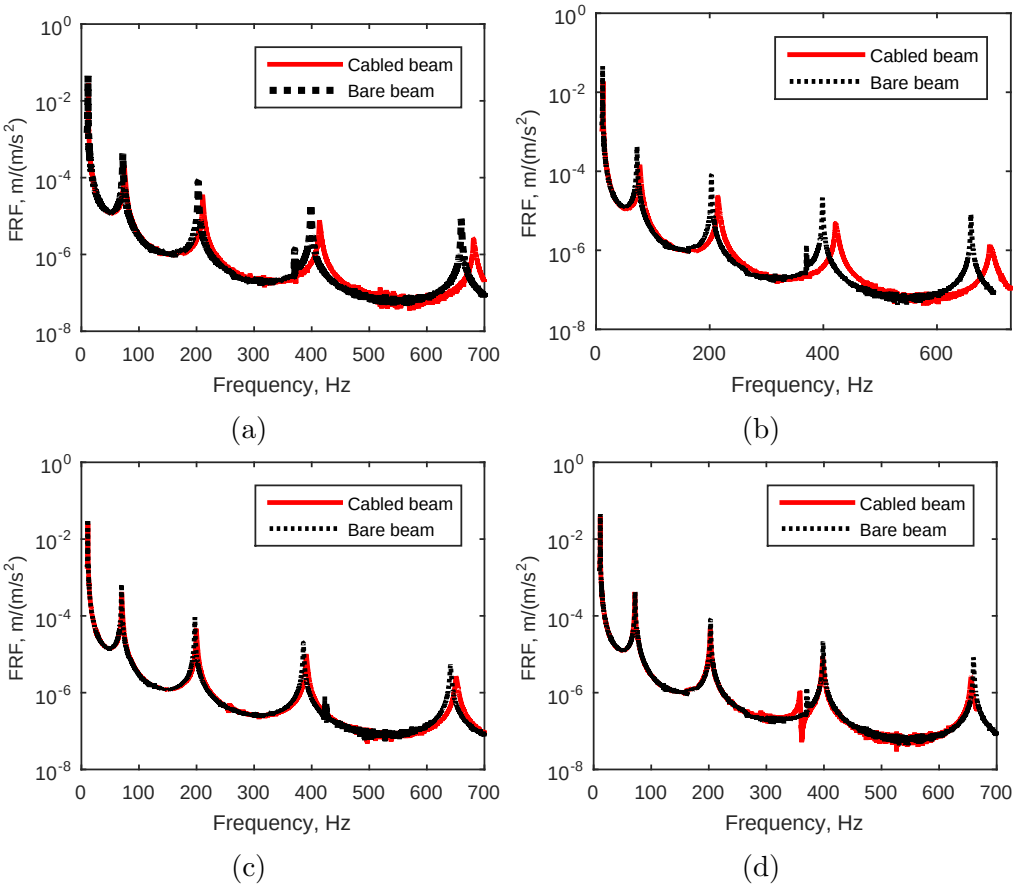

Figure 3.6: Comparison of bare beam and cabled beam FRFs obtained from experiments of zigzag wrapped cable-harnessed beam structures (a) Test 1, (b) Test 2, (c) Test 3, and (d) Test 4

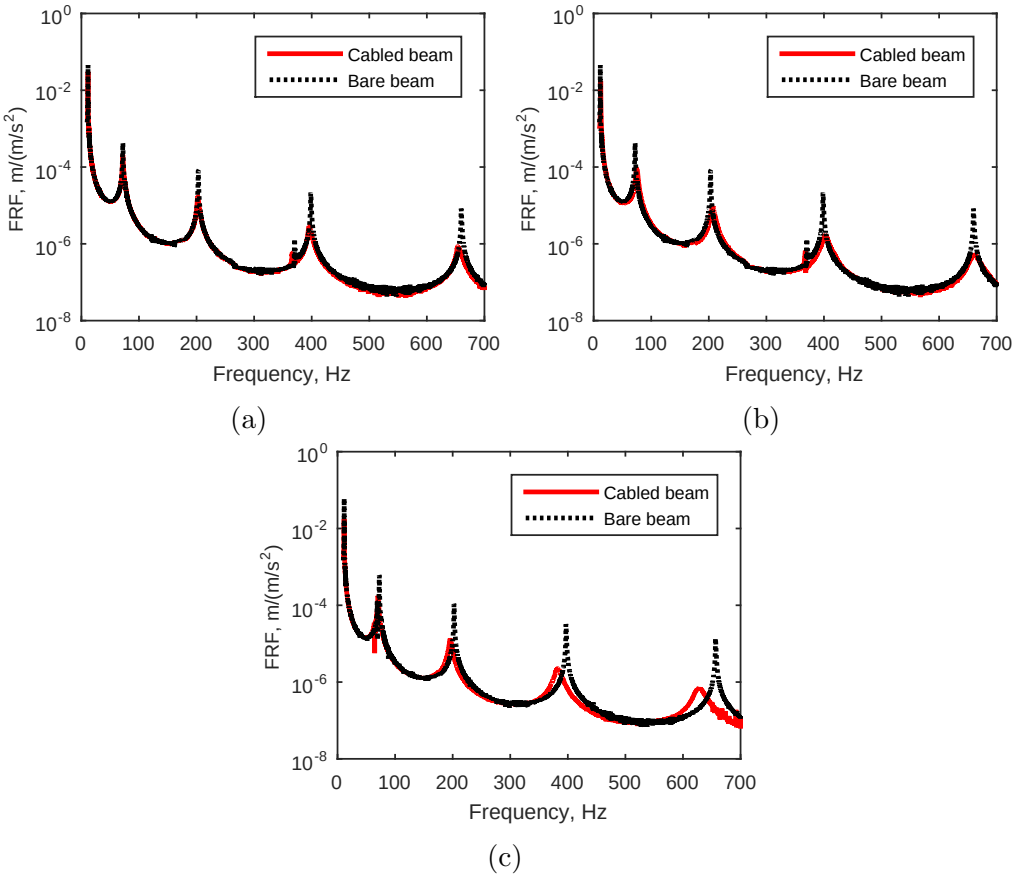

Figure 3.7: Comparison of bare beam and cabled beam FRFs obtained from experiments of longitudinally attached cable-harnessed beam structures (a) Test 5, (b) Test 6, and (c) Test 7

3.3.3 Natural frequency comparison between cable-harnessed model and test

The natural frequencies of the cable-harnessed system obtained from the 7 modal testing experiments and corresponding analytical model are listed in Table 3.4. Details of the test structures was presented earlier in Table 3.3. The data in Table 3.4 is presented for the first five vibration modes for which the testing was conducted. The comparison of the natural frequencies is important to show the capability of the analytical model in predicting accurate mass and stiffness effects due to the cables when they are wrapped around the structure or attached in a longitudinal pattern.

Table 3.4: Comparison of natural frequencies (Hz) between experiments and model for cable-harnessed test cases

		Mode Number				
		1	2	3	4	5
Test 1	Test, ω_n	12.05	74.70	210.55	413.50	681.15
	Model, ω_n	11.973	75.03	210.09	411.7	680.57
	Error in model, %	-0.64%	0.44%	-0.22%	-0.44%	-0.09%
Test 2	Test, ω_n	12.25	76.9	214.24	421.25	692.75
	Model, ω_n	12.2	76.47	214.13	419.62	693.66
	Error in model, %	-0.41%	-0.56%	-0.05%	-0.39%	0.13%
Test 3	Test, ω_n	11.30	70.05	199.40	390.35	650.90
	Model, ω_n	11.56	72.44	202.85	397.5	657.1
	Error in model, %	2.30%	3.41%	1.73%	1.83%	0.95%
Test 4	Test, ω_n	11.45	71.65	202.50	398.05	655.55
	Model, ω_n	11.50	72.08	201.84	395.54	653.85
	Error in model, %	0.44%	0.60%	-0.33%	-0.63%	-0.26%
Test 5	Test, ω_n	11.55	71.90	202.05	395.70	653.55
	Model, ω_n	11.49	72.02	201.67	395.19	653.28
	Error in model, %	-0.52%	0.17%	-0.19%	-0.13%	-0.04%
Test 6	Test, ω_n	12.30	74.40	206.85	402.80	663.30
	Model, ω_n	11.78	73.83	206.75	405.15	669.74
	Error in model, %	-4.23%	-0.77%	0.05%	0.58%	0.97%
Test 7	Test, ω_n	11.45	70.40	196.05	382.10	628.95
	Model, ω_n	11.38	71.32	199.72	391.37	646.96
	Error in model, %	-0.06%	1.30%	1.87%	2.42%	2.86%

The natural frequencies obtained from the tests 1-4, listed for zigzag wrapped cabled beams, are first discussed. The natural frequencies obtained from these tests are clearly a good match with the homogenized model as evident from the low percentage errors in the model frequencies. It shows that the model is fairly accurate in predicting the overall cable mass and stiffness effects.

On a closer observation, it is seen that the tests 1, 2 and 4 have relatively smaller error in frequencies obtained from model compared to the test 3. Recall from Table 3.3 that the tests 1, 2 and 4 utilize the same host beam B-1, whereas the test 3 uses a thinner beam B-2. The higher frequency errors in test 3 are attributed to the averaging assumptions within a fundamental element for the homogenization method and its reliance on the periodicity

of the system. As the beam thickness decreases, the non-homogeneity within an element increases due to the cable becoming a dominant part of the structure, this method starts to show its limitations. Moreover, at the higher frequencies, the ratio of the wavelength of the frequency of interest to length of element decrease and as a result, the error increases for high frequency modes.

Moreover, Table 3.4 also shows the natural frequencies for the systems with cable longitudinally attached on the top surface of the beam corresponding to tests 5-7. For this pattern as well, the natural frequencies show a good match between the test and the model. Between these three tests, a fair comparison can be made between tests 5 and 7 where both the tests have same cable C-2 attached but the former has host beam B-1, whereas the latter has B-3. Recall from Table 3.2 that the beam B-3 is narrower in width direction compared to B-1. It is seen from Table 3.4 that although frequencies of both the tests 5 and 7 are a good match with the model, the latter has an overall higher error in frequencies. These errors in the test 7 are again attributed to the averaging assumptions of the homogenization method. However in this case, the narrower beam used in this test results in the increase of non-homogeneity within a fundamental element as the cable effects become more influential. Additionally, the higher modes of test 6 shows a relatively larger error in model compared to test 5. This is because of the higher density and diameter of cable C-4 used in test 6 compared to C-2 used in test 5 (refer Table 3.1), which results in a relatively larger non-homogeneity in the system, hence resulting in a larger error. Both tests 5 and 6 have same host beam B-1.

3.3.4 Damping comparison between cable-harnessed model and test

In this section, the FRFs are utilized to compare the damping between the proposed models and test. The experimentally obtained FRFs are compared with both the undamped model and hysteretic and Kelvin-Voigt damping models. The FRF plots for the zigzag wrapped patterns are shown in Figs. 3.8 and 3.9, while those for the longitudinally attached cabled beams are shown in Fig. 3.10, for a total of 7 test cases. In these figures, the FRF plots on the left are shown for the first five modes of vibrations in the out-of-plane bending coordinate in the $z-$direction. Additionally, the zoomed-in plots for the highest modes are shown on the right-hand side for better comparisons.

The undamped model FRFs for the zigzag wrapped structure presented in Figs. 3.8 and 3.9 was previously proposed by Martin et al. in [30]. Although the undamped model is successfully able to predict the natural frequencies accurately, it is unable to predict the

FRF shapes due to the absence of damping in the homogenized model. To fill this gap, the models proposed in the current study include the damping effects in the cables and the host structure. It is clear from the FRF plots that the proposed models show a better prediction of the system dynamics of the cable-harnessed structures.

It is seen that the FRFs obtained from the hysteretic damping model overall provide a better match with the test results compared to the Kelvin-Voigt model for tests 1 to 4. Kelvin-Voigt model is seen to over-predict the damping at the higher frequency modes for these tests; whereas, it shows a good prediction of damping for the mid-frequency range. Therefore, the damping effects of cables C-1 and C-3 are best characterized using the hysteretic damping model.

As expected and consistent with the results in Chapter 2, a comparison of the FRFs in Figs. 3.8(a) and 3.8(c) corresponding to tests 1 and 2 clearly show in both test and model that as the number of wrapped cables increases, the damping in the structure increases.

Also, the relatively higher frequency errors in the natural frequencies of test 3 as seen from Fig. 3.9(a) were explained earlier in Sec. 3.3.3. Moreover, in Fig. 3.9(b), an extra peak due to the 1st torsional mode of the system is observed in the test FRF of the cabled-beam system. Since the presented model does not account for vibration in the torsional coordinate, the peak corresponding to the torsional mode is not predicted.

Figure 3.10 shows the FRFs for the longitudinally attached cabled beams for tests 5-7. For this pattern as well, the proposed damped model clearly shows a significant improvement compared to the undamped model in matching the test results. In all the FRFs shown in Fig. 3.10, it is also observed that the Kelvin-Voigt model is a better match with the test results compared to the hysteretic damping model which seems to under-estimate the damping in the structure. The reason for the better match is attributed to the fact that the cables used in these cases, C-2 and C-4, are better-characterized using the Kelvin-Voigt model compared to the hysteresis model.

An important comparison can be made between the damping effects exhibited in the two patterns considered in this study, zigzag and longitudinal. For this exercise, the comparison is made between the tests 4 and 5 conducted for the zigzag and longitudinal cabled beam patterns, respectively. Both tests use similar host beam B-1 and the attached cables have similar geometric and damping properties. In other words, the total diameter and the cable damping constants η_{kc} and η_{hc} for the attached cables in these two tests are similar and can be calculated using Tables 1 and 3. This allows for a fair comparison of the damping properties between the two patterns. Hence, when the corresponding FRFs in Figs. 3.9(c) and 3.10(a) are compared, it is observed that the latter, which corresponds to the longitudinal pattern, shows a significantly higher damping both in the tests and model

results. This interpretation becomes clearer when the zoomed-in FRF plots for the higher modes are compared as shown in Fig. 3.11. The smaller damping in the zigzag wrapped beam is a resultant of the wrapping angle over which the damping force from the cables is projected. On the other hand, for the case of the longitudinal pattern, the damping effects are maximized due to cables being along the centreline of the beam. This is in line with the comparisons presented between model results for various wrapping patterns in Fig. 2.12 in Chapter 2 which also shows that the longitudinally attached cable-harnessed structures have higher damping.

In addition, the relatively higher error in the natural frequencies peaks seen in Figs. 3.10(c) and 3.10(e) compared to Fig. 3.10(a) is related to the larger non-homogeneity in the system considered for tests 6 and 7 as explained previously in Sec. 3.3.3. Finally, the beam width is another aspect that is considered when observing each structures damping. As expected, narrower beams are more affected by the cable damping effects than the wider beams as also shown and supported by the results for tests 5 and 7.

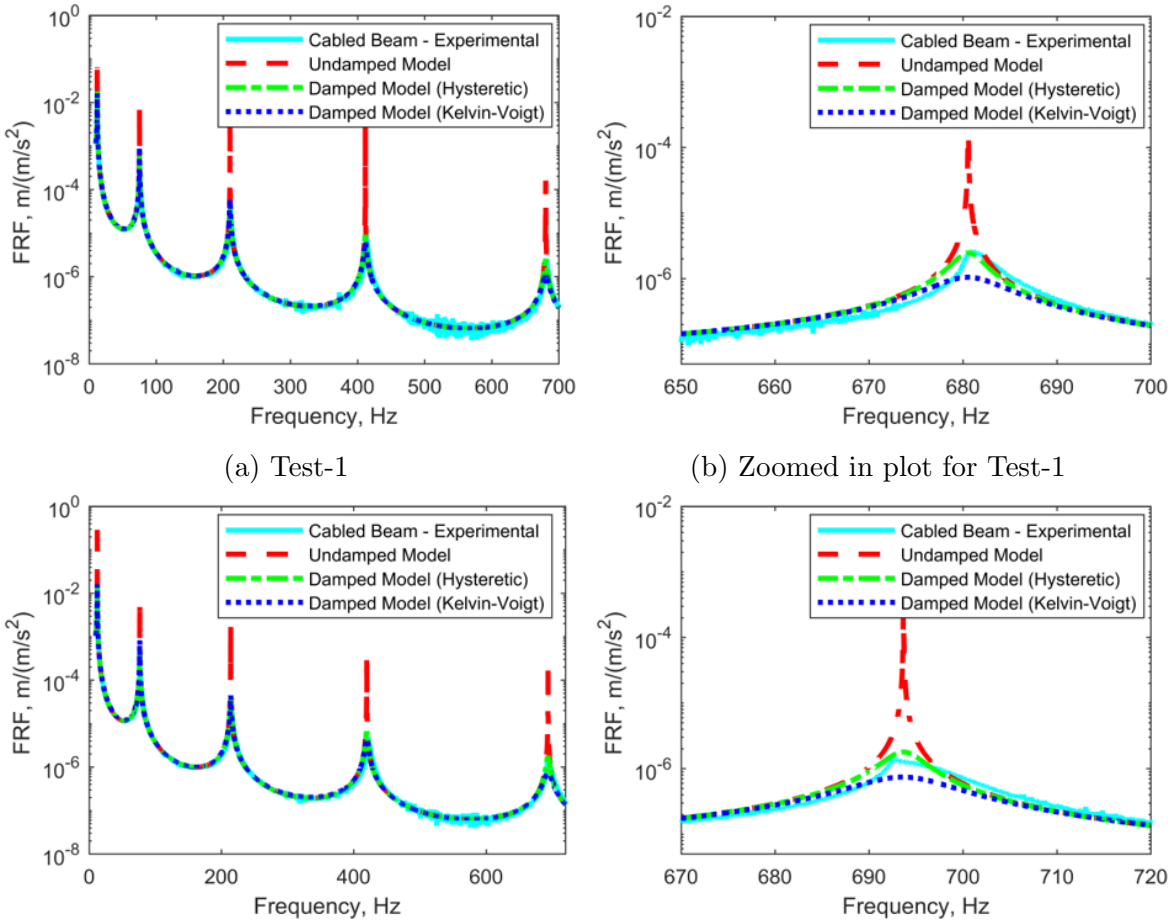

(a) Test-1 (b) Zoomed in plot for Test-1

(c) Test-2 (d) Zoomed in plot for Test-2

Figure 3.8: Comparison of FRFs between undamped model, the two damping models and experiments for zigzag wrapped cabled beams for (a) Test 1 and (c) Test 2; The zoomed-in plots for the highest mode are shown on the right side in (b) and (d).

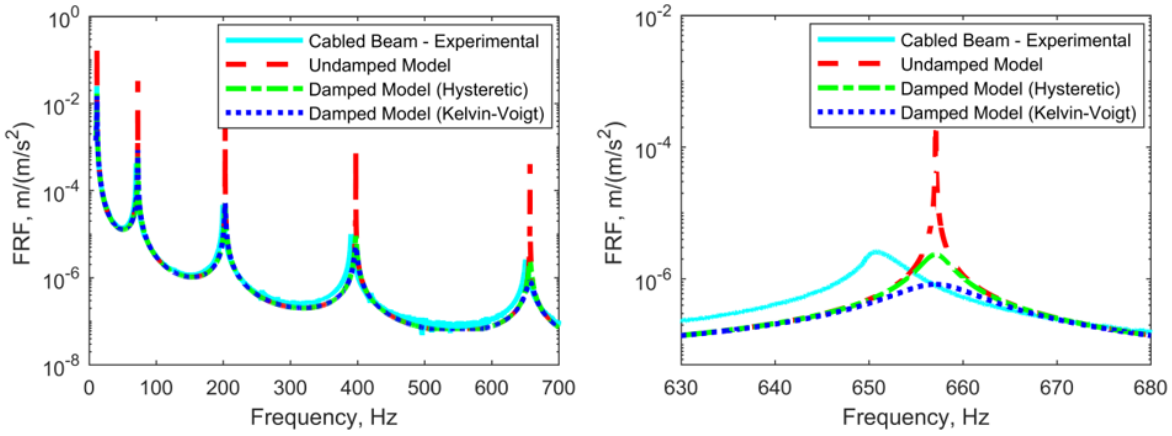

(a) Test-3 (b) Zoomed in plot for Test-3

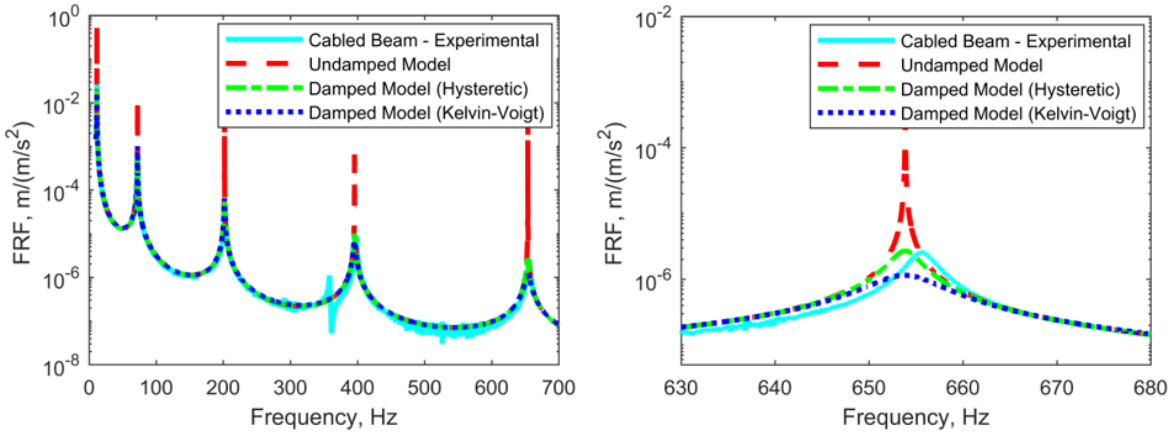

(c) Test-4 (d) Zoomed in plot for Test-4

Figure 3.9: Comparison of FRFs between undamped model, the two damping models and experiments for zigzag wrapped cabled beams for (a) Test 3 and (c) Test 4; The zoomed-in plots for the highest mode are shown on the right side in (b) and (d).

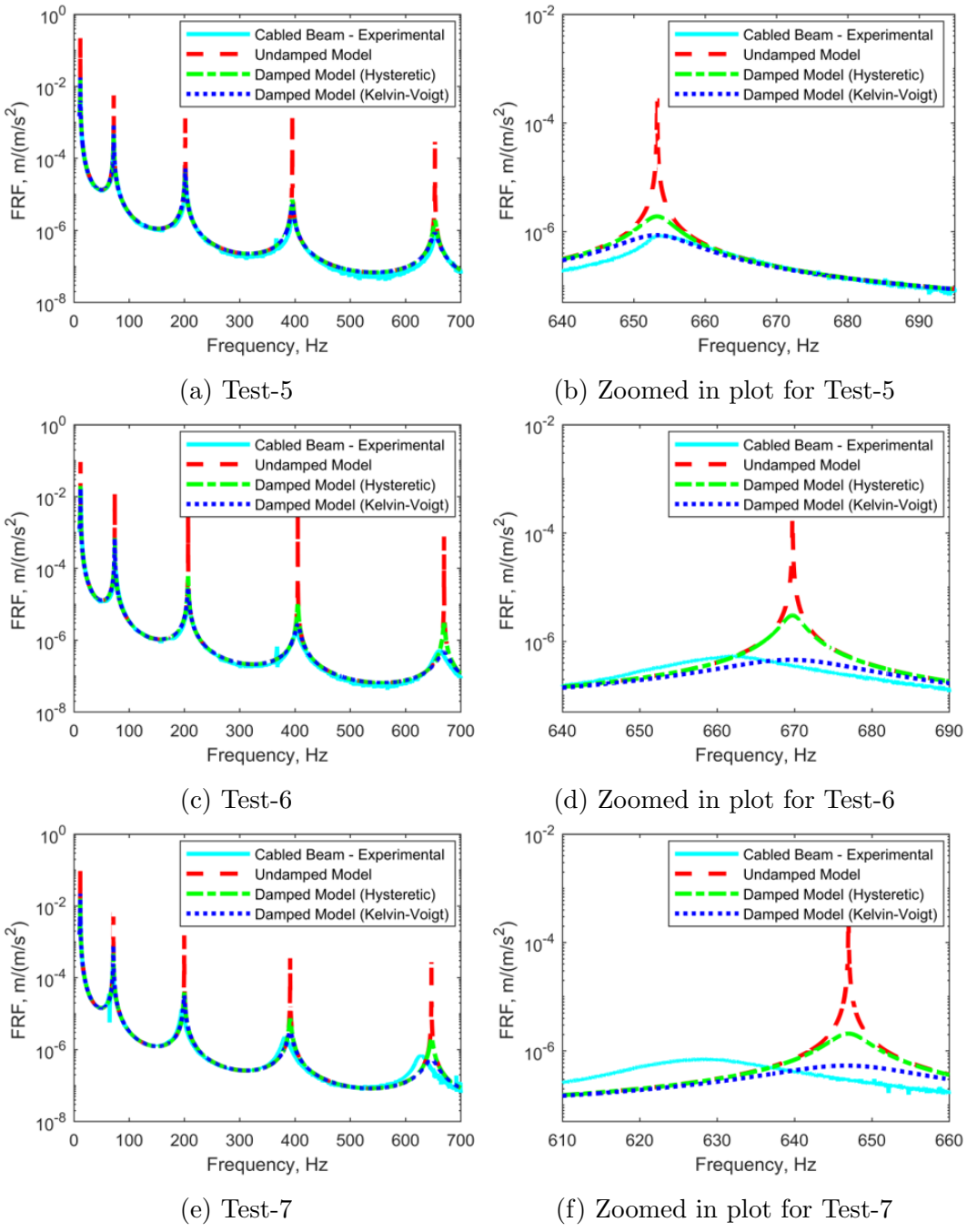

(a) Test-5 (b) Zoomed in plot for Test-5

(c) Test-6 (d) Zoomed in plot for Test-6

(e) Test-7 (f) Zoomed in plot for Test-7

Figure 3.10: Comparison of FRFs between undamped model, the two damping models and experiments for longitudinally attached cabled beams for (a) Test 5, (c) Test 6, (e) Test 7; The zoomed-in plots for the highest mode are shown on the right side in (b), (d) and (f).

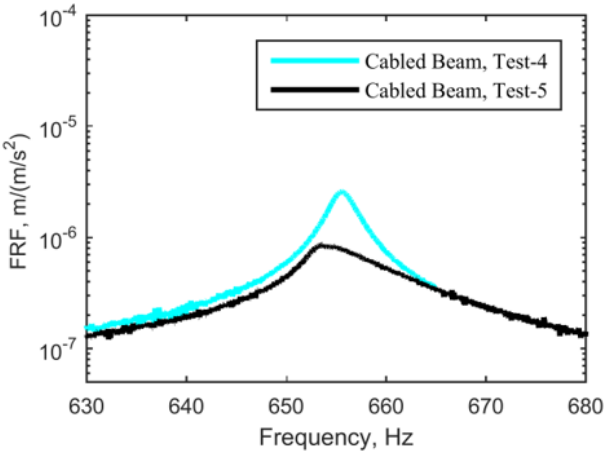

Figure 3.11: Comparison of the zoomed-in experimental FRFs of cable-harnessed beams obtained from tests 4 and 5

3.4 Summary of the Chapter

Following the analytical model developments based on the energy-equivalence homogenization method for cable-harnessed beam structures, the experimental validations for the proposed models are presented in this chapter. This study highlights the importance of modeling the damping mechanisms due to cable attachments. In order to characterize the damping in the cables, a dynamic testing method is used to quantify the energy loss in cables. The experimental modal testing is then performed on various fabricated cable-harnessed beam structures using the base excitation method to obtain FRFs. The cable-harnessed beam structure FRFs are compared to those obtained from the bare beam and to show the importance of modeling the damping due to cable attachment which was ignored in the previous works [30, 31]. It is shown that the homogenization method offers a great tool for incorporating several damping models into a cable-harnessed systems dynamics. The damping in the system is found to be higher when a cable is harnessed to the beam longitudinally compared to the case when it is wrapped in a zigzag pattern. Additionally, the system damping is found to increase on decreasing the beam width or using a cable with higher radius.

The work presented in Chapters 2 and 3 concludes the first phase of the current research which focused on creating analytical models and performing numerical and experimental validations of the damping mechanisms in periodically wrapped cable-harnessed beam structures.

Chapter 4

Analytical Modeling and Experimental Validation of Parallel Cable-Harnessed Plate Structures

In this chapter, analytical modeling of the cable-harnessed plates is proposed where the cables are attached to the plate in a parallel configuration. The proposed model is experimentally validated later in the chapter. It is worth mentioning here that the analytical models of cable-harnessed two-dimensional structures have not been developed in the past as per the author's best knowledge. This chapter presents the details about the successful attempt made by the author towards modeling such structures. These cable-harnessed plate-like structures are common in aerospace industry. Moreover, the current work would act as a stepping stone towards the future developments and understanding of the dynamics of complex cable-harnessed plate structures [1] [2].

Since the rectangular thin plate is considered a two-dimensional structural element during modeling, as opposed to the one-dimensional beam element, the mathematical modeling becomes complicated for the former. This is also one of the reasons why the previous researchers considered the effects of cables on host beams rather than plates, as discussed in Chapter 1. However, considering a plate as a host structure helps in gaining further insights to the dynamics of cable-harnessed system that a beam host structure is

[1] The analytical formulation developed in this chapter was presented in 26^{th} International Congress of Sound and Vibration [86].

[2] The detailed analysis of the formulation presented in this chapter along with the experimental validation has been accepted for publication in *ASME Journal of Vibration and Acoustics* [87].

not able to provide. Also, developing the analytical models of the cable-harnessed plates brings us one step closer to the reality because a lot of spacecraft structures are made of panels that closely resemble thin plates.

To start with, in this chapter, a simple geometry of the cable attachment is considered that assumes multiple cables attached parallel to an edge of a rectangular plate that are equidistant to each other. The model assumptions are then listed. Further, in order to obtain the equation of motion, Hamilton's principle is applied on the developed formulation of strain and kinetic energy of the equivalent continuum model obtained using energy-equivalence homogenization approach. Damping is ignored in the current work for a simplified model. The model is validated using experimental modal testing. Three different samples of fabricated cable-harnessed structures are used for the validation purpose. As a measure of validation, frequency response functions, mode shapes and natural frequencies are compared between test and model. Also, a metric known as modal assurance criterion (MAC), that compares experimental and theoretical mode shapes, is presented for two test cases. Finally, the proposed model is compared with an existing *cable-harnessed beam* model to show the importance of the current work.

4.1 Mathematical modeling of parallel cable-harnessed plates

In this section, the system description and underlying model assumptions are presented. Then, the equivalent continuum model of the cable-harnessed plate is developed using an energy-equivalence homogenization method. For the model development, the total strain and kinetic energy expressions of the system are obtained. Finally, on applying Hamilton's principle, the equation of motion of the system is obtained.

4.1.1 Model description and assumptions

The structure consists of a rectangular thin plate with multiple parallel cables attached to the top surface of the plate as shown in Fig. 4.1(a). The global coordinate system (x, y, z) corresponds to the entire plate, while the local (η, ξ, z) corresponds to a fundamental element. A fundamental element, as shown in Fig. 4.1(b), is defined as the building block of the model which, if repeated in both the directions, forms the entire cable-harnessed plate. The dimension of the plate is $a \times b$ and that of the fundamental element is $L_1 \times L_2$ with similar thickness h. The dimension L_2 is calculated by dividing the host plate's width

b by the number of cables, n, and L_1 is chosen such that the ratio of L_1 to L_2 remains similar as a to b.

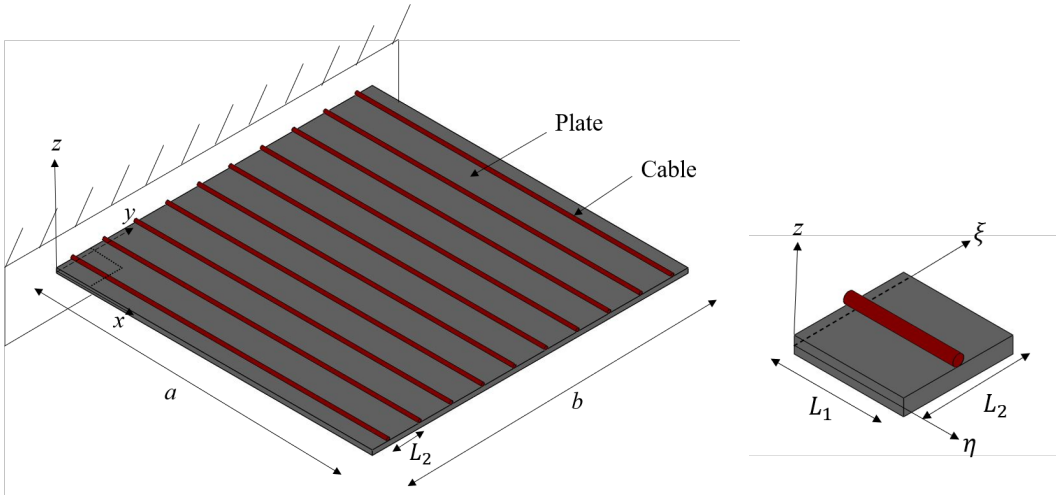

(a) (b)

Figure 4.1: (a) Schematic of the cable-harnessed plate clamped at one edge (b) Fundamental element

As mentioned, the equivalent continuum model of the cable-harnessed plate is developed using an energy-equivalence homogenization method. This method simplifies the mathematical model for structures with repeated patterns and provides the possibility of a closed-form solution that provides more insights into the problem. The major criteria to apply this method is the periodicity within the structure. Hence, the cables are assumed to be equidistant from each other in the parallel cabled plate structure thereby forming a periodic geometry.

In the modeling approach, the strain and kinetic energy of a fundamental element are first calculated in terms of the displacement at the element center. These energy expressions on division by the element area result in the areal energy densities which are a good representative of energy per unit area of the entire structure. Once the total energy expressions are evaluated over the entire structure, Hamilton's principle is used to obtain the governing equation of motion in the transverse coordinate.

The model assumptions applied towards the development of equivalent continuum structures of the cable-harnessed plate are listed as follows:

1. The host structure is assumed to be an isotropic plate and is modeled using classical

plate theory.

2. The cable remains in perfect contact with the plate during vibrations.
3. The cable is under a pretension at the equilibrium position.
4. The axial strain in the cable at a given cross-section is assumed to be uniform.
5. Cable pretension results in the pre-compression of the plate.

Assuming a small transverse displacement $w(x, y, t)$, the linearized displacement field according to the classical plate theory can be written as

$$\begin{aligned} u_x &= -z\ w_{,x}(x, y, t) \\ u_y &= -z\ w_{,y}(x, y, t) \\ u_z &= w(x, y, t) \end{aligned} \tag{4.1}$$

where the subscripts after the commas indicate the partial derivatives in space.

Further, the Green-Lagrange strain tensor is used to obtain the strain-displacement relations. A higher order strain tensor is used to include the effect of cable tension in the system dynamics as the infinitesimal strain tensor fails to include its effect. The Green Lagrange strain tensor for rectangular component form is written as, [88]:

$$\varepsilon_{ij}^{(2)} = \frac{1}{2}\left[u_{i,j} + u_{j,i} + \ u_{m,i}u_{m,j}\right], \quad i, j = x, y, z \tag{4.2}$$

Using Eqs. 4.1 and 4.2, the non-zero component of strain tensor can be obtained as

$$\begin{aligned} \varepsilon_{xx}^{(2)} &= \ -zw_{,xx} + \frac{1}{2}(z^2 w_{,xx}^{\ 2} + z^2 w_{,xy}^{\ 2} + w_{,x}^{\ 2}) \\ \varepsilon_{yy}^{(2)} &= \ -zw_{,yy} + \frac{1}{2}(z^2 w_{,xy}^{\ 2} + z^2 w_{,yy}^{\ 2} + w_{,y}^{\ 2}) \\ \varepsilon_{xy}^{(2)} &= -zw_{,xy} + \frac{1}{2}\left(z^2 w_{,xx}\, w_{,xy} + z^2 w_{,yy}\, w_{,xy} + w_{,x}\, w_{,y}\right) \end{aligned} \tag{4.3}$$

Here, $\varepsilon_{xx}^{(2)}$, $\varepsilon_{yy}^{(2)}$ represents the normal bending strain in the x and y direction, respectively, and $\varepsilon_{xy}^{(2)}$ is the shear strain in the $x - y$ plane.

4.1.2 Strain energy of a fundamental element

In order to calculate the total strain energy stored within a fundamental element, the strain energy of both components of the fundamental element, cable and plate, is to be evaluated. These energy expressions would be summed up to obtain the total strain energy within a fundamental element.

Strain energy of the cable within a fundamental element

The total strain in the cable is resultant of the static strain due to cable pretension, T/E_cA_c, and the resulting dynamic strain due to vibration of the plate evaluated at the plate-cable interface,

$$\varepsilon_c = \frac{T}{E_cA_c} + \varepsilon^{(2)}_{\eta\eta}\big|_{z=z_c} \tag{4.4}$$

where E_c, A_c, and T are the cable's Young's modulus, cross-sectional area and tension, and h is the plate thickness. $z_c = h/2$ denotes the z coordinate of the cable-plate interface, at which the dynamic strain is evaluated. In Eq. 4.4, the local coordinate system is used because the strain energy expression is being evaluated for the fundamental element.

Using Eqs. 4.3 and 4.4, the cable strain energy within a fundamental element is written and expanded as,

$$U_{cable} = \int_0^{L_1}\int_{A_c} \frac{1}{2}E_c\left(\varepsilon_c\right)^2 dA\ d\eta \tag{4.5}$$

$$= \int_0^{L_1}\int_{A_c} \frac{1}{2}E_c\left(\frac{T}{E_cA_c} + \varepsilon^{(2)}_{\eta\eta}\big|_{z=z_c}\right)^2 dA\ d\eta \tag{4.6}$$

$$= \int_0^{L_1}\int_{A_c} \frac{1}{2}E_c\left(\frac{T}{E_cA_c} - z_c\ w_{,\eta\eta} + \frac{1}{2}(z_c^2 w_{,\eta\eta}^2 + z_c^2 w_{,\eta\xi}^2 + w_{,\eta}^2)\right)^2 dAd\eta \tag{4.7}$$

This expression is further expanded and written as

$$\begin{aligned} U_{cable} = \int_0^{L_1}\int_{A_c} \frac{1}{2}E_c\Bigg(&\frac{T^2}{A_c^2\ E_c^2} + \frac{T\ w_{,\eta}^2}{A_cE_c} + \frac{w_{,\eta}^4}{4} - \frac{2\ Tz_c\ w_{,\eta\eta}}{A_cE_c} - w_{,\eta}^2\ w_{,\eta\eta}\ z_c + w_{,\eta\eta}^2\ z_c^2 + \\ &\frac{T\ w_{,\eta\eta}^2\ z_c^2}{A_cE_c} + \frac{1}{2}w_{,\eta}^2\ w_{,\eta\eta}^2\ z_c^2 + \frac{T\ w_{,\eta\xi}^2\ z_c^2}{A_cE_c} + \frac{1}{2}w_{,\eta}^2\ w_{,\eta\xi}^2\ z_c^2 - w_{,\eta\eta}^3\ z_c^3 \\ &- w_{,\eta\eta}\ w_{,\eta\xi}^2\ z_c^3 + \frac{w_{,\eta\ \eta\eta}^4\ z_c^4}{4} + \frac{1}{2}w_{,\eta\eta}^2\ w_{,\eta\xi}^2\ z_c^4 + \frac{w_{,\eta\xi}^4\ z_c^4}{4}\Bigg)dAd\eta \end{aligned} \tag{4.8}$$

In this equation, because the displacements are assumed small, the terms higher than second order in displacement and its derivatives are ignored. Also, since the displacement is constant across the area of the cross section, integration over area can be performed. This simplification results in

$$U_{cable} \approx \int_0^{L_1} \frac{1}{2} E_c A_c \left(\frac{T^2}{A_c^2\ E_c^2} + \frac{T\ w_{,\eta}^2}{A_c E_c} - \frac{2\ T z_c\ w_{,\eta\eta}}{A_c E_c} + w_{,\eta\eta}^2\ z_c^2 + \frac{T\ w_{,\eta\eta}^2\ z_c^2}{A_c E_c} + \frac{T\ w_{,\eta\xi}^2\ z_c^2}{A_c E_c} \right) d\eta \tag{4.9}$$

The term $w_{\eta\xi}^2$ also vanishes because the cable runs along the $\eta-$axis and the derivative of displacement along the ξ axis would result in zero. Hence, the strain energy of the cable is written as

$$U_{cable} \approx \int_0^{L_1} \frac{1}{2} E_c A_c \left(\frac{T^2}{A_c^2\ E_c^2} + \frac{T\ w_{,\eta}^2}{A_c E_c} - \frac{2\ T z_c\ w_{,\eta\eta}}{A_c E_c} + w_{,\eta\eta}^2\ z_c^2 + \frac{T\ w_{,\eta\eta}^2\ z_c^2}{A_c E_c} \right) d\eta \tag{4.10}$$

Strain energy of the plate within a fundamental element

Further, the strain energy of the plate is calculated. Since the cable pretension results in the compression of the plate, it is assumed that a constant distributed compressive loading N_x (units N/m) is present normal to the $\xi - z$ plane due to the compression induced by multiple parallel cables. The total strain energy stored in the plate within the fundamental element due to combined action of lateral and longitudinal forces can be written as [89]:

$$\begin{aligned} U_{plate} = & \frac{1}{2hE_p} \int_0^{L_2} \int_0^{L_1} N_x^2\ d\eta\ d\xi \\ & + \int_{-\frac{h}{2}}^{\frac{h}{2}} \int_0^{L_2} \int_0^{L_1} \left(-\frac{N_x}{h} \right) \left[-z\ w_{,\eta\eta} + \frac{1}{2} \left\{ z^2 \left(w_{,\eta\eta} \right)^2 + z^2 \left(w_{,\eta\xi} \right)^2 + \left(w_{,\eta} \right)^2 \right\} \right] d\eta\ d\xi\ dz \\ & + \frac{D}{2} \int_0^{L_2} \int_0^{L_1} \left[\left(w_{,\eta\eta} + w_{,\xi\xi} \right)^2 - 2\left(1-\nu\right) \left(w_{,\eta\eta}\, w_{,\xi\xi} - \left(w_{,\eta\xi} \right)^2 \right) \right] d\eta\ d\xi \end{aligned} \tag{4.11}$$

where E_p, D, and ν are Young's modulus, flexural rigidity, and Poisson's ratio of the plate, respectively. The flexural rigidity can be written in terms of the two other material parameters as $D = E_p h^3/(12\left(1-\nu^2\right))$. In Eq. 4.11, the first integration denotes the strain energy due to stretching of the middle plane of the plate, the second integration shows the additional work done by compressive forces in bending the plate, and the third integration shows the strain energy stored in the plate due to bending. In the absence of any compressive load, the strain energy of the plate is represented by the third integration.

Also, in the second integration, the integration over the thickness has been included because it is assumed that the pre-compressive load is uniformly distributed over the thickness of the plate.

The distributed compressive load can be related to the cable tension as

$$N_x = T/L_2 \tag{4.12}$$

Total strain energy within a fundamental element

The total strain energy within a fundamental element of the structure can be calculated by summing up the strain energy of its components plate and cables. Hence, using Eqs. 4.10 and 4.11, the strain energy within a fundamental element is expressed as

$$\begin{aligned} U_{tot} = & \int_0^{L_1} \frac{1}{2} E_c A_c \left(\frac{T^2}{E_c^2 A_c^2} + \frac{T w_{,\eta}^2}{E_c A_c} - \frac{2 T z_c w_{,\eta\eta}}{E_c A_c} + z_c^2 w_{,\eta\eta}^2 + \frac{T z_c^2 w_{,\eta\eta}^2}{E_c A_c} \right) d\eta \\ & + \frac{1}{2hE_p} \int_0^{L_2} \int_0^{L_1} N_x^2 \, d\eta \, d\xi \\ & + \int_{-\frac{h}{2}}^{\frac{h}{2}} \int_0^{L_2} \int_0^{L_1} \left(-\frac{N_x}{h} \right) \left[-z \, w_{,\eta\eta} + \frac{1}{2} \left\{ z^2 \left(w_{,\eta\eta} \right)^2 + z^2 \left(w_{,\eta\xi} \right)^2 + \left(w_{,\eta} \right)^2 \right\} \right] d\eta \, d\xi \, dz \\ & + \frac{D}{2} \int_0^{L_2} \int_0^{L_1} \left[\left(w_{,\eta\eta} + w_{,\xi\xi} \right)^2 - 2 \left(1 - \nu \right) \left(w_{,\eta\eta} \, w_{,\xi\xi} - \left(w_{,\eta\xi} \right)^2 \right) \right] d\eta \, d\xi \end{aligned} \tag{4.13}$$

4.1.3 Kinetic energy

Neglecting the rotary inertia, the total kinetic energy of a fundamental element of the structure can be written by integrating oven an infinitesimal element of respective components (plate and cable) corresponding to the transverse motion as:

$$E_k = \int_0^{L_1} \int_{A_c} \frac{1}{2} \rho_c \left(\frac{\partial w}{\partial t} \right)^2 dA d\eta + \int_{-h/2}^{h/2} \int_0^{L_2} \int_0^{L_1} \frac{1}{2} \rho_p \left(\frac{\partial w}{\partial t} \right)^2 d\eta d\xi dz \tag{4.14}$$

where ρ_c and ρ_p denote the mass density of cable and plate, respectively. Note that the variables in the local coordinate system are used in the above integration due to the energy being written for a fundamental element.

4.1.4 Homogenization

In order to apply the homogenization method, the displacement of a point (η, ξ) in the fundamental elements is written in terms of the displacement at the center of the fundamental element $(L_1/2, L_2/2)$ using the Taylors series expansion of $w(\eta, \xi, t)$ upto the second-order as,

$$w(\eta,\xi,t) \approx \left[w\left(\frac{L_1}{2},\frac{L_2}{2},t\right) + w_{,\eta}\left(\frac{L_1}{2},\frac{L_2}{2},t\right)\left(\eta-\frac{L_1}{2}\right) + w_{,\xi}\left(\frac{L_1}{2},\frac{L_2}{2},t\right)\left(\xi-\frac{L_2}{2}\right) + \frac{1}{2}\left(w_{,\eta\eta}\left(\frac{L_1}{2},\frac{L_2}{2},t\right)\left(\eta-\frac{L_1}{2}\right)^2 + 2w_{,\eta\xi}\left(\frac{L_1}{2},\frac{L_2}{2},t\right)\left(\eta-\frac{L_1}{2}\right)\left(\xi-\frac{L_2}{2}\right) + w_{,\xi\xi}\left(\frac{L_1}{2},\frac{L_2}{2},t\right)\left(\xi-\frac{L_2}{2}\right)^2 \right) \right] \quad (4.15)$$

Substituting Eq. 4.15 in Eq. 4.13, and integrating over respective limits yields the homogenized strain energy over the fundamental element of the plate

$$U_{tot}(t) = \frac{1}{2}E_cA_c\left(\frac{T^2}{E_c^2A_c^2} + \frac{Tw^*{}_{,\eta}^{\,2}}{E_cA_c} - \frac{2Tz_cw^*{}_{,\eta\eta}}{E_cA_c} + z_c^2w^*{}_{,\eta\eta}^{\,2} + \frac{Tz_c^2w^*{}_{,\eta\eta}^{\,2}}{E_cA_c}\right)L_1 + \frac{N_x^2\,L_1L_2}{2hE_p} + \left(-\frac{N_x}{2h}\right)\left[\frac{h^3}{12}\left(w^*{}_{,\eta\eta}\right)^2 + \frac{h^3}{12}\left(w^*{}_{,\eta\xi}\right)^2 + h\left(w^*{}_{,\eta}\right)^2\right]L_1L_2 + \frac{D}{2}\left[\left(w^*{}_{,\eta\eta}+w^*{}_{,\xi\xi}\right)^2 - 2(1-\nu)\left(w^*{}_{,\eta\eta}\,w^*{}_{,\xi\xi} - \left(w^*{}_{,\eta\xi}\right)^2\right)\right]L_1L_2 \quad (4.16)$$

In this equation, * denotes the variables evaluated at the center of the fundamental element, $(L_1/2, L_2/2)$. This is the total strain energy of the fundamental element, which is just the function of time. Next, the total energy is divided by area of the element, (L_1L_2), to obtain the energy density, which can be written as:

$$\frac{U_{tot}}{L_1L_2} = \frac{E_cA_c}{2L_2}\left(\frac{T^2}{E_c^2A_c^2} + \frac{Tw^*{}_{,\eta}^{\,2}}{E_cA_c} - \frac{2Tz_cw^*{}_{,\eta\eta}}{E_cA_c} + z_c^2w^*{}_{,\eta\eta}^{\,2} + \frac{Tz_c^2w^*{}_{,\eta\eta}^{\,2}}{E_cA_c}\right) + \frac{N_x^2}{2hE_p} + \left(-\frac{N_x}{2h}\right)\left[\frac{h^3}{12}\left(w^*{}_{,\eta\eta}\right)^2 + \frac{h^3}{12}\left(w^*{}_{,\eta\xi}\right)^2 + h\left(w^*{}_{,\eta}\right)^2\right] + \frac{D}{2}\left[\left(w^*{}_{,\eta\eta}+w^*{}_{,\xi\xi}\right)^2 - 2(1-\nu)\left(w^*{}_{,\eta\eta}\,w^*{}_{,\xi\xi} - \left(w^*{}_{,\eta\xi}\right)^2\right)\right] \quad (4.17)$$

For a sufficiently large number of fundamental elements, this energy density is a good representative of that of an equivalent homogenized element. On multiplying it with the area of an infinitesimal element, $dxdy$, and integrating over the area of the plate results in the total strain energy of the homogenized system

$$U_{sys} = \int_0^b \int_0^a \frac{1}{2} \left\{ D_{11} w_{,xx}^2 + D_{22} w_{,yy}^2 + 4 D_{66} w_{,xy}^2 + 2 D_{12} w_{,xx}\, w_{,yy} - C_1 w_{,xx} + C_2 \right\} dxdy \tag{4.18}$$

where the coefficients can be expanded as

$$\begin{aligned}
D_{11} &= \left[D + \frac{E_c A_c z_c^2}{L_2} + \frac{T z_c^2}{L_2} - \frac{N_x h^2}{12} \right], \\
D_{22} &= D, \\
D_{66} &= \left(\frac{1}{2} \right) \left[D\,(1-\nu) - \frac{N_x h^2}{24} \right], \\
D_{12} &= \nu D, \\
C_1 &= \frac{T z_c}{L_2}, \\
C_2 &= \left[\frac{T^2}{2 E_c A_c L_2} + \frac{N_x^2}{2 h E_p} \right].
\end{aligned} \tag{4.19}$$

Similarly, using the total kinetic energy of the system expressed in Eq. 4.14 and following the similar homogenization approach outlined above, the total kinetic energy in the homogenized system is obtained as

$$E_{k,sys} = \int_0^b \int_0^a \frac{1}{2} K_1 \left(\frac{\partial w}{\partial t} \right)^2 dxdy \tag{4.20}$$

where the homogenized aerial mass density (Units$-Kg/m^2$) is written as

$$K_1 = \rho_p h + \rho_c A_c / L_2. \tag{4.21}$$

4.1.5 Equation of motion

Using the total strain and kinetic energy of the homogenized system obtained in Eqs. 4.18 and 4.20, Hamilton's principle is further used to obtain the following governing equation of motion:

$$D_{11}w_{,xxxx} + 2\left(D_{12} + 2D_{66}\right)w_{,xxyy} + D_{22}w_{,yyyy} + K_1 w_{,tt} = 0 \tag{4.22}$$

where the coefficients of the EOM are expanded in terms of the system parameters in Eqs. 4.19 and 4.21. Further, it is interesting to note that Eq. 4.22 has a similar form of partial differential equation (PDE) as a specially orthotropic laminated plate [89, 3]. This was also discussed in Section 1.2.5 when standard differential equations in structural dynamics were presented in Chapter 1. Hence, with the application of the homogenization approach, the cable-harnessed plate structure can be represented as an equivalent continuum plate model that has properties similar to a specially orthotropic plate.

Also, on substituting the cable parameters, $E_c = T = \rho_c = 0$ in the coefficients of Eq. 4.22, the resulting PDE is same as the equation of motion of a bare plate. The resulting coefficients $D_{11} = D$, $D_{66} = D\left(1-\nu\right)/2$, $D_{12} = \nu D$, $D_{22} = D$ and $K_1 = \rho_p h$ corresponds to the equation of motion of a homogeneous and isotropic rectangular plate, also mentioned in Section 1.2.5.

The first term of the PDE in Eq. 4.22, $D_{11}w_{,xxxx}$, is related to the bending stiffness of the cabled plate system in the $x-$direction. It should be noted that the additional terms in the coefficient D_{11} in Eq. 4.19 compared to the bare plate are responsible for changing the cable-harnessed structure's stiffness in the $x-$direction. As seen from the expression of D_{11}, the second and third terms are the added stiffness due to the cable attachment depending on the cable modulus, cable radius, pretension, plate thickness, and distance between parallel cables. Similarly, the third term of the PDE, $D_{22}w_{,yyyy}$, is related to the bending stiffness of the homogenized structure along the $y-$direction. From Eq. 4.19, it is clear that there is no added cable stiffness present in the $y-$direction because when the cable is attached along the $x-$direction, there is no contribution of cable stiffness in the orthogonal direction. The terms D_{12} and D_{66} are responsible for the twist and coupled-bending stiffness in the system. Additionally, K_1 denotes the homogenized mass per unit area of the system.

For the homogenized model, the boundary conditions at the four edges are obtained as,

$$w_{,x} = 0 \qquad or \qquad M_x + C_1 = 0 \qquad on\ edges\ x = 0\ and\ x = a. \tag{4.23a}$$

$$w = 0 \qquad or \qquad M_{x,x} + 2M_{xy,y} = 0 \qquad on\ edges\ x = 0\ and\ x = a. \tag{4.23b}$$

$$w_{,y} = 0 \qquad or \qquad M_y = 0 \qquad on\ edges\ y = 0\ and\ y = b. \tag{4.23c}$$

$$w = 0 \qquad or \qquad M_{y,y} + 2M_{xy,x} = 0 \qquad on\ edges\ y = 0\ and\ y = b. \tag{4.23d}$$

where $M_x = -(D_{11}w_{,xx} + D_{12}w_{,yy})$, $M_y = -(D_{12}w_{,xx} + D_{22}w_{,yy})$ and $M_{xy} = -2D_{66}w_{,xy}$. In Eq. 4.23, the boundary conditions on the left side represents the geometric boundary conditions, while those on the right side represents the natural boundary conditions. Although the expressions M_x, M_y and M_{xy} have a similar form as the bending and twisting moments in a specially orthotropic plate, they do not necessarily represent the exact bending and twisting moment of the equivalent cable-harnessed plate structure. Here, these expressions have been used to write the boundary conditions in a concise form. A detailed discussion of the total bending and twisting moment is presented in the following paragraphs.

In the current work, attention is given to the CFFF (Clamped-Free-Free-Free) boundary condition for experimental validation purpose. Using Eq. 4.23, the boundary conditions can be specifically written for CFFF boundary with the clamped edge along $x = 0$ as,

$$w(0, y, t) = 0\ and\ w_{,x}(0, y, t) = 0 \tag{4.24a}$$

$$M_x(a, y, t) + C_1 = 0\ and\ M_{x,x}(a, y, t) + 2M_{xy,y}(a, y, t) = 0 \tag{4.24b}$$

$$M_y(x, 0, t) = 0\ and\ M_{y,y}(x, 0, t) + 2M_{xy,x}(x, 0, t) = 0 \tag{4.24c}$$

$$M_y(x, b, t) = 0\ and\ M_{y,y}(x, b, t) + 2M_{xy,x}(x, b, t) = 0 \tag{4.24d}$$

Equation 4.24(a) denotes the geometric boundary condition corresponding to the vanishing displacement and slope at the clamped end. Addition of the cable harness along the $x-$direction introduces a non-homogeneous term C_1 in the moment boundary condition at $x = a$ as shown in Eq. 4.24(b). To gain a better understanding of this boundary condition, the stress resultants on the homogenized cabled plate system needs to be calculated as outlined in [90].

The stress resultants on a system are calculated using the definition

$$\left(M_x^H, P_x\right) = \int_{Area} \sigma_{xx}(z, z^2)dA$$

where M_x^H is the moment resultant representing the bending moment per unit length and P_x is a higher-order stress resultant. For the homogenized structure, the integration is

performed across the entire cross-sectional area that includes the components due to both the cable and plate. While obtaining the stress resultant from the cable, it should be noted that the stress σ_{xx} is assumed to be constant over its cross-section and is equal to the value obtained at the plate-cable interface. The homogenization method is applied in order to obtain the stress resultants. Throughout the method, only constant terms in P_x, and linear terms in derivatives of $w(x, y, t)$ and constant terms for M_x^H are kept. The moment per unit length of the hybrid system at the edge $x = a$ is therefore obtained as

$$M_x^H = \left[- \left\{ D + \frac{E_c A_c z_c^2}{L_2} \right\} w_{,xx} - \nu D w_{,yy} \right] + T z_c / L_2 \tag{4.25}$$

whereas, the higher order stress resultant is obtained as

$$P_x = -\frac{N_x h^2}{12} + \frac{T z_c^2}{L_2} \tag{4.26}$$

The moment M_x^H is composed of two parts; one that is shown in square brackets which is related to the bending stiffness of the homogenized system in the $x-$direction and another is equal to the initial moment per unit length produced by the taut cable when the plate is in undeformed configuration. The moment boundary condition in Eq. 4.24(b) can now be written in terms of the total moment of the homogenized system at the free end $x = a$ using Eqs. 4.25 and 4.26 as

$$M_x^H = P_x w_{,xx} \tag{4.27}$$

From this equation, it can be clearly seen that due to the presence of higher-order stress resultants, the total bending moment do not vanish at the free end where cables are attached. This is also in agreement with a previous study on the homogenization of cable-harnessed beam structures [91] where the bending moment did not similarly vanish at the free end of the beam structure due to the presence of higher-order stress resultants.

The moment boundary condition at the free edge $y^* = 0$ and b, i.e. $M_y(x, y^*, t) = 0$ in Eqs. 4.24(c) and 4.24(d) do not have terms associated with cable because there is no cable attached to those edges. Hence for the edges parallel to the $y-$axis, M_y denotes the total bending moment in the $y-$direction which vanishes at the free end.

In order to solve the governing equation of motion, the non-homogeneous moment boundary condition in Eq. 4.24(b) needs to be transformed to a homogeneous equation. Hence, a steady-state solution of the form

$$S(x, y) = \frac{1}{2}(C_{11} x^2 + C_{22} y^2),$$

where C_{11} and C_{22} are constants, is introduced such that the displacement $w(x,y,t)$ is transformed to a new variable $\bar{w}(x,y,t) = w(x,y,t) + S(x,y)$. Using the equilibrium solution $S(x,y)$, the boundary conditions in the transformed variable $\bar{w}(x,y,t)$ can be made homogeneous. Also, due to the time-independent nature of the function $S(x,y)$, the natural frequencies of the system determined by the PDE in terms of $\bar{w}(x,y,t)$ remain equal to those obtained from the PDE in terms of the original variable $w(x,y,t)$. The transformed PDE becomes

$$D_{11}\bar{w}_{,xxxx} + 2(D_{12} + 2D_{66})\bar{w}_{,xxyy} + D_{22}\bar{w}_{,yyyy} + K_1\bar{w}_{,tt} = 0 \tag{4.28}$$

and the boundary conditions are transformed to

$$\bar{w}(0,y,t) = 0 \; and \; \bar{w}_{,x}(0,y,t) = 0 \tag{4.29a}$$

$$\bar{M}_x(a,y,t) = 0 \; and \; \bar{M}_{x,x}(a,y,t) + 2\bar{M}_{xy,y}(a,y,t) = 0 \tag{4.29b}$$

$$\bar{M}_y(x,0,t) = 0 \; and \; \bar{M}_{y,y}(x,0,t) + 2\bar{M}_{xy,x}(x,0,t) = 0 \tag{4.29c}$$

$$\bar{M}_y(x,b,t) = 0 \; and \; \bar{M}_{y,y}(x,b,t) + 2\bar{M}_{xy,x}(x,b,t) = 0 \tag{4.29d}$$

where $\bar{M}_x = -(D_{11}\bar{w}_{,xx} + D_{12}\bar{w}_{,yy})$, $\bar{M}_y = -(D_{12}\bar{w}_{,xx} + D_{22}\bar{w}_{,yy})$, and $\bar{M}_{xy} = -2D_{66}\bar{w}_{,xy}$. Clearly, the above mentioned boundary conditions have become homogeneous after the transformation.

In order to obtain the natural frequencies and the FRFs for the boundary value problem formed by Eqs. 4.28 - 4.29, Rayleigh-Ritz (RR) method is used. For the RR method, 36 trial functions are formed using the assumed mode shape functions of clamped-free and free-free beam to obtain the solution for the cabled plate system under CFFF boundary.

It should also be noted that the problem has been formulated for the system where cables are parallel to the $x-$direction. However, if the cables are harnessed parallel to the $y-$direction, appropriate modifications in the boundary conditions (clamping at an edge parallel to $x-$axis and remaining edges remain free) would yield the desired result.

One of the limitations of the current model is its inability to predict the buckling in the plate due to the compressive load applied by the cable. The reasoning is based upon a mathematical step in the process of obtaining the homogenized model. When the strain energies of the plate and cable within the fundamental element in Eqs. 4.10 and 4.11 are

summed up and the homogenization principle is applied, the terms associated with $w_{,\eta}^2$ vanishes in process of obtaining total homogenized strain energy in Eq. 4.18. As a result, the governing equation of motion does not exhibit a form similar to a plate subject to external axial compression, and therefore, the buckling behavior is not predicted by the model. This also implies that the cable-tension force and the pre-compression force in the host plate are considered as internal forces in the system. Hence, caution should be exercised to appropriately choose the cable tension values in order to avoid buckling in the host structure prior to employment of the proposed model.

4.2 Experimental validation of parallel cable-harnessed plates

In this section, the proposed model of the cable-harnessed plate presented in the previous section was experimentally validated. The details of the experimental setup is first presented. Then, the FRFs of the bare plate tests are presented and compared with their models in order to gain confidence in the host structure's model. In the next step, the cables are attached to the host plate structures and the modal characteristics are determined. Finally, these characteristics are compared with those obtained from the cable-harnessed plate model to establish the validity of the model.

4.2.1 Experimental Setup

To extract the modal characteristics of cable-harnessed structures, experimental modal testing is performed. In the series of experiments, the impact hammer testing is primarily used, however, shaker excitation is also used for one structure as discussed later. Fig. 4.2(a) shows the experimental setup of a structure attached to the shaker. In this case, Modal Shop 2075 E dual-purpose electrodynamic shaker excites the structure using a stinger that is connected to a force gauge (PCB Piezotronics 208C01) mounted on the structure. A Modal Shop 2050E09 power amplifier is used to provide the excitation signal and the power required to excite the structure. On the other hand, for the impact hammer tests, the plate is excited using a PCB 086C01 impulse force hammer. The data is acquired using the LMS SCADAS mobile data acquisition system connected to a computer. For the displacement sensing purpose, a contact-less Polytec OFV-505 laser vibrometer is used which is operated using a Polytec OFV-5000 vibrometer controller. LMS Testlab version 14.0 is used as a

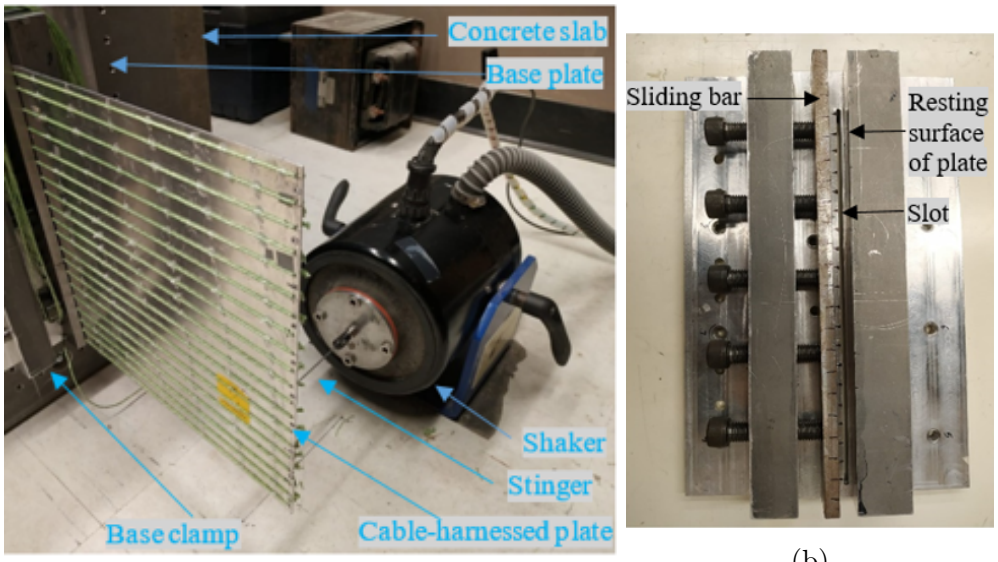

(a) (b)

Figure 4.2: Experimental setup (a) shaker testing setup of the structure-1, (b) Top view of the base clamp

computer software to control the data acquisition settings and analyze the output vibration data.

A base clamp is fabricated to clamp the plate structure as shown in Fig. 4.2(b). The base clamp has a sliding bar that applies the clamp boundary condition on the plate. While clamping, this sliding bar is pressed against the plate structure under test using five bolts. A slot is present in the base clamp to allow the cables to pass through it during the fabrication process. The plate rests on the surface that is on right side of the slot as seen from the top view shown in Fig. 4.2(b). This base clamp is bolted to a thick base plate that is attached to a heavy concrete slab as also shown in Fig. 4.2(a). The fabrication of the cable-harnessed structures is done in such a way that its testing is performed followed by the bare plate. It is made sure that the plate clamp length remains constant throughout these tests and hence, the clamping bolts are not disturbed between tests. Once the bare plate tests are completed, the bare plate and clamp are removed together from the base plate and the entire structure is moved to the work station where cables are kept in tension using hanging masses, while the plate is kept in vertical position for the cable attachments. A small amount of glue is applied at discrete locations for cables to remain in contact with the plate under the applied tension. Once all the cables are attached, experiments on the

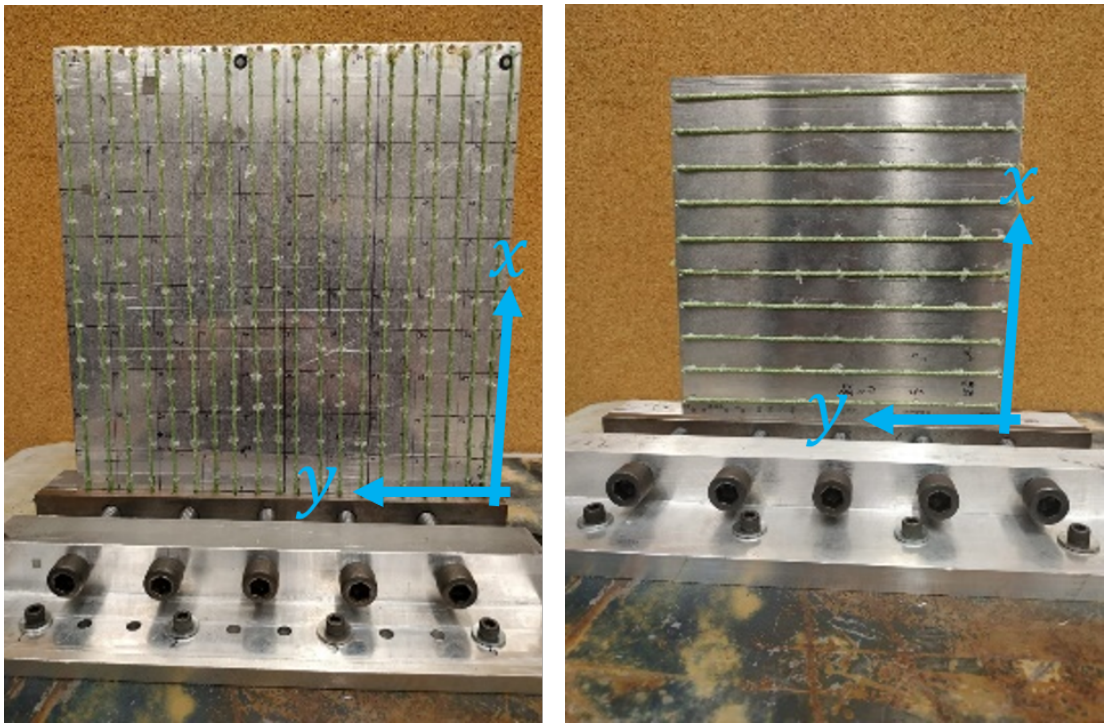

(a) (b)

Figure 4.3: (a) Structure-2 clamped on the base plate, (b) Structure-3 clamped on the base plate

cabled plate are conducted by clamping the system back to the base plate. Figs. 4.2(a) and 4.3(a) show the cables harnessed to the plate parallel to the $x-$axis while Fig. 4.3(b) has cables parallel to the $y-$axis.

4.2.2 Bare plate model and test FRFs

Three different plates are used in the experiments and are referred to as Plate-1, Plate-2, and Plate-3 as listed in Table 4.1. The table reports the geometric properties of the three plates. Plate-1 and Plate-2 have a similar length and width but the former is thinner. Whereas, the Plate-3 has a smaller length and width than both Plate-1 and Plate-2. The testing plan was developed for square plates and hence, the length and width are approximately equal. The material used for host plate specimens is the Aluminum alloy 6061 with the following material properties: $E_p = 68.9\ GPa$, $\rho_p = 2768\ Kg/m^3$, $\nu = 0.33$.

Table 4.1: Geometric parameters of the plates

	Length, a, m	Width, b, m	Thickness, h, mm
Plate-1	0.269	0.271	1.26
Plate-2	0.27	0.269	1.6
Plate-3	0.198	0.202	1.2

To begin with, the experimental FRFs of the bare plates are compared to the analytical FRFs obtained using classical plate theory. The comparison of FRFs for four sets of actuation and sensing location is presented in Figs. 4.4 —4.6 for Plates 1-3, respectively. The coordinates of actuation and sensing locations are mentioned in Table 4.2 which are measured with respect to the global coordinate system defined in the modeling section. The terms 'Structure-1', 'Structure-2', and 'Structure-3', also used in Table 4.2, are utilized to denote either the bare or the cabled plate structure depending on the context of discussion. For now, it can be interpreted from Table 4.2 that both, bare plates and cabled plate structures, undergo testing at all four sets of actuation and sensing locations. Further details of the cabled plate structures are presented in Section 4.2.3. Also, the actuation and sensing locations were chosen so that they do not lie on the nodal lines of the first five modes.

Table 4.2: Actuation and sensing location coordinates in meters

Serial Number	Structure-1		Structure-2		Structure-3	
	Actuation	Sensing	Actuation	Sensing	Actuation	Sensing
Test-1	(0.045,0.258)	(0.040,0.255)	(0.028,0.210)	(0.250,0.215)	(0.024,0.175)	(0.182,0.185)
Test-2	(0.045,0.186)	(0.045,0.186)	(0.029,0.210)	(0.260,0.255)	(0.022,0.120)	(0.182,0.181)
Test-3	(0.202,0.082)	(0.190,0.259)	(0.030,0.210)	(0.260,0.165)	(0.020,0.120)	(0.185,0.120)
Test-4	(0.201,0.085)	(0.211,0.082)	(0.030,0.210)	(0.265,0.095)	(0.023,0.115)	(0.180,0.075)

The test FRF presented in Figs. 4.4(a) and 4.4(b) is obtained using impact hammer test for the bare plate of the structure-1 and is seen to match well with the analytical model FRF. The natural frequencies, listed in Table 4.3, are also predicted accurately by the model except for the second mode. The error in the second mode is not an important concern because, as it is seen later in the discussion, the cable attachment does not change the frequency of this mode substantially. For the impact test shown in Fig. 4.4(a) and 4.4(b), a few extra small spikes are observed which are not predicted by the model. In order to see whether those spikes correspond to the structure's mode, a shaker excitation was used for Test 3 and Test 4 for structure-1, which resulted in very clean FRFs shown in

Fig. 4.4(c) and 4.4(d), respectively. The peaks observed in the test FRFs corresponded to system's natural frequencies as also predicted by the model and no extra spikes were seen in shaker FRFs. Hence, the extra small spikes in the hammer results did not correspond to the system's structural modes.

In Figs. 4.5 and 4.6, the FRFs are obtained using impact hammer test for the bare plate of structures-2 and 3, respectively. For both these structures, the analytical model is able to predict the test results very well. The results are also a good match for both the structures for all the four sets of actuation and sensing location. The natural frequencies of the bare plate of these structures listed in Table 4.3 show a good match between test and model. No extra spikes were seen in the FRF of these tests, therefore, shaker testing was not conducted for these two structures. Also, for the structure-2, there is a mismatch of FRF amplitude near the sixth mode region because the impact location was close to a nodal line of the Mode-6.

Table 4.3: Comparison of experimental and model natural frequencies (Hz), error in the model, for bare and cabled plate for the three structures. The % change in model's frequency on cable attachment is also presented.

		Mode 1	Mode 2	Mode 3	Mode 4	Mode 5	Mode 6	Mode 7	Mode 8	Mode 9	Mode 10
Structure 1	Bare Plate, Test	13.75	37.50	90.25	112.75	130.25	-	-	-	-	-
	Bare Plate, Model (BP1)	14.74	35.30	89.94	113.97	129.70	226.21	260.33*	268.04**	300.23	388.27
	Model error	7.21%	-5.87%	-0.34%	1.08%	-0.42%	-	-	-	-	-
	Cabled Plate, Test	15.25	38.75	95.25	114.50	135.75	-	-	-	-	-
	Cabled Plate, Model (CP1)	15.91	35.81	96.49	114.31	134.54	228.61	267.60**	280.34*	315.77	387.96
	Model error	4.32%	-7.59%	1.30%	-0.16%	-0.89%	-	-	-	-	-
	(CP1-BP1)/BP1	7.93%	1.44%	7.28%	0.30%	3.73%	1.06%	-0.16%**	7.68%*	5.18%	-0.08%
		Mode 1	Mode 2	Mode 3	Mode 4	Mode 5	Mode 6	Mode 7	Mode 8	Mode 9	Mode 10
Structure 2	Bare Plate, Test	19.25	45.00	113.50	147.25	163.75	289.25	328.50*	342.75**	384.50	499.25
	Bare Plate, Model (BP1)	18.58	44.89	113.53	146.10	164.70	288.17	328.24*	344.21**	381.15	498.94
	Model error	-3.48%	-0.24%	0.03%	-0.78%	0.58%	-0.37%	-0.08%	0.43%	-0.87%	-0.06%
	Cabled Plate, Test	20.50	44.25	119.50	147.25	167.00	289.00	342.00**	347.25*	394.50	497.00
	Cabled Plate, Model (CP1)	19.76	45.37	120.33	146.23	169.24	290.60	344.27**	348.40*	395.41	496.40
	Model error	-3.61%	2.54%	0.70%	-0.70%	1.34%	0.55%	0.66%	0.33%	0.23%	-0.12%
	(CP1-BP1)/BP1	6.35%	1.07%	5.99%	0.09%	2.76%	0.84%	0.02%**	6.14%*	3.74%	-0.51%
		Mode 1	Mode 2	Mode 3	Mode 4	Mode 5	Mode 6	Mode 7	Mode 8	Mode 9	Mode 10
Structure 3	Bare Plate, Test	25.00	61.75	153.50	201.75	223.00	394.50	441.50	471.00	-	-
	Bare Plate, Model (BP1)	24.89	60.84	152.39	200.63	222.10	392.12	440.07	472.94	514.46	680.55
	Model error	-0.44%	-1.48%	-0.72%	-0.55%	-0.41%	-0.60%	-0.32%	0.41%	-	-
	Cabled Plate, Test	24.50	60.00	151.50	212.00	218.25	394.50	434.25	479.00	-	-
	Cabled Plate, Model (CP1)	24.65	60.26	151.93	211.40	220.26	395.33	436.06	489.94	530.10	699.37
	Model error	0.63%	0.43%	0.29%	-0.28%	0.92%	0.21%	0.42%	2.28%	-	-
	(CP1-BP1)/BP1	-0.94%	-0.95%	-0.30%	5.37%	-0.83%	0.82%	-0.91%	3.59%	3.04%	2.77%

* and ** are used to denote frequencies with similar mode shapes because the mode switching takes place upon cable attachment in the structures-1 and 2 for particular modes. For instance, Mode-7 of bare plate of the structure-2 has the same shape as Mode-8 of cabled plate and Mode-8 of the bare plate has same shape as Mode-7 of the cabled plate. For other modes, bare plate and cabled plate have similar mode shapes for corresponding mode number.

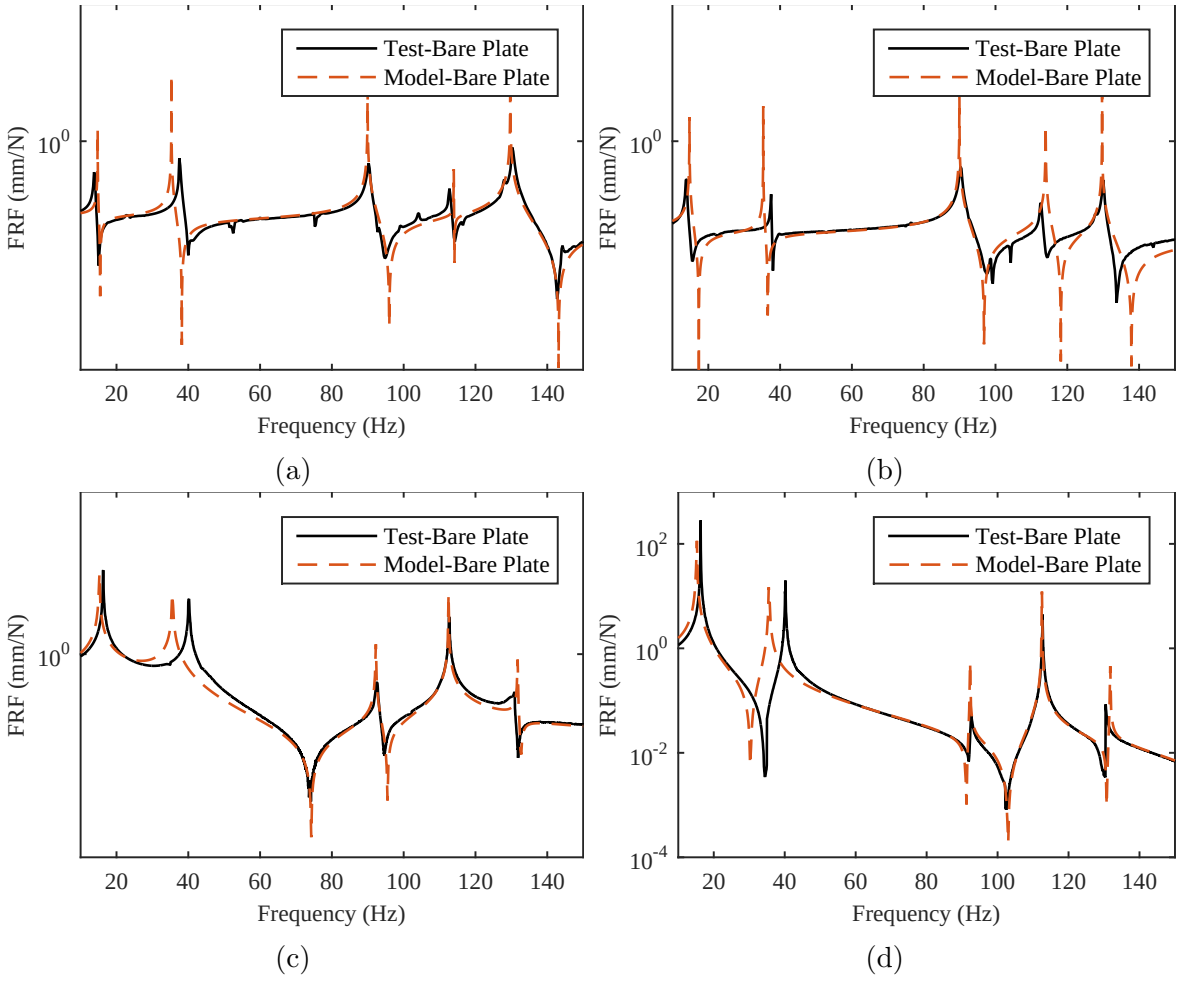

Figure 4.4: Bare Plate FRFs for the Structure-1 (a) Test-1 (Impact), (b) Test-2 (Impact), (c) Test-3 (Shaker), (d) Test-4 (Shaker)

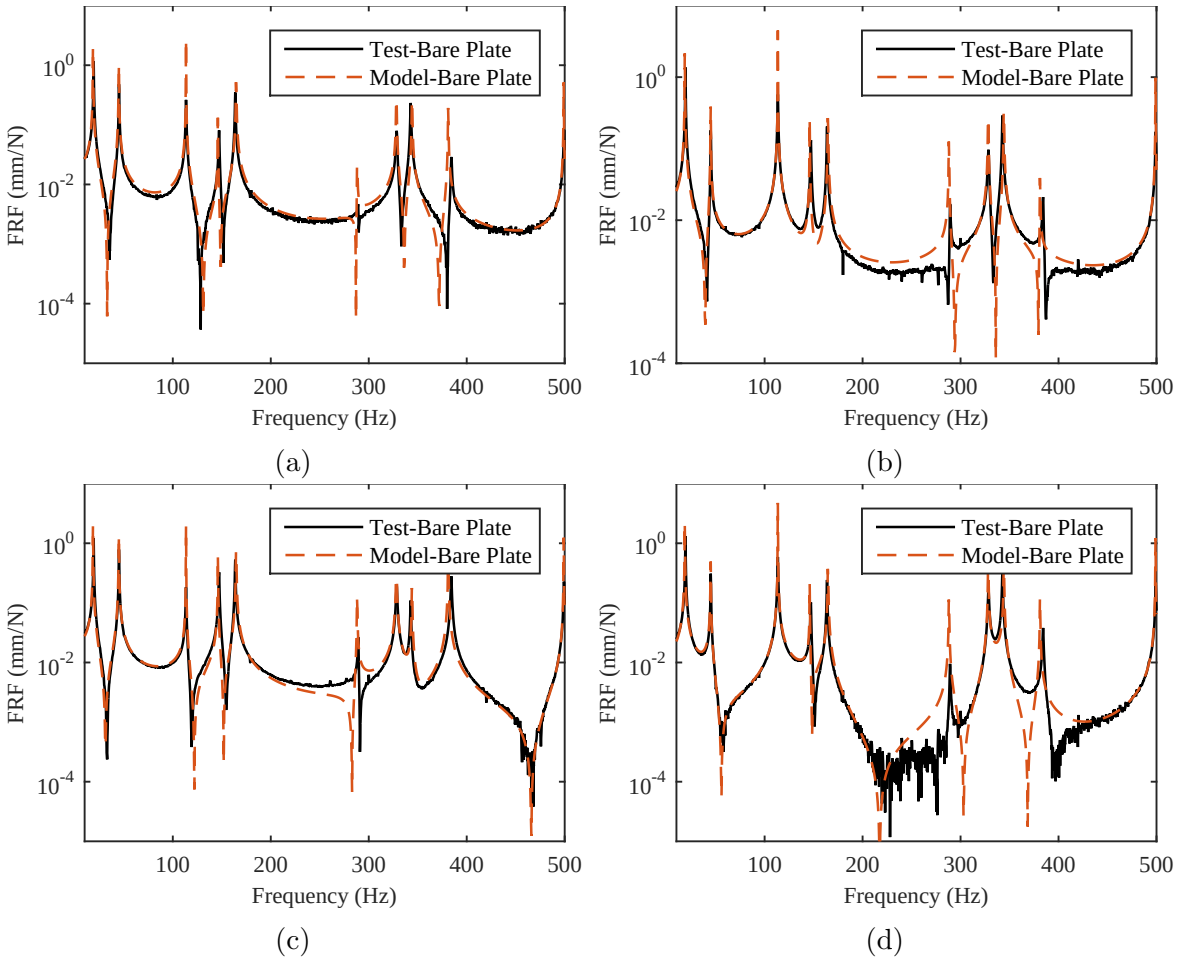

Figure 4.5: Bare Plate FRFs for the Structure-2 (a) Test-1, (b) Test-2, (c) Test-3, (d) Test-4

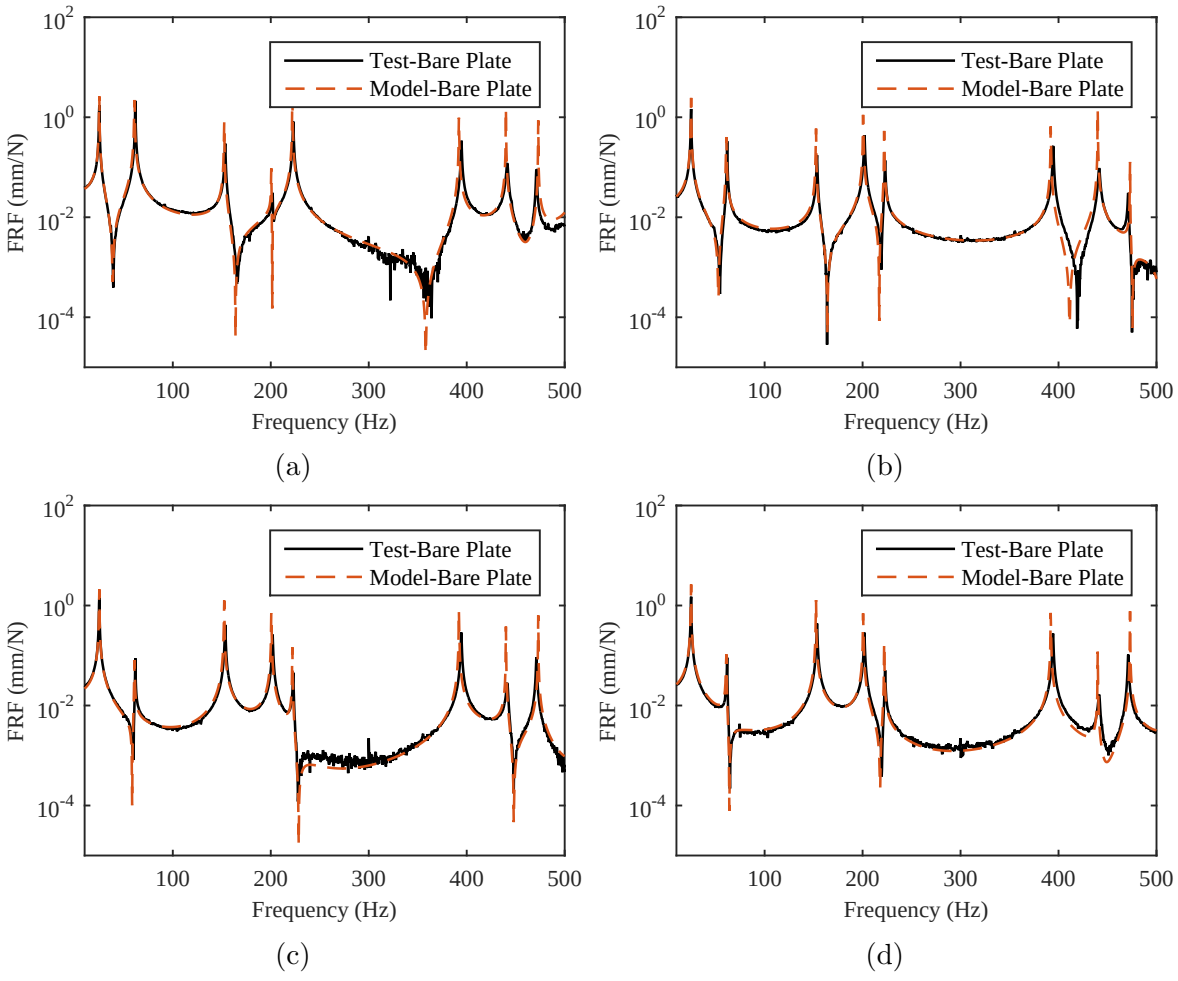

Figure 4.6: Bare Plate FRFs for the Structure-3 (a) Test-1, (b) Test-2, (c) Test-3, (d) Test-4

4.2.3 Cabled plate model and test FRFs

Table 4.4 lists the parameters for the cable used in the testing of the cable-harnessed plates. A Power Pro Super 8 Slick 80 lb break strength fishing line is used. This cable was also used earlier in the previous works on cable-harnessed beam structures [30, 2]. The details of the test structures fabricated for the modal testing experiments are listed in Table 4.5. The three fabricated structures were also shown in Figs. 4.2 and 4.3. For the structure-1, 20 parallel rows of Power Pro cables are attached in a parallel configuration on Plate-1. Each row consists of 5 cables in order to make a cable bundle. The effective radius of the cable bundle can be written as $r_c\sqrt{n}$, where n is the number of cables per row in a bundle [2]. This is calculated by equating the effective area of the cable bundle to the total area of n cables. For the structures 1 and 2, the cables are attached perpendicular to the clamp i.e. parallel to the $x-$axis on plates 1 and 2, respectively. Whereas, for the structure-3, the cables are attached to Plate-3 parallel to the clamp edge (along the $y-$axis). These structures with different parameters allow for a fair comparison between the model and test to validate the ability of the proposed analytical model.

Table 4.4: Cable geometric and material parameters

	Power Pro Cable
Young's Modulus, E_c, GPa	128
Radius, r_c, mm	0.20
Density, $\rho_c, Kg/m^3$	1400

Table 4.5: Cable-harnessed plate test structures

	Structure-1	Structure-2	Structure-3
Plate	Plate-1	Plate-2	Plate-3
Cable	Power Pro	Power Pro	Power Pro
Cable attachment direction	Perpendicular to clamp edge	Perpendicular to clamp edge	Parallel to clamp edge
Number of parallel cable rows	20	20	10
Number of cables per row	5	5	8
Cable Tension, N	2.5	2.5	2.5

The experimental FRFs of the fabricated cabled plate structures 1-3 are compared to those obtained from the proposed model in Figs. 4.7, 4.9, and 4.13 for four sets of different actuation and sensing locations. While, Figs. 4.8, 4.10, and 4.14 show the zoomed-in

Table 4.6: Actuation and sensing location for the cabled plate structure-2

Test Number	Actuation	Sensing
1	(0.029,0.157)	(0.255,0.157)
2	(0.027,0.162)	(0.099,0.196)
3	(0.028,0.157)	(0.141,0.265)
4	(0.027,0.162)	(0.115,0.160)

plots for certain important modes for the Test-1. In these figures, the bare plate FRF is also presented to analyze the effect of cable attachment. The testing on the cabled plate structures were performed for the same set of actuation and sensing locations as the bare plates, except for the structure-2 where a new set of locations as listed in Table 4.6 were used to obtain the cabled plate FRFs. This was done after it was found that the impact location was very close to a nodal line for Mode-6. Since the cable attachment was already done, the testing with a new set of actuation and sensing locations was done only for the cabled plate. Further, the mode shapes obtained from the model and the experiments for cabled plate of the structure-2 is shown in Fig. 4.11. The mode shapes of the structure-1 are found similar to that of the structure-2 for first ten modes according to the model and hence, the reference to Fig. 4.11 would be used for discussion on mode shapes of structure-1 as well. Furthermore, the mode shapes of structure-3 are shown in Fig. 4.15.

Firstly, the FRF comparison shown in Fig. 4.7 for structure-1 is discussed. It is observed that upon the attachment of the cables, the experimental FRF demonstrate a significant change compared to the FRFs prior to the cable attachments. This can be observed by comparing plots of 'Test-cabled plate' and 'Test-bare plate' in the figure. As well, the cabled plate model is able to predict those changes very well and is clearly a good match with the associated test results. Recall that the bare plate model under-estimated the Mode-2 frequency of bare plate in Fig. 4.4; the error is carried over in the cabled plate for the structure-1 as seen in Fig. 4.7. Also, it should be noted from Table 4.3 that this mode is one of the least affected modes when frequencies of the bare and cabled plate are compared. An increment of only 1.44% (0.51 Hz) is seen in Mode-2 when cables are attached. The reason behind the small increment in this mode is related to the twisting-like mode shape shown in Fig. 4.11, in which the bending curvature along both the axes is not as prominent as the other modes. Therefore, due to the balance of cable stiffening and mass effects for this mode, the difference between the frequency of bare plate and cabled plate for this mode is not as significant.

It is seen that upon attachment of the cables for the structure-1, there is an increase in the natural frequencies for modes 1, 3 and 5; whereas, for the second and fourth modes, the

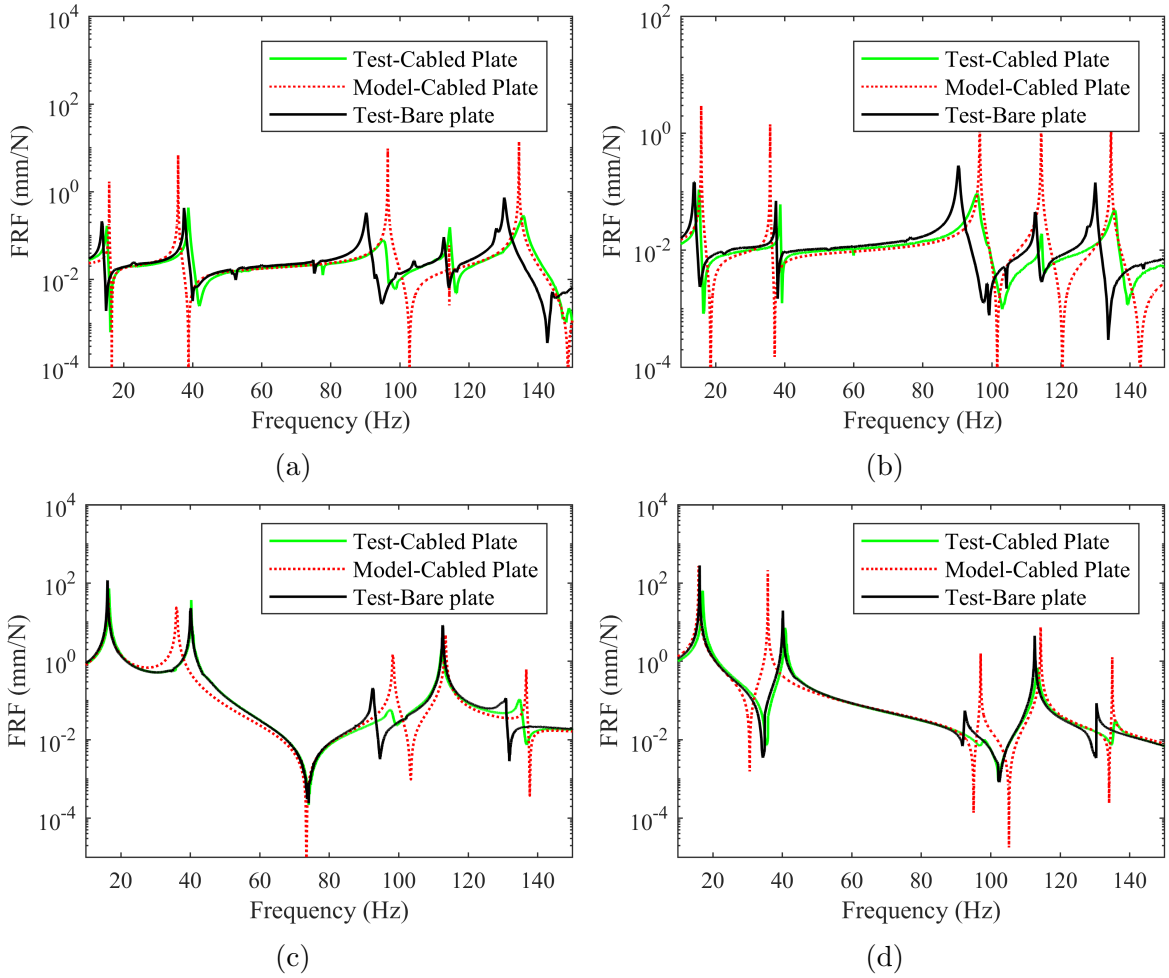

Figure 4.7: Cabled plate FRF comparisons for the Structure-1 (a) Test-1 (Impact), (b) Test-2 (Impact), (c) Test-3 (Shaker), (d) Test-4 (Shaker)

frequencies remain almost similar to the bare plate. The zoomed-in FRF plots for the 1st, 3rd and 5th modes for the structure-1 are shown in Fig. 4.8. Clearly, the overall stiffening effect in these modes after attaching the cables is well-predicted by the model. Regarding the modes that are affected the most upon attaching the cables (1st, 3rd and 5th), a similar observation is made for the structure-2. A close examination of the mode shapes demonstrates the underlying reason behind which modes frequencies are affected the most after adding the cables. This is explained in more detail in the following paragraphs.

As discussed earlier for the structure-1, when the testing of the bare plate was con-

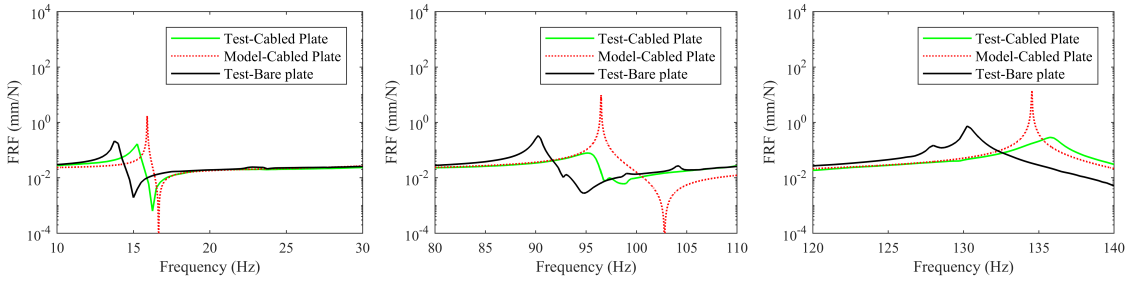

Figure 4.8: Zoomed-in FRF plots for the structure-1 of test-1 (a) Mode-1, (b) Mode-3 and (c) Mode-5

ducted, two plots were obtained each from impact hammer and shaker excitation as shown in Fig. 4.4. The test data for the cabled plate structures are presented in a similar format where Figs. 4.7(a) and (b) correspond to the impact test, while Figs. 4.7(c) and (d) corresponds to the shaker test.

Figure 4.9 shows the FRF comparisons between the proposed model and test results for the cabled plate structure-2. For this structure as well, the experiment and analytical model FRF results match very well. The model is able to predict all the frequencies with very high accuracy as also seen in Table 4.3. With respect to the bare plate, a major increase in the frequencies of the cabled plate is observed for Modes-1, 3 and 7. Additionally, Mode-5 and Mode-9 frequencies also undergo a noticeable increase. The zoomed-in plots for some of the modes that are majorly affected are also shown in Fig. 4.10. An interesting point to note here is that upon the attachment of the cables, there is a switch between the order in which the 7th and 8th modes appear. Hence, in Table 4.3, where the frequencies are tabulated in increasing order, care must be taken when comparing the associated frequencies between the bare plate and the cabled plate. In this case, the frequency for Mode-7 of the bare plate is compared to the Mode-8 of the cabled plate, and similarly, Mode-8 of the bare plate is compared to the Mode-7 of the cabled plate.

To better understand how the stiffening due to the cables affects various modes differently, the mode shapes for cabled plate structure-2 shown in Fig. 4.11, are discussed in addition to the two bare plate mode shown in Fig. 4.12. The Mode-7 of the bare plate pertains to a bending behaviour that is more prominent along the $x-$axis; whereas, the Mode-8 has dominant bending curvature along the $y-$axis. Since the mode with bending along the $x-$axis is affected more by the stiffening impact due to the cables along the same axis, the modal frequency increase for this mode is more significant than the Mode-8

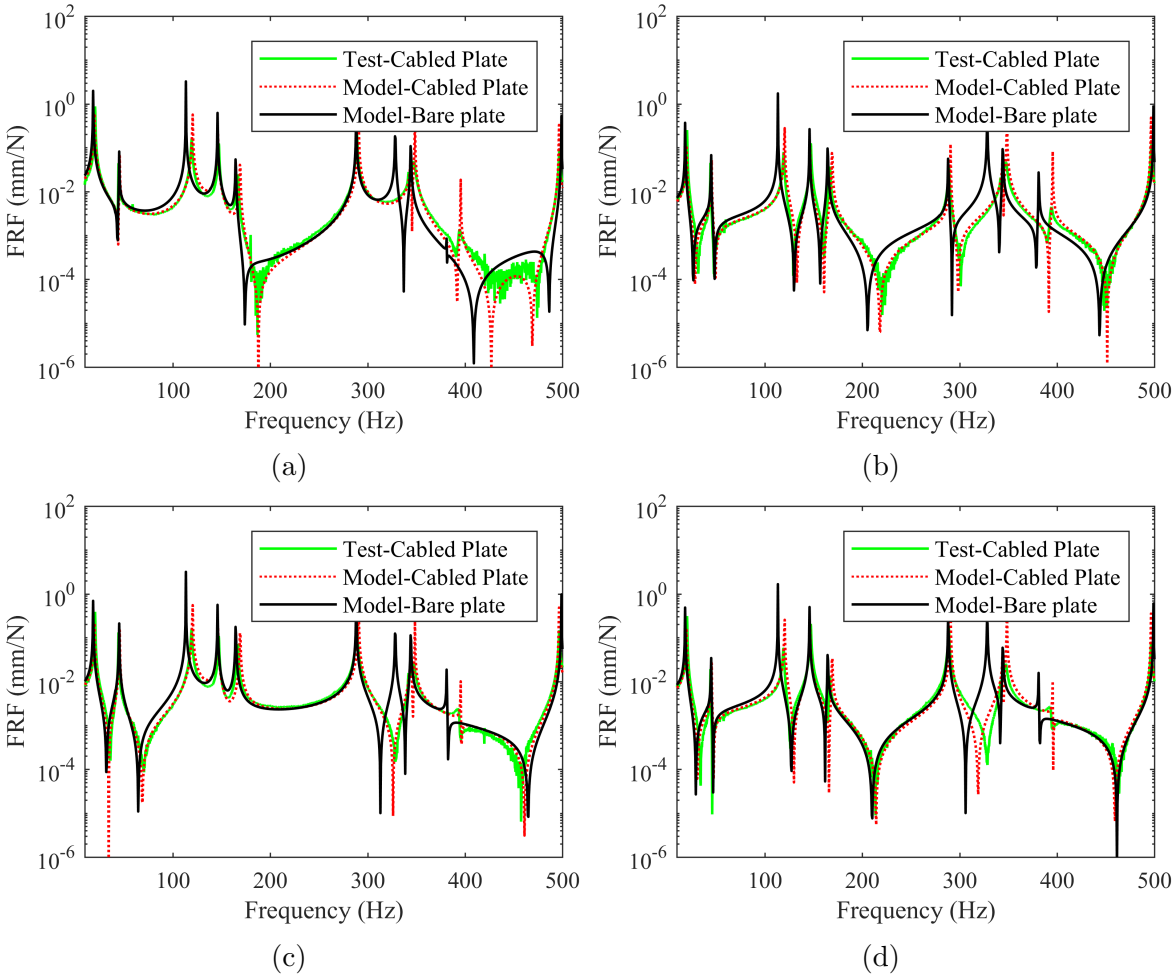

Figure 4.9: Cabled plate FRF comparisons for the Structure-2 (a) Test-1, (b) Test-2, (c) Test-3, (d) Test-4

resulting in its appearance at a higher frequency for the cabled plate system when compared to the bare plate. This is the reason behind the two modes switching orders after attaching the cables. This stiffening effect along the $x-$axis is also the reason for the more significant increase in the frequencies for the Modes-1 and 3 compared to the other modes for this structure.

It is clear that the analytical and experimental modes shown in Fig. 4.11 match well for the cabled plate structure-2. As also discussed in the previous paragraph, the cable stiffening effects are dominant for a certain mode when the mode shape has a large bending

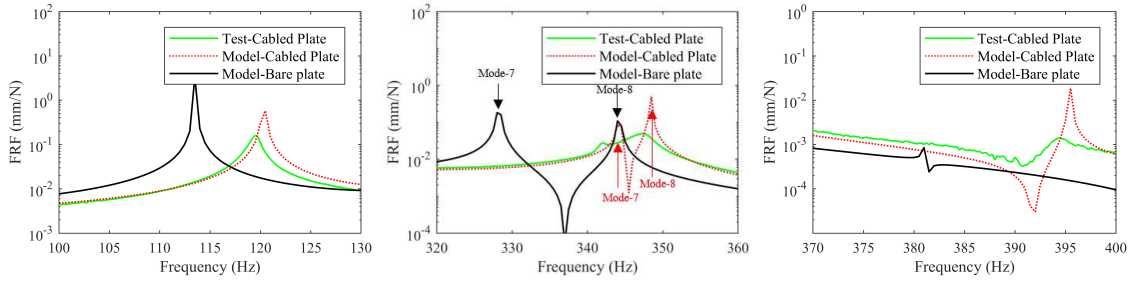

Figure 4.10: Zoomed-in FRF plots for the structure-2 of test-1 (a) Mode-3, (b) Mode-7 and 8 (Mode-7 of bare plate and Mode-8 of cabled plate have similar mode shapes; Mode-8 of bare plate and Mode-7 of cabled plate have similar mode shapes), and (c) Mode-9

curvature in the direction of the cable that ultimately results in a larger strain energy contribution for the cable. As seen from Eq. 4.19, a major contribution of the cable strain energy is reflected in the coefficient D_{11} that also depends on the cable's Young's modulus and area of cross-section. In the expression of the total strain energy in Eq. 4.18, this coefficient is multiplied with the square of bending curvature in the $x-$direction. Hence, the bare plate natural frequencies for Modes-1, 3 and 7 undergo a significant increase upon cable attachment, where the bending curvature is high in $x-$direction. Mode 5 and Mode 9 also possess a high bending curvature in the $x-$direction in different regions of the plate but it also contains a nodal line parallel to the $x-$axis in the center. Hence, the curvature becomes negligible in the region around the nodal line, resulting in the loss of cable stiffness contribution. As a result, the stiffening effect in these modes is moderate.

Similarly, the reasoning for the modes that are minimally impacted upon cable attachment for structure-2 can also be discussed. These include modes-2, 4, 6 and 8 corresponding to the bare plate. As seen in Fig. 4.11, Mode-2 has a nodal line at the center of the plate similar to Mode 5 and 9, however, the stiffening effect is comparatively lower. This is because the Mode-2 has a small curvature along both axes. Compared to Mode-5 and 9, this smaller curvature results in a low contribution of the cable strain energy towards the total strain energy of the homogenized system resulting in a marginal increase in Mode-2 frequency. Modes 4 and 6 also have small cable stiffening effects owing to the presence of the two nodal lines, hence the resulting overall low curvature decreases the cable stiffening effects. Mode 8 of the bare plate that switches its order to Mode 7 of the cabled plate is also an interesting case, as the natural frequency of the cabled plate is almost equal to the bare plate. As seen in Fig. 4.12(b) of the supplementary material, this mode has a high bending curvature along the $y-$direction, whereas, the bending curvature along the

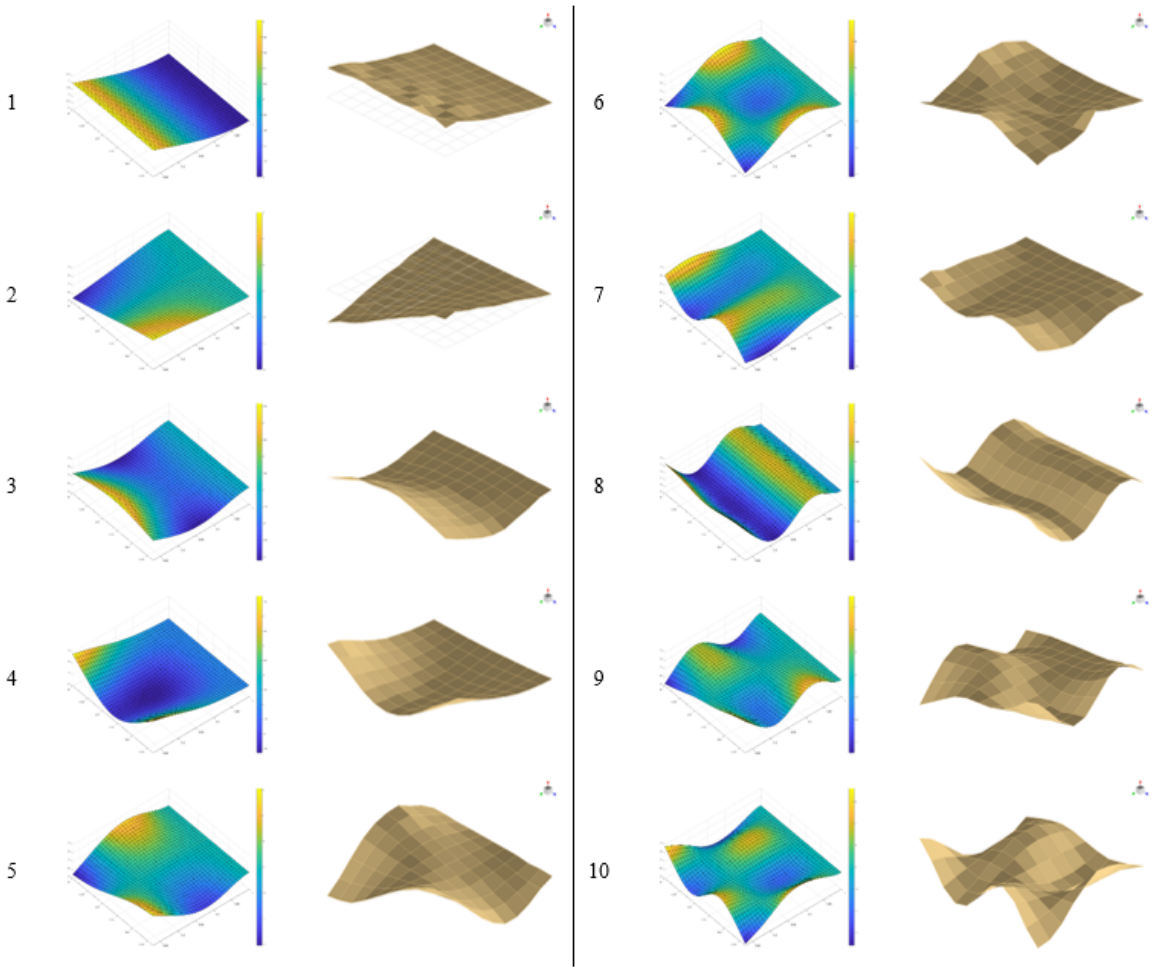

Figure 4.11: First ten mode shapes obtained for the clamped-free-free-free cabled plate structure-2 from proposed analytical model (left) and experiments (right)

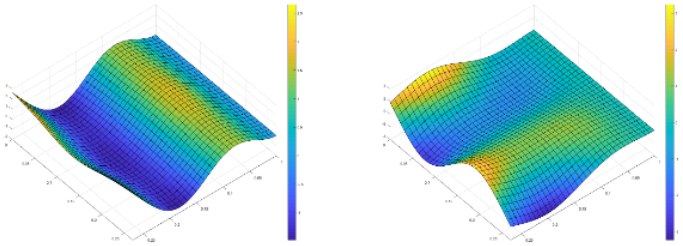

(a) (b)

Figure 4.12: Mode shapes obtained for the clamped-free-free-free bare plate structure-2 using classical plate model for (a) Mode-7 and (b) Mode-8

$x-$direction is very small. Additionally, this mode has three nodal lines thereby reducing the overall cable stiffening effect and producing a similar frequency as the bare plate.

The FRFs for the structure-3 are presented in Fig. 4.13 for all the four tests. In this structure, the cables are attached to the plate parallel to the $y-$axis i.e. parallel to the clamped edge. As also previously mentioned in the modeling section, this structure can be modeled by still assuming cables along the $x-$axis, provided the boundary conditions are accordingly changed in the model such that the clamped edge is now parallel to the direction of cable attachment. As seen from Fig. 4.13, the cables attached parallel to the clamped edge also significantly impacts the vibration modes. The zoomed-in plots of the test-1 FRF region with significant effect on the natural frequencies are shown in Fig. 4.14. Clearly, the cabled plate model is able to predict the change in system dynamics and matches well with the test FRFs of the cabled plate. The stiffening effect is particularly seen in Mode-4 where the natural frequency increase by 5.37% upon cable attachment, as seen from Table 4.3. The dominant cable stiffening effect is also observed and predicted in Mode-8, however, the natural frequency prediction of this higher mode is over-estimated by the model. This is because the homogenized model starts to show its limitations for smaller number of fundamental elements. This structure has considerably smaller number of fundamental elements, 100, compared to the structure-2 that contains 400. As the number of the repeated fundamental elements in a structure decrease, the ratio of the wavelength of the frequency of interest to the size of the element decrease as a result of which the error in the frequency predictions gets higher. This explains the higher error for the highest mode of interest for this structure compared to the structure-2.

Additionally, the zoomed-in FRFs in Figs. 4.14(a) and (b) show a decrease in frequencies on cable attachment for Modes 5 and 7, respectively. This is because the cable inertia

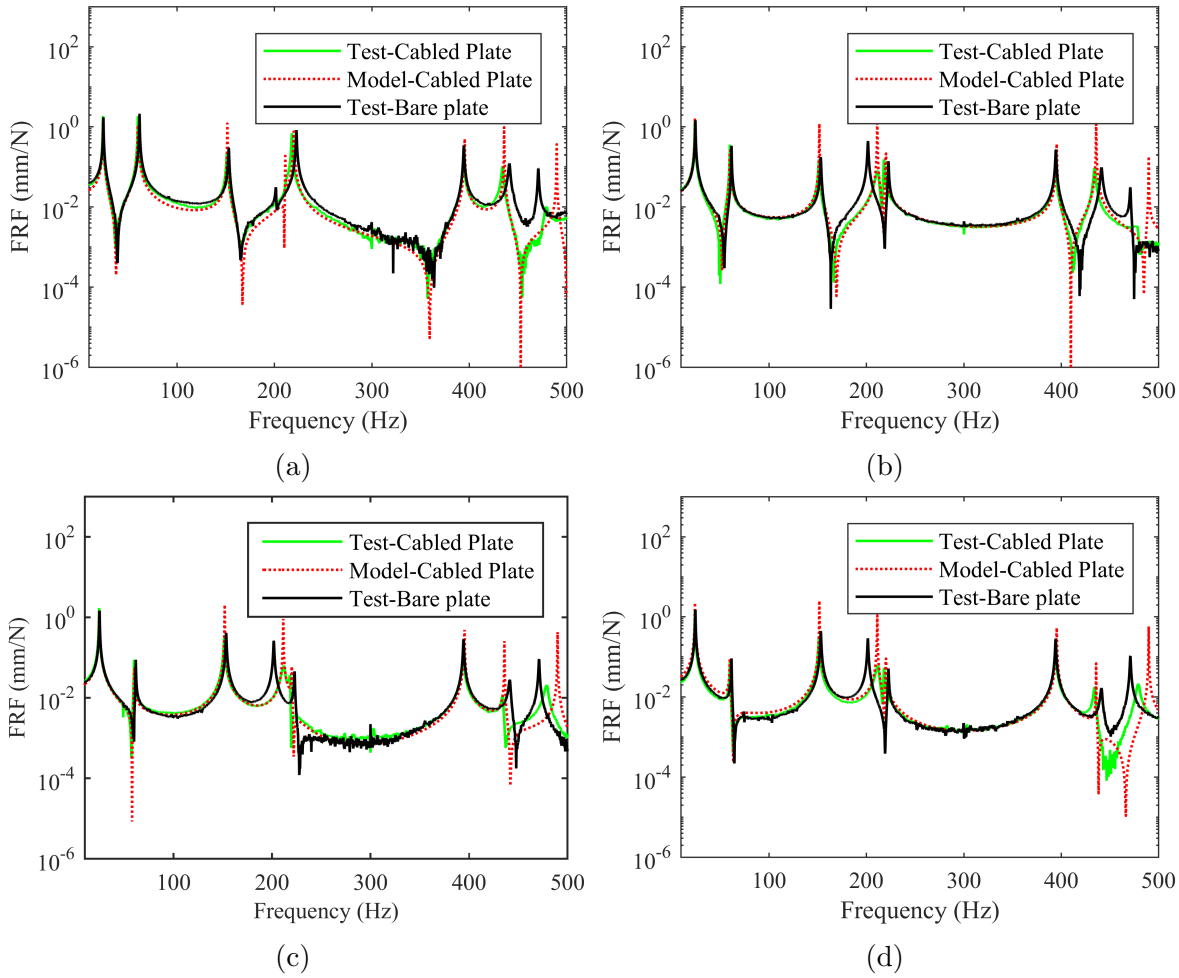

Figure 4.13: Cabled plate FRF comparisons for the Structure-3 (a) Test-1, (b) Test-2, (c) Test-3, (d) Test-4

effects dominate over its stiffening effects for those modes. The model is able to predict the dominant cable inertia effect in these modes. The reason for the cable stiffening and mass effects dominance can be seen from the mode shapes shown in Fig. 4.15. This figure shows the first eight analytical and experimental mode shapes for structure-3 which match very well with each other. As mentioned earlier, Mode-4 exhibits an increase in its frequency due to the cable attachment. This is clear from the fourth mode shape as the bending curvature of the plate is predominantly along the $y-$direction (the direction in which the cables are attached). This results in the significant strain energy contribution

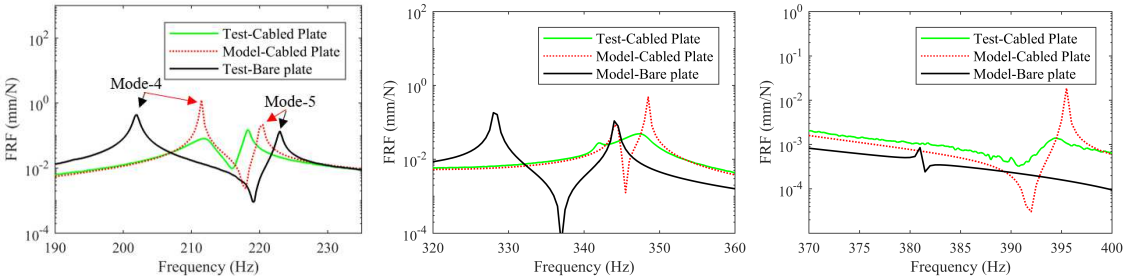

(a) (b) (c)

Figure 4.14: Zoomed-in FRF plots for the structure-3 of test-1 (a) Modes-4 and 5, (b) Mode-7 and (c) Mode-8

for the cables upon bending in this direction that leads to the major stiffening effect for Mode-4. However, in Mode-5 and Mode-7, the cable inertia effects are dominant due to minimal contribution of cable stiffening owing to the presence of the nodal lines as well as small curvatures in the $y-$direction. Therefore, the cable inertia effects become dominant for these modes resulting in smaller frequencies compared to the bare plate system.

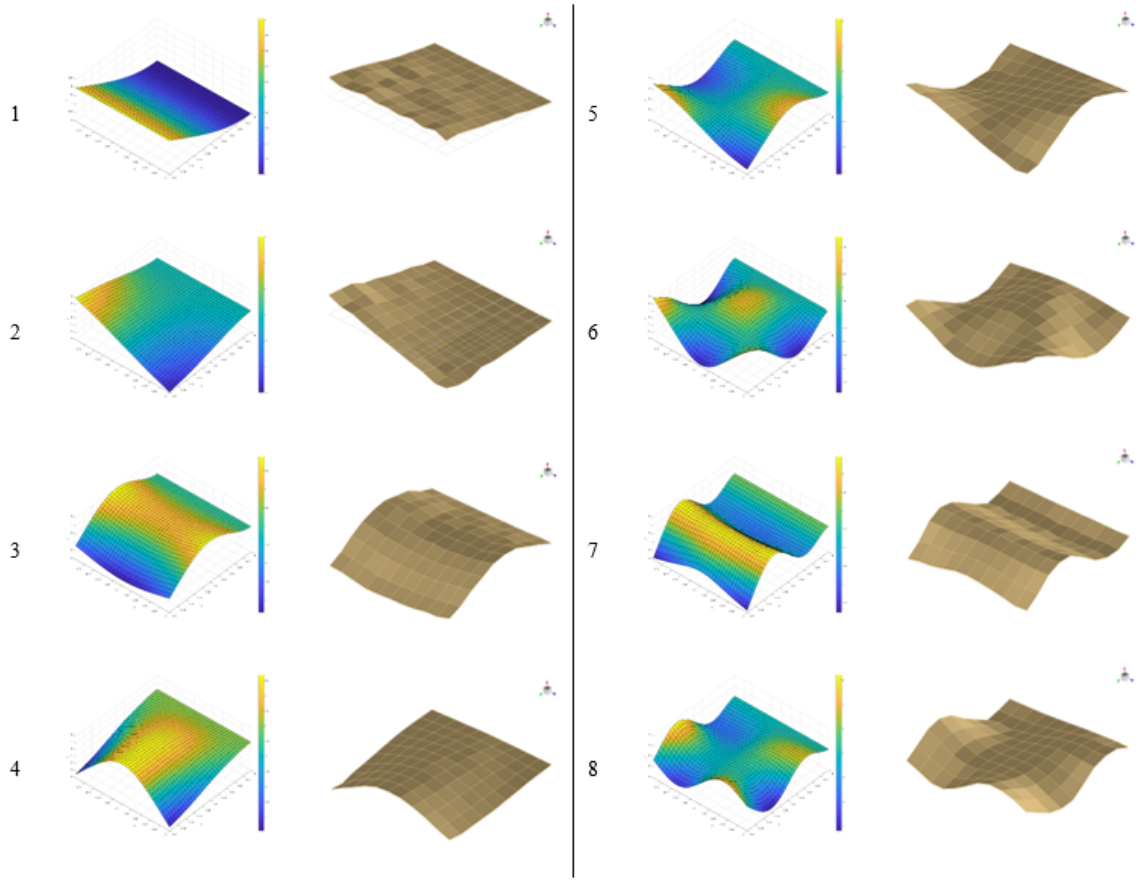

Figure 4.15: Mode shapes obtained for the cabled-free-free-free plate structure-3 from the proposed analytical model (left) and experiments (right)

4.2.4 Comparison of the cable attachment effects between the tested structures

A comparison of the natural frequencies and cable attachment effects between different tested structures is discussed in the following paragraphs. First, the comparison is done between the structures 1 and 2 which are different in terms of the host plate thickness with the former having a thinner host plate. Since the thickness of host plate of the structure-2 is larger, all the natural frequencies of the bare plate are higher as also seen from Table 4.3. A similar observation is made for the cabled plate when the two structures are compared. The interesting part is the comparison of the increase in the stiffening effect upon cable attachment. As seen from Table 4.3, except for Mode-7, all the modes show a higher percentage increase in natural frequencies for the structure-1 compared to the structure-2. The reason behind the high stiffening effect for the structure-1 is the thinner host plate. As the plate thickness decreases in the homogenized model, the contribution of the cable stiffening effects become more dominant. It should be noted that similar to the structure-2, the modes 7 and 8 of the structure-1 also gets switched upon cable attachment according to the model. Also, Mode-7 of the cabled plate structure-2 as seen from Fig. 4.11, which shows bending curvature along the $y-$axis, has a minimal contribution of the cable stiffness and is counter-acted by the cable inertia effects. This results in the frequencies being similar to the bare plate, and is observed for both the structures.

The results obtained from the structures 2 and 3 can also be compared. The major difference between the two structures is the direction of cable attachment where the former has the cables attached parallel to the $x-$axis, whereas, the latter has along the $y-$axis. There are a larger number of parallel rows of cables in the structure-2 but a lower number of cables per row. Additionally, the structure-2 has a thicker and larger host plate structure. The natural frequencies of the bare plate and cabled plate are observed to be higher for the structure-3 for all the tested modes. This is true when similar mode shapes of both the structures are compared. It should be noted that the mode shapes of these structures as shown in Figs. 4.11 and 4.15 are based on increasing frequency order. On comparison, it is seen that the mode shapes of the first six modes are similar. Whereas, the shape of Modes-7 and 8 of cabled plate structure-3 resembles with Modes-8 and 9 of the cabled plate structure-2, respectively. The following discussion is based on modes with similar mode shapes. From Table 4.3, it is seen that except for Mode-4, the stiffening effect is consistently higher for the structure-2 for the corresponding modes. For Modes-1 and 3, the structure-2 exhibits a significantly higher stiffening effect compared to the structure-3 which shows an overall cable inertia effect. The Mode-1 and Mode-3 frequencies increase by 6.35% and 5.99%, respectively, for the structure-2, whereas, they decrease by 0.94% and 0.30% for

the structure-3. The higher stiffness in Modes-1 and 3 in the structure-2 is attributed to the large curvature in the $x-$direction that highlights the cable stiffness and increases the overall stiffness of the system. Whereas in the structure-3, since the cables are attached along the $y-$axis, the cable inertia becomes dominant over cable stiffening effects because of the negligible bending curvature in these modes along the $y-$axis, resulting in reduction of the natural frequencies compared to bare plate. In contrast, the stiffening effect of Mode-4 is substantially larger for the structure-3 showing 5.37% increase in the frequency upon cable attachment because the corresponding mode shape has a high bending curvature along the $y-$axis. Whereas, when the cables are aligned along the $x-$axis in the structure-2, the cable inertia and stiffness effects have almost equal and opposite effect on the frequency and hence, the frequency increases by only 0.09%. Modes-2, 5 and 7 of the structure-3 are examples of other modes which witness an overall mass effect for the structure-3. Whereas, the corresponding Modes-2, 5 and 8 of the structure-2 exhibit an overall cable stiffening effect.

A similar comparison can be made between the structures 1 and 3. The thickness of the host plate in these structures is similar, however, the former has larger length and width. As a result, the natural frequencies of structure-3 are larger for the bare plate and cabled plate. Again, the orientation of cable attachment is different between the two structures. It is seen that the Modes-1 and 3 exhibit a significantly higher stiffening effect for the structure-1, whereas, Mode-4 exhibits a similar effect in the structure-3. These effects are based on the reasoning explained in the previous paragraph. Additionally, Modes-2 and 5 show cable stiffening effect for the structure-1, but a dominant cable inertia effect for the structure-3.

4.2.5 MAC Analysis

One of the best methods to quantitatively correlate the mode shapes obtained from experiments and the analytical model is using the Modal Assurance Criterion (MAC) [92]. It is an indicator that is mainly sensitive to the large differences in the mode shape and relatively insensitive to small differences. The MAC values are calculated between different pairs of mode shapes obtained from both test and model. A close match between the mode shapes results in the value of 1, whereas inconsistent mode shapes results in 0. For the current study, the MAC analysis is conducted for the cabled plate structures 2 and 3, for which experimental mode shapes were extracted. The MAC is presented in a three-dimension bar chart shown in Figs. 4.16 and 4.17 for the structures 2 and 3, respectively.

For the structure-2, MAC values along the diagonal of the chart are close to 1 for all the 10 modes except Mode-6. Also, the MAC values are close to zero in off-diagonal

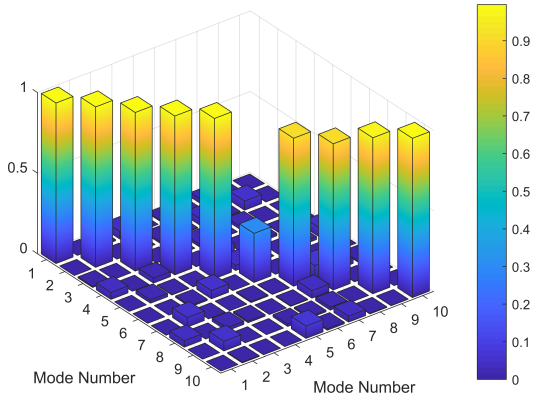

Figure 4.16: MAC bar chart for the cabled plate structure-2

elements when different modes are correlated. The highest MAC value in the off-diagonal elements is 0.07. During the acquisition of the mode shapes, the actuation location is kept fixed whereas the contactless vibrometer is moved through the measurement grid in order to capture mode shapes of the structure. The MAC value corresponding to the Mode-6 correlation is low because the actuation location coordinate (0.03, 0.215) was found close to a nodal line which resulted in an overall smaller modal energy for the Mode-6 causing the poor correlation. As mentioned before, the actuation location was initially decided based on the nodal lines of the first five modes.

In the case of the structure-3, the bar chart is present for correlation of 8 tested modes in Fig. 4.17. The minimum value of the MAC number on the diagonal element is 0.98, while among the off-diagonal elements, the maximum value is 0.04. Clearly, the MAC values being close to one along the diagonal and close to zero among the off-diagonal elements indicate a strong correlation between the model and test.

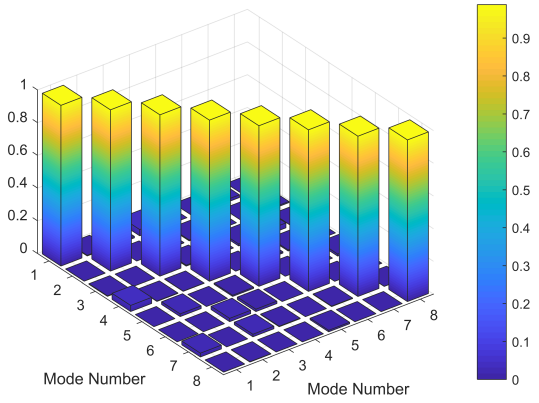

Figure 4.17: MAC bar chart for the cabled plate structure-3

4.2.6 Comparison between cable-harnessed beam-like and plate-like models

Finally, in order to show the importance of developing an equivalent cable-harnessed plate model as one of the major contributions of this work compared to the previously published research on one-dimensional beam theories used for cable-harnessed beam structures, [31], simplified assumptions are made for the structures in this section to implement beam theory assumptions to obtain the FRFs when they are modeled as beam specimen. Mathematical modelling techniques in [31] are used for this comparison where each plate is divided into beam elements along the $x-$direction only.

Also, in order to obtain the FRFs from the cabled beam model, only the $x-$coordinate for the sensing and actuation locations are considered. Figs. 4.18 - 4.20 show the comparison of the presented cabled plate model with that of the cabled beam model for the three structures. The dimensions and material properties of the host beams are considered same as that of the plates used for the three cases. The homogenized cabled beam model is able to incorporate the cable effects in the $x-$direction. Whereas, for the cables attached in the $y-$direction, only the cable inertia effect is added since the beam discretization is made along the $x-$axis and any information regarding the stiffening effects in the $y-$direction is lost in the one-dimensional beam model. Therefore, in addition to the beam model's failure to predict the natural frequencies for modes with dominant curvature along the $y-$axis, other modes predicted by this model are significantly underestimated due to the lack of cable stiffening seen by the beam model, for instance in Figs. 4.19 and 4.20. As a

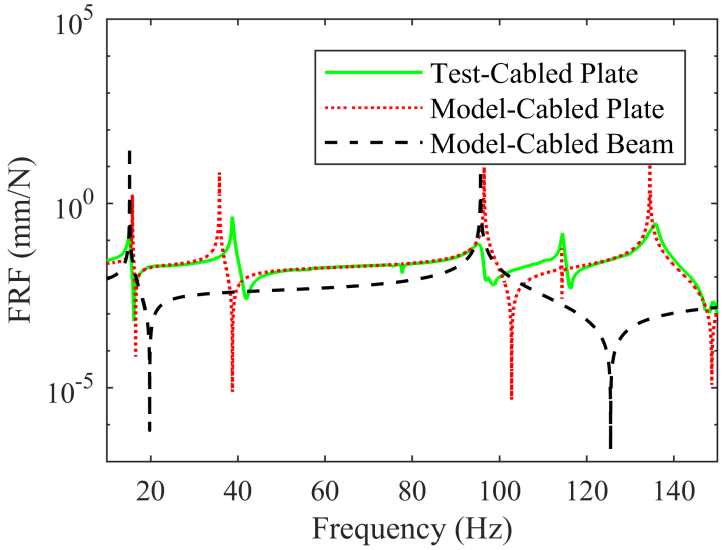

Figure 4.18: FRF comparison of the proposed cabled plate model with an existing cabled beam model of the structure-1 for Test-1

result, the cable mass effects become dominant and the frequencies are underestimated.

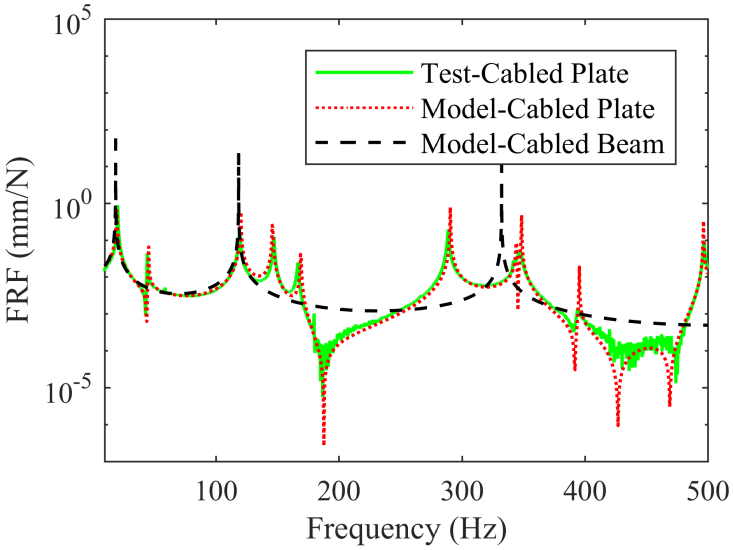

Figure 4.19: FRF comparison of the proposed cabled plate model with an existing cabled beam model of the structure-2 for Test-1

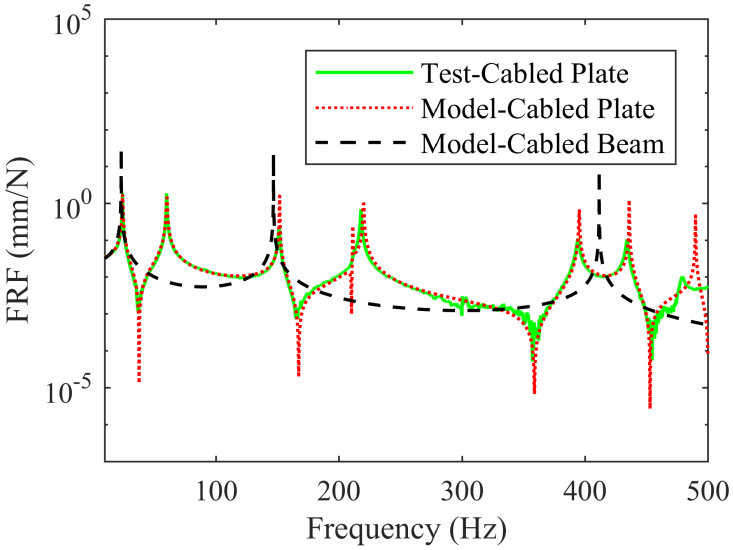

Figure 4.20: FRF comparison of the proposed cabled plate model with an existing cabled beam model of the structure-3 for Test-1

4.3 Summary of the Chapter

In this chapter, a novel analytical technique for modeling the cable-harnessed plate structures was presented followed by the experimental validation. Analytical models with ability to obtain closed-form solutions are preferred due to the deep insights they provide in addition to offering great possibilities for implementations of low-order control algorithms. The analytical formulation was developed using an energy equivalence homogenization technique for cable-harnessed plate structures with cables attached in a parallel configuration. The frequency response functions between model and modal testing experiments were in an excellent agreement for multiple sets of sensing and actuation locations. The experiments were conducted for three different fabricated structures under a clamped-free-free-free boundary. Further, the mode shapes comparisons between model and test were presented and their correlation was shown using MAC analysis.

It is shown that upon the cable attachments, stiffening effects are dominant in some vibration modes while inertia effects in others. In other modes, the inertia and stiffening effects are of equal importance resulting in similar frequencies for these modes compared to the host structure when no cables are attached. The dominance of the stiffening effects of the cables for each mode depends on their major direction of bending with respect to the cable orientations. These observations are consistent between the model and test further indicating the fidelity of the developed method. In addition, the importance of the proposed model was shown by a comparison with an existing cable-harnessed beam model which either fails to predict a majority of the natural frequencies of the system or highly under-estimates them.

Chapter 5

Analytical Modeling of Cable-Harnessed Plates with Cables Wrapped in a Periodic Configuration

In the previous chapter, the analytical modeling for the cable-harnessed plate with parallel configuration was proposed. Although, it was the first ever attempt in proposing an analytical model for a *cable-harnessed plate structure*, the cable pattern chosen was kept simple as a first step. In the current chapter, the cables are attached to the plate in a complex manner, which results in a simple analytical model through an involved mathematical derivation, thereby giving further insights to the dynamics of these structures which have not been discussed in the past. Inspired from the previous works on the cable-harnessed beams by [30, 31], two periodic cable wrapping patterns, namely diagonal and zigzag, are utilized in the current study. Moreover, since the cables are wrapped on a plate structure, the periodicity in two directions is utilized as opposed to only one-direction used in [30, 31]. [1]

The idea of wrapping the cables around the structures should be again emphasized. Since the broad goal of the research on cable-harnessed structures is to understand the change in system dynamics from the attached cables, wrapping the cables on a structure provides us a different perspective altogether as how cable dynamics can affect the host structures. The other common way that researchers study the effect of cables is by attaching the cables in a straight line. Wrapping the cables around a structure is more complex

[1] The research work presented in this chapter has been submitted to the *ASME Journal of Vibration and Acoustics* and the revisions are under review [93].

and gives us deeper insights into a structure. Additionally, in various spacecraft and satellite components, the cables are wrapped and held tightly around the host structure which motivates us further to study the dynamics effect of wrapped cable-harnessed plates. For example, the cables wrapped around a fuel propellent tank was earlier shown in Fig. 1.2.

The chapter is organized as follows: Firstly, the analytical model for the cable-harnessed plate with periodically wrapped pattern is mathematically formulated. The governing equations of motion for both the patterns are obtained. The model results are then analyzed using frequency response functions and are compared using finite element (FE) simulations. Different boundary conditions and multiple cases of patterns are chosen for the FRF analysis. Finally, a detailed parametric analysis is presented by varying cable parameters and pattern parameters in order to study their effects on system dynamics.

5.1 Analytical modeling of periodically wrapped cable-harnessed plates

This section presents the system description, model assumptions, analytical formulation, and further insights into the presented continuum model. The mathematical model is developed using an energy-equivalence homogenization method. This method provides a strong tool to formulate and analyze complex structures and has been successfully used to solve various other dynamics problems in the past [49, 94, 53]. Using the periodicity conditions within a structure, this method aids in obtaining a simplified mathematical model that provides the possibility of a closed-form solution and additional insights into a problem compared to a numerical method. In the current modeling approach, the homogenization method is applied to a cable-harnessed structure that results in an energy-equivalent continuum model. The approach is similar to that applied in Chapter 4. For this purpose, the strain and kinetic energy of a repeated fundamental element are first obtained. Using these energy expressions, the areal energy densities are calculated which are assumed to be a good representative of energy per unit area of an equivalent homogenized continuum plate structure for a large number of fundamental elements. Using the total homogenized strain and kinetic energy of the system, the governing EOM is obtained in the transverse coordinate of motion.

The system consists of a thin rectangular plate with mounted cable harness wrapped in periodic patterns as shown in Fig. 5.1. Two cable wrapping patterns namely zigzag and diagonal are considered. A fundamental element of these patterns as shown in Figs. 5.1(b) and 5.1(d), is defined as the building block of the structure which forms the entire

cable-harnessed plate when repeated in both the orthogonal directions. The global coordinate system (x, y, z) corresponds to the entire system and the local coordinates (η, ξ, z) corresponds to a fundamental element. The dimensions of the plate are $a \times b \times h$ and that of the fundamental elements are $L_1 \times L_2 \times h$. As also mentioned later, the plate is modeled using classical plate theory and hence, the thickness, h, is assumed considerably smaller than the other two dimensions. For a higher thickness plate structure, the host would have to be modeled using a more advanced plate theory that assumes shear deformation effects in the transverse direction, for example Mindlin plate theory. Further, the size of the fundamental element is dependent on the number of fundamental elements in each row (m) and the number of rows (n) which also determines the wrapping angle θ in the system. In Figs. 5.1(a) and (c), the cables are wrapped along the $x-$direction in the zigzag and diagonal pattern, respectively, with $m = 3$ and $n = 5$.

For the zigzag pattern, the wrapping angle can be obtained using the expression:

$$\tan\theta = \frac{2L_2}{L_1} \tag{5.1}$$

Using the definition of L_1 and L_2, this expression can be simplified as

$$\tan\theta = \frac{2bm}{an} \tag{5.2}$$

Similarly, for the diagonal pattern, the wrapping angle can be obtained using

$$\tan\theta = \frac{L_2}{L_1} = \frac{bm}{an} \tag{5.3}$$

Hence, for the same pattern parameters i.e. number of elements per row and number of rows, the wrapping angle in the zigzag pattern is always higher compared to the diagonal pattern.

Further, towards the development of the continuum model, several assumptions are made. The classical plate theory is used for modeling the thin rectangular plate and hence, the plane stress conditions are assumed. The plate's material is assumed to be homogeneous and isotropic. Further, the cable is assumed to have a perfectly circular cross-section which is under a pre-tension T in the equilibrium state of the system. The compression and shear in the plate due to the cable pre-tension is included in the model formulation. During the vibrations, the cable remains in perfect contact with the plate thereby assuming a no-slip condition. Additionally, the axial strain within the cable is

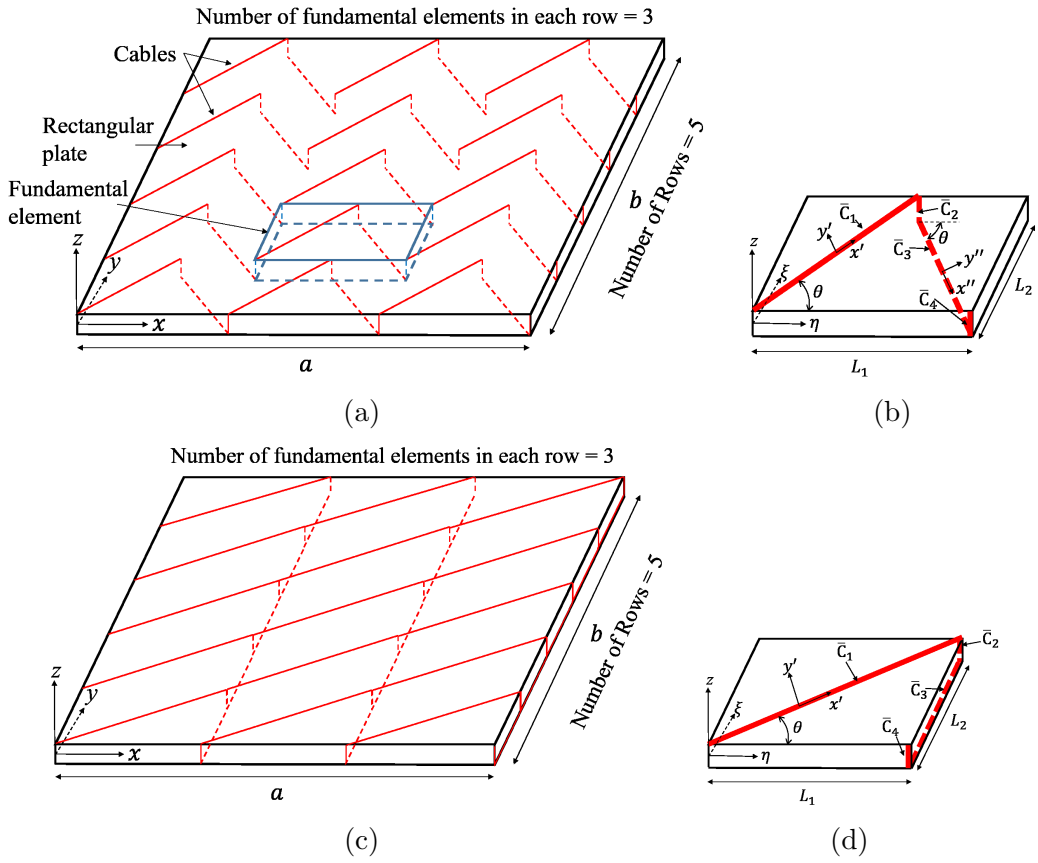

Figure 5.1: Schematic of cable-harnessed plate structure (a) Zigzag pattern, (b) Fundamental element of the zigzag pattern, (c) Diagonal pattern, and (d) Fundamental element of the diagonal pattern

assumed to remain uniform in a given cross-section. In practice, the cables would pass the plate through the holes, which are considered very small for this study. Hence, the change in mass and stiffness effects due to these holes are ignored.

Similar to Chapter 4, the linear assumed displacement field can be written as:

$$\begin{aligned} u_x &= -z\ w_{,x}(x,y,t) \\ u_y &= -z\ w_{,y}(x,y,t) \\ u_z &= w(x,y,t) \end{aligned} \tag{5.4}$$

where $w(x,y,t)$ is a small transverse displacement and the subscripts after the commas

indicate the partial derivatives in space.

The higher-order Green-Lagrange strain tensor is used to obtain the strain-displacement relations which can be written in a rectangular component form as

$$\varepsilon_{ij}^{(2)} = \frac{1}{2}\left[u_{i,j} + u_{j,i} + \ u_{m,i}u_{m,j}\right], \quad i,j = x,y,z \tag{5.5}$$

Using this definition, the non-zero component of the strain tensor can be obtained using Eq. 5.4 as

$$\begin{aligned}
\varepsilon_{xx}^{(2)} &= \ -z\ w_{,xx} + \frac{1}{2}(z^2 w_{,xx}^{\,2} + z^2 w_{,xy}^{\,2} + w_{,x}^{\,2}) \\
\varepsilon_{yy}^{(2)} &= \ -z\ w_{,yy} + \frac{1}{2}(z^2 w_{,xy}^{\,2} + z^2 w_{,yy}^{\,2} + w_{,y}^{\,2}) \\
\varepsilon_{xy}^{(2)} &= -z\ w_{,xy} + \frac{1}{2}\left(z^2 w_{,xx}\, w_{,xy} + z^2 w_{,yy}\, w_{,xy} + w_{,x}\, w_{,y}\right)
\end{aligned} \tag{5.6}$$

Here, $\varepsilon_{xx}^{(2)}$, $\varepsilon_{yy}^{(2)}$ represents the normal bending strain in the x and y direction, respectively, and $\varepsilon_{xy}^{(2)}$ is the shear strain in the $x-y$ plane.

5.1.1 Cable strain energy

To calculate the strain energy of the cable within a fundamental element, the cable is classified into four straight segments as shown in Figs. 5.1(b) and 5.1(d) for both the patterns;

1. Segment $\bar{C}_1$ on the top face,
2. Segment $\bar{C}_2$ on the rear vertical face,
3. Segment $\bar{C}_3$ on the bottom face,
4. Segment $\bar{C}_4$ on the front vertical face

Further, it should be noted that for the segments $\bar{C}_2$ and $\bar{C}_4$, which are aligned parallel to the $z-$axis, no strain energy will be stored during the vibrations. This is because the plate thickness remains constant during the vibrations and hence, the segments $\bar{C}_2$ and $\bar{C}_4$ do not undergo any deformation. Therefore, the strain energy due to the cable is stored only

in the segments $\bar{C}_1$ and $\bar{C}_3$. Further, it should also be noted that for a similar wrapping angle for both the patterns and similar cable geometric and material parameters, the total axial strain within the segment $\bar{C}_1$ would be equal for both the patterns. However, the axial strain would be different for the cable segment $\bar{C}_3$ because the segment is aligned at an angle with the $\xi-$axis for the zigzag pattern, however for the diagonal pattern, the segment is along the $\xi-$axis.

The strain energy stored within the cable segment $\bar{C}_1$ in an arbitrary fundamental element for both the patterns can be written as

$$(U_c)^{\bar{C}_1} = \int_0^{\frac{L_1'}{\cos\theta}} \int_{A_c} \frac{1}{2} E_c \left(\varepsilon_{c'}\right)^2 dA \; dx' \Bigg|_{z=z_c} \tag{5.7}$$

where $L_1' = L_1/2$ for the zigzag pattern, and $L_1' = L_1$ for the diagonal pattern. Also, E_c is the cables Youngs modulus, A_c is the cable cross-section area, z_c is the z coordinate of the plate-cable interface location i.e. $z_c = h/2$ and $x\prime$ denotes the local coordinate as shown in Figs. 5.1(b) and 5.1(d).

In a dynamic state, the net axial strain $\varepsilon_{c'}$ within the cable is composed of two components: first, the strain at the equilibrium state due to cable pre-tension, and second, the dynamic strain due to the bending vibrations which results in

$$(U_c)^{\bar{C}_1} = \int_0^{\frac{L_1'}{\cos\theta}} \int_{A_c} \frac{1}{2} E_c \left(\frac{T}{E_c A_c} + \varepsilon_{x'x'}\right)^2 dA \; dx\prime \Bigg|_{z=z_c} \tag{5.8}$$

where the dynamic strain component along the $x'-$ direction, $\varepsilon_{x'x'}$, is obtained by using the strain transformation of the in-plane strains present at the top face of the plate during the vibrations as

$$\varepsilon_{x'x'} = \varepsilon^{(2)}_{\eta\eta} \cos^2\theta + \varepsilon^{(2)}_{\xi\xi} \sin^2\theta + 2\; \varepsilon^{(2)}_{\eta\xi} \sin\theta\cos\theta \tag{5.9}$$

Substituting Eq. 5.9 in Eq. 5.8 and transforming the variable x' to η, the strain energy within the cable segment $\bar{C}_1$ can be written as

$$(U_c)^{\bar{C}_1} = \int_0^{L_1'} \int_{A_c} \frac{1}{2} E_c \left(\frac{T}{E_c A_c} + \varepsilon^{(2)}_{\eta\eta} \cos^2\theta + \varepsilon^{(2)}_{\xi\xi} \sin^2\theta + 2\; \varepsilon^{(2)}_{\eta\xi} \sin\theta\cos\theta\right)^2 dA \; \left(\frac{d\eta}{\cos\theta}\right) \Bigg|_{z=z_c} \tag{5.10}$$

Using the strain-displacement relation in Eq. 5.6 in the local coordinates and substituting in Eq. 5.10, the strain energy of the cable segment $\bar{C}_1$ is obtained as

$$(U_c)^{\bar{C}_1} \approx \frac{E_c A_c}{2\cos\theta}\int_0^{L_1'}\Big[C_1 + C_2\,(w_{,\eta\eta})^2 + C_3\,(w_{,\xi\xi})^2 + C_4\,(w_{,\eta\xi})^2 + C_5 w_{,\eta}^2 + C_6 w_{,\xi}^2 \\ - C_7 w_{,\eta\eta} + C_8 w_{,\eta\xi} - C_9 w_{,\xi\xi} + C_{10} w_{,\eta\eta}\, w_{,\eta\xi} + C_{11} w_{,\xi\xi}\, w_{,\eta\xi} + C_{12} w_{,\eta}\, w_{,\xi} + C_{13} w_{,\eta\eta}\, w_{,\xi\xi}\Big] d\eta \tag{5.11}$$

where the coefficients are shown in terms of system parameters in appendix section B.1. Also, during the calculation of this energy expression, the terms higher than the second-order of the displacement and its derivatives are ignored.

For the calculation of the strain energy of the cable segment $\bar{C}_3$ present on the bottom face, the axial strain can be written for both the patterns as

$$\varepsilon_{c''} = \frac{T}{E_c A_c} + \varepsilon_{x''x''}\Big|_{z=-z_c} \tag{5.12}$$

where the x'' axis is shown in Fig. 5.1(b) for the zigzag pattern which is inclined at an angle θ with the horizontal. On the other hand, the segment $\bar{C}_3$ for the diagonal pattern is along the $\xi-$direction. The dynamic strain component for the two patterns is therefore written as

$$\begin{aligned} \text{Zigzag pattern}: &\varepsilon_{x''x''} = \varepsilon^{(2)}_{\eta\eta}\cos^2\theta + \varepsilon^{(2)}_{\xi\xi}\sin^2\theta - 2\,\varepsilon^{(2)}_{\eta\xi}\sin\theta\cos\theta \\ \text{Diagonal pattern}: &\varepsilon_{x''x''} = \varepsilon^{(2)}_{\xi\xi} \end{aligned} \tag{5.13}$$

Substituting the Eq. 5.13 in Eq. 5.12, the axial strain energy of the segment $\bar{C}_3$ in both the patterns is written as

$$(U_c)^{\bar{C}_3}_{zigzag} = \int_{L_1/2}^{L_1}\int_{A_c}\frac{1}{2}E_c\left(\frac{T}{E_c A_c} + \varepsilon^{(2)}_{\eta\eta}\cos^2\theta + \varepsilon^{(2)}_{\xi\xi}\sin^2\theta - 2\,\varepsilon^{(2)}_{\eta\xi}\sin\theta\cos\theta\right)^2 dA\,\left(\frac{d\eta}{\cos\theta}\right)\Big|_{z=-z_c} \tag{5.14}$$

and

$$(U_c)^{\bar{C}_3}_{diagonal} = \int_0^{L_2}\int_{A_c}\frac{1}{2}E_c\left(\frac{T}{E_c A_c} + \varepsilon^{(2)}_{\xi\xi}\right)^2 dA\,d\xi\Big|_{z=-z_c} \tag{5.15}$$

Expanding Eq. 5.14 results in the following expression for the zigzag pattern upon substituting the strain-displacement relationship in the local coordinates from Eq. 5.6:

$$(U_c)^{\bar{C}_3}_{zigzag} \approx \frac{E_c A_c}{2\cos\theta}\int_{L_1/2}^{L_1}\Big[C_1 + C_2\,(w_{,\eta\eta})^2 + C_3\,(w_{,\xi\xi})^2 + C_4\,(w_{,\eta\xi})^2 + C_5 w_{,\eta}^2 + C_6 w_{,\xi}^2$$
$$+ C_7 w_{,\eta\eta} - C_8 w_{,\eta\xi} + C_9 w_{,\xi\xi} - C_{10} w_{,\eta\eta}\, w_{,\eta\xi} - C_{11} w_{,\xi\xi}\, w_{,\eta\xi} - C_{12} w_{,\eta}\, w_{,\xi} + C_{13} w_{,\eta\eta}\, w_{,\xi\xi}\Big] d\eta \tag{5.16}$$

Similarly, the expansion of Eq. 5.15 results in

$$(U_c)^{\bar{C}_3}_{diagonal} \approx \frac{E_c A_c}{2}\int_0^{L_2}\left[C_1 + C_3'\,(w_{,\xi\xi})^2 + C_4'\,(w_{,\eta\xi})^2 + C_6' w_{,\xi}^2 + C_9' w_{,\xi\xi}\right] d\xi \tag{5.17}$$

In the process of evaluation of Eqs. 5.16 and 5.17, the terms higher than the second-order of the displacement and its derivatives were ignored. As well, the coefficients in Eqs. 5.16 and 5.17 are listed in appendix section B.1.

As mentioned earlier, the total strain energy due to the cables within the fundamental element is the summation of the energy in the segments $\bar{C}_1$ and $\bar{C}_3$. Hence, upon the summation of the Eqs. 5.11 and 5.16, the total strain energy of the zigzag pattern fundamental element is written as follows:

$$(U_c)_{zigzag} = \frac{E_c A_c}{2\cos\theta}\Bigg\{\int_0^{\frac{L_1}{2}}\Big[C_1 + C_2\,(w_{,\eta\eta})^2 + C_3\,(w_{,\xi\xi})^2 + C_4\,(w_{,\eta\xi})^2 + C_5 w_{,\eta}^2 + C_6 w_{,\xi}^2$$
$$- C_7 w_{,\eta\eta} + C_8 w_{,\eta\xi} - C_9 w_{,\xi\xi} + C_{10} w_{,\eta\eta}\, w_{,\eta\xi} + C_{11} w_{,\xi\xi}\, w_{,\eta\xi} + C_{12} w_{,\eta}\, w_{,\xi} + C_{13} w_{,\eta\eta}\, w_{,\xi\xi}\Big] d\eta$$
$$+ \int_{\frac{L_1}{2}}^{L_1}\Big[C_1 + C_2\,(w_{,\eta\eta})^2 + C_3\,(w_{,\xi\xi})^2 + C_4\,(w_{,\eta\xi})^2 + C_5 w_{,\eta}^2 + C_6 w_{,\xi}^2$$
$$+ C_7 w_{,\eta\eta} - C_8 w_{,\eta\xi} + C_9 w_{,\xi\xi} - C_{10} w_{,\eta\eta}\, w_{,\eta\xi} - C_{11} w_{,\xi\xi}\, w_{,\eta\xi} - C_{12} w_{,\eta}\, w_{,\xi} + C_{13} w_{,\eta\eta}\, w_{,\xi\xi}\Big] d\eta\Bigg\} \tag{5.18}$$

where the coefficients, C_1 to C_{13}, are expanded in appendix section B.1.

Similarly, the total strain energy stored in the cables within the fundamental element of the diagonal pattern can be written upon the summation of Eqs. 5.11 and 5.17 as

(coefficients listed in appendix section B.1)

$$(U_c)_{diagonal} = \frac{E_c A_c}{2\cos\theta}\int_0^{L_1}\Big[C_1 + C_2\left(w_{,\eta\eta}\right)^2 + C_3\left(w_{,\xi\xi}\right)^2 + C_4\left(w_{,\eta\xi}\right)^2 + C_5 w_{,\eta}^2 + C_6 w_{,\xi}^2$$
$$- C_7 w_{,\eta\eta} + C_8 w_{,\eta\xi} - C_9 w_{,\xi\xi} + C_{10} w_{,\eta\eta}\, w_{,\eta\xi} + C_{11} w_{,\xi\xi}\, w_{,\eta\xi} + C_{12} w_{,\eta}\, w_{,\xi} + C_{13} w_{,\eta\eta}\, w_{,\xi\xi}\Big] d\eta$$
$$+ \frac{E_c A_c}{2}\int_0^{L_2}\left[C_1 + C_3'\left(w_{,\xi\xi}\right)^2 + C_4'\left(w_{,\eta\xi}\right)^2 + C_6' w_{,\xi}^2 + C_9' w_{,\xi\xi}\right] d\xi \quad (5.19)$$

5.1.2 Plate strain energy

The compressive loading on the plate fundamental element due to the cable pre-tension is assumed to result in a uniformly distributed resultant loads per unit length N_x, N_y and N_{xy}. This uniformity is assumed due to the presence of multiple fundamental elements. Here, N_x and N_y are the normal compressive loads in the x and y direction, while N_{xy} is the shear load in the xy plane. The sign convention of the normal loads is considered positive for tension, hence the compressive loads N_x and N_y have a negative magnitude. These loads are assumed to be uniformly distributed over the plate thickness and are expressed in terms of the cable pre-tension and wrapping angle using the free body diagrams of the standalone plate for both the patterns. Also, these loads would be different for both the patterns and hence were derived and written separately. For the zigzag pattern, the loads can be written as

$$\begin{aligned} N_x &= -\frac{nT\cos\theta}{b} \\ N_y &= -\frac{2mT\sin\theta}{a} \\ N_{xy} &= 0 \end{aligned} \quad (5.20)$$

For the diagonal pattern, the loads can be written as:

$$\begin{aligned} N_x &= -\frac{nT\cos\theta}{b} \\ N_y &= -\frac{m\left(T + T\sin\theta\right)}{a} \\ N_{xy} &= -\frac{nT\sin\theta}{b} \end{aligned} \quad (5.21)$$

Further, the total strain energy within a plate fundamental element (under uniform loading) can be written by breaking it down into three components as follows [89]:

1. The strain energy due to the stretching of the middle plane of the plate:

$$U_p^{(1)} = \frac{1}{2hE_p} \int_0^{L_2} \int_0^{L_1} \left\{ N_x^2 + N_y^2 - 2\nu N_x N_y + 2\left(1+\nu\right) N_{xy}^2 \right\} d\eta \; d\xi \tag{5.22}$$

2. The additional strain energy of the plate due to strain produced by compressive and shear load while bending of the plate:

$$U_p^{(2)} = \int_{-\frac{h}{2}}^{\frac{h}{2}} \int_0^{L_2} \int_0^{L_1} \frac{1}{h} \left\{ N_x \varepsilon_x' + N_y \varepsilon_y' + N_{xy} \gamma_{xy}' \right\} d\eta \; d\xi \; dz \tag{5.23}$$

   where ε_x', ε_y', and γ_{xy}' represent the normal and shear strain produced when a plate is bent. It is worth noting that the integration over the thickness is included because the normal compressive and the shear loads are assumed to be uniformly distributed over the thickness of the plate. Also, in the previous equation, the strains can be written as $\varepsilon_x' = \varepsilon_{xx}^{(2)}$, $\varepsilon_y' = \varepsilon_{yy}^{(2)}$, and $\gamma_{xy}' = 2\varepsilon_{xy}^{(2)}$ using Eq. 5.6.

3. The strain energy stored in plate due to the bending deformation of the plate:

$$U_p^{(3)} = \frac{D}{2} \int_0^{L_2} \int_0^{L_1} \left[\left(w_{,\eta\eta} + w_{,\xi\xi} \right)^2 - 2\left(1-\nu\right) \left(w_{,\eta\eta}\, w_{,\xi\xi} - \left(w_{,\eta\xi} \right)^2 \right) \right] \; d\eta \; d\xi \tag{5.24}$$

where $D = E_p h^3 / 12(1-\nu^2)$ is the flexural rigidity of the host plate. E_p, ν are the plate's Young's modulus and Poisson's ratio, respectively. Upon adding the Eqs. 5.22, 5.23, and 5.24, the total strain energy within the fundamental element of the plate results in

$$U_p = U_p^{(1)} + U_p^{(2)} + U_p^{(3)} \tag{5.25}$$

Upon performing the integration over the thickness of the plate in Eq. 5.23, the total

strain energy in plate fundamental element is expressed as

$$U_p = \int_0^{L_2}\int_0^{L_1}\Bigg[\left(\frac{1}{2hE_p}\left(N_x^2+N_y^2-2\nu N_xN_y+2\left(1+\nu\right)N_{xy}^2\right)\right) + \left(\frac{N_x}{2}\left(\frac{h^2}{12}w_{,\eta\eta}^2+\frac{h^2}{12}w_{,\eta\xi}^2+w_{,\eta}^2\right)+\frac{N_y}{2}\left(\frac{h^2}{12}w_{,\xi\xi}^2+\frac{h^2}{12}w_{,\eta\xi}^2+w_{,\xi}^2\right)+ N_{xy}\left(\frac{h^2}{12}w_{,\eta\eta}\,w_{,\eta\xi}+\frac{h^2}{12}w_{,\xi\xi}\,w_{,\eta\xi}+w_{,\eta}\,w_{,\xi}\right)\right)+ \frac{D}{2}\left\{\left(w_{,\eta\eta}+w_{,\xi\xi}\right)^2-2\left(1-\nu\right)\left(w_{,\eta\eta}\,w_{,\xi\xi}-\left(w_{,\eta\xi}\right)^2\right)\right\}\Bigg]d\eta\;d\xi \quad (5.26)$$

Note that the derivatives are taken with respect to the variables of local coordinate system because the strain energy is written for an arbitrary fundamental element.

5.1.3 Kinetic energy

Assuming the rotary inertia to be negligible, the kinetic energy of an arbitrary fundamental element within a cable-harnessed structure can be obtained by summing up the respective kinetic energy of the plate and cable

$$T_{el} = T_p + T_c \quad (5.27)$$

where the kinetic energy within the plate fundamental element is written as

$$T_p = \frac{1}{2}\rho_p h\int_0^{L_2}\int_0^{L_1}\left(\dot{w}\right)^2 d\eta d\xi \quad (5.28)$$

where $(\dot{w}) = \frac{\partial w(\eta,\xi,t)}{\partial t}$ indicates the velocity of the plate at a location (η,ξ), and ρ_p denotes the plate's mass density. The kinetic energy of the cable within the fundamental element would be different for both the patterns. For the zigzag pattern, the kinetic energy can be written by summing up the kinetic energy of each segment (refer Fig. 5.1(b)) within the fundamental element as

$$\left(T_c\right)_{zigzag} = \int_0^{\frac{L_1}{2\cos\theta}}\left(\frac{1}{2}\rho_c A_c\right)\left(\dot{w}\right)^2 dx' + \int_0^h\left(\frac{1}{2}\rho_c A_c\right)\left(\dot{w}\right)^2 dz\Bigg|_{(\eta,\xi)=\left(\frac{L_1}{2},L_2\right)} + \int_0^{\frac{L_1}{2\cos\theta}}\frac{1}{2}\rho_c A_c\left(\dot{w}\right)^2 dx'' + \int_0^h\left(\frac{1}{2}\rho_c A_c\right)\left(\dot{w}\right)^2 dz\Bigg|_{(\eta,\xi)=(L_1,0)} \quad (5.29)$$

where ρ_c denotes the cables mass density. Also, in writing this expression, it has been assumed that the velocity is uniform across the cross-section of the cable during the vibrations. Similarly, the kinetic energy for the diagonal pattern is written as

$$\begin{aligned}(T_c)_{diagonal} = &\int_0^{\frac{L_1}{\cos\theta}} \left(\frac{1}{2}\rho_c A_c\right)(\dot{w})^2\, dx' + \int_0^h \left(\frac{1}{2}\rho_c A_c\right)(\dot{w})^2\, dz\Big|_{(\eta,\xi)=(L_1,0)} \\ &+ \int_0^{L_2} \left(\frac{1}{2}\rho_c A_c\right)(\dot{w})^2\, d\xi\Big|_{\eta=L_1} + \int_0^h \left(\frac{1}{2}\rho_c A_c\right)(\dot{w})^2\, dz\Big|_{(\eta,\xi)=(L_1,0)}\end{aligned} \tag{5.30}$$

The total kinetic energy of a fundamental element can, therefore, be calculated by substituting Eqs. 5.28 and 5.29 in Eq. 5.27 for the zigzag pattern, and Eqs. 5.28 and 5.30 in Eq. 5.27 for the diagonal pattern.

5.1.4 Homogenization

The strain energy and the kinetic energy expressions for the cable and plate within a fundamental element of both the patterns have been calculated in the previous sections. In this section, the homogenization technique is used to calculate the total strain and kinetic energy of the entire cable-harnessed system.

First, the total strain energy within the fundamental element for the cable-harnessed plate is written by summing up the Eqs. 5.26 and 5.18 for the zigzag pattern, and Eqs. 5.26 and 5.19 for the diagonal pattern as

$$\begin{aligned}(U_{el})_{zigzag} &= U_p + (U_c)_{zigzag} \\ (U_{el})_{diagonal} &= U_p + (U_c)_{diagonal}\end{aligned} \tag{5.31}$$

To homogenize the strain energy within the fundamental element, the displacement $w(\eta, \xi, t)$ is approximated by its Taylor's series expansion about the element center $(L_1/2, L_2/2)$. The series is truncated at the second-order and can be expressed as

$$\begin{aligned}w(\eta,\xi,t) \approx \Bigg[&w^* + w^*_{,\eta}\left(\eta - \frac{L_1}{2}\right) + w^*_{,\xi}\left(\xi - \frac{L_2}{2}\right) \\ &+ \frac{1}{2}\left\{w^*_{,\eta\eta}\left(\eta - \frac{L_1}{2}\right)^2 + 2w^*_{,\eta\xi}\left(\eta - \frac{L_1}{2}\right)\left(\xi - \frac{L_2}{2}\right) + w^*_{,\xi\xi}\left(\xi - \frac{L_2}{2}\right)^2\right\}\Bigg]\end{aligned} \tag{5.32}$$

In this equation, the terms with the asterisk represent the displacements or its spatial derivatives evaluated at the element center, for example, $w^* = w(L_1/2, L_2/2, t)$. Substituting Eq. 5.32 in the expanded form of Eq. 5.31, and integrating over the respective limits of integration results in the total strain energy of the fundamental element as a function of time. The total energy upon division by the area of the element results in the areal strain energy density. This energy density is a good representation of the equivalent continuum model for the cable-harnessed plate structure due to the presence of a large number of fundamental elements. Integrating the homogenized energy density over the entire area of the plate, the total strain energy of the system is obtained as

$$\begin{aligned}(U_{sys}) = \frac{1}{2}\int_0^a \int_0^b \Big(& H_1 + H_2 w_{,xx}^2 + H_3 w_{,yy}^2 + H_4 w_{,xy}^2 + H_5 w_{,x}^2 + H_6 w_{,y}^2 - H_7 w_{,xx} + H_8 w_{,xy} \\ & - H_9 w_{,yy} + H_{10} w_{,xx}\, w_{,xy} + H_{11} w_{,yy}\, w_{,xy} + H_{12} w_{,x}\, w_{,y} \\ & + H_{13} w_{,xx}\, w_{,yy} \Big) dxdy \end{aligned} \tag{5.33}$$

where the coefficients are listed in terms of the system parameters in appendix section B.2 for both the patterns.

The kinetic energy of the system is also homogenized by considering the velocity of the fundamental element to be constant and equal to the velocity at the element center i.e. $\dot{w}(L_1/2, L_2/2, t)$. Hence, similar to the strain energy homogenization technique, the total homogenized kinetic energy within a fundamental element can be calculated using Eqs. 5.27 - 5.30 for both the patterns and expressed as

$$T_{sys} = \frac{1}{2}\, K_1 \int_0^b \int_0^a (\dot{w})^2\, dxdy \tag{5.34}$$

where the homogenized coefficient K_1 represents mass per unit area of the system and is obtained for both the patterns as

$$\begin{aligned}(K_1)_{zigzag} &= \left[\rho_p h + \frac{\rho_c A_c}{L_2 \cos\theta} + \frac{2\rho_c A_c h}{L_1 L_2}\right] \\ (K_1)_{diagonal} &= \left[\rho_p h + \frac{\rho_c A_c}{L_2 \cos\theta} + \frac{\rho_c A_c}{L_1} + \frac{2\rho_c A_c h}{L_1 L_2}\right]\end{aligned} \tag{5.35}$$

When the wrapping angle is similar for both the patterns, the homogenized mass per unit area is higher for the diagonal pattern as seen from Eq. 5.35.

5.1.5 Equation of motion

The total strain and kinetic energy of the system have been obtained in the previous section for both the patterns and are represented by Eqs. 5.33 and 5.34, respectively. Further, using Hamilton's principle, the dynamics of the system can be determined by solving the variational problem formulated using the Lagrangian $\mathcal{L} = T_{sys} - U_{sys}$. The governing EOM for the equivalent continuum cable-harnessed plate is therefore obtained as

$$H_2 w_{,xxxx} + H_3 w_{,yyyy} + (H_4 + H_{13})\, w_{,xxyy} + H_{10} w_{,xxxy} + H_{11} w_{,xyyy} + K_1 \ddot{w} = 0 \qquad (5.36)$$

It should be noted that the terms H_{10} and H_{11} are found to be zero for the zigzag pattern (refer the appendix section B.2), whereas non-zero for the diagonal pattern. The corresponding derivative terms $w_{,xxxy}$ and $w_{,xyyy}$ represent the bend-twist coupling in the diagonal pattern. Further, Eq. 5.36 is similar in form to the EOM of a symmetric angle-ply laminated rectangular plate as discussed in Chapter 1 in Eq. 1.12. This implies that harnessing cables on a plate in a diagonal pattern results in a homogenized system that would show characteristics similar to a symmetric angle-ply laminate. On the other hand, when the coefficients H_{10} and H_{11} are zero for the zigzag pattern, the EOM is found similar to a specially orthotropic laminate as discussed in Eq. 1.11.

Further, the terms H_2 and H_3 in Eq. 5.36 represent the bending stiffness of the homogenized system in the x and y direction, respectively, which includes the contribution of both, plate and cables. H_4 is the twisting stiffness, and H_{13} corresponds to the stiffness of coupled-bending in the x and y direction.

It is well established that the bend-twist coupling effects are present when the shear center and centroid of a beam cross-section do not coincide with each other [74]. A similar concept can be applied to a plate element as well. As mentioned earlier, the additional bend-twist coupling stiffness terms H_{10} and H_{11} are present only in the governing PDE of the cabled plate with a diagonal pattern. This happens because the shear center of a fundamental element of the diagonal pattern does not coincide with its centroid due to the absence of twofold axes of symmetry. Whereas, on applying averaging assumptions in the homogenization method for the symmetrical structure of the zigzag pattern as shown in Fig. 5.1(b), the two points coincide. Mathematically, the disappearance of H_{10} and H_{11} for the zigzag pattern lies in the process of homogenizing the fundamental element strain energy when the terms corresponding to C_{10} and C_{11} shown in Eq. 5.18 vanish for the top left and bottom right of the element due to the two inclined symmetric cable segments mounted on the opposite sides of the plate. This results in cancellation of the terms H_{10} and H_{11} for the zigzag pattern and a simpler PDE in which the bend-twist coupling in

absent. In case of the diagonal pattern, there is no anti-symmetric term corresponding to C_{10} and C_{11} in the cable strain energy shown in Eq. 5.19 because the cable segments $\bar{C}_1$ and $\bar{C}_3$ are not symmetrically placed, unlike the zigzag pattern. Hence, the coefficients do not vanish for the diagonal pattern on homogenizing the system's total strain energy resulting in the appearance of the bend-twist coupling.

Further, the boundary conditions for the homogenized system are obtained as

$$w_{,x} = 0 \quad \text{or} \quad M_x + H_7/2 = 0 \quad \text{on edges x=0 and x=a.} \tag{5.37a}$$

$$w = 0 \quad \text{or} \quad M_{x,x} + 2M_{xy,y} = 0 \quad \text{on edges x=0 and x=a.} \tag{5.37b}$$

$$w_{,y} = 0 \quad \text{or} \quad M_y + H_9/2 = 0 \quad \text{on edges y=0 and y=b.} \tag{5.37c}$$

$$w = 0 \quad \text{or} \quad M_{y,y} + 2M_{xy,x} = 0 \quad \text{on edges y=0 and y=b.} \tag{5.37d}$$

where

$$\begin{aligned} M_x &= -\left(H_2 w_{,xx} + \frac{1}{2}\left(H_{10} w_{,xy} + H_{13} w_{,yy} \right) \right), \\ M_y &= -\left(H_3\ w_{,yy} + \frac{1}{2}\left(H_{11} w_{,xy} + H_{13} w_{,xx} \right) \right), \text{and} \\ M_{xy} &= -\frac{1}{4}\left(H_8 + 2H_4 w_{,xy} + H_{10} w_{,xx} + H_{11} w_{,yy} \right). \end{aligned} \tag{5.38}$$

In Eq. 5.37, the geometric and natural boundary conditions are present on the left and right sides, respectively. Also, the expressions M_x, M_y and M_{xy} have a similar form as the bending and twisting moments per unit length in a symmetric angle-ply laminated plate for the diagonal pattern [3] where H_{10} and H_{11} do not vanish. For the zigzag pattern, the boundary conditions are similar to that of a specially orthotropic laminate. In addition, the Kirchhoff boundary conditions valid for a free edge of a bare plate can be easily obtained by substituting the cable parameters to be zero in Eq. 5.37.

Further, it should be noted that since the coefficients H_7 and H_9 are zero for the zigzag pattern, all the boundary conditions are homogeneous equations in Eq. 5.37. In contrast, these coefficients do not vanish for the diagonal pattern and hence, the moment boundary conditions, in particular, are non-homogeneous in nature. Earlier, these non-homogeneous moment boundary conditions were obtained for the *diagonally wrapped cable-harnessed*

beams studied by Martin et al. [31] and likewise, the zigzag pattern had homogeneous equations. The reason behind the occurrence of non-homogeneous terms for the diagonal cable-harnessed plates is the presence of the unequal components of pre-tension force due to cable segments $\bar{C}_1$ and $\bar{C}_3$ along x or y axis for which moment is written. This produces a non-zero moment per unit length of $\frac{H_7}{2} = \frac{Tz_c \cos\theta}{L_2}$ and $\frac{H_9}{2} = \left(\frac{Tz_c}{L_1} - \frac{Tz_c \sin\theta}{L_1}\right)$ in the equilibrium state of the homogenized system. In the case of the zigzag pattern, the pre-tension forces act on the opposite faces with similar magnitude and hence, the total moment due to these forces vanishes upon applying the homogenization technique. To solve the boundary value problem that has a non-homogeneous boundary condition, a transformation of the displacement variable can be made to convert them to homogeneous equations as discussed in Chapter 4.

In this chapter, attention is given to the clamped-free-free-free (CFFF) and all ends simply supported (SSSS) boundary conditions. The solution to the governing differential equation cannot be obtained in closed-form for the diagonal pattern for any of these boundaries due to the presence of H_{10} and H_{11} terms. Hence, the Rayleigh-Ritz method is used to obtain the natural frequencies, mode shapes, and frequency response function. It should be however noted that the closed-form solution for SSSS boundary is possible for the PDE obtained for the zigzag pattern.

5.2 Results and Discussion

In this section, the dynamic effects of the added cable predicted by the analytical model of the cable-harnessed system are discussed. As also shown in the previous chapters, these effects can be visualized using frequency response functions (FRFs) of the system with and without cables. In this section, the FRF results are compared with the simulation results obtained using a commercially available FE software ANSYS. In the ANSYS model, the plate is modeled using the 3-Dimensional 20-Node (SOLID 186) finite elements. On the other hand, the cable is modeled using the LINK 180 elements that are uniaxial elements with three degrees of freedom per node. The connection between the cable and plate was established using CONTA 175 elements that assumed a bonded contact for the no-slip condition.

The system parameters considered for the presented analysis are listed in Table 5.1. The properties are representative of an Aluminum plate and Power Pro cables. The same host structures and cables were also used for experiments on the parallel cable-harnessed plates presented in Chapter 4. In the current numerical study, the results for six cases shown

Table 5.1: Material and geometric properties of the cable-harnessed plate structure

Plate	
Length (a)	0.201 m
Width (b)	0.099 m
Thickness (h)	0.0012 m
Mass density (ρ_p)	2768 Kg/m^3
Young's Modulus (E_p)	68.9 GPa
Poisson's Ratio (ν)	0.33
Cable	
Radius (r_c)	0.55 mm
Young's modulus (E_c)	128 GPa
Mass density (ρ_c)	1400 Kg/m^3
Pretension (T)	3 N

Table 5.2: Different case of cable-harnessed system

Case number	Boundary conditions	Cable wrapping pattern	Wrapping direction
Case-1	CFFF	Zigzag	$x-$axis
Case-2	CFFF	Diagonal	$x-$axis
Case-3	CFFF	Zigzag	$y-$axis
Case-4	CFFF	Diagonal	$y-$axis
Case-5	SSSS	Zigzag	$x-$axis
Case-6	SSSS	Diagonal	$x-$axis

in Table 5.2 are presented which encompass different patterns and boundary conditions. For the CFFF boundary conditions, the clamped edge is always along the edge $x = 0$. The wrapping direction denotes the direction along which the cable is harnessed. It could be either perpendicular to the clamped edge or parallel to it. In the former case, the wrapping direction is the $x-$axis and for the latter, it is the $y-$axis. A schematic of the cable-harnessed structures with wrapping along the $y-$axis is shown in Fig. 5.2. For both the diagonal and zigzag pattern, the FRF analysis is done for a fixed set of pattern parameters. For all the cases, the number of fundamental elements, m, considered in the direction of cable alignment is 3, while the number of rows, n, is considered 5. It should also be noted that while the number of elements and rows remain the same, the cable wrapping angle would be different for both the patterns as shown in Eqs. 5.2 and 5.3. When the wrapping angle is measured with respect to the wrapping direction, the angle would be smaller for the diagonal pattern.

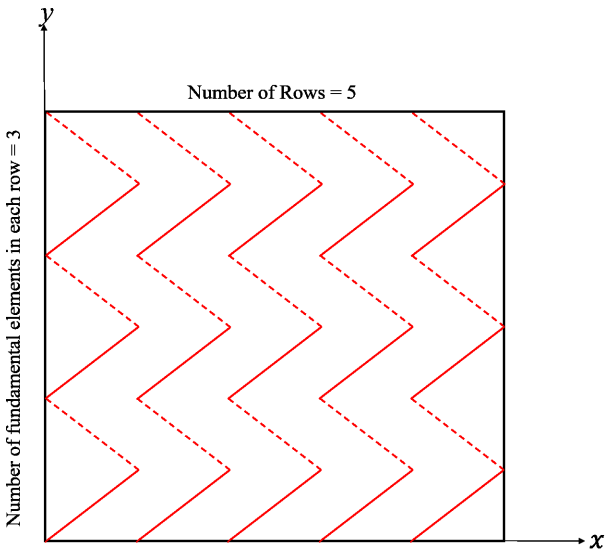

(a)

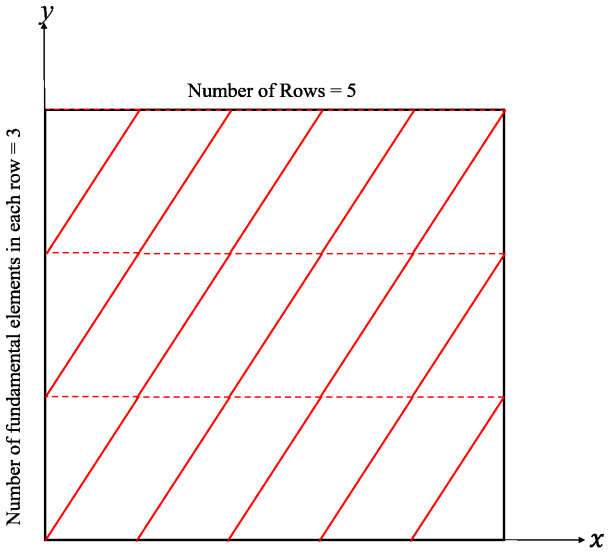

(b)

Figure 5.2: Cable-harnessed structures with cables wrapped along the $y-$axis direction (a) Zigzag pattern, (b) Diagonal pattern; The red lines denote the cables on the host plate structures. The solid lines represent the cables harnessed on the top face and the dashed lines are the cables on the bottom face of the plate.

5.2.1 Frequency response functions

The system dynamics for different cases of cable-harnessed structures listed in Table 5.2 is presented using the FRF plots shown in Figs. 5.3, 5.6, and 5.7. For all the cases, FRF plots are obtained by actuating at $(0.1a, 0.8b)$ and sensing at $(0.4a, 0.8b)$ with respect to the defined global coordinate system. These FRFs show a comparison between the bare plate model, cabled plate homogenized model, and cabled plate ANSYS model. The deviation of the cabled plate FRF from the bare plate FRF shows the change in the dynamic behavior of the system due to cable attachment. It also shows the importance of modeling the cable dynamics in the system. Further, the mode shapes of the cabled plate structure for case-1 are shown in Fig. 5.4, whereas for case-5 are shown in Fig. 5.8. The mode shapes of cases 2-4 and case 6 were found similar to that of case-1 and case-5, respectively, and hence are not shown explicitly. Reference of mode shapes for cases 2-4 would be Fig. 5.4 and similarly, for case 6, the reference would be Fig. 5.8.

Discussion on FRFs for the cases 1 and 2

Firstly, the FRFs for cases 1 and 2 shown in Fig. 5.3 is discussed. For both the patterns, the FRFs obtained from the homogenized model and ANSYS are in good agreement. This can also be observed from the natural frequency comparison shown in Table 5.3. The maximum error in the homogenized model for the zigzag pattern is 2.14%, whereas for the diagonal pattern is 2.12%.

Table 5.3: Natural Frequencies for analytical and FEM cable-harnessed plate model under CFFF boundary conditions (Hz)

Mode	ANSYS, Case-1	HOM, Case-1	Error	ANSYS, Case-2	HOM, Case-2	Error	ANSYS, Case-3	HOM, Case-3	Error	ANSYS, Case-4	HOM, Case-4	Error
1	25.754	25.96	0.81%	26.28	26.52	0.91%	26.34	26.68	1.28%	26.23	26.47	0.91%
2	109.43	111.49	1.89%	107.48	107.82	0.32%	109.27	110.20	0.85%	109.55	110.57	0.93%
3	159.92	161.41	0.93%	163.59	165.36	1.08%	163.45	165.97	1.54%	163.06	164.77	1.05%
4	356.46	363.98	2.11%	350.08	354.45	1.25%	356.75	361.64	1.37%	358.09	362.04	1.10%
5	448.21	453.20	1.11%	457.69	464.28	1.44%	457.81	465.58	1.70%	456.90	462.61	1.25%
6	680.83	694.63	2.03%	677.32	691.69	2.12%	680.54	690.43	1.45%	682.17	695.87	2.01%
7	687.47	702.15	2.14%	699.32	705.47	0.88%	689.16	703.31	2.05%	692.65	702.67	1.45%
8	880.72	892.67	1.36%	898.51	905.91	0.82%	892.47	907.30	1.66%	892.29	905.30	1.46%
9	940.03	957.62	1.87%	946.27	956.16	1.05%	941.54	956.42	1.58%	943.00	959.93	1.80%
10	1135.2	1159.09	2.10%	1138.80	1152.37	1.19%	1143.1	1169.43	2.30%	1147.90	1164.07	1.41%

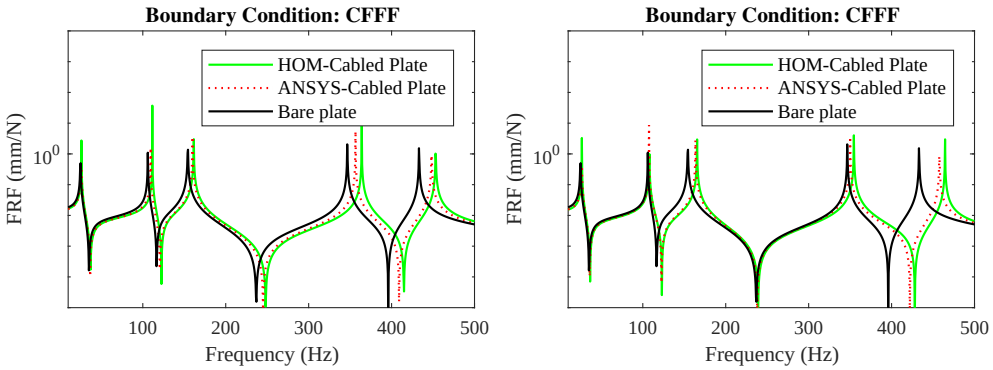

Figure 5.3: Comparison between FRFs obtained from homogenized (HOM) model and finite element (ANSYS) model for cables harnessed along the $x-$axis in (a) zigzag pattern, (b) diagonal pattern under a CFFF boundary. The natural frequency peaks of the cabled plate exhibit a cable stiffening effect (increase in natural frequency with respect to the bare plate). This increase is frequency peaks are well predicted by the ANSYS model of the cabled plate

Additionally, the natural frequencies of the system are observed to increase when cables are harnessed on the bare plate as predicted by both the homogenized and ANSYS models. The frequencies increase because the cable stiffness effects are dominant over its mass effect. Analyzing the first five modes for the cases 1 and 2 in Table 5.3, it is seen that the diagonal pattern has more cable stiffening effect compared to the zigzag pattern for 1st, 3rd, and 5th mode; hence, the natural frequencies are higher for the diagonal pattern for these modes. The reason is attributed to the smaller wrapping angle in the diagonal pattern and dominant bending curvature of corresponding mode shapes in the $x-$direction as shown in Fig. 5.4. As discussed before, the diagonal pattern has smaller wrapping angle θ as compared to the zigzag pattern when the number of elements and the rows is the same. When the wrapping angle gets smaller, the projection of the cable stiffness of the inclined cable segment over the $x-$axis becomes larger resulting in an increased cable stiffening effect. This is also seen from the increased homogenized stiffness in the $x-$direction, H_2.

On the other hand, the zigzag pattern exhibits a higher cable stiffening effect for the 2nd and 4th modes. The corresponding modes have a twist and coupled bending dominant shapes as seen from Fig. 5.4 and therefore, the homogenized stiffness coefficients $(H_4 + H_{13})$ are accountable for the added cable stiffness in these modes. These coefficients vary with the wrapping angle as $(\cos\theta \sin^2\theta)$ since the effect of second-order terms was found

negligible. On plotting the coefficients $(H_4 + H_{13})$ as a function of wrapping angle, a maximum at $\theta_{max} = \tan^{-1}\sqrt{2} \approx 54.7°$ was observed as shown in Fig. 5.5. In other words, twisting stiffness of the structure can be maximized if the cables have a wrapping angle of θ_{max}. Further, the calculation of the wrapping angle for the zigzag and diagonal pattern results in a value of 30.5° and 16.4°, respectively. Referring Fig. 5.5, $(H_4 + H_{13})$ is found larger for the zigzag pattern thereby exhibiting a higher stiffening effect for 2nd and 4th modes.

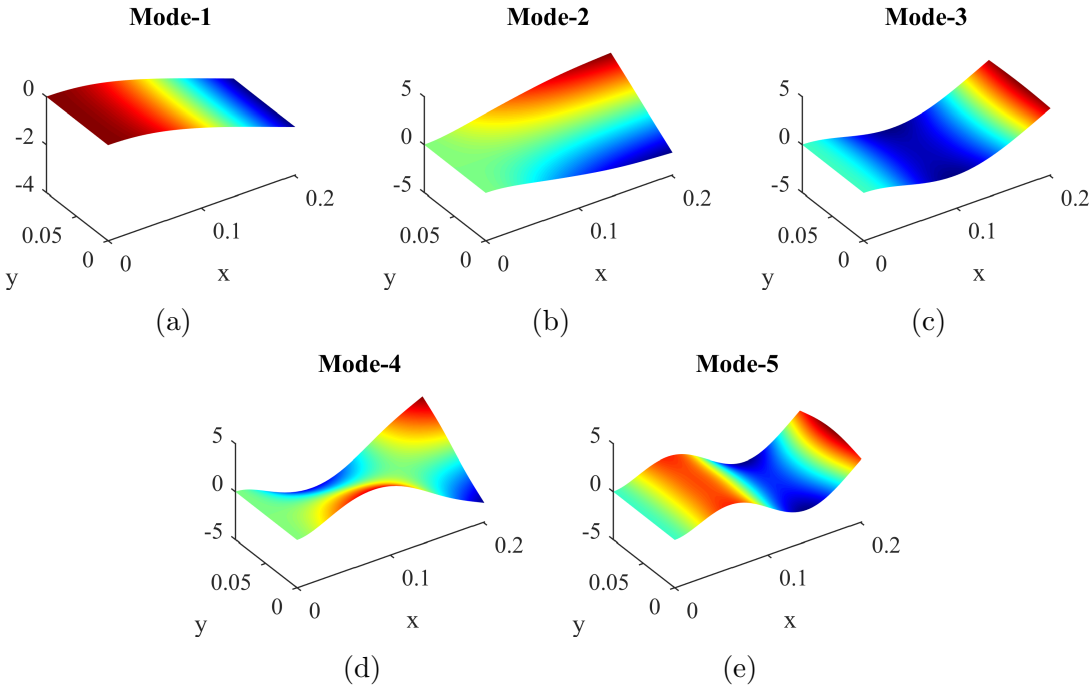

Figure 5.4: Mode shapes obtained from the homogenized model of the cable-harnessed plate for case-1: CFFF boundary with cables harnessed along the $x-$axis in a zigzag pattern. The first, third and fifth mode shapes have a bending dominant curvature in the x-axis direction. The second mode is a twist/torsional shape, and the fourth mode is a coupled bend-twist mode.

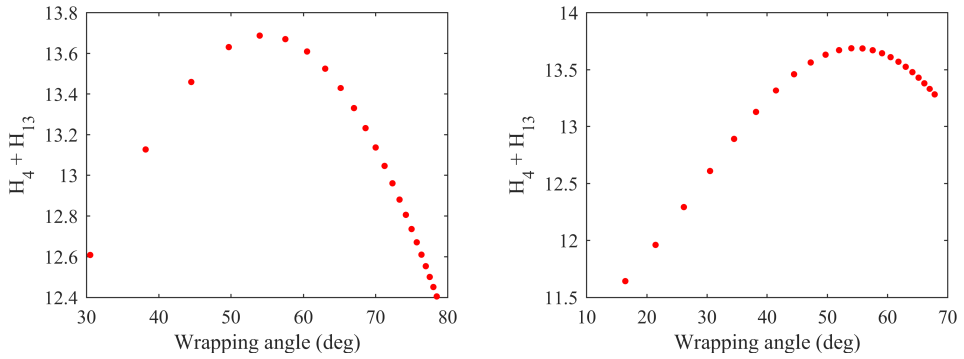

Figure 5.5: Variation of $(H_4 + H_{13})$ as a function of wrapping angle for (a) zigzag pattern, (b) diagonal pattern

Discussion on FRFs for the cases 3 and 4

The FRFs for cases 3 and 4 with cable wrapping along the $y-$axis is shown in Fig. 5.6. For these cases, the wrapping angle is measured with respect to the $y-$axis (wrapping direction). Hence, with an increase in the wrapping angle, the cable stiffening effects would increase in the $x-$direction. This is in contrast to cases 1 and 2 where the increase in wrapping angle decreased the cable stiffening in the $x-$direction. Therefore, the zigzag pattern in case-3, which has a higher wrapping angle for the same number of elements exhibits higher natural frequencies for 1st, 3rd, and 5th mode compared to the diagonal pattern in case-4. It should be noted that the corresponding mode shapes have dominant bending curvature in the $x-$direction as shown in Fig. 5.4.

Additionally, the frequencies for modes 2 and 4 are found to be higher for the diagonal pattern (case-4) compared to the zigzag pattern (case-3). Similar to the previous cases, the reason is attributed to their twist dominant and coupled bending mode shapes; however, in the cases 3 and 4, the wrapping angle is 67.7° for the zigzag and 50.7° for the diagonal pattern for the considered pattern parameters. In addition to the wrapping angle closer to θ_{max}, the stiffness coefficient $(H_4 + H_{13})$ is found higher for the diagonal pattern thereby resulting in higher frequencies compared to the zigzag pattern. It should be noted that in general, the higher natural frequency between the two patterns for the 2nd and 4th mode would depend on the plates aspect ratio and the pattern parameters that decide the wrapping angle.

Discussion on FRFs for the cases 5 and 6

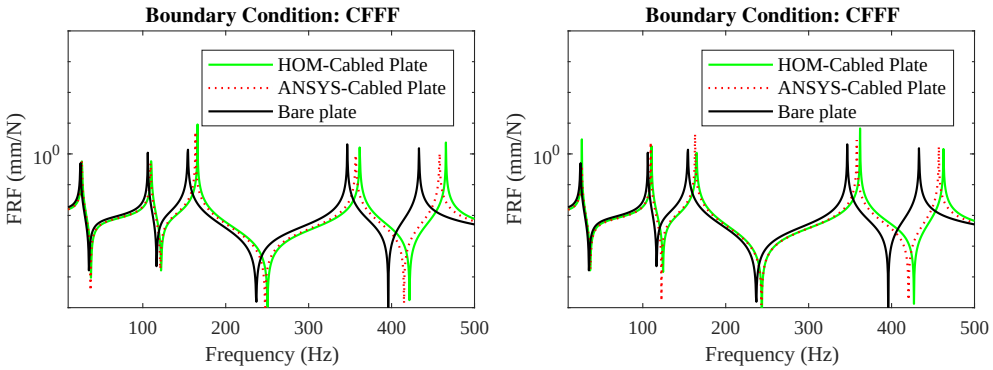

Figure 5.6: Comparison between FRFs obtained from homogenized (HOM) model and finite element (ANSYS) model for cables harnessed along the $y-$axis in (a) zigzag pattern, (b) diagonal pattern under a CFFF boundary

The discussion related to the stiffening effects in cases 1-4 had their reasoning associated with the mode shapes and hence, the boundary conditions play an important role in determining the effects of the cable harness. Therefore, an SSSS boundary is studied in cases 5 and 6 for both patterns with corresponding FRFs presented in Fig. 5.7 and natural frequencies listed in Table 5.4. Clearly, the FRFs for the first six vibration modes obtained from the homogenized model of the cabled plate match well with the ANSYS model.

For SSSS boundary, modes can be represented as (p,q) where p and q are the numbers of half-sine waves in the x and y directions, respectively. Fig. 5.7 shows a noticeable stiffening effect for Mode 3 (3,1) and Mode 6 (4,1) which can be seen by their increased frequency with respect to the bare plate. The Mode (4,1) appears as the Mode 5 for a bare plate; however, on attaching cables, the frequency of the mode increases so much that it becomes higher than mode (2,2) for the bare plate,also highlighted in Table 5.4. In contrast to the first five mode shapes of the CFFF boundary, the modes from SSSS boundary have a dominant bending curvature in both x and y axis. Analytically, the added cable stiffness is governed by the coefficients H_2 and H_3; where the former is responsible for adding stiffness in the $x-$direction and the latter is for the $y-$direction. The contribution from each term is dependent on various factors such as the mode shape (determines curvature in both the directions), pattern parameters, and the aspect ratio of the plate (determines the wrapping angle). As a result, the frequencies are higher in the zigzag pattern for the Modes 2 and 3, whereas, they are higher for the diagonal pattern in Modes 1, 4, 5, and 6.

For all these cases, the homogenized model is found to marginally over-predict the

Table 5.4: Natural Frequencies for analytical and FEM cable-harnessed plate model under SSSS boundary conditions (Hz)

Mode number (p,q)	ANSYS, Case-5	HOM, Case-5	Error	ANSYS, Case-6	HOM, Case-6	Error
1 (1,1)	365.76	369.78	1.10%	366.34	370.02	1.00%
2 (2,1)	590.40	597.72	1.24%	586.20	591.60	0.92%
3 (3,1)	962.06	972.36	1.07%	959.88	966.82	0.72%
4 (1,2)	1235.20	1246.58	0.92%	1248.80	1263.59	1.18%
5 (2,2)*	1461.20	1479.13	1.23%	1462.20	1480.09	1.22%
6 (4,1)*	1480.60	1494.11	0.91%	1482.90	1495.17	0.83%
7 (3,2)	1835.40	1861.43	1.42%	1813.30	1846.71	1.84%
8 (5,1)	2145.40	2163.64	0.85%	2156.10	2175.81	0.91%
9 (4,2)	2356.10	2390.88	1.48%	2341.30	2366.55	1.08%
10 (1,3)	2680.90	2706.99	0.97%	2714.70	2753.85	1.44%

*The mode 5 of the bare plate has the mode shape of the form (4,1) which switches to mode 6 of the cabled plate. Also, mode 6 of the bare plate has the shape (2,2) and switches to mode 5 of the cabled plate.

frequencies compared to the FE model. It is due to the absence of the degrees of freedom in the x and y directions that make the homogenized model inherently stiffer. However, the significance of the homogenized model can be highlighted when compared either with an ad hoc modeling technique which includes only cable inertia effects (that would always decrease frequencies on attaching cables) or no cable effects whatsoever. The proposed model shows the importance of modeling the cables stiffness and mass effects which result in an accurate prediction of the system dynamics.

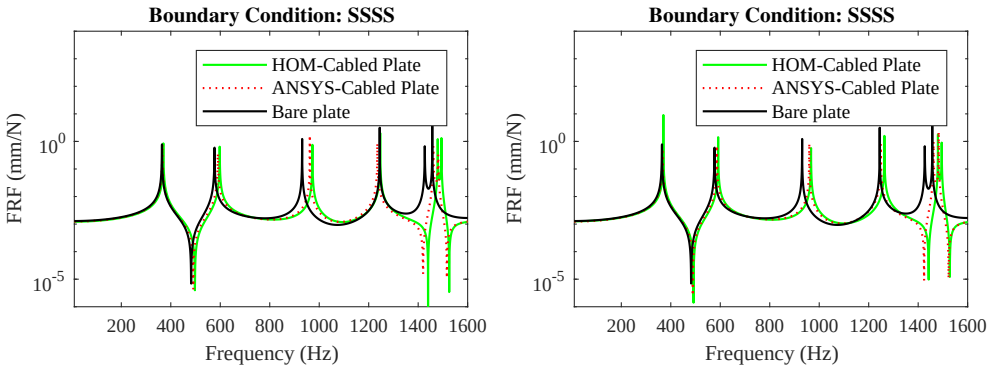

(a) (b)

Figure 5.7: Comparison between FRFs obtained from homogenized (HOM) model and finite element (ANSYS) model for cables harnessed along the $x-$axis in (a) zigzag pattern, (b) diagonal pattern under an SSSS boundary

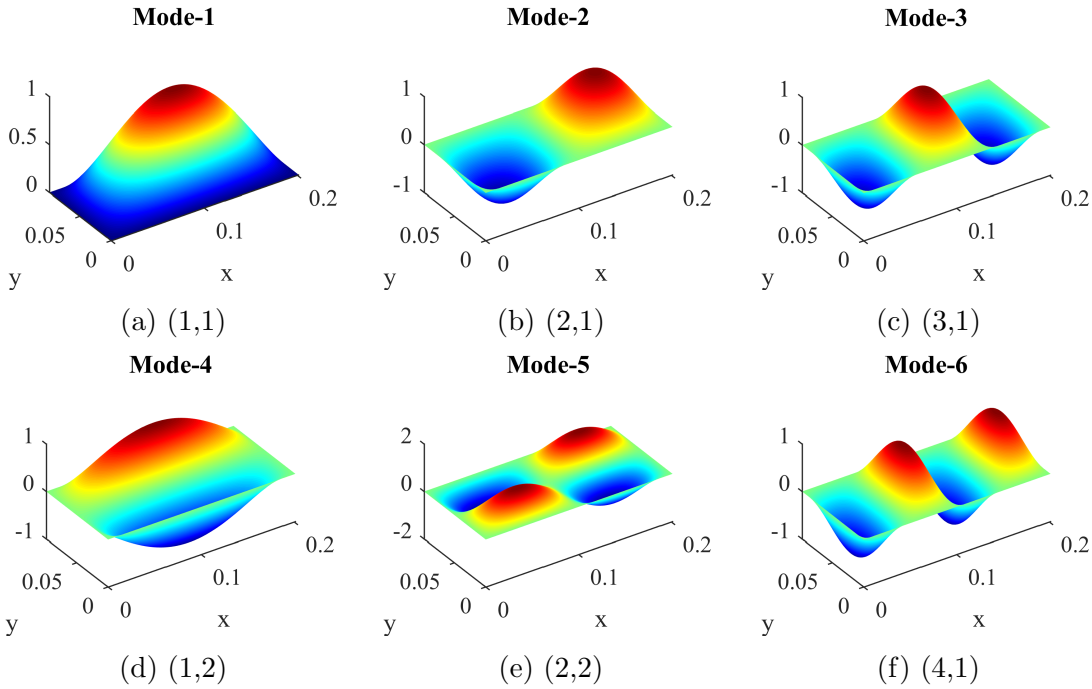

(a) (1,1) (b) (2,1) (c) (3,1)

(d) (1,2) (e) (2,2) (f) (4,1)

Figure 5.8: Mode shapes obtained from the homogenized model of the cable-harnessed plate for case-5: SSSS boundary with cables harnessed along the $x-$axis in a zigzag pattern

A general comparison with the parallel cabled plate presented in Chapter 4

A comparison of the dynamic effects of the wrapped cabled plate structures can also be done with the structures that have cables attached in parallel configuration studied in the previous chapter. Mathematically, the governing PDE for the zigzag pattern is similar to that for the parallel configuration (Eq. 4.22), however, the diagonal pattern has two additional terms as discussed in the Section 5.1.5. Although the form of the PDE is similar for the zigzag and parallel cable-harnessed plate, the contribution of the cable strain energy is quite different. For example, when the same number of cables are harnessed along the $x-$axis, the frequencies of the bending modes with dominant curvature in $y-$direction in the parallel cabled plate tends to be lower. This is because the cable stiffening for parallel cables along $x-$direction does not contribute to increasing bending stiffness in the $y-$direction. Whereas, the system is stiffened in the $y-$direction for the wrapped patterns due to the cable stiffness component of the inclined segments. Similarly, the cable strain energy does not contribute towards the twisting and coupled-bending stiffness corresponding to H_4 and H_{13} in the parallel cabled plate. However, the contribution of

cable stiffness is highlighted in these coefficients for the wrapped patterns.

Discussion on the possibility to obtain an optimal pattern such that cables have minimal dynamic impact

It is interesting to draw a general comparison between different cable harness patterns and how their dynamics are affected in a general engineering case compared to the bare plate. For this comparison, a CFFF boundary condition with 20 parallel cables is chosen for a parallel cabled plate structure, and $n = 20$, $m = 5$ for zigzag and diagonal patterns, harnessed along the $x-$direction, with similar cable and host plate parameters. Also, because the cable stiffening effect is of most concern, it is assumed that the cable mass effect is almost negligible. Now, if a design engineer is interested in considering the least impact on bending frequencies with y dominant modes, the parallel cabled plate should be chosen over the wrapped patterns because there is no added cable stiffening in the $y-$direction in the former. Similarly, if the least impact on twist mode frequencies is concerned, the parallel cabled plate would still be the best choice because of the absence of any cable segments in an inclined direction that increases the twisting stiffness. However, in the case of bending dominant modes in the $x-$direction, the least impact would be observed in the zigzag pattern because, for the same number of rows and fundamental elements, the zigzag pattern has a higher wrapping angle and lower stiffening in the $x-$direction compared to the diagonal pattern. The parallel cabled plate will have the highest stiffening effect in the $x-$direction. These outcomes can change based on the host and cables material and geometric properties, consideration of dominant cable mass effects, and boundary conditions; however, the proposed modeling technique can provide appropriate solutions and insights to the design engineer to choose an optimal pattern that would minimally affect the dynamics of the system. One of the author's works that caters to the optimal cable placement for minimal impact on dynamics of a *host beam structure* can be found in Ref. [37].

5.2.2 Parametric Analysis

In this section, the effects of cable properties and wrapping pattern parameters on the dynamics of the cable-harnessed structure are discussed. The analysis is carried out for the variations in cable modulus, cross-sectional radius, mass density, number of fundamental elements per unit row, and the number of rows. While analyzing the effects of each parameter, the other parameters are held constant as listed in Table 5.1.

As the system parameters are varied, the variation of natural frequencies is different for different modes as seen later in this section. For the CFFF boundary conditions, the

behavior is found similar for bending dominant modes which are Modes 1, 3, and 5 for the given system parameters. Similarly, the behavior for twist and coupled bending modes-2 and 4 are found to show similar behavior. Hence, to show the change in natural frequencies for each mode of the cabled plate with respect to the bare plate on the same scale, a Normalized Frequency Difference (NFD) is plotted which is defined as $(\omega_{CP}^{(i)} - \omega_{BP}^{(i)})/\omega_{BP}^{(i)}$, where $\omega_{CP}^{(i)}$ and $\omega_{BP}^{(i)}$ denote the natural frequencies of the ith mode of the cabled plate and bare plate, respectively. Since $\omega_{BP}^{(i)}$ does not change on the variation of cable parameters, the changes in NFD are essentially reflected due to $\omega_{CP}^{(i)}$.

Effect of cable parameters

The effect of cable modulus on the system dynamics for the first five vibration modes is shown in Fig. 5.9 for the cases 1-4. Clearly, the cabled plate's natural frequencies increase with the cable modulus because there is a net increase in the total strain energy of the system on increasing cable modulus while the kinetic energy remains unaffected.

The rate of change of the NFD is not necessarily similar. When the variation of NFD for the zigzag pattern shown in Fig. 5.9(a) is considered, the rate of increase is almost same for all the five modes; however, for the diagonal pattern shown in Fig. 5.9(b), it is seen that the frequencies of bending dominant modes increase at a higher rate compared to the twist and coupled bending modes. It is attributed to the small wrapping angle of the diagonal pattern with the $x-$axis resulting in a higher contribution of cable strain energy in the bending dominant modes compared to the zigzag pattern where the contribution is found almost similar for the first five modes.

Similar to the discussion on cases 1 and 2 on the variation of cable's Young's modulus in the previous paragraph, a higher rate of increase in bending dominant frequencies is observed for cable harnessing along the $y-$direction in cases 3 and 4 as well as shown in Figs. 5.9(c) and (d). Likewise, for the SSSS boundaries presented for cases 5 and 6, the natural frequencies are predicted to increase with cable modulus for the first five modes for both the patterns as seen from Figs. 5.10(a) and (b). It should be noted that the mode numbers for SSSS boundary are with respect to the bare plate and hence, Mode-5 presented for SSSS boundary parametric analysis plots represents the mode (4,1).

For both the zigzag and diagonal pattern in Figs. 5.10(a) and (b), NFD increase rate is highest for Mode-5 and is lowest for Mode-4. In Mode-5 (4,1), the curvature of the mode shape is dominant in the $x-$direction and is highest amongst the other four modes. Since the cable is harnessed along the $x-$axis, the contribution of the cable strain energy becomes largest for the mode that has the highest curvature as also seen from the total strain energy term, $H_2 w,_{xx}^2$ in Eq. 5.33. On the other hand, when Mode-4 is considered, where the curvature is dominant along the $y-$axis, the strain energy contribution is not

significantly high because of a large angle between the $y-$axis and the cable segment; hence the additional cable stiffness in the Mode-4 through the term $H_3 w,^2_{yy}$ is not as significant.

Additionally, the homogenized model is seen to agree well with the ANSYS results for the smaller values of cable modulus and begin to diverge as the modulus increases. As the cable modulus increases, it results in an increased coupling between different coordinates of motion. Since only transverse motion is modeled in the homogenized system, it results in errors in frequencies for higher values of cable modulus.

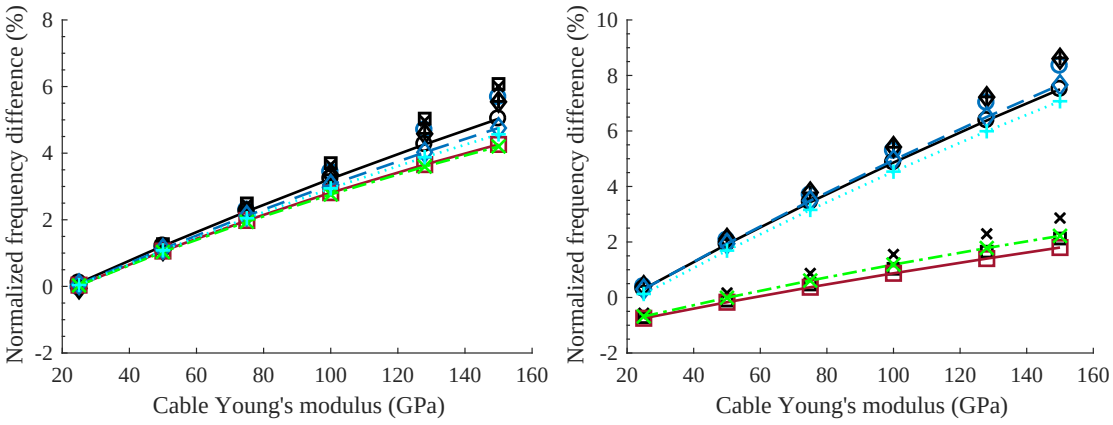

(a) Zigzag pattern along $x-$axis

(b) Diagonal pattern along $x-$axis

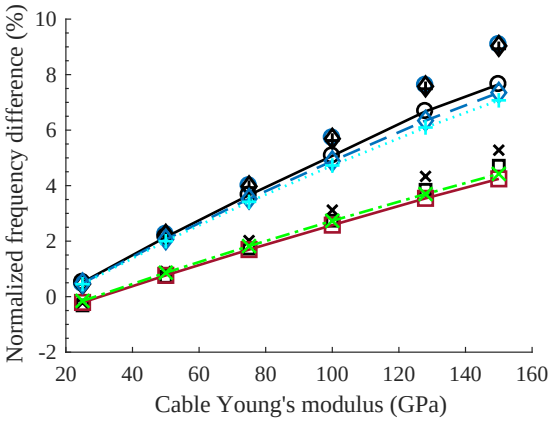

(c) Zigzag pattern along $y-$axis

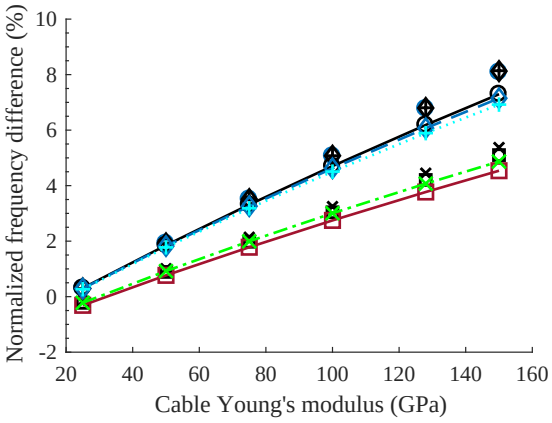

(d) Diagonal pattern along $y-$axis

Figure 5.9: Effect of the change in cable modulus for cases 1-4 (CFFF boundary). Legends: HOM Mode-1, HOM Mode-2, HOM Mode-3, HOM Mode-4, HOM Mode-5, FE Mode-1, FE Mode-2, FE Mode-3, FE Mode-4, FE Mode-5. As the cable's Young's modulus increase, there is an increase in the natural frequency of the cable-harnessed structure. The unequal slope for different modes indicate that the frequency of all the modes do not increase at a similar rate.

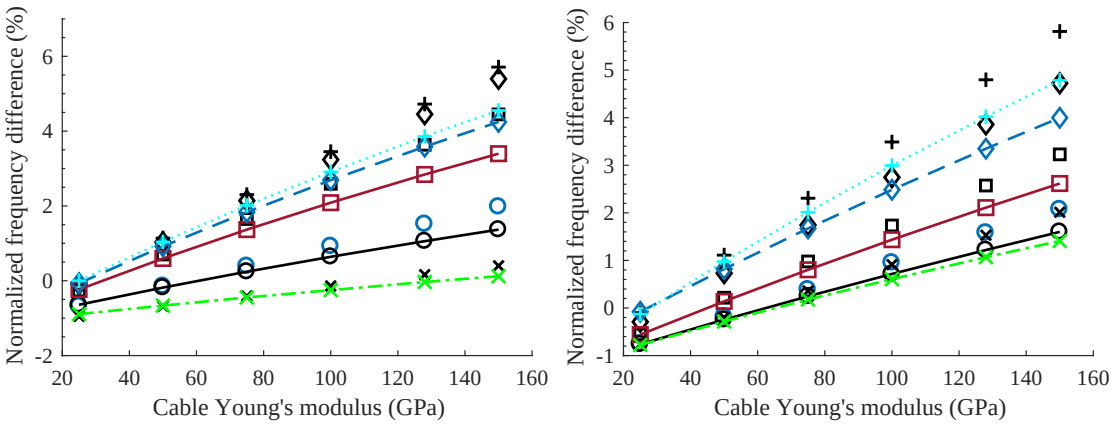

(a) Zigzag pattern along $x-$axis (b) Diagonal pattern along $x-$axis

Figure 5.10: Effect of the change in cable modulus for cases 5-6 (SSSS boundary). Legends: ○ HOM Mode-1, □ HOM Mode-2, ◇ HOM Mode-3, × HOM Mode-4, + HOM Mode-5, —○— FE Mode-1, —□— FE Mode-2, –◇– FE Mode-3, -·×·- FE Mode-4, ···+··· FE Mode-5. As the cable's Young's modulus increase, there is an increase in the natural frequency of the cable-harnessed structure. The unequal slope for different modes indicate that the frequency of all the modes do not increase at a similar rate.

To analyze the effects of cable radius on the system dynamics, NFD is plotted for both the patterns in Figs. 5.11 and 5.12. The natural frequencies of the cabled plate in Fig. 5.11 are shown to increase on increasing the radius. This is because as the cable radius increase, the increase is system stiffness is dominant over the increased cable mass effect. The increase in overall stiffness can also be observed by analyzing the homogenized stiffness coefficients H_2, H_3, H_4, and H_{13} (and H_{10} and H_{11} in case of the diagonal pattern) which are linearly dependent on the cable's cross-sectional area for both the patterns. The model predictions are also a good match with the corresponding ANSYS model.

For the zigzag pattern along the $x-$axis (Fig. 5.11(a)), the frequencies for the first five modes increase with cable radius at a similar rate. However, for the diagonal pattern along the $x-$axis (Fig. 5.11(b)), the rate of change is higher for bending dominant modes compared to the other modes. This observation is in line with the previous discussion on the effect of cable modulus. Since the diagonal pattern has a smaller wrapping angle compared to the zigzag pattern, the contribution of cable stiffness in the dominant bending modes in the $x-$direction is higher. This is also evident from the coefficient H_2 that is dependent on the wrapping angle by the factor of $\cos^3\theta$. Hence, bending dominant mode frequencies increase at a higher rate in the diagonal pattern compared to the zigzag pattern as seen from Figs. 5.11(a) and (b).

The variation of cable radius when cables are wrapped along the $y-$axis is shown in Figs. 5.11(c) and (d) for zigzag and diagonal pattern, respectively. For both the patterns, it is seen that the NFD of the bending dominant modes in the $x-$direction shows a higher rate of increase with cable radius compared to the other two modes. Moreover, the zigzag pattern's bending dominant modes' frequencies increase at a higher rate. For the zigzag pattern, the higher wrapping angle with the $y-$axis compared to the diagonal pattern for similar pattern parameters results in a lower angle of its cable segments with the $x-$axis. This results in a higher contribution of cable stiffening effects in the zigzag pattern and when the cable radius increase, the frequencies of modes with dominant bending in $x-$direction increase at a higher rate.

The variation of NFD with cable radius for the SSSS boundary is shown in Figs. 5.12(a) and (b). As shown, the frequencies of all the modes except Mode-4 of the zigzag pattern increase with the cable radius. As mentioned earlier, the cable radius is responsible for both, increasing the stiffness and inertia due to the cable harness. In the case of Mode-4 in the zigzag pattern, the added stiffness effect due to the increase in cable radius is neutralized by the added inertia effect and hence, the frequency remains almost constant with increasing cable radius. However, for the diagonal pattern, since the cable segment $\bar{C}_3$ in the fundamental element is parallel to the $y-$axis, Mode-4 (with dominant curvature along the $y-$axis) gets a higher contribution of cable stiffness and hence shows an increasing

trend with cable radius. Moreover, Mode 5 is seen to increase at the highest rate for both the patterns due to the large stiffening contribution of the cable owing to the highest curvature along the $x-$axis.

Moreover, the homogenization and ANSYS results are a good match for small values of cable radius but as the cable radius increase, the former seems to over-predict the frequencies. This is because of the increased in-homogeneity in the system owing to the large cable radius thereby causing the inaccuracies in the homogenization method.

Next, the variation of the cable density on the system dynamics is shown in Figs. 5.13 and 5.14 for the six cases. It is expected that on increasing the cable density, the overall mass of the system would increase, and therefore, the natural frequencies would also decrease. Analytically, only the homogenized coefficient K_1 is affected that increases linearly with cable density. This increases the system's kinetic energy without affecting the strain energy and hence, the natural frequencies of the system decrease.

It is also worth noting that the decrease in the natural frequencies occurs at the same rate for all the modes in contrast to the other two cable parameters studied before. However, on a closer inspection, it is observed that the NFD decays at a marginally higher rate for diagonal pattern in Fig. 5.13(b) due to a larger length of cable attached. It results in a higher increased cable mass compared to the zigzag pattern (Fig. 5.13(a)) for similar density increment. Moreover, the trend predicted by the homogenized model matches well with the ANSYS results; however, the homogenized model is expected to marginally over-predict the frequencies for all the modes.

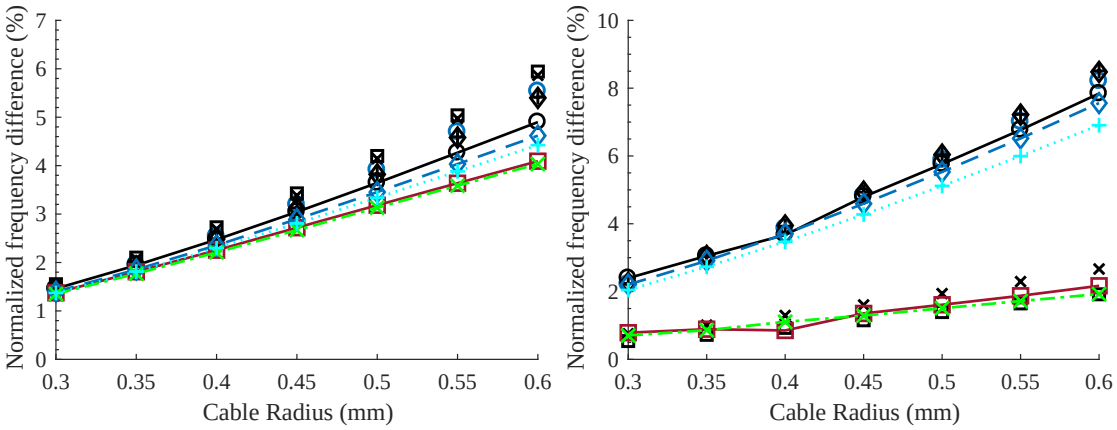

(a) Zigzag pattern along $x-$axis

(b) Diagonal pattern along $x-$axis

(c) Zigzag pattern along $y-$axis

(d) Diagonal pattern along $y-$axis

Figure 5.11: Effect of the change in cable radius for cases 1-4 (CFFF boundary). Legends: HOM Mode-1, HOM Mode-2, HOM Mode-3, HOM Mode-4, HOM Mode-5, FE Mode-1, FE Mode-2, FE Mode-3, FE Mode-4, FE Mode-5

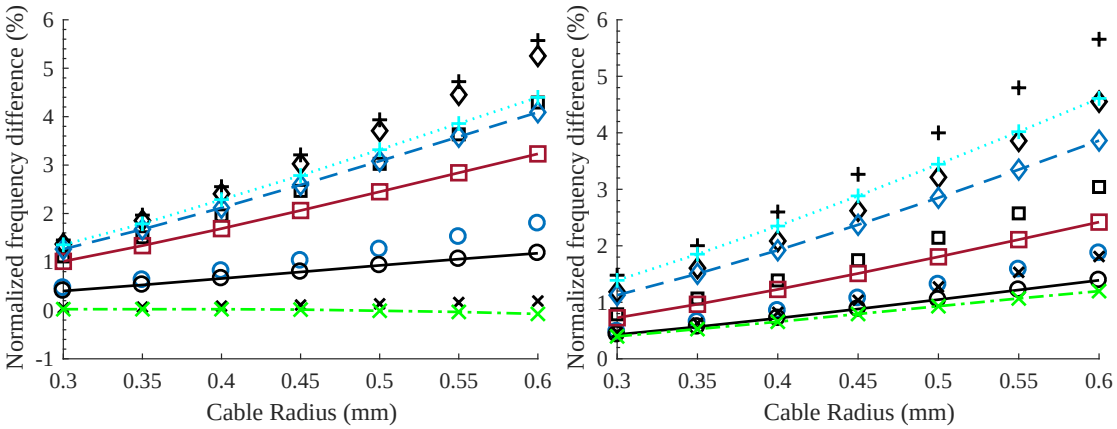

(a) Zigzag pattern along $x-$axis (b) Diagonal pattern along $x-$axis

Figure 5.12: Effect of the change in cable radius for cases 5-6 (SSSS boundary). Legends: HOM Mode-1, HOM Mode-2, HOM Mode-3, HOM Mode-4, HOM Mode-5, FE Mode-1, FE Mode-2, FE Mode-3, FE Mode-4, FE Mode-5

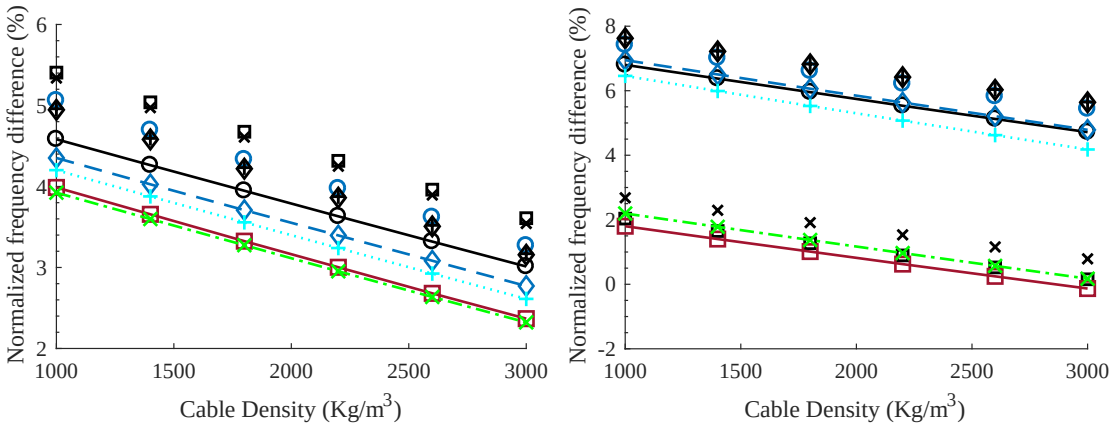

(a) Zigzag pattern along $x-$axis

(b) Diagonal pattern along $x-$axis

(c) Zigzag pattern along $y-$axis

(d) Diagonal pattern along $y-$axis

Figure 5.13: Effect of the change in cable density for cases 1-4 (CFFF boundary). Legends: HOM Mode-1, HOM Mode-2, HOM Mode-3, HOM Mode-4, HOM Mode-5, FE Mode-1, FE Mode-2, FE Mode-3, FE Mode-4, FE Mode-5

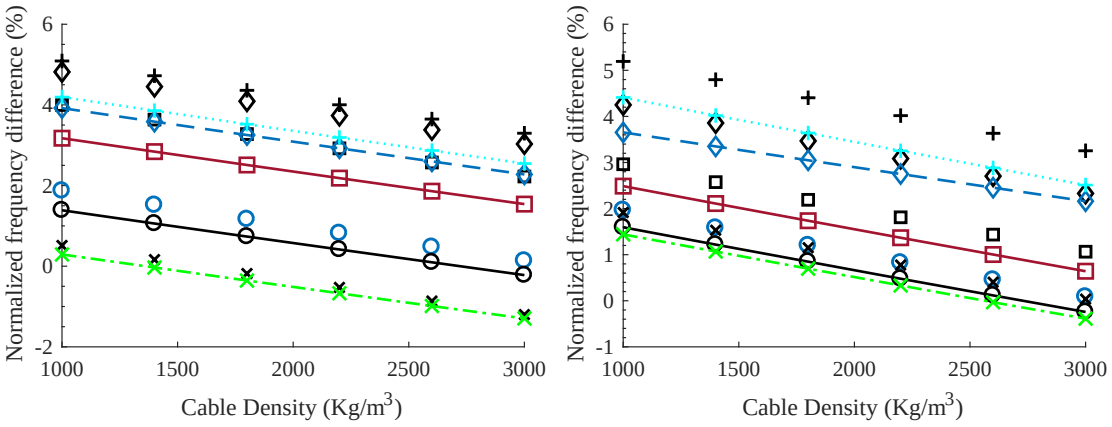

(a) Zigzag pattern along $x-$axis (b) Diagonal pattern along $x-$axis

Figure 5.14: Effect of the change in cable density for cases 5-6 (SSSS boundary). Legends: HOM Mode-1, HOM Mode-2, HOM Mode-3, HOM Mode-4, HOM Mode-5, FE Mode-1, FE Mode-2, FE Mode-3, FE Mode-4, FE Mode-5

Effect of wrapping pattern parameters

Figures 5.15 and 5.16 shows the variation of natural frequencies as a function of the number of fundamental elements per unit row. The frequency change and the trends estimated by the homogenized method matches well with ANSYS. It should be noted that the number of elements is allowed to be positive integers only. Also, with an increase in the number of elements, the wrapping angle with respect to the wrapping axis increases.

Figure 5.15(a) exhibits the variation of cabled plate frequencies for the zigzag pattern wrapped along the $x-$axis. Although the cable stiffening effect is found almost similar for the first five modes for a lower number of elements, it changes for different modes when the number of elements is increased. For the twist and coupled-bending modes (Modes 2 and 4), the cable stiffening effect is higher compared to the bending dominant modes in the $x-$direction. Also, the stiffening effect in Modes 2 and 4 increases at first and then starts to decrease, whereas, for the bending dominant modes, the stiffening effects monotonically decrease as the number of elements is increased. The contribution of the cable strain energy in increasing twist stiffness is low when the cable segments have a small wrapping angle with either x or y axis. Hence, there exists a wrapping angle at which the twisting stiffness becomes maximum. Analytically, it is due to the presence of the term $\cos\theta \sin^2\theta$ in the homogenized twist and coupled-bending stiffness coefficient $(H_4 + H_{13})$ at $\theta_{max} \approx 54.7°$. For the system parameters considered for the zigzag pattern, the maximum frequency for Mode-2 occurs when the number of elements is 7 and that corresponds to a wrapping angle of 54.05°. This is the closest possible wrapping angle to θ_{max} that can be attained because the number of elements can only hold integer values. Also, the decrease in the bending dominant modes frequencies is due to the decreased overall stiffness in the $x-$direction due to the higher wrapping angles as seen from the $\cos^3\theta$ dependency of the coefficient H_2. Moreover, as the number of fundamental elements increases, the cable inertia also increases, but because the stiffness effects of the cable are dominant over its mass effects, the dynamics is governed by the stiffness coefficients.

For the diagonal pattern, the effect of the variation of the number of fundamental elements along the x-axis is shown in Fig. 5.15(b). Similar to the case of the zigzag pattern, it is observed that the frequency of the bending dominant modes decreases with an increasing number of elements due to increasing wrapping angles. On the other hand, Modes 2 and 4 increase with the increase in the number of elements for the range shown in the plot. As discussed later, these plots also show a maximum at a higher number of elements that is not explicitly clear from Fig. 5.15(b). Since these discussions are dependent on the wrapping angle, the trends in these plots could vary when the number of rows in both patterns is changed.

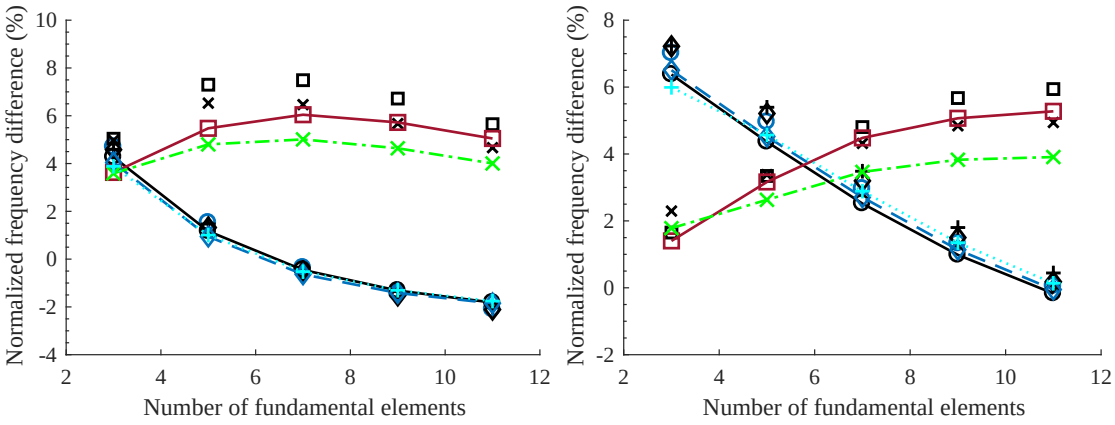

(a) Zigzag pattern along $x-$axis (b) Diagonal pattern along $x-$axis

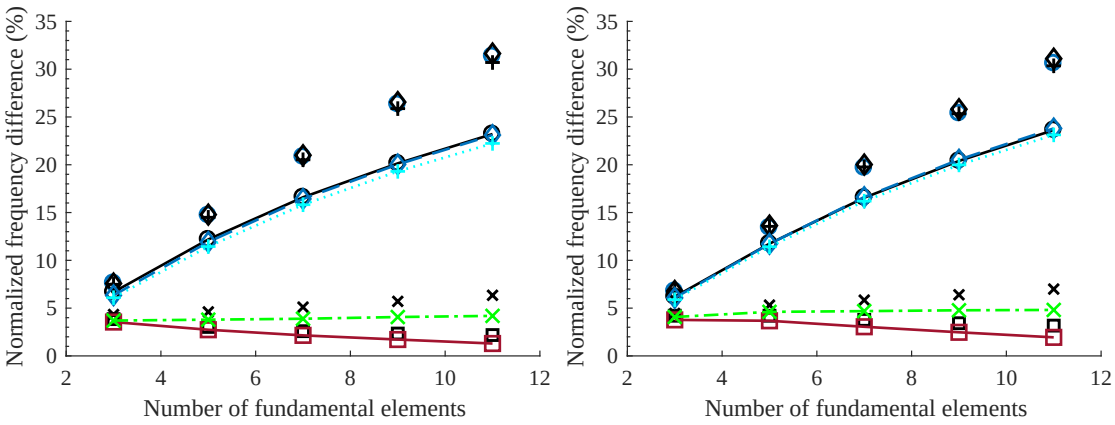

(c) Zigzag pattern along $y-$axis (d) Diagonal pattern along $y-$axis

Figure 5.15: Effect of the change in number of fundamental elements along the wrapping direction for cases 1-4 (CFFF boundary). Legends: ○ HOM Mode-1, □ HOM Mode-2, ◇ HOM Mode-3, × HOM Mode-4, + HOM Mode-5, —○— FE Mode-1, —□— FE Mode-2, –◇– FE Mode-3, -·×·- FE Mode-4, ···+··· FE Mode-5

For the wrapping along the $y-$axis, as shown in Figs. 5.15(c) and (d), the effect on dynamics is found in contrast to the above discussion. For both the patterns, the frequencies of bending dominant modes increase with the number of elements due to the increased wrapping angle with the $y-$axis thereby increasing overall stiffening effect in the $x-$direction. Again, this increase is because the attached cable has a dominant stiffening effect over its mass effect. Also, for the given number of rows, the frequency of the twist

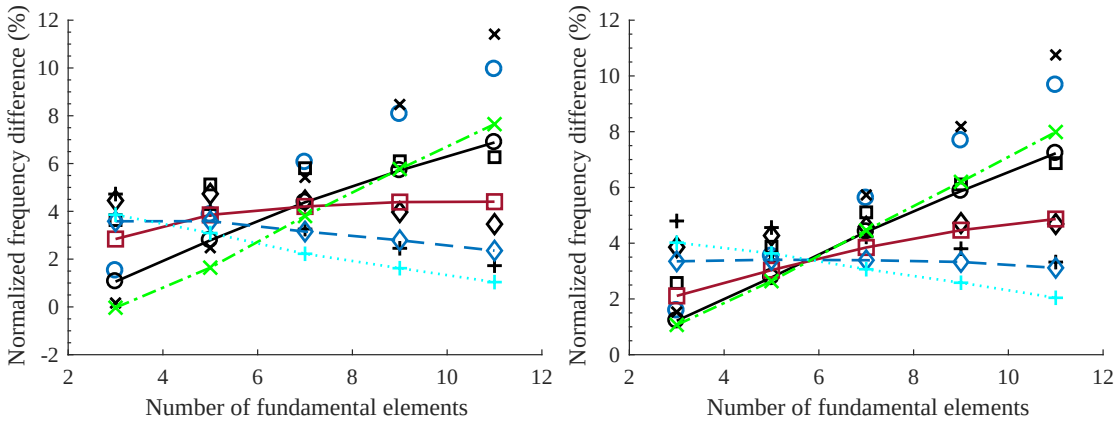

(a) Zigzag pattern along $x-$axis (b) Diagonal pattern along $x-$axis

Figure 5.16: Effect of the change in number of fundamental elements along the wrapping direction for cases 5-6 (SSSS boundary). Legends: HOM Mode-1, HOM Mode-2, HOM Mode-3, HOM Mode-4, HOM Mode-5, FE Mode-1, FE Mode-2, FE Mode-3, FE Mode-4, FE Mode-5

dominant mode (Mode 2) decreases at a slow rate with increasing elements. The Mode 4 frequency is found to remain almost constant with the variation in the number of elements. The observations predicted by proposed model match well with ANSYS results.

With an increase in the number of fundamental elements, Modes-1, 2, and 4 are observed to increase for both the patterns as shown in Fig. 5.16 with Mode-4 increasing at the highest rate while Mode-2 at the least. Moreover, Modes 3 and 5 show a decreasing trend for both the patterns as also estimated by ANSYS results. The highest rate of Mode-4 (with dominant curvature along the $y-$axis) is attributed to the increase of cable stiffening effects in the $y-$direction as the wrapping angle increases with fundamental elements and the inclined cable segments get more aligned with the $y-$axis. A decreasing trend in Modes-3 and 5 is also attributed to a similar reason. Since both these modes have dominant bending curvature along the $x-$axis, the increase in wrapping angle decreases the contribution of the cable stiffness along the $x-$direction, and hence, the frequencies of these modes decrease. The rate of decay is higher for Mode-5 because of a higher curvature along $x-$axis than Mode-3 and hence, a greater cable stiffening loss with an increasing number of fundamental elements.

Figure 5.17 presents the effects of the change in the number of rows on the system dynamics. For the wrapping along the $x-$axis, it is observed that increasing the number

of rows stiffens the modes that are bending dominant along the $x-$axis as shown in Figs. 5.17(a) and (b). This is because the cable stiffening effects are dominant over its inertia effects and the coefficient H_2 increases as a result of the increasing number of rows (that decreases θ). This behavior is seen for both the zigzag and diagonal patterns. In contrast, the Mode 4 frequency remains almost constant, while the Mode-2 frequency decreases slowly on increasing number of rows. The added contribution of the cable stiffness is neutralized by the added cable inertia effects for Mode-4 when the rows are increased. On the other hand, the added cable inertia effects are marginally dominant for Mode-2 when the rows are increased. This behavior is observed when the number of fundamental elements in a row is considered small (3 in this case), but it changes on varying the number of fundamental elements as discussed later.

Next, the effect of increasing the number of rows is discussed when the cable is wrapped along the $y-$axis. The wrapping angle with respect to the $y-$axis decreases with the number of rows and hence, the frequencies of the bending dominant modes in $x-$direction decrease with an increase in the number of rows. This applies to both the zigzag and diagonal patterns shown in Figs. 5.17(c) and (d). Additionally, for the zigzag pattern, the frequencies of Modes 2 and 4 increase with the number of rows, while for the diagonal pattern, a maximum is seen. A maximum is also seen for the zigzag pattern but at a higher number of rows which is discussed later. The reason behind the maximum seen in Fig. 5.17(d) is related to the earlier discussion where the stiffening in the twisting and coupled bending modes are maximized for a particular value of wrapping angle, θ_{max}. In this case, when the number of rows in the diagonal pattern is 7 with three fundamental elements in each row, the wrapping angle with the $y-$axis becomes close to θ_{max}.

The variation of the NFD for cases 5 and 6 for the SSSS boundary is shown in Fig. 5.18. The frequencies of the Modes 1 and 4 decrease on an increasing number of rows while Mode 2 almost remains insensitive for both the patterns. Also, the frequencies of modes 3 and 5 are found to increase. These trends predicted by the homogenization method are verified with the ANSYS simulations very well. The reasons behind these observations are attributed to the decrease of wrapping angle with the number of rows. With a decrease in wrapping angle, the cable stiffening effects become dominant along the $x-$direction, and hence, the Mode-5, which has the highest bending curvature in the $x-$axis amongst the first five modes, shows the highest rate of frequency increase. On the other hand, a steep decrease in the frequency of Mode-4 and Mode-1 with cabled plate frequency becoming less than that of the bare plate for the zigzag pattern is attributed to a large decrease in the cable stiffening along the $y-$direction.

It is also observed from both Figs. 5.16 and 5.18 that when the cable stiffening effects are prominent for modes at either high number of fundamental elements or rows, the

frequencies diverge from the ANSYS results. This is due to the large stiffness contribution of the inhomogeneous component of the system in particular modes thereby showing the limitations of the homogenization approach.

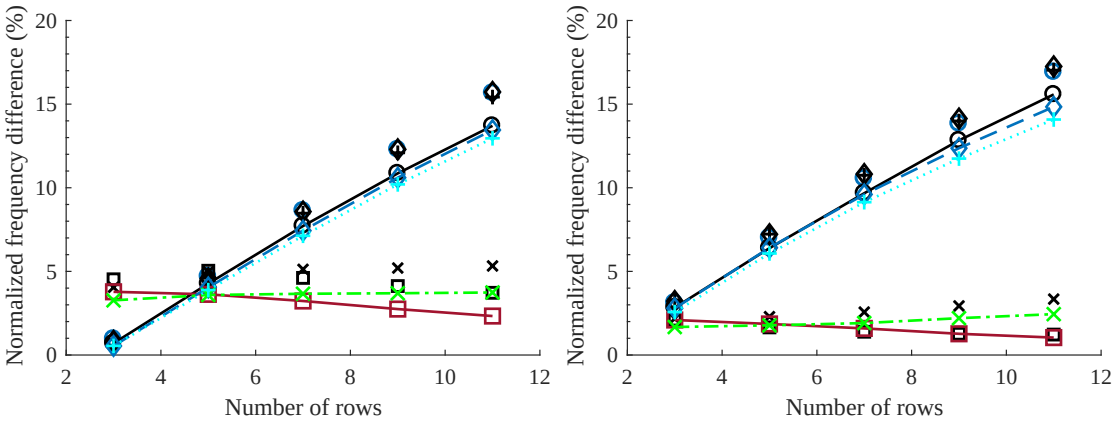

(a) Zigzag pattern along $x-$axis

(b) Diagonal pattern along $x-$axis

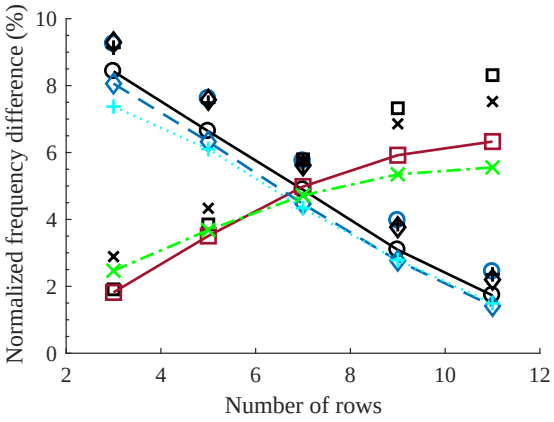

(c) Zigzag pattern along $y-$axis

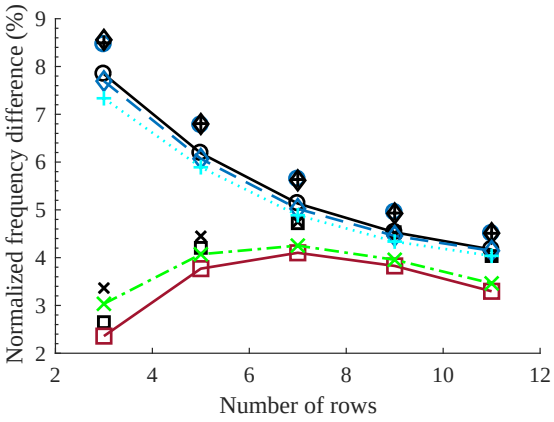

(d) Diagonal pattern along $y-$axis

Figure 5.17: Effect of the change in number of rows for cases 1-4 (CFFF boundary). Legends: HOM Mode-1, HOM Mode-2, HOM Mode-3, HOM Mode-4, HOM Mode-5, FE Mode-1, FE Mode-2, FE Mode-3, FE Mode-4, FE Mode-5

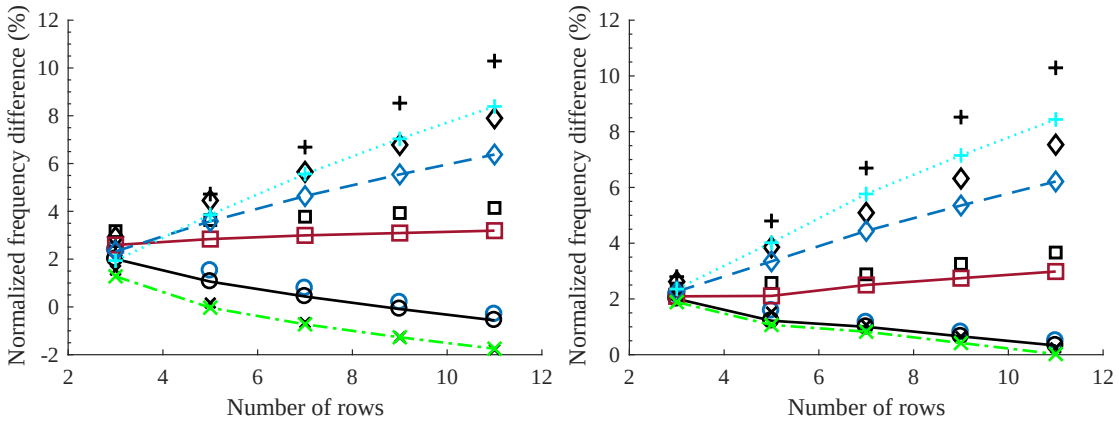

(a) Zigzag pattern along $x-$axis (b) Diagonal pattern along $x-$axis

Figure 5.18: Effect of the change in number of rows for cases 5-6 (SSSS boundary). Legends: HOM Mode-1, HOM Mode-2, HOM Mode-3, HOM Mode-4, HOM Mode-5, FE Mode-1, FE Mode-2, FE Mode-3, FE Mode-4, FE Mode-5

The previous discussion on the effect of the pattern parameters considered the variations of either the number of fundamental elements per unit row or the number of rows. In each of the cases, the other parameter was held fixed. As it was noted earlier, the trends of the natural frequencies of cabled plate modes can depend on the value of the fixed pattern parameter. Therefore, it is important to study the variation of the frequencies as a function of both the pattern parameters. In the following discussion, only the zigzag pattern is considered under a CFFF boundary.

Figure 5.19 shows the plots of the variation in the first five natural frequencies as a function of both fundamental elements per unit row and number of rows for a zigzag pattern wrapped along the $x-$axis. Clearly, the modes with dominant bending in the $x-$direction (Modes 1, 3, and 5) show similar trends in variation, while the twist and coupled-bending modes (Modes 2 and 4) also have similar characteristics. The bending dominant modes show the highest frequency at a large number of rows and a small number of fundamental elements; for this pattern configuration, the wrapping angle is least and hence, the cable stiffening effect is maximum.

The trend shown in Modes 2 and 4 in Fig. 5.15(a) is consistent with the observation from Figs. 5.19(b) and (d) where a maximum is seen when fundamental elements are increased keeping the number of rows fixed. It is however evident from these plots that the optimal

number of elements increase as the fixed number of rows is increased. Moreover, when the number of fixed rows is large, for example, 20, the frequency is seen to increase with the number of elements at a much higher rate compared to that observed for a low number of rows.

Similarly, the trend for Modes 2 and 4 shown in Fig. 5.17(a) is evident from Figs. 5.19(b) and (d). When the number of fundamental elements is low and held fixed, the change in frequencies is minimal for both of these modes for the varying number of rows. However, for a higher number of elements, a local maximum is seen on the variation of the number of rows. The reason for this behavior is attributed to a wrapping angle being smaller than θ_{max} when the number of fundamental elements is low. Now, when the number of rows is increased, the wrapping angle becomes even smaller and the optimal wrapping angle is not encountered. Whereas, for a large number of elements when the wrapping angle is higher than θ_{max}, the decrease of wrapping angle with an increasing number of rows results in a maximum for an optimal number of rows.

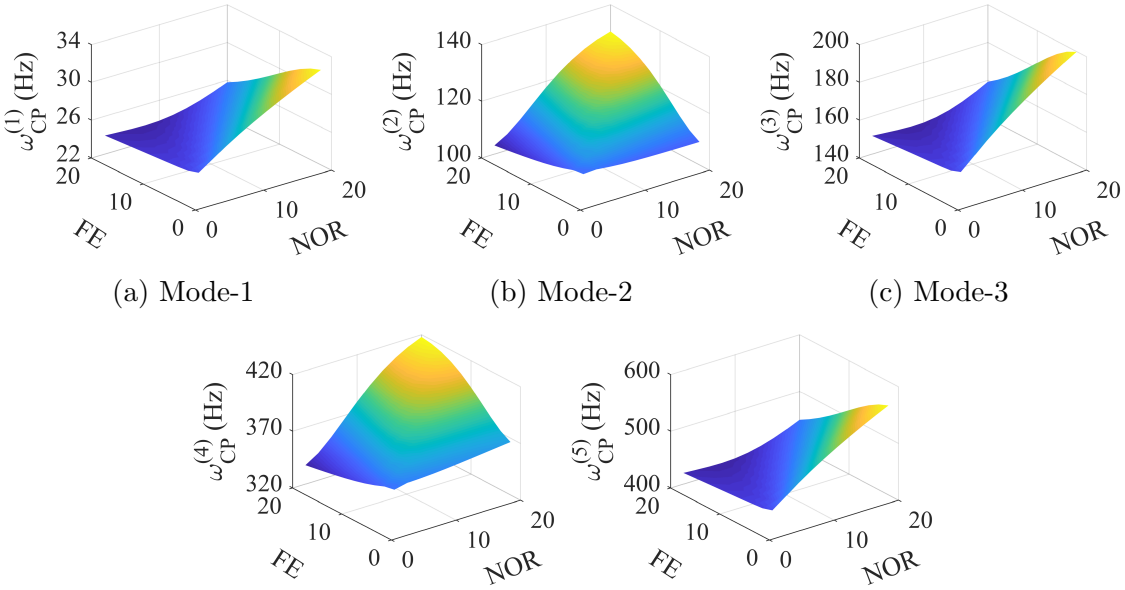

(a) Mode-1 (b) Mode-2 (c) Mode-3

(d) Mode-4 (e) Mode-5

Figure 5.19: Variation of natural frequency for first five modes with a change in the number of fundamental element (FE) along the harness direction and the number of rows (NOR) for the zigzag pattern in $x-$direction under a CFFF boundary

Figure 5.20 shows the similar plots for the zigzag pattern but with cables wrapped along

the $y-$axis. In contrast to the wrapping along the $x-$axis, the frequencies of the bending dominant modes increase on increasing the number of elements per row and decreasing the number of rows as seen from Figs. 5.20(a), (c) and (e). This is because of the increased contribution of the cable stiffness in the $x-$direction due to the smaller angle between the inclined cable segments and the $x-$axis. For the twist dominant modes shown in Figs. 5.20(b) and (d), when the number of fundamental elements is held constant and are small, the natural frequencies show a local maximum with varying number of rows, as also shown in Fig. 5.17(c) up to 11 rows. However, when the number of constantly held elements is increased, it is seen that the natural frequencies monotonically increases for the range of rows shown in Figs. 5.20(b) and (d).

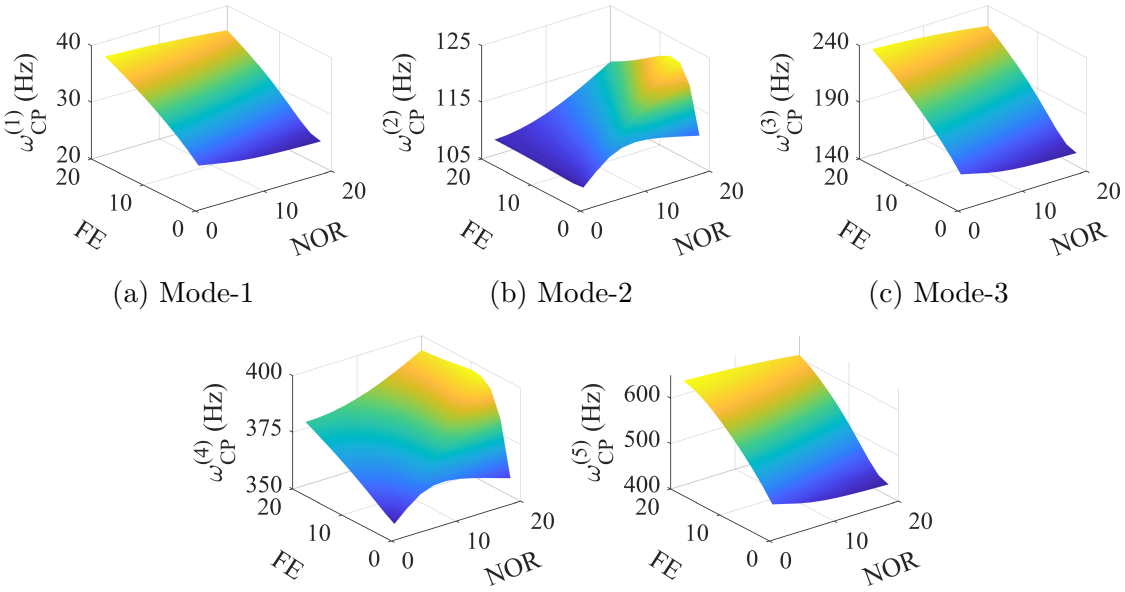

(a) Mode-1 (b) Mode-2 (c) Mode-3

(d) Mode-4 (e) Mode-5

Figure 5.20: Variation of natural frequency for first five modes with a change in the number of fundamental element (FE) along the harness direction and the number of rows (NOR) for the zigzag pattern in $y-$direction under a CFFF boundary

On the other hand, when the number of rows is held fixed and is very small, the frequency is seen to remain almost constant for Mode-2, whereas it increases for Mode-4 with fundamental elements. Although, when the number of rows is slightly increased, it is seen that the Mode-2 frequency decreases marginally and Mode-4 becomes almost constant with the number of elements as also previously seen in Fig. 5.15(c) where the

number of fixed rows is 3. Further, when a large number of fixed rows are considered, both Mode-2 and Mode-4 frequencies are shown to first increase and then decrease with the number of elements showing a maximum. This is because, for the low number of fixed rows, the wrapping angle with respect to $y-$axis is larger than the optimal wrapping angle θ_{max}; hence, on further increasing the wrapping angle by increasing the number of elements, the homogenized twist stiffness coefficient $(H_4 + H_{13})$ decreases and the critical angle for maximum stiffness is not encountered. However, when the number of rows is larger, the wrapping angle for a smaller number of fundamental elements is initially less than θ_{max}. Now, when the number of elements is increased, the maximum twist stiffness can be observed at an optimal number of elements.

5.3 Summary of the Chapter

In this chapter, the energy equivalence homogenization technique was used to find an analytical model for the cable-harnessed plate structures of repeated zigzag and diagonal geometries. The proposed model was verified using a commercially available finite element (FE) analysis software. Promising results were shown in determining the cable dynamics effects which matched very well with those from the FEA. The governing PDEs for each of the patterns was found and compared to the previous chapter on the parallel system configurations. It is shown that the diagonal pattern results in the governing equation of motion similar to a symmetric angle-ply laminated plate, whereas the zigzag pattern has equations similar to a specially orthotropic laminated plate. It is interesting to see that upon harnessing the plate with cables, the vibration modes are affected differently. Some modes show major stiffening effects due to the addition of the cables and others show inertia dominant effects or no major changes in their frequencies. This may further result in mode switching in which the order of appearance for certain modes of given shapes changes after the addition of the cables compared to the bare plate.

The effects of various cable parameters such as the wrapping geometry and cable material properties have additionally been thoroughly investigated. It is shown further that the maximum stiffening effects in the bending dominant modes are observed when the cable wrapping angle is smallest with respect to the axis along which bending occurs. On the other hand, the stiffening effect in the twist and coupled-bending dominant modes is maximum when wrapping angle is $\tan^{-1}\left(\sqrt{2}\right)$ with respect to the wrapping direction. Finally, a brief discussion on the optimal cable placement is also presented. The proposed model can be ultimately used to help engineers with the optimal placement of these cables in order to minimize the dynamic impacts of the harnessing cables on the host structure.

Chapter 6

Experimental Validation of Cable-Harnessed Plates with Cables Attached in a Periodic Configuration

The objective of this chapter is to experimentally validate the analytical modeling technique proposed in Chapter 5 for the cable-harnessed plate with cables wrapped in periodic configuration. For this purpose, the cable-harnessed plates are fabricated using the metallic host plates of different sizes by wrapping the cables in both zigzag and diagonal manner.

The chapter is organized as follows: firstly, the experimental setup is described that is used to measure the dynamic behavior of the cable-harnessed structure. In the subsequent sections, the test and model FRFs are compared, first for the bare plate and then for the cabled plate model. The changes in natural frequencies on cable attachment is discussed in detail. Further, the mode shapes and MAC analysis are also presented for several experiments. A comparison between different patterns, namely parallel, zigzag and diagonal, is then presented. In the next section, a comparison of change in natural frequencies is presented for cable-harnessed plate with different host plate dimensions but similar fundamental element size. Finally, the novelty of the proposed modeling technique is highlighted by comparing it with an existing cable-harnessed beam model.

6.1 Experimental Setup

Figure 6.1 shows the experimental setup to measure the vibration characteristics of the cable-harnessed plate system using the impact hammer testing. The system consists of a plate harnessed with cables in a periodic wrapping pattern that is clamped at one edge and free at the other three edges (CFFF boundary). The system is excited using a PCB 086C01 impulse force hammer. To measure the displacement at a selected point on the plate, a contactless Polytec OFV-505 laser vibrometer is used which is operated using a Polytec OFV-5000 vibrometer controller. A small reflecting tape is attached at the selected location for capturing a good quality sensing data through the reflected laser beam. Finally, the impact and sensing data is acquired using an LMS SCADAS mobile data acquisition system connected to a laptop. LMS Testlab version 14.0 is used as computer software to control the data acquisition settings and analyze the output vibration data.

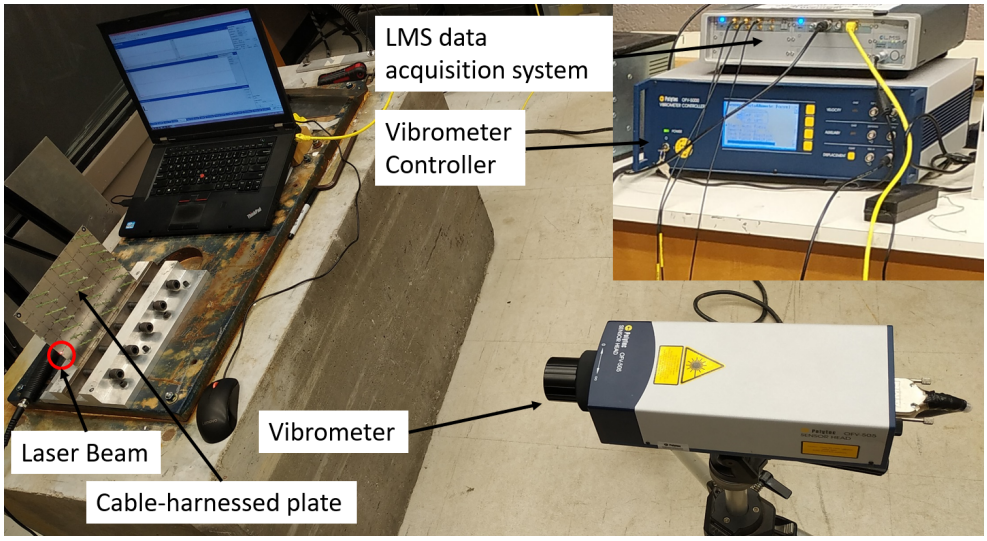

Figure 6.1: Experimental setup of the clamped cable-harnessed plate under impact testing

As mentioned earlier, for the experiments, both the zigzag and diagonal patterns are considered. In this chapter, the results are presented for four test cases, the details of which are listed in Table 6.1. For each test case, four sets of FRFs (I - IV) are presented each with a different sensing or actuation location coordinates (in meters) listed in Table 6.2. Also, Fig. 6.2 shows the zoomed-in pictures of the experimental setup displaying the cable-harnessed plates corresponding to the four test cases. It should be noted that the cable can be harnessed either along the $x-$axis direction or along the $y-$axis and hence, both the

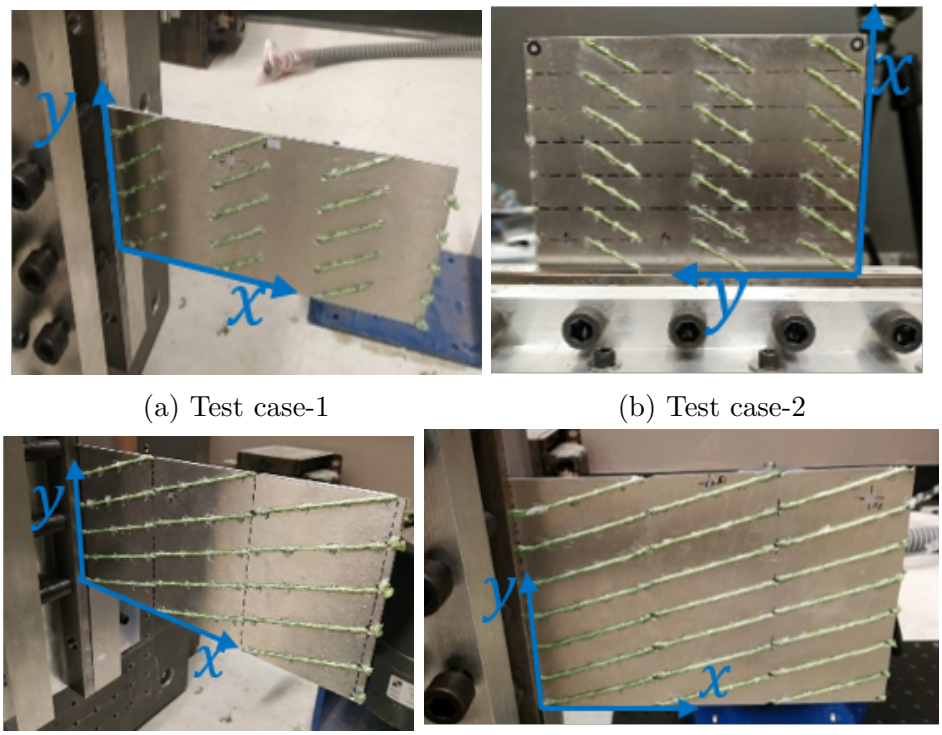

(a) Test case-1 (b) Test case-2

(c) Test case-3 (d) Test case-4

Figure 6.2: Zoomed-in pictures of the zigzag and diagonal pattern cable-harnessed plates used for experimental modal testing

wrapping alignments are considered. Earlier, a detailed analysis of both the patterns and wrapping along both directions was presented in Chapter 5. Different dimensions of the host plates are considered in some test cases in the current chapter for validation purposes in addition to different wrapping parameters i.e. number of fundamental elements and number of rows. In all the structures, the host plate is made of Aluminum (Al-6061) alloy with the following material properties: Young's Modulus $E_p = 68.9\ GPa$, mass density $\rho_p = 2768\ Kg/m^3$, and Poisson's ratio $\nu = 0.33$. Also, the attached cable used for testing is Super 8 Slick Power Pro cable, also used previously in experiments in Chapter 4, has the following material properties: $E_c = 128\ GPa$, $\rho_c = 1400\ Kg/m^3$. The cable radius is $r_c = 0.20\ mm$, however, to enhance the effects of cables on the harnessed system, eight fully tensioned cables are wrapped on the structure. Hence, the effective radius of the cable becomes$\sqrt{8} * (0.20\ mm) = 0.56\ mm$ [2]. The applied pre-tension in the cable is $5N$.

Table 6.1: Details of the tested cable-harnessed plate structure cases

Test Case	Host Plate				Cable wrapping pattern			
	Material	Dimensions			Zigzag/ Diagonal	Wrapping alignment	No.of fundamental elements	No. of rows
		$a\ (m)$	$b\ (m)$	$h\ (mm)$				
1	Al-6061	0.202	0.099	1.2	Zigzag	$x-$axis	3	5
2	Al-6061	0.143	0.197	1.2	Zigzag	$y-$axis	3	7
3	Al-6061	0.201	0.099	1.2	Diagonal	$x-$axis	3	5
4	Al-6061	0.2	0.136	1.2	Diagonal	$x-$axis	3	7

Table 6.2: Actuation and sensing location coordinates (in meters) of the four test cases (coordinate system shown in Fig. 6.2)

Test Case	Set	Actuation Location	Sensing Location
1	I	(0.023,0.079)	(0.08,0.079)
	II	(0.023,0.058)	(0.082,0.08)
	III	(0.023,0.038)	(0.08,0.08)
	IV	(0.023,0.018)	(0.08,0.08)
2	I	(0.021,0.022)	(0.19,0.135)
	II	(0.08,0.022)	(0.195,0.135)
	III	(0.019,0.023)	(0.005,0.14)
	IV	(0.08,0.022)	(0.005,0.135)
3	I	(0.023,0.079)	(0.0801,0.0803)
	II	(0.022,0.058)	(0.0801,0.0803)
	III	(0.022,0.039)	(0.0801,0.0803)
	IV	(0.022,0.02)	(0.0801,0.0803)
4	I	(0.0235,0.115)	(0.1,0.13)
	II	(0.023,0.095)	(0.103,0.135)
	III	(0.023,0.075)	(0.105,0.135)
	IV	(0.024,0.057)	(0.1,0.13)

6.2 Bare plate model and test FRFs

Figures 6.3 - 6.6 show the FRFs obtained from the impact tests of the four different bare host plates, dimensions of which are mentioned in Table 6.1. For each case, the FRF plots are shown for the four sets of actuation and sensing locations mentioned in Table 6.2 and are compared with the model results of the bare plate. All the natural frequency peaks and the anti-resonance frequencies were well-predicted by the model and hence, these host plate parameters can be confidently used further in the cable-harnessed models. In some FRFs, a small spike at 60 Hz is present due to the electrical noise and does not correspond to a structural mode.

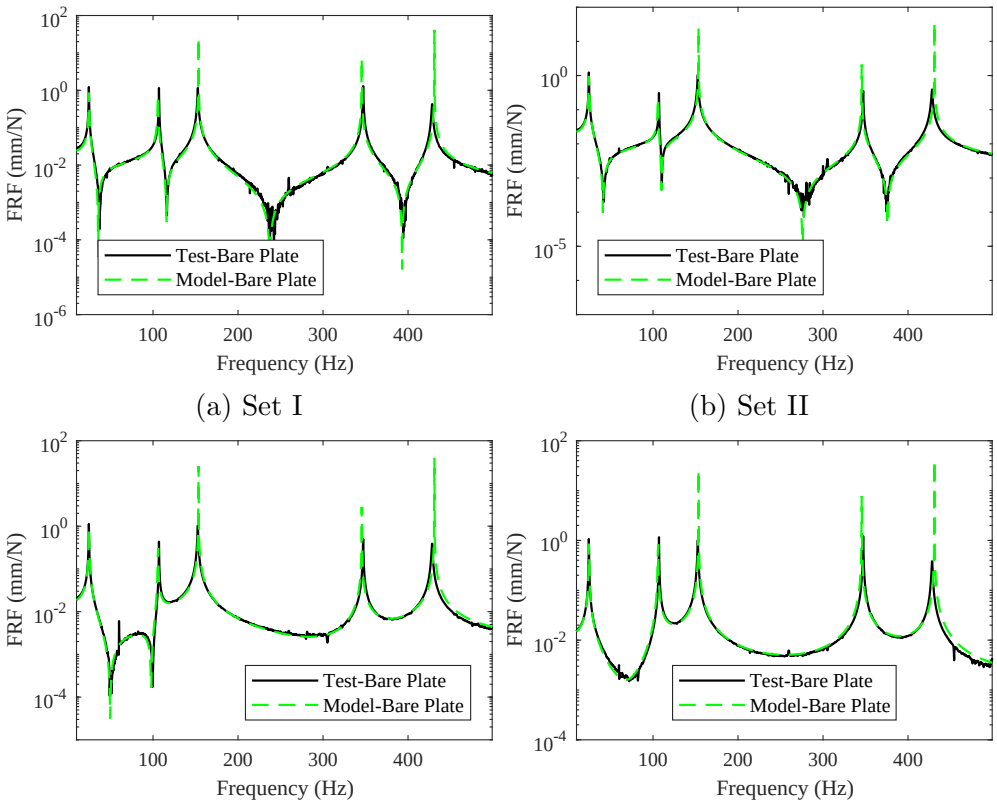

(a) Set I (b) Set II

(c) Set III (d) Set IV

Figure 6.3: Bare plate FRFs comparison between test and model for test case 1. Sets I - IV denote the FRFs for different sets of actuation and sensing locations

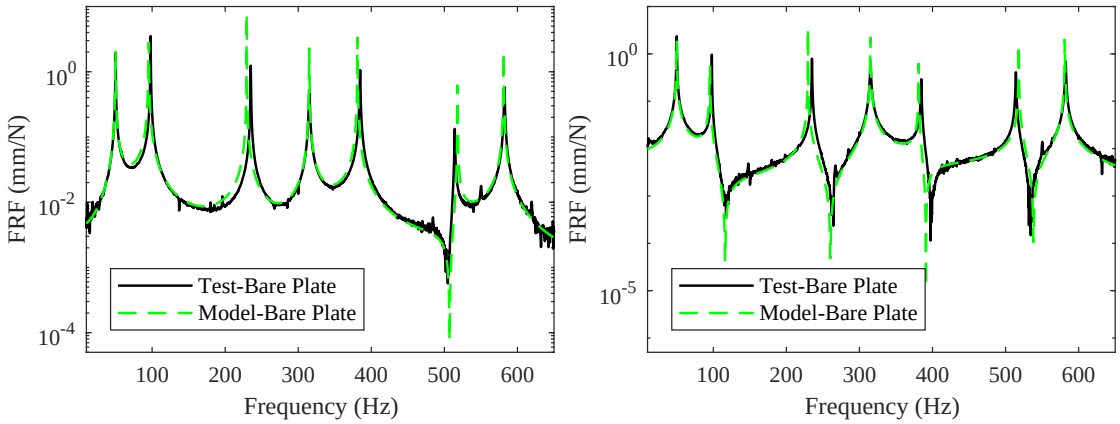

(a) Set I

(b) Set II

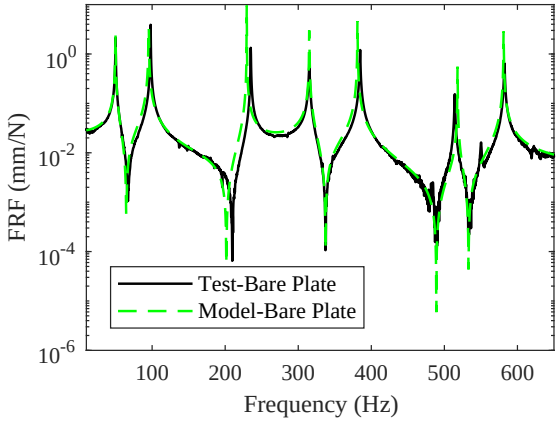

(c) Set III

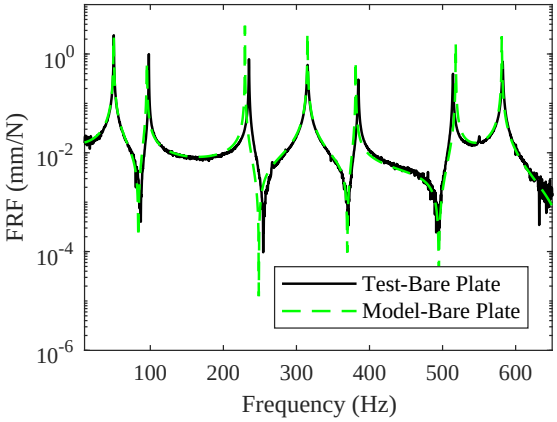

(d) Set IV

Figure 6.4: Bare plate FRFs comparison between test and model for test case 2. Sets I - IV denote the FRFs for different sets of actuation and sensing locations

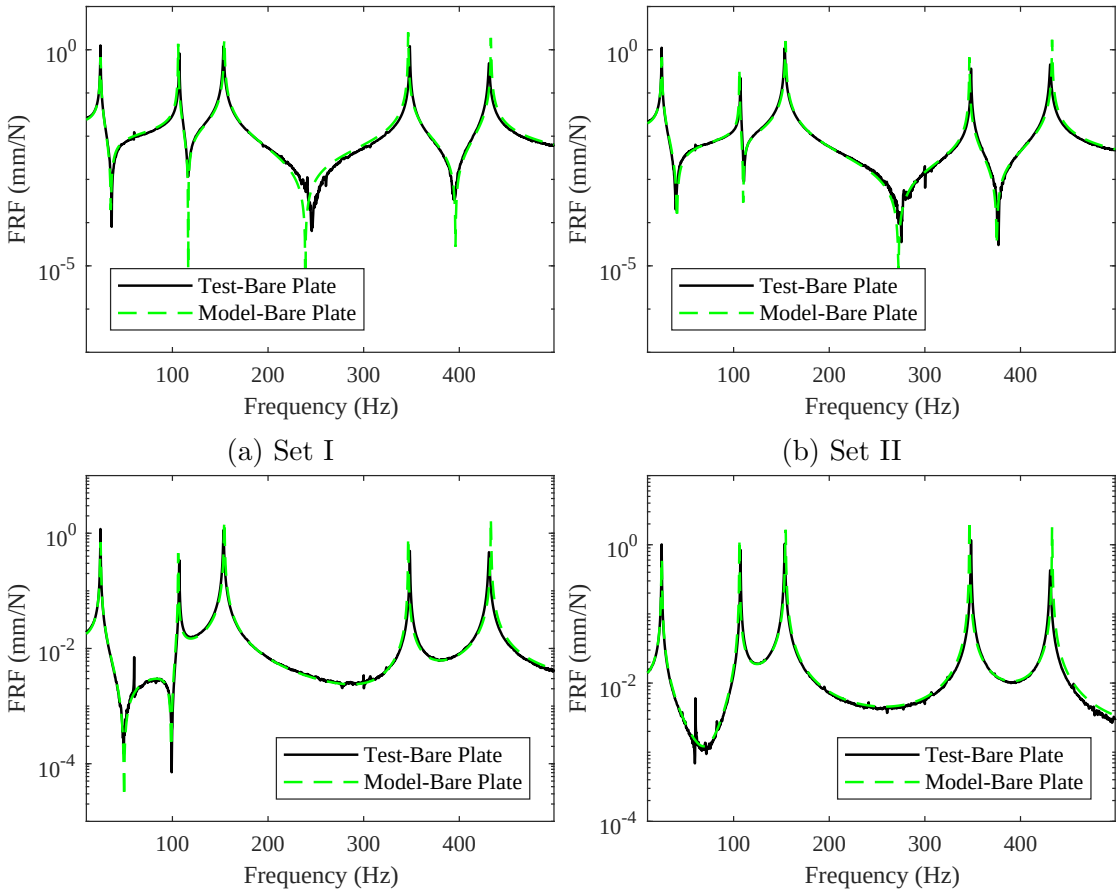

(a) Set I (b) Set II

(c) Set III (d) Set IV

Figure 6.5: Bare plate FRFs comparison between test and model for test case 3. Sets I - IV denote the FRFs for different sets of actuation and sensing locations

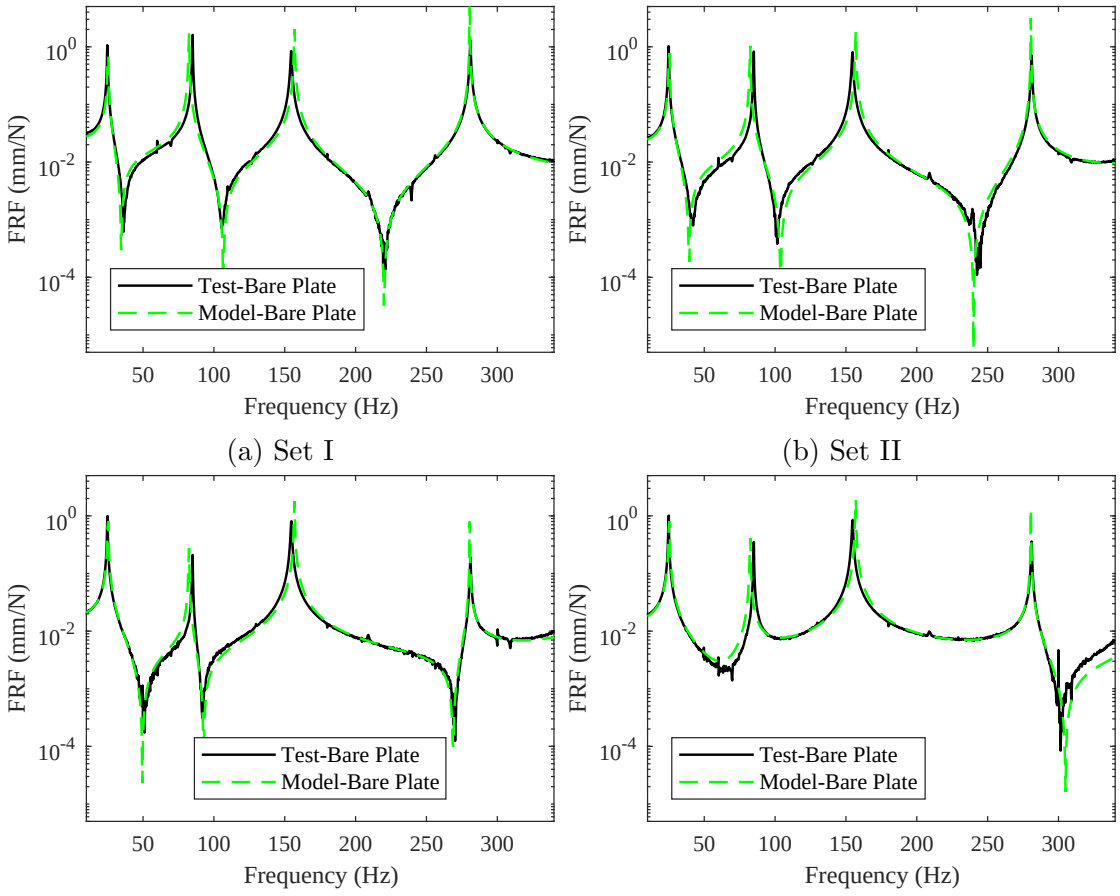

(a) Set I (b) Set II

(c) Set III (d) Set IV

Figure 6.6: Bare plate FRFs comparison between test and model for test case 4. Sets I - IV denote the FRFs for different sets of actuation and sensing locations

6.3 Comparison between cabled plate model and test

In this section, experimental results are presented for the cable-harnessed plate with zigzag and diagonal pattern. These results are presented in form of FRFs and are compared with proposed model and bare plate test results. Mode shapes of tests 1 and 2 are presented for both model and test. Additionally, MAC analysis for these tests is also presented.

6.3.1 Cabled plate model and test FRFs for zigzag pattern

Figures 6.7 and 6.8 show the FRF comparisons of the cable-harnessed plate wrapped in the zigzag pattern corresponding to the test cases 1 and 2, respectively. Recall that for the test case 1, the wrapping direction is along the $x-$axis, whereas for the test case 2, the wrapping is along the $y-$axis. The four plots (sets I —IV) shown each in Figs. 6.7 and 6.8 correspond to the four sets of actuation and sensing locations listed earlier in Table 6.2.

The three FRFs shown in each plot of Fig. 6.7 help to deduce two important points: First, comparison of the bare plate test FRF (black line) with the cabled plate test FRF (green line) shows the importance of modeling the cable dynamics that can not be ignored. Second, the cabled plate model FRF (red dotted line) obtained using the proposed technique is able to well predict the change in the systems natural frequencies upon adding the cables.

Overall, it is evident for the Test case-1 that the cable stiffness effects are dominant over its inertia effects, and as a result, the natural frequencies increase on harnessing cables. Table 6.3 lists the natural frequencies predicted by the cable-harnessed model and shows that the % increase in frequencies on harnessing cables is significant for Test case-1 in the frequency range of interest. A similar % increase for the test results that matches well with the model is shown. On the other hand for the Test case-2, it is seen that in addition to some modes showing a dominant cable stiffening effect, natural frequencies of a few modes either do not undergo a significant change or decrease on harnessing cables. The reasoning is based on the mode shapes of the structure and is discussed in the following paragraphs.

The mode shapes corresponding to the test cases 1 and 2 are shown in Figs. 6.9 and 6.10, respectively. Clearly, the mode shapes obtained from both the homogenized model and experiments match well with each other. It is clear from Fig. 6.9 that the Modes 1, 3, and 5 are bending modes with a dominant curvature along the $x-$direction, whereas the Modes 2 and 4 are twist and coupled-bending dominant modes. The increase in natural frequencies in all these modes for test case-1 is due to the dominant effect of the cable stiffness in the coefficient H_2 for the bending modes, and the coefficients $(H_4 + H_{13})$ for

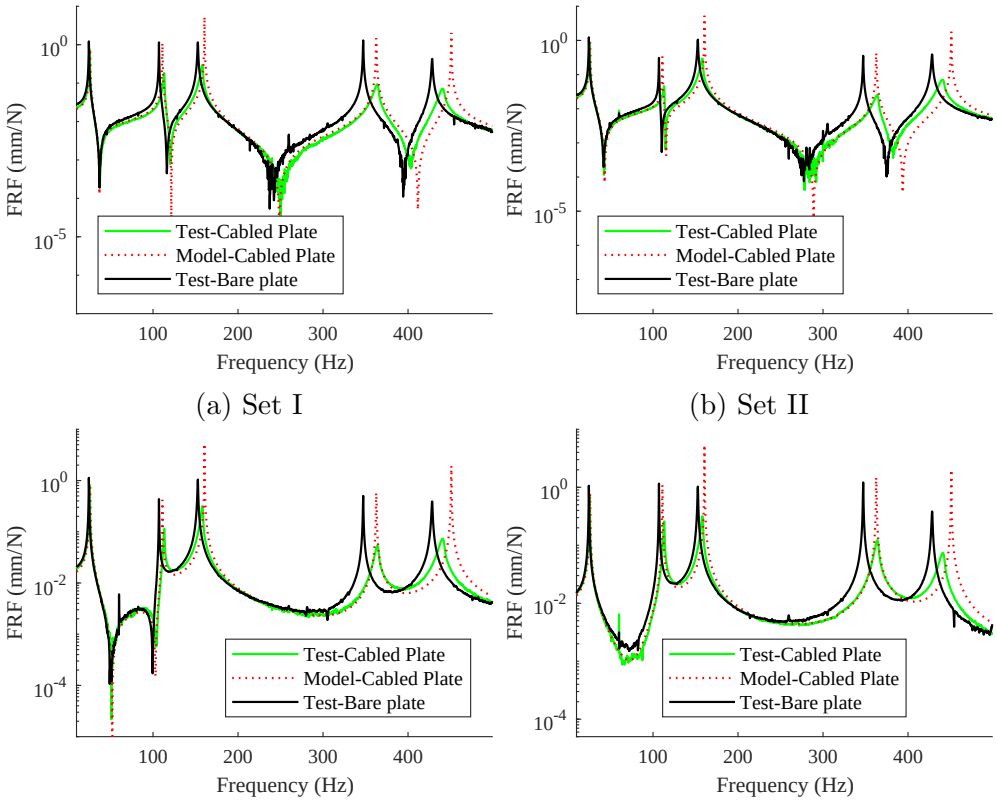

Figure 6.7: FRF comparisons of cabled plate test, cabled plate model, and bare plate test for test case 1 (zigzag pattern) for different sets of actuation and sensing locations. The shift of the peaks from black to green denotes the change in natural frequencies on harnessing cables. The green curve plotted using the proposed model is able to well predict the changes.

the twist and coupled-bending dominant modes, over the cable inertia effect. A detailed discussion on the coefficients was presented in the Chapter 5. Additionally, it should be noted that since the cable segments are aligned at an angle with the horizontal $x-$axis, the cable stiffness contribution in the bending dominant modes would be smaller compared to the case when the same number of cables are harnessed parallel to the $x-$axis. This is because, in the case of zigzag pattern, the effective increase in stiffness in the $x-$direction would be a projection of the cable stiffness on the $x-$axis which would be smaller compared to the case when the cable is harnessed parallel to the $x-$axis. On the other hand, for the twist and coupled-bending dominant modes, since the added cable stiffening effect is

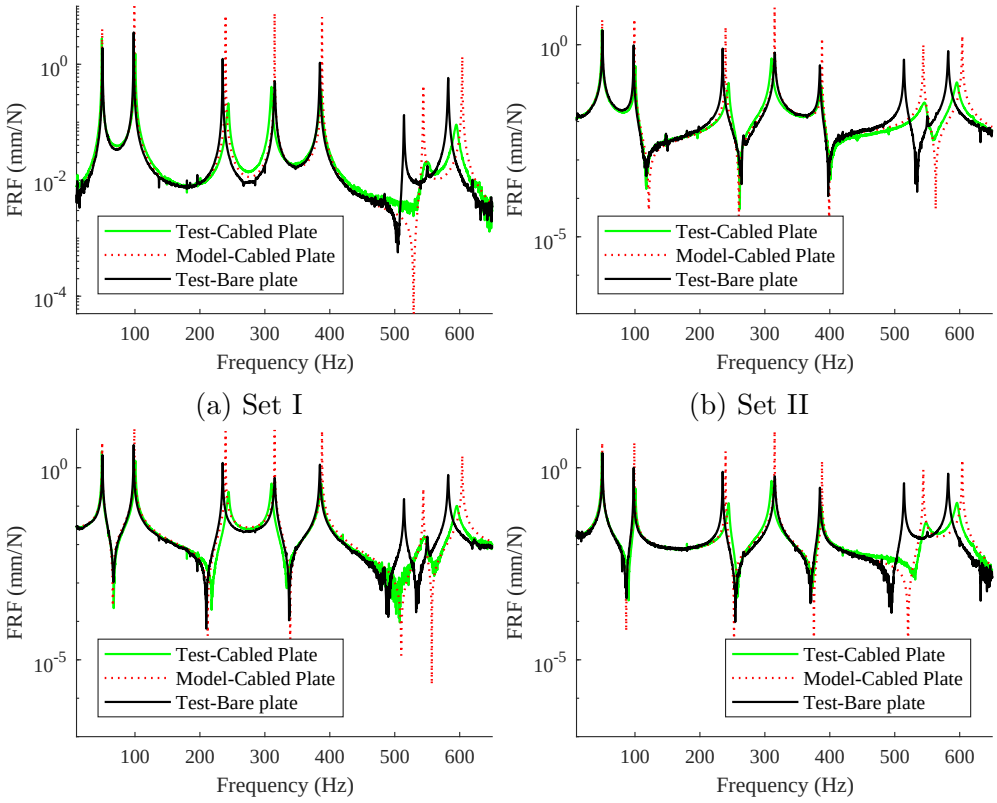

(a) Set I (b) Set II

(c) Set III (d) Set IV

Figure 6.8: FRF comparisons of cabled plate test, cabled plate model, and bare plate test for test case 2 (zigzag pattern) for different sets of actuation and sensing locations. The shift of the peaks from black to green denotes the change in natural frequencies on harnessing cables. The green curve plotted using the proposed model is able to well predict the changes. The amplitudes near the peaks are not a good match because of the absence of damping in the model.

proportional to $\cos\theta \sin^2\theta$ (as seen from the first-order cable effects from the coefficient $(H_4 + H_{13})$), the natural frequencies increase is higher for zigzag pattern compared to the parallel pattern.

For the test case 2, the mode shapes in Fig. 6.10 can also be similarly categorized. Here, the modes 1 and 4 have a dominant bending curvature in the $x-$direction, the modes 3 and 6 have a dominant bending in the $y-$direction, while the others are twist and coupled-bending modes in the range of frequency shown in Fig. 6.8. It should be noted from Table

Table 6.3: Natural frequencies of bare plate (BP) and cable-harnessed plate (CP) obtained from model and test for test cases 1 and 2 corresponding to the zigzag pattern

Mode	Model-BP (Hz)	Test-BP (Hz)	% error in model-BP	Model-CP (Hz)	Test-CP (Hz)	% error in model-CP	Model frequency increase, %	Test frequency increase, %
Test case-1								
1	24.67	24.50	0.68%	25.83	25.50	1.29%	4.71%	4.08%
2	105.81	107.00	-1.11%	111.13	113.00	-1.66%	5.03%	5.61%
3	153.51	152.75	0.50%	160.57	158.00	1.63%	4.60%	3.44%
4	345.54	347.25	-0.49%	362.69	363.50	-0.22%	4.96%	4.68%
5	431.01	428.50	0.58%	450.87	440.75	2.30%	4.61%	2.86%
Test case-2								
1	49.83	50.00	-0.34%	49.59	49.00	1.20%	-0.48%	-2.00%
2	95.30	98.00	-2.75%	98.97	100.50	-1.52%	3.85%	2.55%
3	229.54	235.00	-2.32%	239.54	243.80	-1.75%	4.36%	3.74%
4	315.13	315.25	-0.04%	314.96	310.25	1.52%	-0.06%	-1.59%
5	381.11	384.75	-0.95%	387.94	386.75	0.31%	1.79%	0.52%
6	518.09	514.25	0.75%	543.84	545.50	-0.30%	4.97%	6.08%
7	581.13	582.25	-0.19%	603.83	595.75	1.36%	3.91%	2.32%

6.3 that the natural frequency of the modes 1 and 4 show a dominant cable mass effect over the cable stiffening effect on harnessing the cables. Hence, the cabled plate frequencies are lower than the bare plate for the model as well as the test for these modes. Because the cable segments have a large angle with the $x-$axis in this case, the projection of cable stiffening along the $x-$direction is very small and hence, the cable inertia effect dominates.

On the other hand, the modes 3 and 6 show a noticeable increase in natural frequency on harnessing cables along the $y-$direction. These modes, with dominant bending curvature in the $y-$direction, are stiffened due to a large projection of cable stiffness along the $y-$axis. This increases the effective bending stiffness in the $y-$direction that is dominant over the added cable inertia effect. Additionally, the modes 2, 5 and, 7, which are twist and coupled-bending modes, are also shown to exhibit a dominant stiffening effect which is well predicted by the model. Also, a larger error is observed in the cable-harnessed plate model for the higher modes. It is because of the smaller number of fundamental elements per wavelength of the frequency of interest for the higher modes.

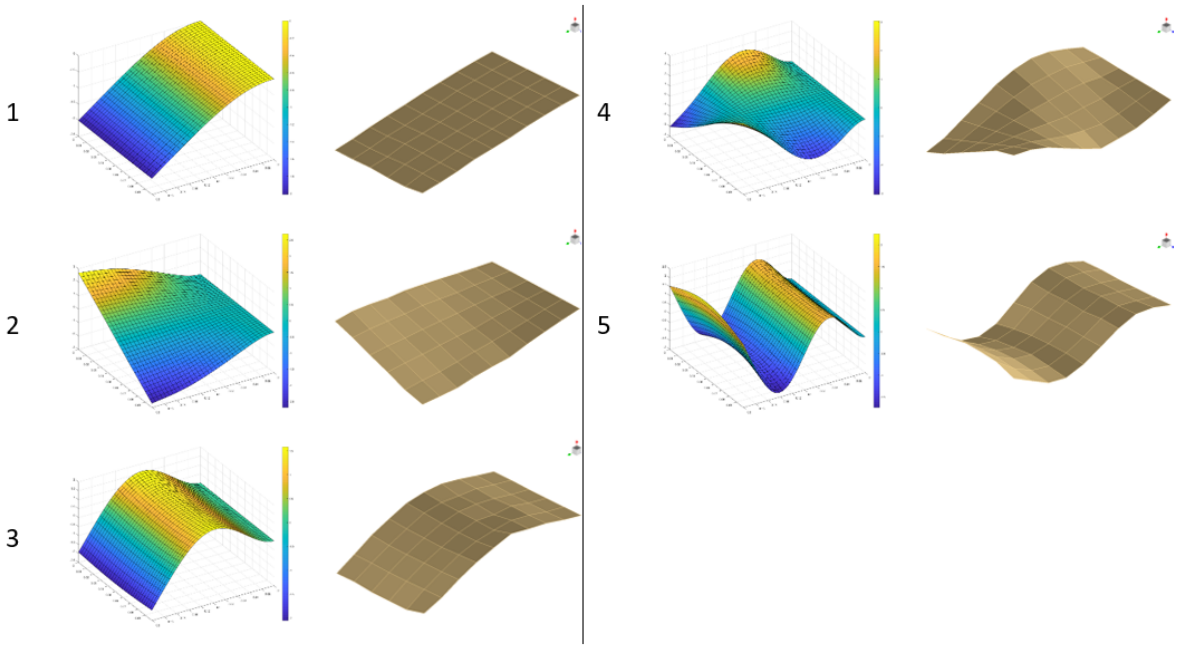

Figure 6.9: Mode shapes obtained from homogenized model (left) and experiments (right) for the first five modes corresponding to Test Case 1 (Zigzag pattern with cable harnessing along the $x-$direction)

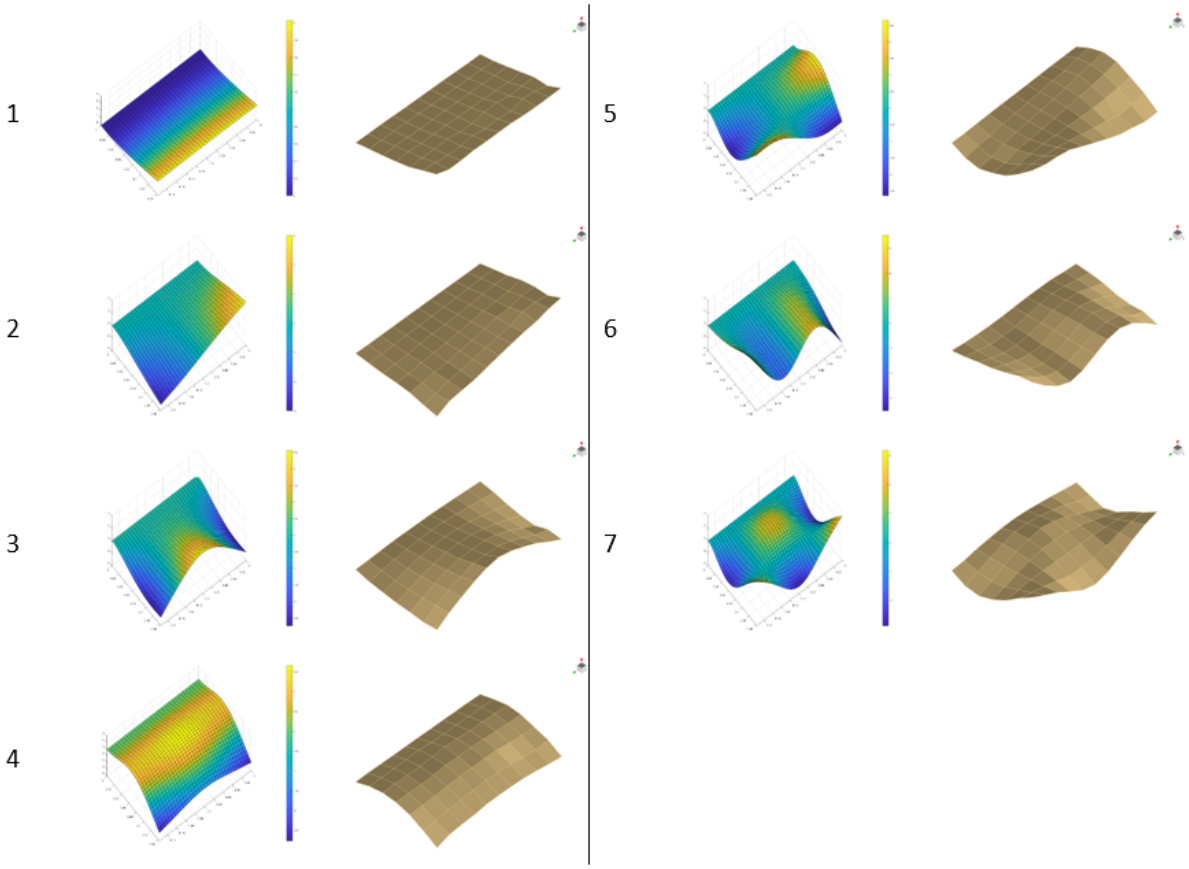

Figure 6.10: Mode shapes obtained from homogenized model (left) and experiments (right) for the first seven modes corresponding to Test Case 2 (Zigzag pattern with cable harnessing along the $y-$direction)

6.3.2 MAC Analysis

One of the best methods to quantitatively correlate the mode shapes obtained from experiments and the analytical model is using the Modal Assurance Criterion (MAC) [92]. This was also used in Chapter 4 for the correlation of the mode shapes. Recall, it is calculated between different pairs of mode shapes obtained from both test and model; it results in the value of 1 when the modes are similar and 0 when modes are completely non-correlated. For the current study, the MAC analysis is conducted for the test cases 1 and 2 for which experimental mode shapes were obtained. The MAC is presented in a three-dimensional bar chart shown in Figs. 6.11 and 6.12 for the test case 1 and 2, respectively. Clearly, the MAC values being close to one along the diagonal and close to zero among the off-diagonal elements indicate a strong correlation between the model and test.

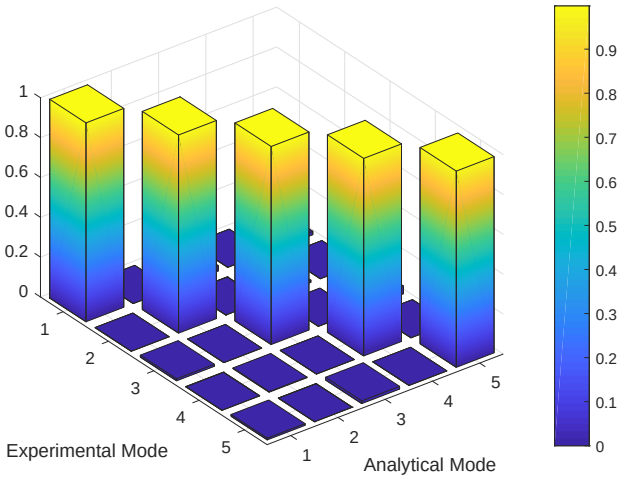

Figure 6.11: Modal Assurance Criterion (MAC) analysis bar chart for the test case 1

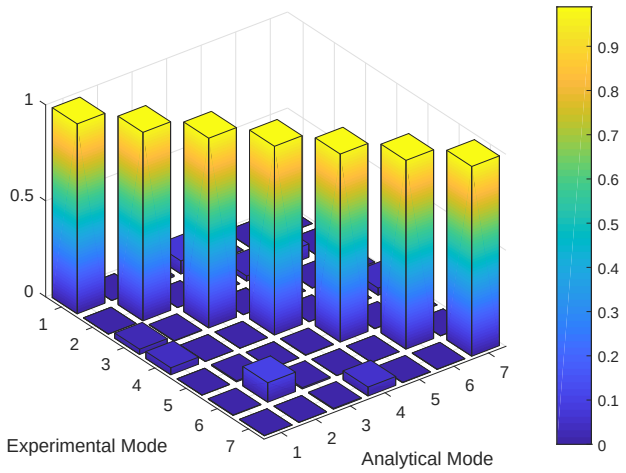

Figure 6.12: Modal Assurance Criterion (MAC) analysis bar chart for the test case 2

6.3.3 Cabled plate model and test FRFs for diagonal pattern

The FRFs obtained from the experiments on the diagonally wrapped cable-harnessed structures are presented in Figs. 6.13 and 6.14. The corresponding natural frequencies are listed in Table 6.4. The FRFs corresponds to the cases 3 and 4 and shown for the four sets of actuation and sensing locations presented in Table 6.2. In both the structures studied in this case, the cable is wrapped along the $x-$axis direction but on different host plates and with a different number of cable rows as shown previously in Table 6.1. The proposed model for the diagonal pattern is able to well predict the cable dynamics effects and hence, matches well with the test results for both the test structures.

As seen from Fig. 6.13 and Table 6.4, the natural frequencies of the modes 1, 3, and 5 show a large increase on harnessing cables, whereas the frequencies of modes 2 and 4 increase by only a small percentage. This is because the number of fundamental elements and number of rows chosen for the diagonal pattern results in a small wrapping angle θ with the $x-$axis. Similar to the case-1 of zigzag pattern, this results in the stiffening of the modes that have dominant bending curvature in the $x-$direction. However, the % increase in frequencies is different for both the patterns as discussed later in detail. For the test case-3, the modes 1, 3, and 5 have a bending dominant curvature in the $x-$direction (similar to modes shown for test case-1 in Fig. 6.9); hence, the cable stiffening effect is higher for these modes.

Similar to the case 3, the natural frequency of the modes 1 and 3 of the test case 4 were also observed to increase significantly owing to a similar reason as discussed in the previous

Table 6.4: Natural frequencies of bare plate (BP) and cable-harnessed plate (CP) obtained from model and test for test cases 3 and 4 corresponding to the diagonal pattern

Mode	Model-BP (Hz)	Test-BP (Hz)	% error in model-BP	Model-CP (Hz)	Test-CP (Hz)	% error in model-CP	Model frequency increase, %	Test frequency increase, %
Test case-3								
1	24.79	24.75	0.16%	26.53	27.00	-1.75%	7.01%	9.09%
2	106.11	107.25	-1.06%	107.86	108.75	-0.82%	1.65%	1.40%
3	154.28	153.50	0.51%	165.42	164.25	0.71%	7.22%	7.00%
4	346.62	348.25	-0.47%	354.57	353.50	0.30%	2.29%	1.51%
5	433.14	431.00	0.50%	464.45	448.75	3.50%	7.23%	4.12%
Test case-4								
1	25.28	24.75	2.13%	27.08	27.25	-0.62%	7.14%	10.10%
2	82.34	85.00	-3.13%	83.99	86.00	-2.33%	2.01%	1.18%
3	156.82	154.50	1.50%	168.31	166.25	1.24%	7.33%	7.61%
4	280.57	281.00	-0.15%	289.06	286.75	0.81%	3.03%	2.05%

paragraph. It is noticed that different modes undergo a different change in frequencies and that depends on the mode shape as well as the pattern parameters. This was studied in detail in Chapter 5. In this chapter, it is clearly witnessed that these dissimilar changes of frequencies in different modes occur in experimental results as well and are a very close match with the model prediction.

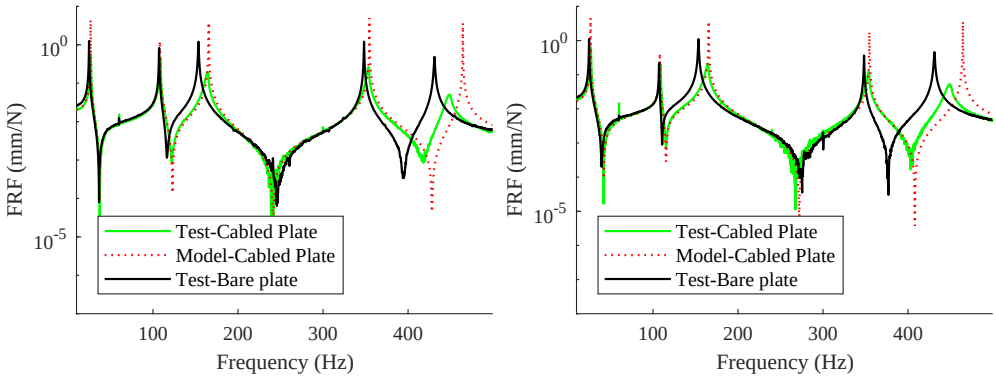

(a) Set I

(b) Set II

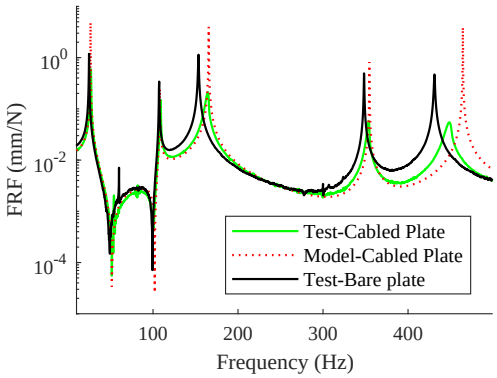

(c) Set III

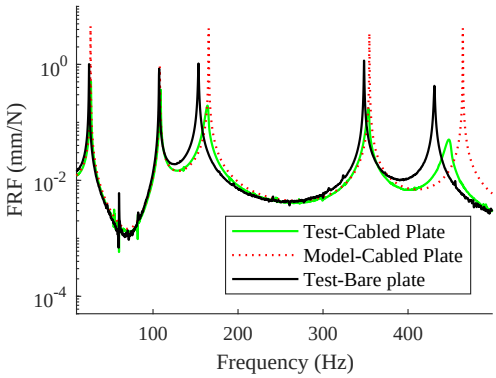

(d) Set IV

Figure 6.13: FRF comparisons of cabled plate test, cabled plate model, and bare plate test for test case 3 (diagonal pattern) for different sets of actuation and sensing locations

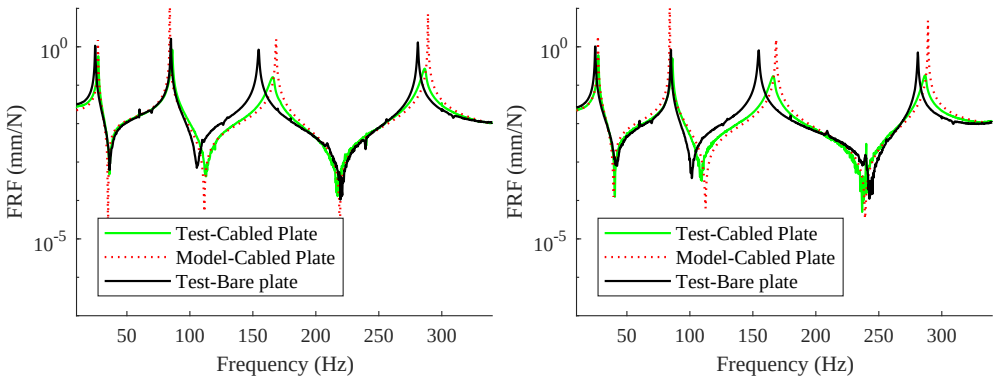

(a) Set I

(b) Set II

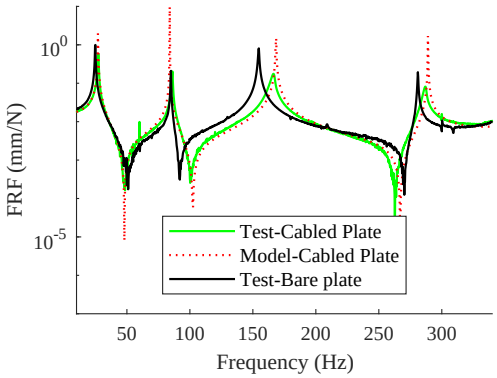

(c) Set III

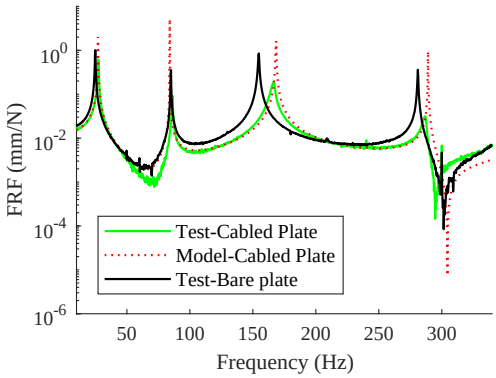

(d) Set IV

Figure 6.14: FRF comparisons of cabled plate test, cabled plate model, and bare plate test for test case 4 (diagonal pattern) for different sets of actuation and sensing locations

6.4 Comparison between different cable attachment patterns

Next, the change in system dynamics on harnessing cables in different patterns can be discussed by comparing the test cases-1 and 3 as shown in Fig. 6.15. The former case has the cables wrapped in the zigzag pattern, while the latter has wrapped in the diagonal pattern with the same number of fundamental elements and rows. Also, the host plate in both cases has similar dimensions that allow for a fair comparison. The model data of a cabled plate with parallel cables (discussed in Chapter 4) is also plotted for the comparison with the two wrapping patterns. The host plate for the parallel cabled plate is similar to that to plate-3 with 5 rows of parallel cables attached parallel to the $x-$axis having same geometric and material properties as the tested cases of wrapped structures.

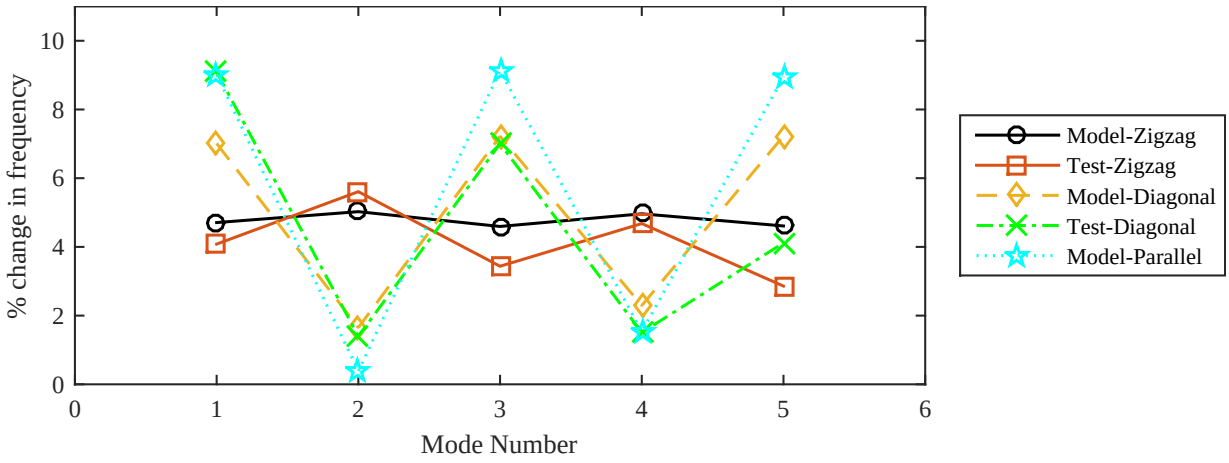

Figure 6.15: Comparison of % change in first five natural frequencies of cable-harnessed plates with respect to the bare plate for test case-1 (zigzag), test case-3 (diagonal), and a parallel cabled plate model

For the two wrapping patterns, the % increase in frequencies predicted by the model matches well with the test results. For the diagonal pattern, it is seen that the increase in frequencies on harnessing cables is significantly higher for the modes 1, 3, and 5 compared to the zigzag pattern. This is because of the higher contribution of the cable stiffening in the bending dominant modes in the $x-$direction due to the smaller wrapping angle of the inclined cable segments (with respect to the $x-$axis) in the diagonal pattern. On the other hand, the modes 2 and 4 show a higher frequency increase for the zigzag pattern. Analytically, the cable stiffening terms present in the twist and coupled-bending stiffness

$(H_4 + H_{13})$ are accountable for the higher natural frequencies in the zigzag pattern. These added cable stiffness in these coefficients is directly proportional to the term $(\cos\theta \sin^2\theta)$ that exhibits a maximum at a wrapping angle of 54.7° as also shown in Fig. 5.5 discussed in Chapter 5. For the pattern parameters considered in this study, the wrapping angle of zigzag pattern and diagonal pattern is approximately 30.5° and 16.4°, respectively, and as a result, the added twist and coupled-bending stiffness due to the cables is higher for the zigzag pattern. A detailed discussion and analysis of the model corresponding to test cases 1 and 3 was done in Chapter 5, whereas the present chapter validates the model predictions.

The first five mode shapes for the parallel cabled plate were also found to be same as the wrapped cabled plates considered in case-1 and case-3. Compared to the wrapped patterns, the parallel cabled plate shows the highest % change in bending frequencies in the $x-$direction. This happens because the cables are aligned along the $x-$axis for the parallel cabled plate and hence, for similar number of rows, the added cable stiffening effect is maximum; in case of the wrapped patterns, the added stiffening is due to the projection of stiffness of inclined cable segments in the $x-$axis and hence, it is lower compared to the parallel cabled plate. For the twist dominant mode, the cable attachment has almost no effect on the natural frequency as was also observed in Chapter 4. This is because the cable stiffening effects in this mode only becomes higher when the cable is at an angle with the plate's edge.

Figure 6.15 can also be analyzed with a design perspective for wrapping cables on a plate-like structure. The length of the wrapped cable in each row is fairly similar for both the patterns for a similar number of fundamental elements. In the cases 1 and 3, these lengths are 0.24 m and 0.27 m, respectively for a cable row. Hence, for a given cable length, one can select a pattern such that either specific vibration modes can be highly stiffened or all the structural modes in a broad range of frequency can be moderately stiffened. On the other hand, the designer can also choose an optimal cable pattern such that there is least impact on the system dynamics of the host structure. And, in the best case scenario, the cable modeling can be completely ignored in a structure wrapped with cables in such optimal pattern.

6.5 Comparison of change in system dynamics for a special case

An interesting observation is made when the test cases 3 and 4 corresponding to the diagonal pattern are compared. In both these cases, although the host plate dimensions are different, the size of the fundamental element in the cabled plates is approximately the same. Further, on a closer inspection of % increase in frequency (on cable attachment) from Table 6.4, it can be seen that certain modes have similar shift when the two tests are compared. This motivated me to conduct some simulations in which the dimensions of host plate were varied while those of fundamental elements were kept fixed.

Four different host plates were used with dimensions listed in Table 6.5, all of them with thickness 1.2 mm and made of aluminum-6061 alloy. The natural frequencies of the bare plate was calculated for a CFFF boundary and was classified according to their mode shape. Next, the natural frequencies of the cabled plate (with the diagonal pattern) corresponding to these host plates were calculated with the pattern parameters shown in Table 6.5. The same properties of the Power Pro cables were used to model the cable. It should be noted that for all the cases listed in Table 6.5, the dimensions of the fundamental elements would be 6.67 cm x 2 cm.

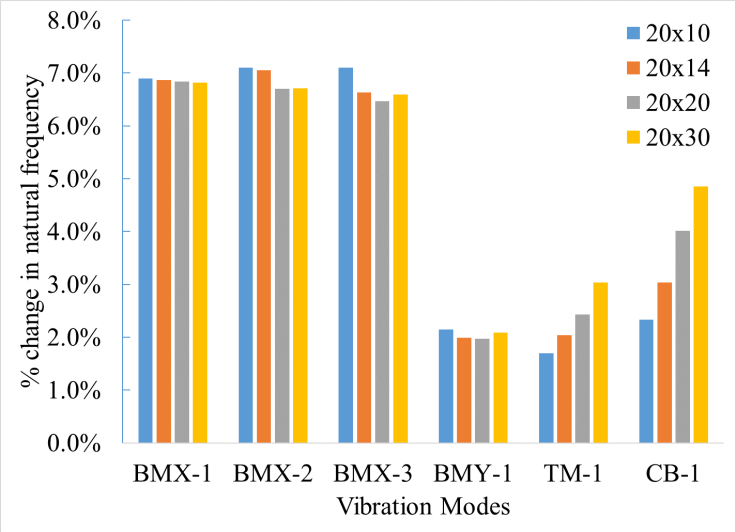

Figure 6.16: Comparison of the % change in natural frequencies for host plate with different dimensions (shown in Table 6.5) but with similar dimensions of the fundamental element of the diagonal pattern

The % change in natural frequencies are presented in Fig. 6.16 for the first three dominant bending modes in the $x-$direction (BMX-1—BMX-3), first bending dominant mode in the $y-$direction (BMY-1), 1st twist dominant mode (TM-1), and 1st coupled bending dominant mode (CB-1). It is interesting to note that the % change in bending modes (both with dominant curvature in the x and y direction) frequencies is insensitive of the host plate parameters when the fundamental element dimensions are held constant. On the other hand, the twist and coupled-bending mode frequency increases as the aspect ratio (a/b) of the host plate is decreased.

Table 6.5: Host plate and diagonal pattern parameters considered for simulations of a special case

S. No.	Length (a)	Width (b)	Diagonal pattern	
			Fundamental elements	Rows
1	20 cm	10 cm	3	5
2	20 cm	14 cm	3	7
3	20 cm	20 cm	3	10
4	20 cm	30 cm	3	15

6.6 Comparison between cable-harnessed beam-like and plate-like models

Finally, it is worth discussing the importance of the proposed cable-harnessed plate model over the previously established work on the cable-harnessed beam model [31] that considers the host structures as a one-dimensional beam-like structure. Hence, simplified assumptions are made for the periodic structures in this study to implement beam theory assumptions to obtain the FRFs when they are modeled as beam specimens. The mathematical modeling technique developed in [31] is used for plotting the FRFs obtained by dividing each plate into beam segments along the $x-$direction and comparing it with those obtained from the model proposed in this paper.

Figures 6.17 and 6.18 show the comparison of the cabled beam model with the test and model results of the cabled plate for both the zigzag and diagonal patterns, respectively. The results are shown for one set of actuation and sensing locations referred to as set I in Table 6.2. Clearly, the cabled beam FRF is unable to predict all the natural frequencies

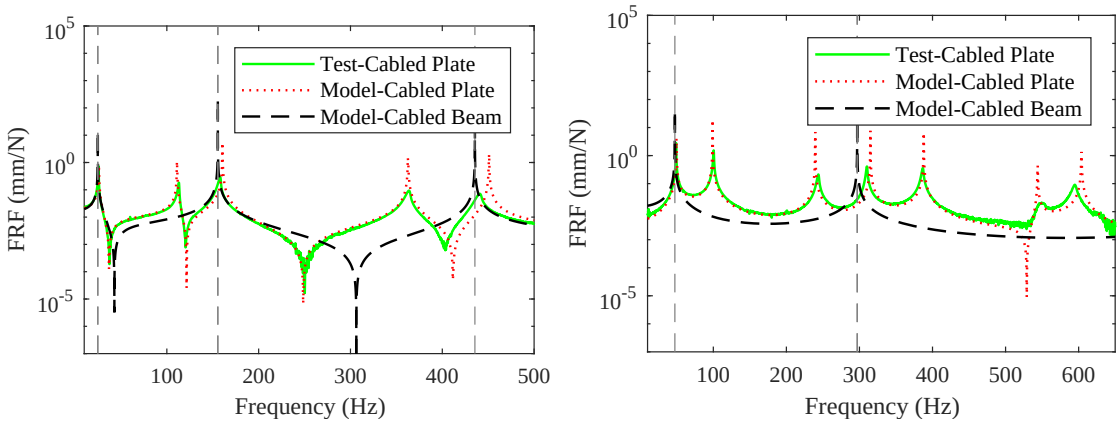

Figure 6.17: FRF comparison with an equivalent cabled beam model for the zigzag pattern corresponding to (a) test case 1, and (b) test case 2, for set I of sensing and actuation location

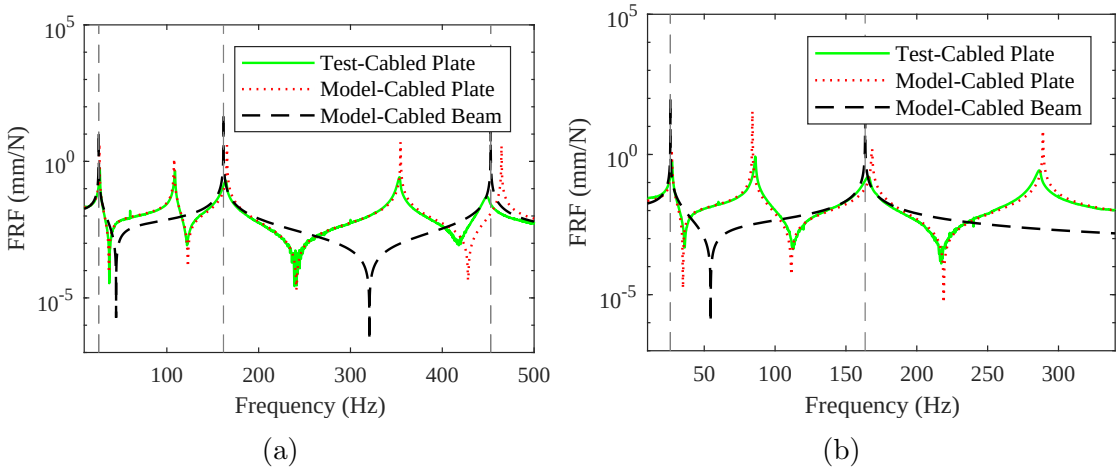

Figure 6.18: FRF comparison with an equivalent cabled beam model for the zigzag pattern corresponding to (a)test case 3, and (b) test case 4, for set I of sensing and actuation location

in the range of interest. This is primarily because of the absence of the variation of displacement along the $y-$axis in the homogenized beam model. Whereas, the current model, which is based on the plate theory assumptions, is able to predict the accurate dynamics. In Fig. 6.17(a), the modes 1, 3, and 5 have dominant bending curvature in the $x-$direction and hence are predicted well by the beam model, but the other two modes that are responsible for twist and coupled-bending behavior are missed.

Similarly, the modes in Fig. 6.17(b) that corresponds to the dominant bending curvature in $y-$direction, along with the twist and coupled-bending modes are not predicted. Likewise, for the diagonal patterns structures shown in Fig. 6.18, the cabled beam model fails to predict the vibration modes that have transverse displacements varying along the $y-$direction. Additionally, the cabled beam model also fails to predict the important anti-resonance frequencies that are well predicted by the proposed model for the FRF of both the wrapping patterns.

6.7 Summary of the chapter

In this chapter, experimental validation of the analytical model developed for the cable-harnessed plate-like structures in Chapter 5 was conducted successfully. These structures consist of homogeneous and isotropic rectangular host plates that are harnessed with cables in the periodic wrapping patterns. The natural frequencies, mode shapes, and frequency response functions were obtained for four test cases of cable-harnessed and host plate structures using the experimental modal testing. It was found that harnessing cables on the plate structure significantly impacts the frequency of the natural vibration modes. Also, different vibration modes exhibit a different change in natural frequency with respect to the corresponding bare plate mode depending on the mode shape. One interesting observation was regarding the insensitivity of normalized frequency difference of the bending dominant modes when the host plate dimensions are changed but the fundamental element dimensions were held constant for the diagonal pattern; the torsional and coupled-bending modes were however found sensitive. Finally, a comparison with an existing cabled beam model exhibited the novelty of the proposed model. These observations would increase researcher's confidence in modeling these cable-harnessed plate-like structures and further complex structures that include but is not limited to the non-periodic cable wrapping patterns on the plate structures. In addition, this model can also be used for optimizing the cable harness patterns such that the cables play a minimal role in altering the system dynamics of the host structure.

Chapter 7

Stability Analysis of the Analytical Models Developed for Cable-Harnessed Plate Structures

The major contribution of the current research includes the development of analytical models for the cable-harnessed plate structures. The models have been presented for cables attached to the host plate in parallel configuration in Chapter 4, and for cabled wrapping in a periodic pattern in Chapter 5. Although, the experimental validation was done for these proposed models, it is necessary to study the stability of the system through the obtained governing differential equations. Hence, in this chapter, the stability analysis of the cable-harnessed plate structures with all the attachment patterns is discussed. The work presented in this chapter has been discussed in the manuscripts [87, 93] submitted in the *ASME Journal of Vibration and Acoustics*.

The chapter is organized as follows: firstly, the stability of the cable-harnessed plate with parallel configuration is discussed. The conditions on the coefficients of the PDE are obtained that ensures the stability of the system and then, those conditions are discussed for cable attached along either x or y axis. In the subsequent section, the stability conditions are obtained for the coefficients of the PDEs of the cabled plate with zigzag and diagonal pattern. A proof of those conditions being satisfied by the PDE coefficients is then presented.

7.1 Parallel Cable-Harnessed Plates

In this section, the stability of the governing equation of motion of the parallel cabled plate presented in Eq. 4.22 is discussed. Because of the similar form of PDE with the specially orthotropic laminated plate, the stability conditions are first obtained for its coefficients. These conditions are then discussed for the PDE coefficients of the parallel cable-harnessed plate system.

7.1.1 Constraints on the coefficients of the PDE of a specially orthotropic laminated plate

The developed equation of motion for parallel cabled plate can be re-written from Eq. 4.22 as

$$D_{11}w_{,xxxx} + 2\left(D_{12} + 2D_{66}\right)w_{,xxyy} + D_{22}w_{,yyyy} + K_1 w_{,tt} = 0 \tag{7.1}$$

where the coefficients can be expanded in terms of system parameters as

$$\begin{aligned} D_{11} &= \left[D + \frac{E_c\ A_c\ z_c^2}{L_2} + \frac{T z_c^2}{L_2} - \frac{N_x h^2}{12}\right], \\ D_{22} &= D, \\ D_{66} &= \left(\frac{1}{2}\right)\left[D\left(1-\nu\right) - \frac{N_x h^2}{24}\right], \\ D_{12} &= \nu D, \\ K_1 &= \rho_p h + \rho_c A_c / L_2. \end{aligned} \tag{7.2}$$

Recall, that the Eq. 7.1 was compared to that of a specially orthotropic laminated plate, the governing equation of which was shown in Eq. 1.11 and was written as

$$D_{11}^o \frac{\partial^4 w(x,y,t)}{\partial x^4} + 2(D_{12}^o + 2D_{66}^o)\frac{\partial^4 w(x,y,t)}{\partial x^2 \partial y^2} + D_{22}^o \frac{\partial^4 w(x,y,t)}{\partial y^4} + \rho_p^o h_o \frac{\partial^2 w(x,y,t)}{\partial t^2} = 0 \tag{7.3}$$

For a specially orthotropic laminated plate, the PDE coefficients corresponding to the

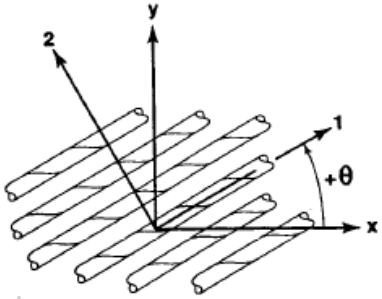

Figure 7.1: Schematic showing natural body axis (x-y) and material axis (1-2). Image courtesy: Jones [3]

stiffness can be written in terms of engineering constants and the plate thickness as [3]

$$\begin{aligned} D^o_{11} &= \frac{E_1 h_o^3}{12\left(1-\nu_{12}\nu_{21}\right)} \\ D^o_{22} &= \frac{E_2 h_o^3}{12\left(1-\nu_{12}\nu_{21}\right)} \\ D^o_{66} &= \frac{G_{12} h_o^3}{12} \\ D^o_{12} &= \frac{\nu_{12} E_2 h_o^3}{12\left(1-\nu_{12}\nu_{21}\right)} = \frac{\nu_{21} E_1 h_o^3}{12\left(1-\nu_{12}\nu_{21}\right)} \end{aligned} \tag{7.4}$$

where D^o_{ij} represents the coefficients of the PDE of specially orthotropic plate consisting of a single lamina of thickness h_o, E_1, E_2 represents Young's moduli along the perpendicular material axis in the plane $1-2$. G_{12} represents the shear modulus in the plane $1-2$. The difference between the material and geometry axis is shown in Fig. 7.1. It should be noted that for the specially orthotropic material, the material axis coincides with the geometry axis. Further, ν_{ij} represents the Poisson's ratio defined as the ratio of the negative of the strain in the $j-$direction to the strain in the $i-$direction, when the stress is applied in the $i-$direction.

In order to develop mathematical stability conditions for this PDE, firstly, the positive-definiteness of the stiffness matrix is used to obtain the following conditions on elastic and shear moduli [3]:

$$E_1 > 0,\ E_2 > 0,\ G_{12} > 0 \tag{7.5}$$

Similarly, the constraints on the Poisson's ratio are obtained as [3]

$$(1 - \nu_{12}\nu_{21}) > 0,\ |\nu_{21}| < \sqrt{E_2/E_1},\ |\nu_{12}| < \sqrt{E_1/E_2} \tag{7.6}$$

Using Eqs. 7.5 and 7.6, the following relations can be obtained for the coefficients of the specially orthotropic plate listed in Eq. 7.4

$$D^o_{11} > 0,\ D^o_{22} > 0,\ D^o_{66} > 0,\ (D^o_{12})^2 < D^o_{11}D^o_{22} \tag{7.7}$$

These conditions are sufficient to prove the stability of the PDE of a specially orthotropic laminated plate written in Eq. 7.3. Now, since the form of PDE is similar for a specially orthotropic laminated plate and parallel cable-harnessed plate, similar conditions are required to be fulfilled by the coefficients of the PDE written in Eq. 7.1.

$$D_{11} > 0,\ D_{22} > 0,\ (D_{12})^2 < D_{11}D_{22},\ D_{66} > 0 \tag{7.8}$$

7.1.2 Discussion on the coefficients of cable-harnessed plates satisfying the stability conditions

In this section, the conditions listed in Eq. 7.8 are discussed, which are related to the stability of the parallel cabled plate system.

1. $D_{11} > 0$

   The first condition in Eq. 7.8 is shown to hold true for all the possible values of system parameters. Using Eq. 7.2, the coefficient D_{11} can be expanded as

   $$D_{11} = \left[D + \frac{E_c A_c z_c^2}{L_2} + \frac{T z_c^2}{L_2} - \frac{N_x h^2}{12}\right] \tag{7.9}$$

   where $\left(D + \frac{E_c A_c z_c^2}{L_2}\right)$ is always positive because both the terms in the parenthesis are always positive. Moreover, the term $\left(\frac{T z_c^2}{L_2} - \frac{N_x h^2}{12}\right) = \left(\frac{T h^2}{4L_2} - \frac{T h^2}{12 L_2}\right) = \frac{T h^2}{6L_2}$ also remains positive. Here, the value of N_x was used from Eq. 4.12.

   Hence, the condition $D_{11} > 0$ always holds.

2. $D_{22} > 0$

   The second condition in Eq. 7.8 also holds true because, $D_{22} = D$ is always positive.

3. $(D_{12})^2 < D_{11}D_{22}$

Substituting the values of the coefficients from Eq. 7.2 on both the sides and analyzing them separately:

$$\begin{aligned} D_{11}D_{22} &= \left[D + \frac{E_c\ A_c\ z_c^2}{L_2} + \frac{Tz_c^2}{L_2} - \frac{N_x h^2}{12}\right] D \\ &= D^2 + D\left[\frac{E_c\ A_c\ z_c^2}{L_2} + \frac{Tz_c^2}{L_2} - \frac{N_x h^2}{12}\right] > D^2 \\ &\text{because } D\left[\frac{E_c\ A_c\ z_c^2}{L_2} + \frac{Tz_c^2}{L_2} - \frac{N_x h^2}{12}\right] > 0 \end{aligned} \tag{7.10}$$

Moreover, the left hand side of the conditions can be written as

$$D_{12}^2 = \left(\nu^2 D^2\right) < D^2 \tag{7.11}$$

because $\nu^2 < 1$ holds true for all the isotropic materials. Clearly, $D_{12}^2 < D^2$ and $D_{11}D_{22} > D^2$ proves that the third condition always holds.

4. $D_{66} > 0$

For the coefficient $D_{66} = \left(\frac{1}{2}\right)\left[D\,(1-\nu) - \frac{N_x h^2}{24}\right] > 0$ to hold true, the first term $D(1-\nu)$, which is always positive, should always be greater than $N_x h^2/24$. Hence, the condition $N_x < 2E_p h/(1+\nu)$ should always be true for stability. To obtain the upper bound on N_x, the maximum value of cable tension must be calculated to ensure the stability of the system. To calculate the maximum value of cable tension, two types of cable attachment patterns are considered: (a) Cables attached perpendicular to the clamped edge, (b) Cables attached parallel to the clamped edge, as also considered in Chapter 4 for experimental purpose. Although in both these cases, the $x-$axis is assumed to be along the direction of the cable attachment for the modeling purpose.

(a) Cables attached perpendicular to the clamped edge

The compressive loading on the plate is perpendicular to the direction of the clamped edge. In this case, the maximum value of cable tension can be restricted by the critical buckling load of a cantilevered plate under a uniformly distributed compressive loading perpendicular to the clamped edge. This can be approximated by the critical buckling load of a cantilevered beam as:

$$P_{cr} = \frac{\pi^2 E_p}{4a^2}\left(\frac{bh^3}{12}\right) \tag{7.12}$$

Since the total compressive force exerted by the cables on the plate is nT, where n represents the number of cables, the critical tension becomes $T_{cr} = P_{cr}/n$. Therefore, the maximum value of N_x can be written as

$$(N_x)_{cr} = \frac{1}{nL_2}\frac{\pi^2 E_p}{4a^2}\left(\frac{bh^3}{12}\right) \tag{7.13}$$

Substituting the maximum value of N_x in the expression of D_{66}, we get

$$D_{66} \geq \frac{1}{2}\left[D\left(1-\nu\right) - \frac{h^2}{24}\left(\frac{1}{nL_2}\right)\frac{\pi^2 E_p}{4a^2}\left(\frac{bh^3}{12}\right)\right] \tag{7.14}$$

This can be further simplified and written as:

$$D_{66} \geq \frac{E_p h^3}{24}\left[\frac{1}{1+\nu} - 0.102\left(\frac{h}{a}\right)^2\right] \tag{7.15}$$

Since, for the thin plates, $h \ll a$, the condition $D_{66} > 0$ holds true for isotropic host plate materials as seen from Eq. 7.15.

(b) Cables attached parallel to the clamped edge

The distributed compressive load now acts parallel to the clamped edge on the opposite free edges. The maximum value of N_x can be obtained using formulation of critical buckling load presented in [95] as

$$(N_x)_{cr} = D/a^2\left(207.6 + 2.03k^4 - 19.08k^2 - 167.08\nu - 3.79\nu k^2 + 34.193\nu^2\right) \tag{7.16}$$

where $k = a/b$ is the plate's aspect ratio. Further, if it is assumed that $\nu = 0.33$, the above expression can be simplified as

$$(N_x)_{cr} = \frac{D}{a^2}\left(155.85 - 20.34\ k^2 + 2.03\ k^4\right) \tag{7.17}$$

Now, on analyzing $D_{66} = \left(\frac{1}{2}\right)\left[D\left(1-\nu\right) - \frac{N_x h^2}{24}\right]$, it can be seen that $D(1-\nu)$ is independent of dimensions a and b. However, the maximum value of allowable N_x to avoid buckling depends on both a and b as shown in Eq. 7.16 and has a biquadratic dependency on the aspect ratio (a/b). Hence, it increases upon either increasing or decreasing the aspect ratio about its minimum point. As a result, for cases with very small or large aspect ratios, the critical load limit will increase tremendously leading in the term $N_x h^2/24$ increasing and resulting

in negative D_{66} values for large tension loads. The coefficient D_{66} is equivalent to the in-plane shear modulus dependent term in a specially orthotropic plate and it being negative will result in an unstable condition. As an example, this condition can happen for a plate with a very high aspect ratio with the longer edge clamped and cables running parallel to the clamp edge.

Now one reasonable question is that if the tension remains below the critical buckling then what will be the source of instability in the system arising from the negative D_{66}. The kind of instability happening in this case pertains to a form of a torsional instability. This is also evident as the D_{66} coefficient is equivalent to the shear modulus in a specially orthotropic plate which is related to the torsion. Therefore, the torsional instability occurs prior to reaching critical buckling and both conditions from Eq. 7.16 and D_{66} remaining positive should be used in practice to create a stable system when considering the allowable tension values. Hence, the maximum tension should be applied using the following formulation:

$$\begin{aligned} &T_{max} < \min\left(T_1, T_2\right), \text{where} \\ &T_1 = \frac{Db}{a^2 n}\left(207.6 + 2.03k^4 - 19.08k^2 - 167.08\nu - 3.79\nu k^2 + 34.193\nu^2\right) \\ &T_2 = \left(\frac{2E_p bh}{n\left(1+\nu\right)}\right) \end{aligned} \tag{7.18}$$

Regarding the stability, one can also examine the twist strain energy of the plate as follows:

$$U_{twist} = \int_0^a \int_0^b \left[\left\{-\frac{N_x h^2}{24} + D\left(1-\nu\right)\right\} w_{,xy}^2\right] dx\ dy \tag{7.19}$$

The term within curly brackets shown in Eq. 7.19 starts to become negative for large tension values due to the N_x term. As a result, the system will have a negative torsional stiffness which will lead to a torsional instability. It should be noted that the term $\left(-\frac{N_x h^2}{24} w_{,xy}^2\right)$ originates from considering the second-order strain-displacement relation.

To summarize, the first three conditions shown in Eq. 7.8 were found to always hold. However, care must be taken while choosing the tension values for very large or very small aspect ratio plates such that the fourth stability condition also holds. The maximum cable tension to ensure that this condition also holds is shown in Eq. 7.18.

7.2 Periodically Wrapped Cable-Harnessed Plates

In this section, emphasis is given to the stability of the PDEs obtained for the periodically wrapped cabled plates in Chapter 5. The governing equation of motion presented in Eq. 5.36 was obtained for both, zigzag and diagonal pattern. With the coefficients H_{10} and H_{11} vanishing for the zigzag pattern, it was discussed that the form of PDE was similar to that of the parallel cabled plate. Hence, the stability conditions developed for the parallel cabled plate can be used for the zigzag cabled plate, however, the stability conditions for the diagonal pattern are derived further in this section due to a new form of PDE.

7.2.1 Stability of the PDE for the zigzag pattern

Since the PDE for the zigzag pattern is similar in form to a specially orthotropic laminate (or the parallel cabled plate), the following conditions on the coefficients of the PDE ascertain the stability in the system:

$$H_2 > 0,\ H_3 > 0, H_4 > 0,\ H_{13}^2 < 4H_2H_3 \tag{7.20}$$

These conditions are similar to those obtained for the parallel cabled plate in Eq. 7.8. In order to prove the cable-harnessed plate model with zigzag pattern is stable, the four conditions listed in Eq. 7.20 need to be satisfied by the system parameters.

Proof of stability conditions for the zigzag pattern

1. $H_2 > 0$

   This coefficient can be written from appendix section B.2.1 as:

   $$H_2 = D + \frac{E_c A_c z_c^2 \cos^3\theta}{L_2} + \frac{T z_c^2 \cos\theta}{L_2} + \frac{N_x h^2}{24} \tag{7.21}$$

   Since $z_c = \frac{h}{2}$ and $N_x = -\frac{n\ T\cos\theta}{b} = -\frac{T\cos\theta}{L_2}$, the expression of H_2 can be simplified and written as

   $$H_2 = D + \frac{E_c A_c h^2 \cos^3\theta}{4\ L_2} + \frac{5}{24}\frac{T h^2 \cos\theta}{L_2} \tag{7.22}$$

   All the parameters listed in this equation is greater than zero and hence, $H_2 > 0$.

2. $H_3 > 0$

Using section B.2.1, the coefficient H_3 is expanded as:

$$H_3 = D + \frac{E_c A_c z_c^2 \sin^4\theta}{L_2 \cos\theta} + \frac{T z_c^2 \sin^2\theta}{L_2 \cos\theta} + \frac{N_y h^2}{24} \tag{7.23}$$

Since $z_c = \frac{h}{2}$ and $N_y = -\frac{2mT\sin\theta}{a} = -\frac{2T\sin\theta}{L_1}$, the expression of H_3 can be simplified and written as

$$H_3 = D + \frac{E_c A_c h^2 \sin^3\theta}{4L_2} + \frac{T h^2 \sin\theta}{2L_1} - \frac{T h^2 \sin\theta}{12 L_1} \tag{7.24}$$

In writing the above expression, the relation $\tan\theta = 2L_2/L_1$ is used. $H_3 > 0$ is obvious from this equation.

3. $H_4 > 0$

   Expansion of H_4 using section B.2.1 results in

$$H_4 = 2D(1-\nu) + \frac{4E_c A_c z_c^2 \cos\theta \sin^2\theta}{L_2} + \frac{T z_c^2}{L_2 \cos\theta} + \frac{N_x h^2}{24} + \frac{N_y h^2}{24} \tag{7.25}$$

   Substituting the values of N_x and N_y in this equation, it can be simplified as

$$H_4 = 2D(1-\nu) + \frac{E_c A_c h^2 \cos\theta \sin^2\theta}{L_2} + \frac{T h^2}{4\ L_2}\left(\frac{1}{\cos\theta} - \frac{\cos\theta}{3}\right) \tag{7.26}$$

   Since $\theta \in (0, \pi/2)$ and $\nu < 0.5$, the condition $H_4 > 0$ would always hold.

4. $H_{13}^2 < 4H_2H_3$

   On substituting the values of H_2, H_3, and H_{13} from section B.2.1 by moving all the terms on the right-hand side (RHS), and ignoring the higher-order terms that are originated due to considering the second-order strain displacement relation, we get:

$$4H_2H_3 - H_{13}^2 = 4D^2\left(1-\nu^2\right) + \frac{4DE_cA_cz_c^2}{L_2}\left(\cos^3\theta + \sin^3\theta\tan\theta - 2\nu\cos\theta\sin^2\theta\right) \tag{7.27}$$

   In this equation, the first term of the RHS is always positive and the term outside the parenthesis of the second terms is also always positive. To prove that $4H_2H_3 - H_{13}^2 > 0$ always hold, it has to be proven that

$$\Upsilon = \cos^3\theta + \sin^3\theta\tan\theta - 2\nu\cos\theta\sin^2\theta > 0 \tag{7.28}$$

This expression can be written as

$$\Upsilon = \cos^3\theta \left\{ \left(1 + \tan^2\theta\right)^2 - 2\left(1+\nu\right)\tan^2\theta \right\} \tag{7.29}$$

The minimum value of Υ would be attained when $\nu = 0.5$. Hence,

$$\Upsilon_{min} = \cos^3\theta \left\{ \left(1 + \tan^2\theta\right)^2 - 3\tan^2\theta \right\} \tag{7.30}$$

Since $\left(1 + \tan^2\theta\right)^2 - 3\tan^2\theta$ can be written as $\left(1 - \tan^2\theta\right)^2 + \tan^2\theta$, it is clear that $\Upsilon_{min} > 0$ for $\theta \in (0, \pi/2)$. This implies the condition $4H_2H_3 - H_{13}^2 > 0$ holds for the zigzag pattern.

In summary, all the four conditions required to prove the stability of the PDE for the zigzag pattern are satisfied and hence, the analytical model developed for the zigzag pattern is always stable.

7.2.2 Stability of the PDE for the diagonal pattern

In the case of diagonal pattern, due to the presence of the additional terms corresponding to H_{10} and H_{11} in the equation of motion (Eq. 5.36), the stability conditions mentioned in the previous section for zigzag pattern can not be used. Therefore, for the diagonal pattern, the stability conditions are firstly derived and then it is proven that the PDE coefficients satisfy those conditions.

Derivations of stability conditions for the diagonal pattern

To obtain the stability conditions of the homogenized model for the cable-harnessed plate with a diagonal pattern, the positive-definiteness of the stiffness matrix is used. The strain energy corresponding to the equation of motion (Eq. 5.36) for the diagonal pattern can also be written in the form:

$$U_{sys,diag} = \frac{1}{2}\int_0^a \int_0^b X^T K_{diag} X \; dxdy \tag{7.31}$$

where $X = \{w_{,xx} \;\; w_{,yy} \;\; w_{,xy}\}^T$ and the stiffness matrix is written as

$$K_{diag} = \begin{bmatrix} H_2 & H_{13}/2 & H_{10}/2 \\ H_{13}/2 & H_3 & H_{11}/2 \\ H_{10}/2 & H_{11}/2 & H_4 \end{bmatrix} \tag{7.32}$$

The positive definiteness of this matrix ensures the stability of the system. This implies that all three eigenvalues of this matrix should be positive real numbers. Since the eigenvalues of a symmetric matrix are always real, the conditions need to be obtained such that the eigenvalues are positive. To do so, the characteristic cubic equation in terms of eigenvalue λ is obtained using $|K_{diag} - \lambda\ I| = 0$, where $|\bullet|$ denotes the determinant of the matrix within it, and I denotes the identity matrix. The characteristic equation is obtained as

$$f_d(\lambda) = \lambda^3 + A_d\lambda^2 + B_d\lambda + C_d = 0 \tag{7.33}$$

where

$$\begin{aligned} A_d &= -(H_2 + H_3 + H_4), \\ B_d &= -\frac{1}{4}\left(H_{10}^2 + H_{11}^2 + H_{13}^2\right) + H_2H_3 + H_2H_4 + H_3H_4, \text{and} \\ C_d &= -H_2H_3H_4 - \frac{1}{4}H_{10}H_{11}H_{13} + \frac{1}{4}\left(H_{11}^2H_2 + H_{10}^2H_3 + H_{13}^2H_4\right). \end{aligned} \tag{7.34}$$

The conditions for the cubic equation shown in Eq. 7.33 to have positive roots are:

1. The roots of the equation $\frac{\partial f_d(\lambda)}{\partial \lambda} = 0$ should be positive, and
2. $f_d(0)$ should be negative.

These conditions can be interpreted graphically by plotting a general cubic equation plot (with leading coefficient as 1) and analyzing the λ's at zero slopes along with the $y-$axis intercept of the plot. Additionally, these conditions hold for different cases of positive roots: all roots are discrete, two repeated roots, three repeated roots as shown in Fig. 7.2. The condition 1 can be further broken down into two conditions to simplify the calculations: the sum of the roots and the product of the roots of the quadratic equation, $\frac{\partial f_d(\lambda)}{\partial \lambda} = 0$ should be positive. These conditions along with the condition 2 can be written in terms of the PDE coefficients as

$$\begin{aligned} H_2 + H_3 + H_4 &> 0, \\ H_{10}^2 + H_{11}^2 + H_{13}^2 &< 4\left(H_2H_3 + H_2H_4 + H_3H_4\right), \text{and} \\ 4H_2H_3H_4 + H_{10}H_{11}H_{13} &> H_{11}^2H_2 + H_{10}^2H_3 + H_{13}^2H_4 \end{aligned} \tag{7.35}$$

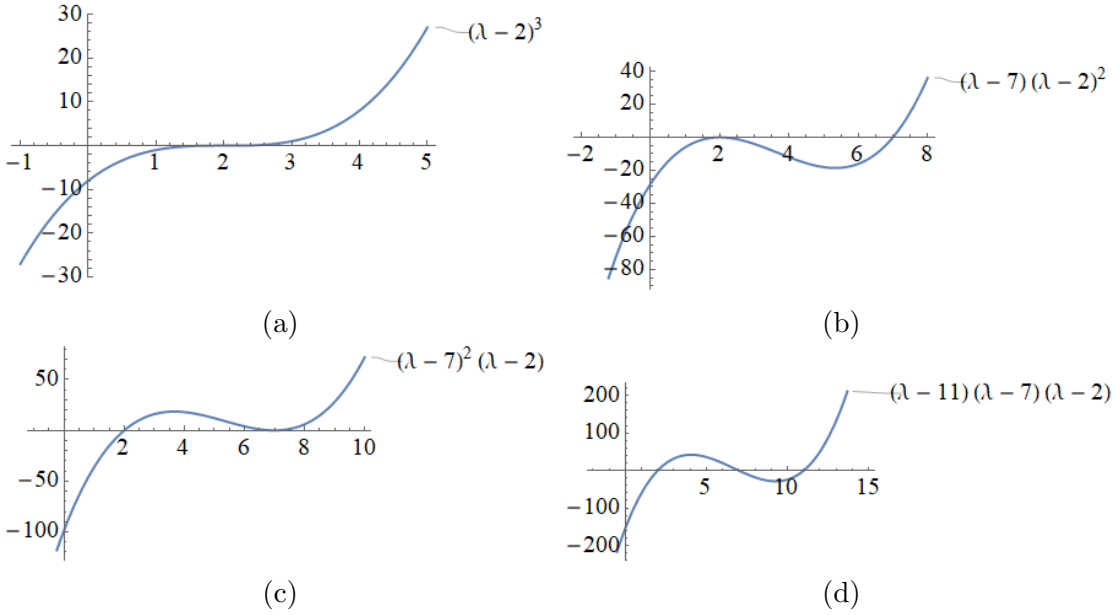

Figure 7.2: Four possible sample cases of cubic polynomials with positive real roots

These are the three stability conditions that needs to be satisfied by the coefficients of the PDE corresponding to the diagonal pattern. The proofs for each condition holding true are outlined as follows:

Proof of stability conditions for diagonal pattern

1. $H_2 + H_3 + H_4 > 0$

   In order to prove this condition, the coefficients, H_2, H_3, and H_4 are substituted from appendix section B.2.2 for the diagonal pattern. Substituting $z_c = h/2$ and the values of N_x and N_y from Eq. 5.21, one can easily proove $H_2 > 0$, $H_3 > 0$ and $H_4 > 0$ similar to that done for the zigzag pattern done in the previous section. This proves the first condition.

2. $H_{10}^2 + H_{11}^2 + H_{13}^2 < 4\,(H_2H_3 + H_2H_4 + H_3H_4)$

   Substituting the coefficients from appendix section B.2.2 in terms of the system parameters and after taking all the terms on the right hand side, the second condition

can be expanded as

$$
\begin{aligned}
&4\left(H_2H_3+H_2H_4+H_3H_4\right)-\left(H_{10}^2+H_{11}^2+H_{13}^2\right)\\
&\quad=D^2\left(20-16\nu-4\nu^2\right)+\frac{A_cDE_cz_c^2}{L_1}\left(12-8\nu^2\right)+\frac{4A_c^2E_c^2z_c^4\cos^3\theta}{L_1L_2}\\
&\qquad+\frac{A_cDE_cz_c^2\cos^3\theta}{L_2}\left(12-8\nu\right)+\frac{16A_c^2E_c^2z_c^4\cos\theta\sin^2\theta}{L_1L_2}\\
&\qquad+\frac{A_cDE_cz_c^2\cos\theta\sin^2\theta}{L_2}\left(32-8\nu\right)+\frac{A_cDE_cz_c^2\sin^3\theta}{L_1}\left(12-8\nu\right)\\
&\qquad+\frac{4A_c^2E_c^2z_c^4\cos^3\theta\sin^3\theta}{L_1L_2}+\frac{16A_c^2E_c^2z_c^4\cos\theta\sin^5\theta}{L_1L_2}\\
&\qquad-\frac{4A_c^2E_c^2z_c^4\cos^2\theta\sin^4\theta}{L_2^2}-\frac{16A_c^2E_c^2z_c^4\sin^6\theta}{L_2^2}
\end{aligned}
\tag{7.36}
$$

During the simplification of Eq. 7.36, the terms originating from higher-order terms of strain-displacement relation are ignored because of their small magnitude. Using $\tan\theta = L_2/L_1$, the last four terms of this equation vanishes on simplification. The remaining terms of this equation are positive provided $\theta \in (0, \pi/2)$ and $\nu < 0.5$. This proves that the PDE coefficients for the diagonal pattern satisfies the second stability condition

3. $4H_2H_3H_4 + H_{10}H_{11}H_{13} > H_{11}^2H_2 + H_{10}^2H_3 + H_{13}^2H_4$

   Similar to the previous condition, substituting the coefficients in terms of system parameters from appendix section B.2.2 and taking all the terms on the left-hand

side, the condition can be written as

$$
\begin{aligned}
4H_2H_3H_4 + H_{10}H_{11}H_{13} - \left(H_{11}^2H_2 + H_{10}^2H_3 + H_{13}^2H_4\right) \\
= 8D^3\left(1-\nu\right)\left(1-\nu^2\right) + \frac{8A_cD^2E_cz_c^2}{L_1}\left(1-\nu\right) \\
+ \frac{8A_cD^2E_cz_c^2}{L_2}\left(1-\nu\right)\cos^3\theta + \frac{8A_c^2DE_c^2z_c^4}{L_1L_2}\left(1-\nu\right)\cos^3\theta \\
+ \frac{16A_cD^2E_cz_c^2}{L_2}\left(1-\nu\right)\cos\theta\sin^2\theta + \frac{16A_c^2DE_c^2z_c^4}{L_1L_2}\cos\theta\sin^2\theta \\
+ \frac{8A_cD^2E_cz_c^2\sin^3\theta}{L_1}\left(1-\nu\right) + \frac{8A_c^2DE_c^2z_c^4}{L_1L_2}\cos^3\theta\sin^3\theta\left(1-\nu\right) \\
- \frac{8A_c^2DE_c^2z_c^4}{L_2^2}\cos^2\theta\sin^4\theta\left(1-\nu\right) + \frac{16A_c^2DE_c^2z_c^4}{L_1L_2}\cos\theta\sin^5\theta \\
- \frac{16A_c^2DE_c^2z_c^4}{L_2^2}\sin^6\theta \quad (7.37)
\end{aligned}
$$

The terms originating from higher-order terms of strain-displacement relation are ignored during the simplification of this equation. Also, the last four terms of this equation vanish on simplification. The remaining terms are positive since $\theta \in (0, \pi/2)$ and $\nu < 0.5$. This proves the third stability condition.

Hence, for the coefficients of the cable-harnessed plate with the diagonal pattern, all the three stability conditions are satisfied and the system model is found stable.

7.3 Summary of the chapter

In this chapter, the stability of the analytical models developed for the cable-harnessed plate structures in Chapters 4 and 5 was discussed. When the system is unstable, the response of that system can be very high (theoretically infinite) upon giving a small finite input. Hence, it is important that the system remains stable under operating conditions.

The analytical model for cable-harnessed structure with parallel cable configuration was found to be generally stable, however, care should be taken when the cable tension is chosen. This is because, when the plate aspect ratios were chosen to be either very large or very small, the system is found to become unstable at extremely high tension values due to the occurrence of torsional instability. Additionally, for the zigzag and diagonally

wrapped cable-harnessed structures, the system was found stable. In contrast to parallel cabled-plates, the torsional instability did not occur in these systems due to the presence of the cable inclined segments which increases the twisting stiffness of the structure and avoids the instability.

Chapter 8

Preliminary Study on Cable-Harnessed Cylindrical Shells

In this thesis, so far, the research work focused on the accurate model development of cable-harnessed systems that have either beams or plates as host structures. The plate structure, although more complicated, but due to the presence of an additional dimension, was able to provide better insights into the dynamics of the system compared to the host beam structure. This further motivates us to look into other host structures that are more practical and provides further insights into the dynamics of cable-harnessed systems which have not been studied before. One such practical structure which is considered as a host in this chapter is a thin cylindrical shell structure. Cylindrical shells are the principal structural elements of various marine and airborne structures. For example, the fuselage of an aircraft can be roughly modeled as a cylindrical structure. Similarly, the submarines are also generally in the shape of a cylindrical shell. As per the author's knowledge, no published works are present in the literature on developing the models of cable-harnessed shells.

The objective of this chapter is to propose the analytical models for cable-harnessed cylindrical shells using the shell theory developed for analyzing thin closed cylindrical shells. In this chapter, the preliminaries of the shell theories are first presented. Further, the cable-harnessed shell is modeled by assuming the cables to be attached parallel to the axis of the cylinder along its length. For the purpose of obtaining an analytical model, multiple cables are attached that are equidistant. The host cylindrical shell is modeled using Donnell-Mustari Shell theory. This chapter is an additional extension of the research work proposed during the PhD comprehensive exam. Hence, the discussion of the proposed model has been limited to comparing the natural frequencies with ANSYS. A more detailed

analysis and experimental validation of the proposed model can be carried out as a future work.

8.1 Preliminaries of the thin shell theory

A shell is defined as a three-dimensional body that is bounded by two closely spaced surfaces. For the thin shells, the distance between the two surfaces is very small compared to the other dimensions. A shell can be regarded as generalization of a flat plate that can has a curvature; in other words, a flat plate is a special case of a shell with no curvature.

There are several shell theories which have been proposed in the literature. Differences in these theories arise from slight simplifying assumptions that lead to different governing equations. Some of the common shell theories that are studied in the literature are obtained from Love's Postulates (discussed later) and are attributed to Donnell [96], Mushtari [97], Love [98], Timoshenko [89], Reissner [99], Naghdi and Berry [100], Vlasov [101], Sanders [102], Flugge [103], Goldenveizer [104]. Some of these theories are dependent on each other and hence, certain equations are common between them. In the present study, the theories presented by Donnell-Mushtari are considered, mainly for its simpler formulation. At certain stages, the comparison of this theory has been made with a more accurate Flugge theory, which can be considered in the future for a more accurate model development.

The detailed derivations of the governing equations using the above mentioned theories have been very well explained in a monologue by Leissa [4]. In this work, the shell theory is first derived for a general coordinate system, which can be used for shell of any shape (conical, cylindrical, spherical, etc.). Since the focus of the current work is based on the cylindrical shells, some basics are presented in the following sections.

8.1.1 Equation of motion of a cylindrical shell

The classical shell theory through which the governing equations of motion of cylindrical shell are derived are based on the following assumptions (also known as Love's Postulates [98]):

1. The thickness of the shell is small compared to the other dimensions.
2. The displacements and strains are very small. Mathematically, the higher-order magnitude in the strain-displacement relations may be neglected compared to the first-order terms.

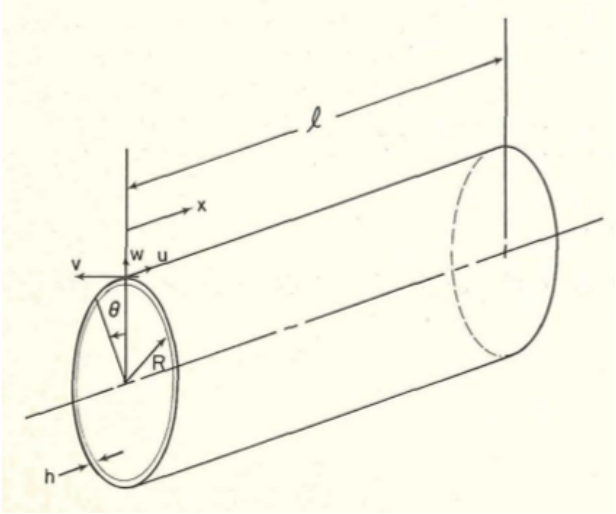

Figure 8.1: Closed circular cylindrical shell and coordinate axis. Image courtesy: Leissa [4]

3. The transverse normal stress (in the thickness direction) is small compared to the other normal stresses and may be neglected.

4. The shearing and warping of the cross section is neglected during the vibrations. This means that the normals to the undeformed middle surface remain straight and normal to the deformed middle surface and suffer no extension.

A schematic of a cylindrical shell is shown in Fig. 8.1 with the coordinates x and θ. Note that the variable, θ, used in this chapter is corresponding to the cylindrical coordinate system, and is different from the wrapping angle used in previous chapters. The length coordinate x is replaced by a non-dimensionless length defined by

$$s = x/R \tag{8.1}$$

where R is the cylindrical radius.

The equation of motion of the cylindrical shell can be expressed in a matrix form [4] as

$$[L]\{u_i\} = \{0\} \tag{8.2}$$

where $[L]$ is a matrix differential operator defined differently for various shell theories, and

$\{u_i\}$ is the displacement vector written as

$$\{u_i\} = \begin{Bmatrix} u \\ v \\ w \end{Bmatrix} \tag{8.3}$$

In this equation, u, v, and w are the orthogonal component in axial, circumferential, and radial directions, respectively, as also shown in Fig. 8.1.

Commonly, the vibrations of circular cylinders are modeled using eighth order differential equation. In Eq. 8.2, the operator $[L]$ can be treated as sum of two operators

$$[L] = [L_{D-M}] + k\,[L_{MOD}] \tag{8.4}$$

where $[L_{D-M}]$ is the differential operator according to the Donnell-Mushtari (DM) theory and $[L_{MOD}]$ is a 'modifying' operator which alters DM theory to yield another shell theory. Also, k is a dimensionless constant defined by

$$k = \frac{h^2}{12R^2} \tag{8.5}$$

where h is the shell thickness. Therefore, each eighth order shell theory differs from DM theory by an operator $[L_{MOD}]$ which is multiplied by a constant k, which is very small for low thickness to radius ratio.

The $[L]$ operator for the DM theory takes the form [4]:

$$[L_{DM}] = \begin{bmatrix} \frac{\partial^2}{\partial s^2} + \frac{(1-\nu)}{2}\frac{\partial^2}{\partial \theta^2} - \frac{\rho\left(1-\nu^2\right)}{E}R^2\frac{\partial^2}{\partial t^2} & \frac{1+\nu}{2}\frac{\partial^2}{\partial s \partial \theta} & \nu\ \frac{\partial}{\partial s} \\ \frac{1+\nu}{2}\frac{\partial^2}{\partial s \partial \theta} & \frac{1-\nu}{2}\frac{\partial^2}{\partial s^2} + \frac{\partial^2}{\partial \theta^2} - \frac{\rho\left(1-\nu^2\right)}{E}R^2\frac{\partial^2}{\partial t^2} & \frac{\partial}{\partial \theta} \\ \nu\ \frac{\partial}{\partial s} & \frac{\partial}{\partial \theta} & 1 + k\nabla^4 + \frac{\rho\left(1-\nu^2\right)}{E}R^2\frac{\partial^2}{\partial t^2} \end{bmatrix} \tag{8.6}$$

where $\nabla^4 = \nabla^2\nabla^2$ and $\nabla^2 = \frac{\partial^2}{\partial s^2} + \frac{\partial^2}{\partial \theta^2}$. E is the shell's Young's modulus, ν is Poisson's ratio and ρ is the shell's mass density. Clearly, using Eqs. 8.6 and 8.2, three coupled equations of motion can be obtained which govern the motion in axial, circumferential and radial directions. Similarly, $[L_{MOD}]$ can be written for various cylindrical shell theories, refer [4]. The modifying operator for Flugge shell theory can be written as

$$[L_{MOD}] = \begin{bmatrix} \frac{(1-\nu)}{2}\frac{\partial^2}{\partial \theta^2} & 0 & -\frac{\partial^3}{\partial s^3} + \frac{(1-\nu)}{2}\frac{\partial^3}{\partial s\ \partial \theta^2} \\ 0 & 3\frac{(1-\nu)}{2}\frac{\partial^2}{\partial s^2} & -\frac{(3-\nu)}{2}\frac{\partial^3}{\partial s^2\ \partial \theta} \\ -\frac{\partial^3}{\partial s^3} + \frac{1-\nu}{2}\frac{\partial^3}{\partial s\ \partial \theta^2} & -\frac{(3-\nu)}{2}\frac{\partial^3}{\partial s^2\ \partial \theta} & 1 + 2\frac{\partial^2}{\partial \theta^2} \end{bmatrix} \tag{8.7}$$

8.1.2 Energy formulation

In order to develop the governing equations of motion for a cable-harnessed structure, it is necessary to obtain the strain and kinetic energy of the thin cylindrical shell. Using these energy expressions, Hamilton's principle can be applied to obtain the governing equations of motion.

Strain Energy

Assuming the general shell coordinates to be α and β, where for cylindrical coordinates $\alpha = s$, and $\beta = \theta$, the strain energy expression can be written as

$$U = \int_V (\sigma_\alpha e_\alpha + \sigma_\beta e_\beta + \ \sigma_{\alpha\beta} e_{\alpha\beta})\, dV \tag{8.8}$$

where σ_α and σ_β represent normal stress in α and β directions, respectively, and e_α and e_β represent the normal strain in α and β directions, respectively. Also, the terms with subscripts $\alpha\beta$ represents the shear counterparts. The stress-strain relationships are further written as

$$\begin{aligned} \sigma_\alpha &= \frac{E}{1-\nu^2}\left(e_\alpha + \nu e_\beta\right) \\ \sigma_\beta &= \frac{E}{1-\nu^2}\left(e_\beta + \nu e_\alpha\right) \\ \sigma_{\alpha\beta} &= \frac{E}{2\left(1+\nu\right)}\gamma_{\alpha\beta} \end{aligned} \tag{8.9}$$

The total strain energy by substituting Eq. 8.9 in Eq. 8.8 is obtained as

$$U = \frac{E}{4\left(1-\nu^2\right)} \int_V (2e_\alpha^2 + 2e_\beta^2 + \gamma_{\alpha\beta}^2\left(1-\nu\right) + 4\nu e_\alpha e_\beta) dV \tag{8.10}$$

The strain-displacement relations for the DM theory are written as [4]:

$$\begin{aligned} e_\alpha &= \frac{1}{R}\frac{\partial u}{\partial \alpha} - \frac{z}{R^2}\frac{\partial^2 w}{\partial \alpha^2} \\ e_\beta &= \frac{1}{1+\frac{z}{R}}\left(\frac{1}{R}\frac{\partial v}{\partial \beta} + \frac{w}{R} - \frac{z}{R^2}\frac{\partial^2 w}{\partial \beta^2}\right) \\ \gamma_{\alpha\beta} &= \frac{1}{1+\frac{z}{R}}\left(\frac{1}{R}\left(\frac{\partial u}{\partial \beta} + \frac{\partial v}{\partial \alpha}\right) + z\left(1+\frac{z}{2R}\right)\left(-\frac{2}{R^2}\right)\frac{\partial^2 w}{\partial \alpha \partial \beta}\right) \end{aligned} \tag{8.11}$$

In this equation, the total strains, at a distance z from the mid-surface in the transverse direction, are written using the normal strains on the mid-surface and the change in curvature or twist of the mid-surface. In the next step, the relations in Eq. 8.11 are substituted in Eq. 8.10 to obtain the total strain energy of a shell according to DM theory:

$$U = \frac{Eh}{2\left(1-\nu^2\right)} \int_0^{2\pi} \int_0^1 \left[I_{DM}\right] ds d\theta \tag{8.12}$$

where

$$I_{DM} = \left(\frac{\partial u}{\partial s} + \frac{\partial v}{\partial \theta} + w\right)^2 - 2\left(1-\nu\right)\left(\frac{\partial u}{\partial s} w - \frac{1}{4}\left(\frac{\partial v}{\partial s} - \frac{\partial u}{\partial \theta}\right)^2\right) + k\left\{\left(\nabla^2 w\right)^2 - 2\left(1-\nu\right)\left(\frac{\partial^2 w}{\partial s^2}\frac{\partial^2 w}{\partial \theta^2} - \left(\frac{\partial^2 w}{\partial s\, \partial \theta}\right)^2\right)\right\} \tag{8.13}$$

It should be noted that the total energy is composed of two components. First, the membrane strain energy that is due to the stretching of the mid-surface and second, due to the bending of the shell. The bending component is shown within the curly braces in Eq. 8.13. Also, while writing this equation, the general shell variables (α, β) were replaced by the cylindrical coordinate variables (s, θ).

Kinetic Energy

Neglecting rotary inertia and considering the velocities in all the three directions, the kinetic energy of the shell is written as

$$T = \frac{1}{2}\rho h \int_0^{2\pi} \int_0^1 \left[\left(\frac{\partial u}{\partial t}\right)^2 + \left(\frac{\partial v}{\partial t}\right)^2 + \left(\frac{\partial w}{\partial t}\right)^2\right] R^2 ds d\theta \tag{8.14}$$

Using the strain and kinetic energy expressions obtained in Eq. 8.12 and 8.14, applying the Hamilton's principle, the governing equations of motion shown in Eq. 8.2 can be developed, for which the differential operator $[L]$ for the DM theory is shown in Eq. 8.6.

8.1.3 Calculation of natural frequencies for Shear-Diaphragm boundaries

In this section, the closed form and exact natural frequencies of a thin closed circular cylinder are presented that satisfies the following boundary conditions

$$w = M_x = P_x = v = 0 \qquad x = 0, l \tag{8.15}$$

where M_x and P_x denote the bending moment and longitudinal membrane force, respectively, as the shell deforms. The conditions listed in Eq. 8.15 closely approximates the physical application where the shell is rigidly attached to a thin, flat, circular cover plate at each end. These plates have considerable stiffnesses in their own plane, hence, constraining the transverse displacements v and w, however, the stiffness along the $x-$direction is very low. This generates negligible bending moment and longitudinal membrane forces and hence, these boundaries are called *shear diaphragm* (SD-SD). These boundary conditions have received the largest attention so far in the literature due to the fact that one can obtain closed form solutions for the frequency and is relatively easy to analyze. Later in this chapter, these boundary conditions would be used to study the cable-harnessed shell structures as well.

Consider the following solution of displacements that satisfy the SD-SD boundary conditions exactly

$$\begin{aligned} u &= A\cos\lambda s \;\; \cos n\theta \;\; \cos\omega t \\ v &= B\sin\lambda s \;\; \sin n\theta \;\; cos\omega t \\ w &= C\sin\lambda s \;\; \cos n\theta \;\; cos\omega t \end{aligned} \tag{8.16}$$

where A, B, and C are undetermined coefficients, n is an integer, and ω is the vibration frequency expressed in rad/s. In order to satisfy the conditions presented in Eq. 8.15 exactly, the value of λ is chosen as

$$\lambda = m\pi R/l \qquad \text{where } m = 1, 2, 3... \tag{8.17}$$

Substituting the displacements written in Eq. 8.16 in Eqs. 8.2 and 8.6 results in three homogeneous equations in the variables A, B, and C. In order to obtain the non-trivial solutions of the homogeneous equations, the characteristic determinant can be obtained as follows:

$$\text{Det}\begin{bmatrix} -\lambda^2 - \frac{(1-\nu)}{2}n^2 + \frac{\rho(1-\nu^2)R^2\omega^2}{E} & \frac{(1+\nu)}{2}\lambda n & \nu\lambda \\ \frac{(1+\nu)}{2}\lambda n & -\frac{(1-\nu)}{2}\lambda^2 - n^2 + \frac{\rho(1-\nu^2)R^2\omega^2}{E} & -n \\ -\nu\ \lambda & n & 1 + k(\lambda^2+n^2)^2 - \frac{\rho(1-\nu^2)R^2\omega^2}{E} \end{bmatrix} \tag{8.18}$$

This characteristic determinant has been written using DM theory. The only variable in this determinant is ω, which can be obtained in terms of system parameters, m and n by equating the determinant to zero (which yields characteristic equation). It should be noted that the integer m corresponds to the axial wave number as can be seen from Eq.

8.16 where the wave in s coordinate is associated with λ, which in turn is dependent on m as shown in Eq. 8.17. Similarly, the integer n is associated to the circumferential wave number (associated with θ).

Further, the characteristic equation can be simplified and written as

$$\Omega^6 - (K_2)\Omega^4 + K_1\Omega^2 - K_0 = 0 \tag{8.19}$$

where Ω is dimensionless frequency parameter expressed as

$$\Omega^2 = \frac{\rho(1-\nu^2)R^2\omega^2}{E} \tag{8.20}$$

and the constant coefficients are written as

$$\begin{aligned} K_2 &= 1 + \frac{1}{2}(3-\nu)(n^2+\lambda^2) + k(n^2+\lambda^2)^2 \\ K_1 &= \frac{1}{2}(1-\nu)\left[(3+2\nu)\lambda^2 + n^2 + (n^2+\lambda^2)^2 + \frac{(3-\nu)}{(1-\nu)}k(n^2+\lambda^2)^3\right] \\ K_0 &= \frac{1}{2}(1-\nu)\left[(1-\nu^2)\lambda^4 + k(n^2+\lambda^2)^4\right] \end{aligned} \tag{8.21}$$

Equation 8.19 is a cubic polynomial in Ω^2 and hence, for a fixed value of λ (or m) and n, the equation would have three roots. This implies that the shell can vibrate in any of three distinct modes, each having same number of circumferential and longitudinal waves, with distinct frequencies. The mode shape associated with each frequency can be classified as primarily flexural, axial or torsional mode. The mode shape corresponding to a natural frequency can be obtained by using the homogeneous equations in A, B and C, whose characteristic determinant was written in Eq. 8.18.

8.2 Analytical modeling of cable-harnessed shells

In this section, mathematical modeling is presented for the cable-harnessed shell structures. The host structure is assumed to be a thin cylinder and the cables are assumed to be attached in a parallel configuration as shown in Fig. 8.2 (a). The cables are attached such that they are equidistant along the circumference. The analytical model is obtained using the energy-equivalence homogenization approach. This powerful approach was used in the previous chapters for modeling the cable-harnessed beam and plate structures. Utilizing

the periodicity condition, this approach is able to homogenize the system which results in an equivalent continuum structure.

As mentioned earlier, the periodicity of the structure forms the core of the homogenization approach and hence, it is important to define a fundamental element. When this element is repeated in the domain of the structure, it yields the overall structure. The fundamental element of the cable-harnessed system under consideration is shown in Fig. 8.2 (b). The dimensions of the host of cable-harnessed shell consist of length L, radius R, and thickness h. On the other hand, the dimensions of the fundamental element consists of the length L_e, subtends an angle ϕ_e at the center and has the same radius R. The global coordinate system is defined as (x, r, θ) while the local coordinate system defined for the fundamental element is $(\bar{x}, \bar{r}, \bar{\theta})$. The number of cables attached on the cylinder are N_c. Hence, the angle subtended at the center can be written as

$$\phi_e = \frac{2\pi}{N_c} \tag{8.22}$$

Additionally, the length of the fundamental element is defined using

$$L_e = \frac{L}{N_c} \tag{8.23}$$

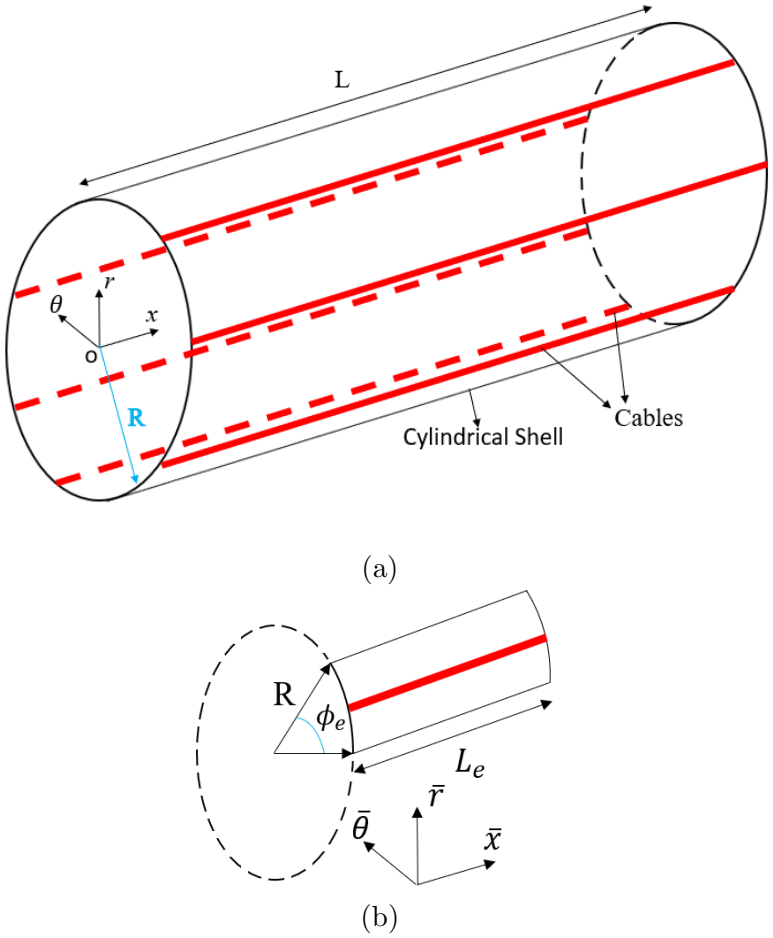

Figure 8.2: (a) Schematic of a cable-harnessed cylindrical shell, (b) A fundamental element

8.2.1 Model Assumptions

The model assumptions applied towards the development of equivalent continuum structure of the cable-harnessed cylindrical shells are listed as follows:

1. The host structure is assumed to be an isotropic cylindrical shell and is modeled using classical shell theory that uses Love's postulates.
2. The cable remains in perfect contact with the cylindrical shell during vibrations.
3. In the equilibrium position, cables are harnessed along the $x-$direction and under a constant pre-tension.
4. The axial strain in the cable at a given cross-section is assumed to be uniform. This means that all the points within the cable, at a given cross-section, are assumed to undergo similar deformation.
5. Cable pretension results in the pre-compression of the cylindrical shell.

In the next two sections, the total strain and kinetic energy expressions of the system are found to obtain the governing equation of motion of the homogenized system.

8.2.2 Strain Energy

In order to obtain the total strain energy of the homogenized system, the strain energy of the fundamental element is first calculated. The fundamental element consists of two components viz., cylindrical shell and the cable. Therefore, the strain energy expressions for both the components are calculated individually and then summed up to calculate the strain energy of the fundamental element.

Strain energy of the cable

The strain energy of the cable within an arbitrary fundamental element can be written as

$$U_c = \frac{1}{2} E_c \int_0^{L_e} \int_{A_c} {\varepsilon_c}^2 \, dA \, d\bar{x} \tag{8.24}$$

Note that $\bar{x}$ is used because the differential element of cable is considered for the fundamental element and hence, the local coordinate is used. Since the cable is attached along the $\bar{x}$ direction, the total strain in the cable is written as the summation of the pre-strain

in the cable and the dynamic strain induced due to the vibration of the shell. This dynamic strain is obtained by calculating the normal strain of the cylindrical shell at the outer surface in the $\bar{x}$ direction. This calculated strain is assumed to be constant over the cross-section of the cable at any point x. Hence, the total strain in the cable is written as

$$\varepsilon_c = \frac{T}{E_c A_c} + e_{\bar{x}}|_{z=z_c} \tag{8.25}$$

where z is the distance of any point in the shell from the mid-surface along the radial direction, and z_c is the distance between mid-surface and plate-cable interface i.e. $z_c = h/2$. Now, using the strain along the $\bar{x}$ direction from Eq. 8.11 (where α represents s)

$$e_{\bar{x}}|_{z=z_c} = \frac{1}{R}\frac{\partial \bar{u}}{\partial \bar{s}} - \frac{z_c}{R^2}\frac{\partial^2 \bar{w}}{\partial \bar{s}^2} \tag{8.26}$$

In this equation, $\bar{u} = \bar{u}(\bar{s}, \bar{\theta}, t)$ is the axial displacement of any point within the fundamental element, whereas, $\bar{w} = \bar{w}(\bar{s}, \bar{\theta}, t)$ is the transverse displacement. Also, the dimensionless quantity $\bar{s} = \bar{x}/R$ is defined for the fundamental element. It should be noted that this strain is similar when obtained using either DM or Flugge shell theory.

As a next step, the cable's strain energy can be written by substituting Eqs. 8.25 and 8.26 in Eq. 8.24, and integrating over the cable's cross sectional area as

$$U_c = \frac{1}{2} E_c A_c \int_0^{L_e/R} \left(\frac{T}{E_c A_c} + \frac{1}{R}\frac{\partial \bar{u}}{\partial \bar{s}} - \frac{z_c}{R^2}\frac{\partial^2 \bar{w}}{\partial \bar{s}^2} \right)^2 d\bar{s}\ R \tag{8.27}$$

The expression is expanded further and written as

$$U_c = \frac{1}{2} E_c A_c R \int_0^{L_e/R} \left[\left(\frac{T^2}{E_c^2 A_c^2} \right) + \frac{1}{R^2}\left(\frac{\partial \bar{u}}{\partial \bar{s}} \right)^2 + \frac{z_c^2}{R^4}\left(\frac{\partial^2 \bar{w}}{\partial \bar{s}^2} \right)^2 - \frac{2z_c}{R^3}\frac{\partial \bar{u}}{\partial \bar{s}}\frac{\partial^2 \bar{w}}{\partial \bar{s}^2} - \frac{2z_c}{R^2}\frac{T}{E_c A_c}\frac{\partial^2 \bar{w}}{\partial \bar{s}^2} + \frac{2T}{E_c A_c R}\frac{\partial \bar{u}}{\partial \bar{s}} \right] d\bar{s} \tag{8.28}$$

This is the total strain energy stored in cable within a fundamental element shown in Fig. 8.2(b). Next, the strain energy stored in the cylindrical shell within a fundamental element is written.

Strain energy of the cylindrical shell

Assuming that the cable tension induces an uniform compressive load on the shell element, as shown in Fig. 8.3, the strain energy in the cylindrical shell element within an arbitrary fundamental element can be written as

$$U_s = \int_{V_s} (\sigma_{\bar{x}} e_{\bar{x}} + \sigma_{\bar{\theta}} e_{\bar{\theta}} + \ \sigma_{\bar{x}\bar{\theta}} e_{\bar{x}\bar{\theta}}) dV + \int_{V_s} \left(\sigma^i_{\bar{x}} e^i_{\bar{x}} \right) dV \tag{8.29}$$

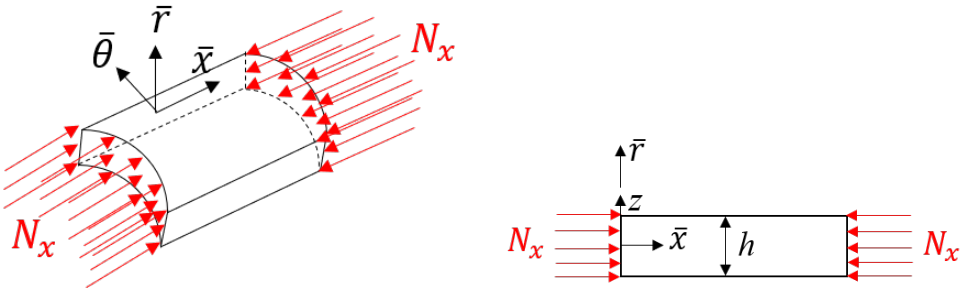

(a) (b)

Figure 8.3: Normal compressive forces shown on cylindrical shell element due to the taut cables

In this expression, the first integral is written similar to Eq. 8.8, but corresponding to the local coordinates of the fundamental element. The second integral corresponds to the strain energy stored in the shell due to the additional compressive loading acting along the $\bar{x}$ direction. The stress $\sigma^i_{\bar{x}}$ is the constant initial stress acting in the direction of cylinder's length on the cross-section due to the distributed loading N_x shown in Fig. 8.3. N_x is the compressive force acting per unit circumferential length which can be expressed in terms of cable tension as,

$$N_x = \frac{N_c T}{2\pi R} \tag{8.30}$$

And, because the compressive loading is assumed to be distributed along the thickness as well, the initial stress can be written as

$$\sigma^i_{\bar{x}} = \frac{N_x}{h} \tag{8.31}$$

Moreover, in Eq. 8.29, initial normal stress in the $\bar{\theta}$ direction and shear stress is assumed to be negligible due to the cable tension and is ignored while writing the strain energy. Further, in the second integral of Eq. 8.29, the strain $e^i_{\bar{x}}$ is written by including a second order displacement term in strain-displacement relation [4], in addition to the two terms written in the first equation of Eq. 8.11. Because, the initial stresses may be large, this second order nonlinear term is essential to be included. Also, this maintains the homogeneity of the order of displacement derivative terms in the strain energy expression. By including the second order term, the initial strain is written as [4]

$$e^i_{\bar{x}} = \frac{1}{R}\frac{\partial \bar{u}}{\partial \bar{s}} - \frac{z}{R^2}\frac{\partial^2 \bar{w}}{\partial \bar{s}^2} + \frac{1}{2R^2}\left(\frac{\partial \bar{w}}{\partial \bar{s}}\right)^2 \tag{8.32}$$

Now, the strain energy written in Eq. 8.29 can be further simplified. Since, the first integral represents the strain energy in absence of any body forces, the simplification can be done similar to the steps carried out in Eqs. 8.8 - 8.12. The second integral in Eq. 8.29 can be simplified using Eqs. 8.31 and 8.32 as

$$U_s^i = \int_{V_s} \left(\frac{N_x}{h}\right) \left(\frac{1}{R}\frac{\partial \bar{u}}{\partial \bar{s}} - \frac{z}{R^2}\frac{\partial^2 \bar{w}}{\partial \bar{s}^2} + \frac{1}{2R^2}\left(\frac{\partial \bar{w}}{\partial \bar{s}}\right)^2\right) dV \tag{8.33}$$

Using $dV = R^2 dr d\theta ds$, and integrating over the thickness direction (radial), the above expression is simplified as

$$U_s^i = (N_x) \int_0^{2\pi} \int_0^{L_e/R} \left[R\frac{\partial \bar{u}}{\partial \bar{s}} + \frac{1}{2}\left(\frac{\partial \bar{w}}{\partial \bar{s}}\right)^2\right] \, d\bar{s} \, d\bar{\theta} \tag{8.34}$$

Using Eqs. 8.34 and 8.12 in Eq. 8.29, we obtain

$$U_s = \int_0^{2\pi} \int_0^{L_e/R} \left[\frac{Eh}{2(1-\nu^2)}\left[\left(\frac{\partial \bar{u}}{\partial \bar{s}} + \frac{\partial \bar{v}}{\partial \bar{\theta}} + \bar{w}\right)^2 - 2(1-\nu)\left(\frac{\partial \bar{u}}{\partial \bar{s}}\bar{w} - \frac{1}{4}\left(\frac{\partial \bar{v}}{\partial \bar{s}} - \frac{\partial \bar{u}}{\partial \bar{\theta}}\right)^2\right)\right.\right.$$
$$\left.\left. + k\left\{\left(\nabla^2 \bar{w}\right)^2 - 2(1-\nu)\left(\frac{\partial^2 \bar{w}}{\partial \bar{s}^2}\frac{\partial^2 \bar{w}}{\partial \bar{\theta}^2} - \left(\frac{\partial^2 \bar{w}}{\partial \bar{s}\,\partial \bar{\theta}}\right)^2\right)\right\}\right] + N_x\left(R\frac{\partial \bar{u}}{\partial \bar{s}} + \frac{1}{2}\left(\frac{\partial \bar{w}}{\partial \bar{s}}\right)^2\right)\right] d\bar{s} d\bar{\theta} \tag{8.35}$$

This is the total strain energy expression obtained for a compressed shell element using the DM shell theory. The term k was defined in Eq. 8.5. In a simplified form, this equation can be expressed as

$$(U_s)_{DM} = \frac{Eh}{2(1-\nu^2)} \int_0^{2\pi} \int_0^{L_e/R} \left[I_{DM} + \frac{2}{C} I_i\right] d\bar{s} d\bar{\theta} \tag{8.36}$$

where I_{DM} is same as that written in Eq. 8.13 with the bar signs over the displacements and coordinates, while the other terms are defined as

$$\begin{aligned} C &= \frac{Eh}{(1-\nu^2)} \\ I_i &= (N_x)\left(R\frac{\partial \bar{u}}{\partial \bar{s}} + \frac{1}{2}\left(\frac{\partial \bar{w}}{\partial \bar{s}}\right)^2\right) \end{aligned} \tag{8.37}$$

For the Flugge's shell theory, an additional term in added in Eq. 8.36 and is expressed as [4]

$$(U_s)_{Flugge} = \frac{Eh}{2(1-\nu^2)} \int_0^{2\pi} \int_0^{L_e/R} \left[I_{DM} + \frac{2}{C} I_i + k I_{Flugge} \right] d\bar{s} d\bar{\theta} \tag{8.38}$$

where

$$I_{Flugge} = \frac{1-\nu}{2} \left(\frac{\partial \bar{u}}{\partial \bar{\theta}} \right)^2 + (1-\nu) \frac{\partial \bar{u}}{\partial \bar{\theta}} \frac{\partial^2 \bar{w}}{\partial \bar{s} \partial \bar{\theta}} - 2 \frac{\partial \bar{u}}{\partial \bar{s}} \frac{\partial^2 \bar{w}}{\partial \bar{s}^2} + \frac{3(1-\nu)}{2} \left(\frac{\partial \bar{v}}{\partial \bar{s}} \right)^2 - 3(1-\nu) \frac{\partial \bar{v}}{\partial \bar{s}} \frac{\partial^2 \bar{w}}{\partial \bar{s} \partial \bar{\theta}} - 2\nu \frac{\partial \bar{v}}{\partial \bar{\theta}} \frac{\partial^2 \bar{w}}{\partial \bar{s}^2} + \bar{w}^2 + 2\bar{w} \frac{\partial^2 \bar{w}}{\partial \bar{\theta}^2} \tag{8.39}$$

Total strain energy

In order to obtain the total energy within a fundamental element of cable-harnessed shell, the energy components of both cable and shell would have to be added. As noted earlier, the energy component of the cable was similar for both, DM and Flugge's shell theory. Hence, the total strain energy within a fundamental element according to the DM theory can be written by summing up Eqs. 8.28 and 8.36 for the DM theory, while, Eqs. 8.28 and 8.38 for the Flugge's theory.

$$\begin{aligned} (U_{tot})_{DM} &= (U_s)_{DM} + U_c \\ (U_{tot})_{Flugge} &= (U_s)_{Flugge} + U_c \end{aligned} \tag{8.40}$$

As, it was mentioned earlier that the Flugge's theory yields better approximation compared to the DM theory, the strain energy expressions from both the shell theories are presented. However, due to relative mathematical simplicity, the EOM will be derived only for the DM theory.

Homogenization

The strain energy of the fundamental element using two shell theories have been listed in Eq. 8.40. Now, in order to apply the homogenization principle, recall that the displacements $\bar{u}(\bar{s}, \bar{\theta}, t)$, $\bar{v}(\bar{s}, \bar{\theta}, t)$, and $\bar{w}(\bar{s}, \bar{\theta}, t)$ are replaced by its Taylor's series expansion about the center of the fundamental element $(L_e/(2R), \phi_e/2)$. Upon substitution, the total strain energy in Eq. 8.40 can be obtained simply by integrating over respective limits in space. As a next step, this expression of total energy is divided by the element's area yielding the energy density of an equivalent continuum shell element. Upon integration of this energy density over the entire surface of the cylinder, the system's total strain energy, U_{sys} is obtained. Due to mathematically intensive formulations, the steps involved in the homogenization approach are not presented here.

8.2.3 Kinetic Energy

Following the similar approach as strain energy. the kinetic energy of the fundamental element is also obtained by summing up the respective energies of cable and shell within a fundamental element. The kinetic energy for the cables can be written as

$$T_c = \frac{1}{2}\rho_c \int_{V_c} \left[\left(\frac{\partial \bar{u}}{\partial t}\right)^2 + \left(\frac{\partial \bar{v}}{\partial t}\right)^2 + \left(\frac{\partial \bar{w}}{\partial t}\right)^2 \right] dA d\bar{x} \tag{8.41}$$

Since the displacement along the cross-section area is assumed to be constant, integrating over the area results in

$$T_c = \frac{1}{2}\rho_c A_c R \int_0^{L_e/R} \left[\left(\frac{\partial \bar{u}}{\partial t}\right)^2 + \left(\frac{\partial \bar{v}}{\partial t}\right)^2 + \left(\frac{\partial \bar{w}}{\partial t}\right)^2 \right] d\bar{s} \tag{8.42}$$

In this equation, the displacement $\bar{x}$ was transformed to the dimensionless variable $\bar{s}$. The total kinetic energy within the fundamental element can now be written by summing the Eq. 8.42 and 8.14 written in local coordinates

$$\begin{aligned} T_{tot} = \frac{1}{2}\rho_c A_c R \int_0^{L_e/R} & \left[\left(\frac{\partial \bar{u}}{\partial t}\right)^2 + \left(\frac{\partial \bar{v}}{\partial t}\right)^2 + \left(\frac{\partial \bar{w}}{\partial t}\right)^2 \right] d\bar{s} \\ & + \frac{1}{2}\rho h R^2 \int_0^{\frac{2\pi}{N_c}} \int_0^{L_e/R} \left[\left(\frac{\partial \bar{u}}{\partial t}\right)^2 + \left(\frac{\partial \bar{v}}{\partial t}\right)^2 + \left(\frac{\partial \bar{w}}{\partial t}\right)^2 \right] d\bar{s} d\bar{\theta} \end{aligned} \tag{8.43}$$

In order to obtain the total kinetic energy within the fundamental element, the Taylor's series expansion of the displacements about the center are substituted in Eq. 8.43 resulting in

$$\begin{aligned} T_{tot} = \frac{1}{2}\rho_c A_c R & \left[\left(\frac{\partial \bar{u}*}{\partial t}\right)^2 + \left(\frac{\partial \bar{v}*}{\partial t}\right)^2 + \left(\frac{\partial \bar{w}*}{\partial t}\right)^2 \right] \left(\frac{L_e}{R}\right) \\ & + \frac{1}{2}\rho h R^2 \left[\left(\frac{\partial \bar{u}*}{\partial t}\right)^2 + \left(\frac{\partial \bar{v}*}{\partial t}\right)^2 + \left(\frac{\partial \bar{w}*}{\partial t}\right)^2 \right] \left(\frac{L_e}{R}\right) \left(\frac{2\pi}{N_c}\right) \end{aligned} \tag{8.44}$$

where the terms with asterisk $(*)$ indicates that they are evaluated at the center of the fundamental element, $\bar{s} = L_e/(2R)$ and $\bar{\theta} = \phi_e/2$. Also, the relation shown in Eq. 8.22 is used while simplifying the expression.

Next, the energy density of the homogenized shell element is obtained by dividing the total kinetic energy by the area of the fundamental element, $\frac{L_e}{R}\frac{2\pi}{N_c}$. Upon multiplying it by $d\theta ds$, and integrating over the domain of entire cable-harnessed shell, the system's total kinetic energy can be obtained

$$T_{sys} = \frac{1}{2} M_1 R^2 \int_0^{2\pi} \int_0^{\frac{L}{R}} \left[\left(\frac{\partial u}{\partial t} \right)^2 + \left(\frac{\partial v}{\partial t} \right)^2 + \left(\frac{\partial w}{\partial t} \right)^2 \right] ds d\theta \tag{8.45}$$

where the homogenized mass per unit area of the system, M_1, is written as

$$M_1 = \frac{1}{2} \left(\frac{\rho_c A_c N_c}{2\pi R} + \rho h \right) \tag{8.46}$$

8.2.4 Equations of Motion

To obtain the governing equations of motion, the Euler-Lagrange's equations [4] are used on the functional invoked by the Hamilton's principle. The calculations to obtain the equations of motions were done using the software *Mathematica*. Following are the resulting equations of motion obtained for the homogenized cable-harnessed shell (using DM theory):

$$\begin{aligned} -2M_1 R^2 \frac{\partial^2 u}{\partial t^2} + \frac{1}{4} Eh \left\{ \frac{2}{1+\nu} \left(\frac{\partial^2 u}{\partial \theta^2} - \frac{\partial^2 v}{\partial s\, \partial \theta} \right) - \frac{4}{-1+\nu^2} \left(\nu \frac{\partial w}{\partial s} + \frac{\partial^2 v}{\partial s\, \partial \theta} + \frac{\partial^2 u}{\partial s^2} \right) \right\} \\ + \frac{A_c N_c E_c}{2\,\pi R^2} \left(R \frac{\partial^2 u}{\partial s^2} - z_c \frac{\partial^3 w}{\partial s^3} \right) = 0 \end{aligned} \tag{8.47}$$

$$2M_1 R^2 \frac{\partial^2 v}{\partial t^2} + \frac{Eh}{2\,(-1+\nu^2)} \left\{ 2 \frac{\partial w}{\partial \theta} + 2 \frac{\partial^2 v}{\partial \theta^2} + (1+\nu) \frac{\partial^2 u}{\partial s\, \partial \theta} + (1-\nu) \frac{\partial^2 v}{\partial s^2} \right\} = 0 \tag{8.48}$$

$$\begin{aligned} -2M_1 R^2 \frac{\partial^2 w}{\partial t^2} + \frac{Eh}{(-1+\nu^2)} \left\{ -\frac{N_x}{C} \frac{\partial^2 w}{\partial s^2} + \nu \frac{\partial u}{\partial s} + \frac{\partial v}{\partial \theta} + w + k \nabla^4 w \right\} \\ + \frac{A_c N_c E_c}{2\,\pi R^3} \left(R\, z_c \frac{\partial^3 w}{\partial s^3} - z_c^2 \frac{\partial^4 w}{\partial s^4} \right) = 0 \end{aligned} \tag{8.49}$$

The three equations shown above denote the coupled governing equations of motion for an equivalent continuum model of a cable-harnessed shell. The first term in all the

three equations represent the inertia component which includes the mass per unit area of the homogenized shell element, defined in Eq. 8.46. The terms in the curly brackets of Eqs. 8.47 - 8.49 essentially corresponds to the stiffness effect due to the cylindrical shell. Furthermore, the effect of the cable stiffness is shown in the last term in parenthesis in Eqs. 8.47 and 8.49. Cable stiffness effects are not seen in Eq. 8.48 as this equation primarily corresponds to the motion in tangential direction. Additionally the term multiplied by N_x within the curly brackets in Eq. 8.49 is associated with the compressive effect on cylindrical shell due to the taut cables.

In order to do some sanity checks for Eqs. 8.47 - 8.49, firstly, the dimensional analysis was done and it was found that all terms have similar dimensions. Next, the cable parameters such as T, E_c, A_c, ρ_c were substituted as zero, and the obtained EOM was found same as that of a bare shell (DM shell theory) as shown by Eqs. 8.2 and 8.6. It should be noted that the equations of motion presented here corresponds to the assumption that the host cylindrical shell has been modeled using DM shell theory. For the Flugge's shell theory, similar derivations can be carried out to obtain a more accurate model.

8.3 Results and Discussion

In this section, some preliminary results are presented for the cable-harnessed structure as obtained from the developed mathematical model. In order to do so, natural frequencies are obtained for the SD-SD boundary conditions. This was previously discussed for a bare cylindrical shell in section 8.1.3. To calculate the frequencies, the displacements written in Eq. 8.16 are substituted in the governing equations presented in the Eqs. 8.47 - 8.49. A similar approach outlined in section 8.1.3 is followed where solving a characteristic determinant yields the closed-form polynomial equation in terms of natural frequency with m and n as additional integer parameters corresponding to the axial wave number and circumferential wave number, respectively.

Two sets of results are presented with different host shell parameters as shown in Table 8.1. As shown, four cables are attached on a circular closed cylindrical shell which are equidistant to each other. From the axial view of the system, these cables would be 90 degrees apart. Also, the two sets of different host shell parameters have different l/R and R/h ratios. A high value of R/h ratio with a lower value of l/R ensure a good accuracy according to DM shell theory.

Firstly, the results for set-1 are discussed. The first five natural frequencies are presented for the bare shell in Table 8.2 from ANSYS and analytical model (following DM

Table 8.1: Cable-harnessed shell system parameters selected for numerical simulations

Set-1				Set-2			
Cylinder		Cable		Cylinder		Cable	
Length, l	15 m	Number of cables, N_c	4	Length, l	2.5 m	Number of cables, N_c	4
Radius, R	0.75 m	Cable Radius, r_c	10 mm	Radius, R	0.5 m	Cable Radius, r_c	10 mm
Thickness, h	1.5 mm	Youngs Modulus, E_c	128 GPa	Thickness, h	1.0 mm	Youngs Modulus, E_c	128 GPa
Youngs Modulus, E	68.9 GPa	Density, ρ_c	1400 Kg/m^3	Youngs Modulus, E	68.9 GPa	Density, ρ_c	1400 Kg/m^3
Density, ρ	2768 Kg/m^3	Tension, T	0.5 N	Density, ρ	2768 Kg/m^3	Tension, T	0.5 N
Poisson' Ratio, ν	0.3			Poisson' Ratio, ν	0.3		

Table 8.2: Natural frequencies of bare shell for set-1

Mode	ANSYS (Hz)	Donnell-Mushtari (Hz)	Error
(1,3)	5.61	6.13	9.28%
(1,2)	6.06	6.24	2.98%
(1,4)	9.53	10.08	5.76%
(2,4)	11.37	11.82	3.96%
(2,3)	11.98	12.20	1.90%

theory). In the ANSYS model, the cylindrical shell is modeled using SHELL181 element, the cable using LINK180, and the contact is established using the CONTA175 elements. The mathematical model of ANSYS does not have any direct connection with the analytical model established through the Eqs. 8.47-8.49. On the comparison of the two model, it is shown that the natural frequencies are close to each other with errors in the reasonable limits. The differences in frequencies can be attributed to the imperfect incoporation of SD-SD boundary condition in ANSYS. While only nodal displacements can be constrained in ANSYS, the vanishing bending moment and longitudinal membrane forces could not be enforced in finite element domain.

Next, the natural frequencies of the cabled shell for set-1 are presented using ANSYS and proposed analytical method in Table 8.3. The natural frequencies are presented in the increasing order of magnitude. It should be noted that the effects of the cables on the bare shell can be analyzed by comparing the % increase in frequency. As seen from the table, the % increase in frequency is similar when the proposed analytical model is compared with ANSYS. This presents a strong validation of the proposed model. The mismatch of the bare shell's natural frequency using the two methods is attributed to the inaccuracies in the Donell-Mushtari shell theory. An advanced shell theory would help in decreasing the errors in the baseline system.

Table 8.3: Natural frequencies of cabled shell for set-1

Mode (m,n)	ANSYS, BS* (Hz)	ANSYS, CS* (Hz)	% increase in freq in ANSYS	Analytical, BS (Hz)	Proposed, CS (Hz)	% increase in frequency in analytical model
(1,3)	5.61	5.53	-1.38%	6.13	6.07	-1.06%
(1,2)	6.06	6.54	8.02%	6.24	6.77	8.43%
(1,4)	9.53	9.17	-3.74%	10.08	9.7	-3.82%
(2,4)	11.37	11.29	-0.72%	11.82	11.85	0.22%
(2,3)	11.98	12.56	4.87%	12.20	13.11	7.42%

*Abbreviations: BS Bare Shell, CS Cabled Shell

Table 8.4: Natural frequencies obtained from ANSYS for cabled shell for set-1

Mode (m,n)	ANSYS (Hz)		Avg. of ANSYS frequency (Hz)
(1,3)	5.53	5.53	5.53
(1,2)	5.95	7.14	6.55
(1,4)	8.87	9.48	9.18
(2,4)	11.27	11.31	11.28
(2,3)	12.56	12.56	12.56

It should be further noted that corresponding to each mode shape, ANSYS predicts two natural frequencies. These two frequencies are similar for the bare shell, however, they are different for the cabled shell as shown in Table 8.4. The reasoning for this behavior can be explained on the basis of mode shapes corresponding to the frequencies. Consider the two mode shapes for mode (1,2) obtained from ANSYS as shown in Fig. 8.4. As mentioned, the two modes have same frequencies for a bare shell which is homogeneous and symmetric. However, when the four cables are attached, the two mode shapes (which are similar in shape but shifted by 45 degrees along the axis) have different contribution of cable's strain energy. The deformation of the cable for the mode shown in Fig. 8.4(a) is higher compared to Fig. 8.4(b) and hence, the cable strain energy contribution in the former would be more highlighted. On the other hand, the proposed analytical model based on homogenization approach do not 'see' the cables at those locations as the cable effect is homogenized over the circumference of the shell. Hence, the two distinct frequencies are not obtained. Moreover, the difference in frequencies for same mode shapes, as predicted by ANSYS, is primarily due to the inhomogeneity introduced in the system due to the cables. This difference should decrease as the number of cables around the circumference of the shell increase.

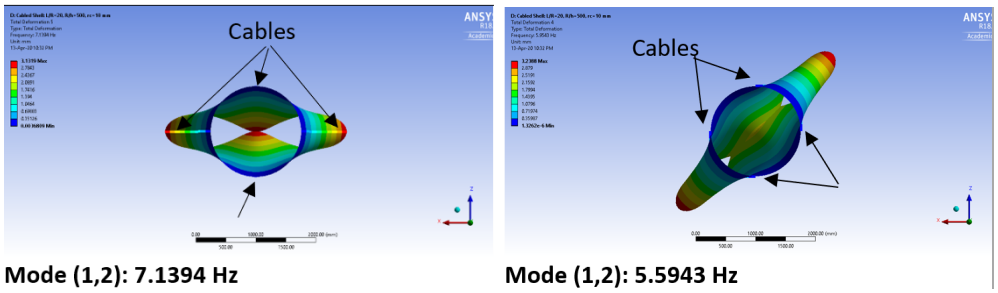

(a) (b)

Figure 8.4: Front view of the mode shapes (1,2) obtained for the set-1 of cabled shell from ANSYS

In the following paragraphs, the results obtained for set-2 are presented. Similar to the 1st set, the natural frequencies are compared using DM shell theory and ANSYS. The comparison in natural frequency is presented for the first ten modes as shown in Table 8.5. The natural frequencies are arranged in the increasing order of magnitude. The R/h of the shell in set-2 is same as that of set-1, however, the l/R ratio is lower for set-2 and hence, the % error in natural frequencies as shown in Table 8.5 are comparatively lower in set-2. As discussed before, for DM theory, the lower values of l/R ratios yields higher accuracy. Also, the increasing order of frequencies in cylindrical shell do not necessarily mean that the integers m and n would also increase in the order. As seen from the table, with the increasing natural frequency, the increasing circumferential mode number do not follow a set pattern.

Further, when the errors are compared, they do not seem to follow a trend with increase in natural frequencies. However, the trend of error can be determined when the frequencies are analyzed by varying the number n and keeping m as constant or vice versa. For a visual interpretation, the % error shown in Table 8.5 is plotted with varying n as shown in Fig. 8.5. Clearly, as the value of n increases, the magnitude of error increase. Hence, in the following analysis, $m = 1$ is held fixed and n is varied. The natural frequencies of the bare shell corresponding to the fixed m and varying n is listed in Table 8.6.

Now, the natural frequencies of the cable-harnessed shell corresponding to set-2 are presented. Table 8.7 shows the natural frequencies obtained using the proposed model and ANSYS for $m = 1$ and $n = 1$ to 5. It can be seen that there is a considerable difference between the natural frequencies of the cabled shell and bare shell. For example, for mode (1,1), the bare shell resonates at 310 Hz, whereas cabled shell at 319 Hz according to Homogenization method and at 323 Hz according to ANSYS. Further, a comparison of the

Table 8.5: Natural frequencies for bare shell for set-2

Mode	Axial Mode Number, m	Circumferential Mode number, n	DM Theory (Hz)	ANSYS (Hz)	Error in DM theory
1	1	5	34.02	34.24	-0.63%
2	1	6	38.45	39.28	-2.11%
3	1	4	40.08	40.26	-0.45%
4	1	7	48.64	50.84	-4.34%
5	1	8	62.16	66.66	-6.74%
6	1	3	63.70	63.98	-0.44%
7	2	7	68.71	71.75	-4.24%
8	2	8	73.13	78.08	-6.33%
9	2	6	74.79	76.98	-2.85%
10	1	9	78.12	86.09	-9.25%

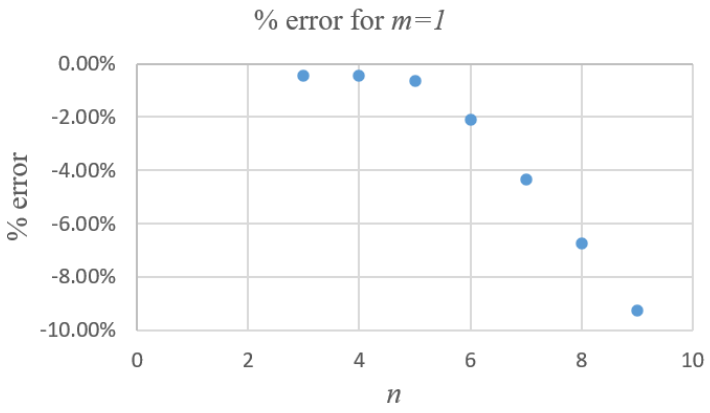

Figure 8.5: Percentage error in natural frequency obtained in DM theory for set-2 with variation in n for $m = 1$

Table 8.6: Comparison of natural frequencies of bare shell for set-2 for $m = 1$ and $n = 1$ to 5

m	n	DM Theory (Hz)	ANSYS (Hz)	% Error in DM Theory
1	1	310.24	310.19	0.02%
1	2	126.41	126.63	-0.18%
1	3	63.71	63.99	-0.44%
1	4	40.08	40.27	-0.45%
1	5	34.02	34.24	-0.63%

Table 8.7: Comparison of natural frequencies of cable-harnessed shell for set-2

m	n	Proposed Model (Hz)	ANSYS-1 (Hz)	ANSYS-2 (Hz)	ANSYS (Average of 1 and 2)	Error in proposed model
1	1	318.96	323.27	323.62	323.445	-1.39%
1	2	141.74	121.86	155.93	138.895	2.05%
1	3	73.9	67.68	67.73	67.705	9.15%
1	4	46.09	39.77	42.9	41.335	11.50%
1	5	36.3	33.59	33.62	33.605	8.02%

mode shapes for the five modes corresponding to both bare shell and cabled shell obtained from ANSYS are presented in Fig. 8.6.

The errors increase with the increase in the values of n. One possible way to reduce these errors is by increasing the number of cables attached on the cylindrical shell so that the inhomogeneity due to cable is reduced at higher values of n.

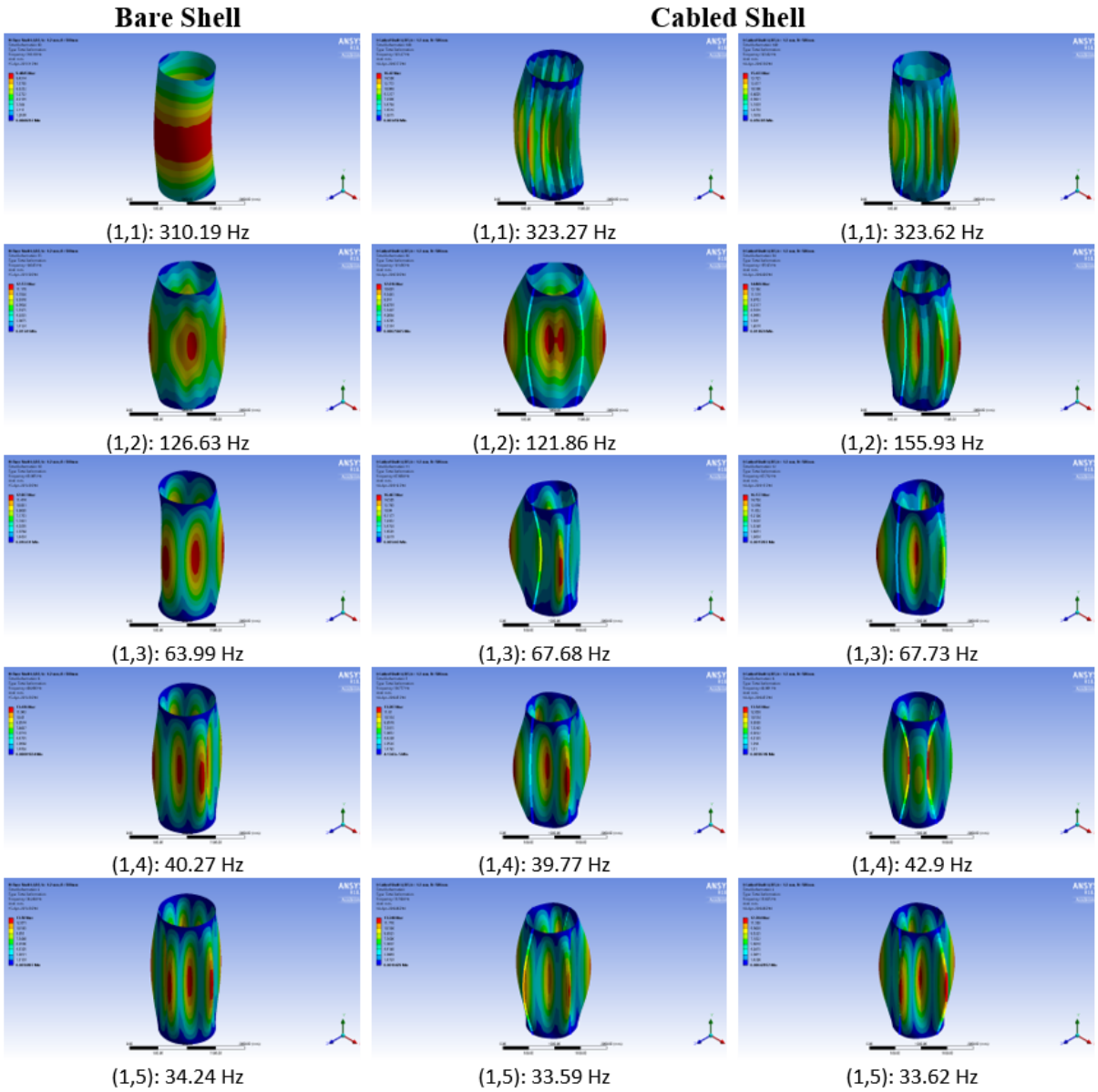

Figure 8.6: Mode shapes for bare and cable-harnessed cylindrical shell for set-2

8.4 Summary of the chapter

In this chapter, the analytical model for cable-harnessed cylindrical shell structure is proposed. These structures are very common and find applications in aerospace and marine industry. Creating simple and accurate dynamics models of these structures are important because they form the basis of efficient and robust control algorithms. In this work, the host cylindrical shell was modeled using the Donnell-Mushtari shell theory. The cables were assumed to be attached equidistant from each other along the axis of the cylinder. The pre-compression in the shell due to the taut cable was also accounted for. The coupled governing equations of motion were obtained following the application of energy-equivalence homogenization approach. The results were presented for two different sets of shell structures. The natural frequencies obtained from the proposed model was compared with those obtained using ANSYS. The results show promising evidence of verification of the homogenized model.

More accurate models based on other shell theories can be investigated further with a scope of detailed parametric analysis. Additionally, experimental validation of these results would help in building more confidence on the proposed model.

Chapter 9

Future Work and Conclusions

The current chapter discusses the possible future work which can be based on the current research. The final section of the thesis contains the concluding remarks and a list of major contributions of the thesis.

9.1 Future Work

For the future developments and improvements in the presented research work, following ideas can be explored and implemented:

1. An optimal cable wrapping parameter can be obtained for a cable-harnessed plate structure such that the cable attachment has a minimal impact on the dynamics of the host structure. This optimization scheme can highly simplify the modeling of complicated structures such that the cable dynamics can be completely ignored while modeling when the cable is attached in the optimal pattern on the host structure. The work on obtaining an optimal cable geometry wrapped on a rectangular beam has been recently published by Shilei et al. [37]. The work presented in the current research would be further advantageous in finding an optimal geometry to minimize cable dynamics effect when the cable is harnessed to a plate or a cylindrical shell structures.

2. There is a lot of scope to build upon the presented analytical model of cable-harnessed plate structures. Some of the ideas are presented as follows:

(a) Including the damping mechanism in cable and host plate structure. This would improve the accuracy of the frequency response functions near the resonance and anti-resonance regions.

(b) Extending the work to model non-periodic cable geometry. This would help in further generalizing the modeling approach of cable-harnessed plate structures.

(c) The current work on the cable-harnessed plate structure assumes thin rectangular plates as the host structures and hence, Kirchhoff-Love plate theory is utilized for modeling purposes. To model the effect of cable harness on thick plates, shear deformation effects through the plate thickness would have to be considered. Hence, the current modeling technique can be further extended by modeling the host plates using Mindlin-Reissner plate theory which takes the shear deformation into account.

3. To further analyze some interesting effects of the cable harness on two-dimensional host structures, circular plates can be considered as hosts and cable can be assumed to be harnessed in different patterns. One of the patterns can be the attachment of multiple cables along the diameter. Since the mode shapes of the circular plates are considerably different from those of rectangular plates, the effect of shift in system dynamics on cable attachment can be very interesting to analyze.

4. To extend the preliminary work done on analytical model development of cable-harnessed cylindrical shell, following are the directions in which this work can be further continued:

   (a) Modeling the strain energy of the cables using a higher-order strain-displacement relationship to include the effect of cable tension in the cable's strain energy.

   (b) Modeling the host shells using more accurate theories which include but is not limited to widely used Flugge's shell theory. As mentioned, the presented model using Donnell-Mushtari theory, although known for mathematical simplicity, starts to show its limitations for short and thick cylindrical shells.

   (c) Modeling the dynamics of cable-harnessed shells with cable wrapped around the cylindrical structure. This would bring the analytical modeling of the cable-harnessed space structure very close to practical applications and would closely resemble the cable harnessed propellant tank structure shown in Fig. 1.2.

9.2 Conclusions

The research presented in the current thesis is motivated by the need of the accurate analytical models for the cable-harnessed structures that finds their applications in the space industry. Other applications include structural components present in aerospace, automotive and marine structures harnessed with cables.

The thesis starts by focusing on extending the research conducted by Martin et al. [31, 30] on the cable-harnessed *beam* structures by incorporating the effects of material damping in the cable harness and the host beam structure. In these previous works, damping was ignored during the model development; however, damping plays an important role in obtaining accurate dynamic characteristics of the system. In the current work, the cable harness was assumed to be wrapped along the beam in zigzag, diagonal, and longitudinal pattern. An analytical model based on energy-equivalence homogenization method was obtained for two damping models viz. Kelvin-Voigt and hysteretic damping model. The damping in the system was analyzed using frequency response functions (FRFs) for different boundary conditions. The FRFs were verified using the distributed transfer function method (DTFM). This was followed by a detailed parametric analysis. The system damping was found to increase with cable radius and decrease with beam width and number of fundamental element. The higher modes for Kelvin-Voigt damping showed higher damping ratios whereas, the damping ratios for hysteretic damping remained constant for different modes.

Subsequently, the material damping in the cables was characterized using an elastomer test system. Beam's material damping and air damping was also characterized, but using an inverse approach where vibration data of bare beam resulted in desired damping coefficients. Finally, the modal testing experiments of the fabricated cable-harnessed beam structures were conducted and the proposed analytical model was validated against the test results for seven different cases. The comparison of FRFs between model and test validated the changes in natural frequency and the increased damping when the cable was harnessed on the host beam structure. Some of the important findings include that the damping in the system increased when the cable was attached longitudinally compared to being wrapped along the beam structure. Also, the system damping was shown to increase on decreasing the beam width or using a cable with larger radius which was also predicted by the model.

As a next step, and regarded as the major contribution of this thesis, analytical models of the cable-harnessed *plate* structures were developed. As per the best knowledge of the author, no analytical models have been proposed on cable-harnessed plates in the

literature. Hence, as a stepping stone, the mathematical modeling was developed for the cables harnessed in a straight configuration parallel to the edge of a rectangular host plate. For the parallel cabled plates, the governing equation of motion derived for the equivalent continuum structure was found similar to that of a specially orthotropic laminated plate. Next, the experimental validation was performed on the fabricated structures with cables attached parallel to either of two plate's edges. One of the most interesting findings in this research was regarding the the shift in natural frequencies after cables were attached. After the cables were attached, the cable stiffening effects were found dominant in some vibration modes (which increases the corresponding frequency), whereas, the cable inertia effects in others (decreases the corresponding frequency). While, in some modes, the cable inertia and stiffness effects were found to be equally dominant and the natural frequencies of the those modes remained unaffected after the cable was attached. The shift in the dynamic behavior after cable attachment, as observed from the experiments, was well predicted by the proposed model. This helped in gaining the confidence in modeling technique and motivated me to further build on this work on more complicated cable attachment geometry.

To model a more complicated geometry, wrapping patterns were considered on the host plate structures. Motivated by the works of Martin et al. [31], the patterns studied in the presented work consider zigzag and diagonal wrapped geometry in a two-dimensional framework. Although, the mathematical model became more complicated, this model was able to provide important insights into the dynamics of cable-harnessed structures. Firstly, it was observed that the diagonally wrapped cable-harnessed plate structure can be modeled as symmetric angle-ply laminated plate. On the other hand, the zigzag wrapped structure was found to be modeled as a specially orthotropic laminated plate. These important conclusions highly simplify the mathematical modeling of the studied complex structures. Further, similar to the parallel cabled plates, upon harnessing the plate with cables, different vibrations modes were affected differently. Some modes showed major stiffening effects due to the addition of the cables and others exhibited inertia dominant effects or no major changes in their frequencies. This further resulted in mode switching phenomenon in which the order of appearance for certain modes of given shapes changes after the addition of the cables compared to the bare plate. The proposed analytical model was initially verified using ANSYS simulations and later experimentally validated using modal testing experiments for four different fabricated cable-harnessed plate structures.

The PDE for the cable-harnessed structure with parallel cable configuration was found to be generally stable, however, it was found that care should be taken when the cable tension is chosen. This is because, when the plate aspect ratios was chosen to be either very large or very small, the system was found to become unstable at extremely high tension

values due to the occurrence of torsional instability. Additionally, for the PDEs of zigzag and diagonally wrapped cable-harnessed structures, the model was found to remain stable with no additional constraints.

In the final part of the thesis, the analytical model for a cable-harnessed *cylindrical shell* structure was proposed. The cylindrical shell was modeled using the Donnell-Mushtari (DM) theory and the cable harness using the string theory. Comparison of the proposed model using the DM theory for two different set of simulation parameters with ANSYS verifies the initial attempt of model development. The change in the natural frequencies and the mode shapes on harnessing the cables were used as the parameters for verification. However, the accuracy of the model still needs to be improved which can be addressed in the future works.

The contributions of the work presented in the thesis are summarized as follows:

1. Modeling the damping mechanisms in cable-harnessed beam structures
2. Analytical model development for cable-harnessed two dimensional plate-like structures
3. Application of energy-equivalence homogenization approach for predicting the dynamic characteristics of complex two-dimensional cable-harnessed structure
4. Development of the conditions of the differential equation coefficients required to prove the stability of the governing PDEs of the cable-harnessed systems
5. Experimental validation of the analytical models proposed for cable-harnessed beam structures and cable-harnessed plate structures.
6. Preliminary analytical model development of cable-harnessed cylindrical shell structures.

References

[1] D. Insider, "India's 1st Cable-Stayed Bridge B/W North and North-East Delhi Is Opening On 4th November!," 2018.

[2] K. Yerrapragada and A. Salehian, "Coupled dynamics of cable-harnessed structures: Experimental validation," *Journal of Vibration and Acoustics*, vol. 141, no. 6, 2019.

[3] R. M. Jones, *Mechanics of composite materials*. CRC press, 1998.

[4] A. W. Leissa, *Vibration of shells*, vol. 288. Scientific and Technical Information Office, National Aeronautics and Space , 1973.

[5] D. M. Coombs, J. C. Goodding, V. Babuška, E. V. Ardelean, L. M. Robertson, and S. A. Lane, "Dynamic modeling and experimental validation of a cable-loaded panel," *Journal of Spacecraft and Rockets*, vol. 48, no. 6, pp. 958–974, 2011.

[6] V. Babuska, D. M. Coombs, J. C. Goodding, E. V. Ardelean, L. M. Robertson, and S. A. Lane, "Modeling and experimental validation of space structures with wiring harnesses," *Journal of Spacecraft and Rockets*, vol. 47, no. 6, pp. 1038–1052, 2010.

[7] E. Ardelean, J. Goodding, G. Mehle, D. Coombs, V. Babuska, L. Robertson, S. Lane, B. Ingram, and E. Hansen, "Dynamics of cable harnesses on large precision structures," in *48th AIAA/ASME/ASCE/AHS/ASC Structures, Structural Dynamics, and Materials Conference*, p. 2388, 2007.

[8] L. Robertson, S. Lane, B. Ingram, E. Hansen, V. Babuska, J. Goodding, M. Mimovich, G. Mehle, D. Coombs, and E. Ardelean, "Cable effects on the dynamics of large precision structures," in *48th AIAA/ASME/ASCE/AHS/ASC Structures, Structural Dynamics, and Materials Conference*, p. 2389, 2007.

[9] J. Goodding, V. Babuska, D. T. Griffith, B. Ingram, and L. Robertson, "Studies of free-free beam structural dynamics perturbations due to mounted cable harnesses," in *48th AIAA/ASME/ASCE/AHS/ASC Structures, Structural Dynamics, and Materials Conference*, p. 2390, 2007.

[10] J. Goodding, J. Griffee, and E. Ardelean, "Parameter estimation and structural dynamic modeling of electrical cable harnesses on precision structures," in *49th AIAA/ASME/ASCE/AHS/ASC Structures, Structural Dynamics, and Materials Conference, 16th AIAA/ASME/AHS Adaptive Structures Conference, 10th AIAA Non-Deterministic Approaches Conference, 9th AIAA Gossamer Spacecraft Forum, 4th AIAA Multidisciplinary Design Optimization Specialists Conference*, p. 1852, 2008.

[11] J. C. Goodding, "Spacecraft electrical cable harness structural test and analysis methods," in *IMAC: Conference and Exposition on Structural Dynamics*, pp. 437–443, 2008.

[12] E. Ardelean, J. Goodding, D. Coombs, J. Griffee, V. Babuška, L. Robertson, and S. Lane, "Cable effects study: Tangents, rat holes, dead ends, and valuable results," in *51st AIAA/ASME/ASCE/AHS/ASC Structures, Structural Dynamics, and Materials Conference 18th AIAA/ASME/AHS Adaptive Structures Conference 12th*, p. 2806, 2010.

[13] J. C. Goodding, E. V. Ardelean, V. Babuska, L. M. Robertson III, and S. A. Lane, "Experimental techniques and structural parameter estimation studies of spacecraft cables," *Journal of Spacecraft and Rockets*, vol. 48, no. 6, pp. 942–957, 2011.

[14] G. A. Lesieutre, "Frequency-independent modal damping for flexural structures via a viscous" geometric" damping model," *Journal of guidance, control, and dynamics*, vol. 33, no. 6, pp. 1931–1935, 2010.

[15] G. A. Lesieutre and J. L. Kauffman, "A viscous geometricbeam damping model for nearly constant modal damping," *AIAA Journal*, vol. 5, no. 7, pp. 1688–1694, 2013.

[16] J. L. Kauffman and G. A. Lesieutre, "Damping models for timoshenko beams with applications to spacecraft wiring harnesses," in *54th AIAA/ASME/ASCE/AHS/ASC Structures, Structural Dynamics, and Materials Conference*, p. 1890, 2013.

[17] J. L. Kauffman, G. A. Lesieutre, and V. Babuška, "Damping models for shear beams with applications to spacecraft wiring harnesses," *Journal of Spacecraft and Rockets*, vol. 51, no. 1, pp. 16–22, 2014.

[18] B. N. McPherson, G. A. Lesieutre, and J. L. Kauffman, "Investigation of viscous damping terms for a timoshenko beam," in *2018 AIAA/ASCE/AHS/ASC Structures, Structural Dynamics, and Materials Conference*, p. 0456, 2018.

[19] K. Spak, G. Agnes, and D. Inman, "Cable modeling and internal damping developments," *Applied Mechanics Reviews*, vol. 65, no. 1, 2013.

[20] K. Spak, G. Agnes, and D. Inman, "Comparison of damping models for space flight cables," in *Topics in Dynamics of Civil Structures, Volume 4*, pp. 183–194, Springer, 2013.

[21] K. S. Spak, G. S. Agnes, and D. Inman, "Towards modeling of cable-harnessed structures: cable damping experiments," in *54th AIAA/ASME/ASCE/AHS/ASC Structures, Structural Dynamics, and Materials Conference*, p. 1889, 2013.

[22] K. Spak, G. Agnes, and D. Inman, "Parameters for modeling stranded cables as structural beams," *Experimental Mechanics*, vol. 54, no. 9, pp. 1613–1626, 2014.

[23] J. Choi and D. Inman, "Development of predictive modeling for cable harnessed structure," in *54th AIAA/ASME/ASCE/AHS/ASC Structures, Structural Dynamics, and Materials Conference*, p. 1888, 2013.

[24] J. Choi and D. J. Inman, "Spectrally formulated modeling of a cable-harnessed structure," *Journal of sound and vibration*, vol. 333, no. 14, pp. 3286–3304, 2014.

[25] K. S. Spak, G. S. Agnes, and D. J. Inman, "Modeling vibration response and damping of cables and cabled structures," *Journal of Sound and Vibration*, vol. 336, pp. 240–256, 2015.

[26] B. Martin and A. Salehian, "Cable-harnessed space structures: A beam-cable approach," in *24th International Association of Science and Technology for Development International Conference on Modelling and Simulation*, pp. 280–284, ACTA Press Banff, Canada, 2013.

[27] B. Martin and A. Salehian, "Dynamic modelling of cable-harnessed beam structures with periodic wrapping patterns: a homogenization approach," *International Journal of Modelling and Simulation*, vol. 33, no. 4, pp. 185–202, 2013.

[28] B. Martin and A. Salehian, "Vibration analysis of string-harnessed beam structures: A homogenization approach," in *54th AIAA/ASME/ASCE/AHS/ASC Structures, Structural Dynamics, and Materials Conference*, p. 1892, 2013.

[29] B. Martin and A. Salehian, "Vibration modelling of string-harnessed beam structures using homogenization techniques," in *ASME International Mechanical Engineering Congress and Exposition*, vol. 46483, p. V04BT04A074, American Society of Mechanical Engineers, 2014.

[30] B. Martin and A. Salehian, "Homogenization modeling of periodically wrapped string-harnessed beam structures: experimental validation," *AIAA Journal*, vol. 54, no. 12, pp. 3965–3980, 2016.

[31] B. Martin and A. Salehian, "Mass and stiffness effects of harnessing cables on structural dynamics: continuum modeling," *AIAA Journal*, vol. 54, no. 9, pp. 2881–2904, 2016.

[32] B. Martin and A. Salehian, "String-harnessed beam structures: An inverse problem approach for model approximation," in *International Conference on Inverse Problems in Engineering, Waterloo, ON, Canada, May*, pp. 23–26, 2017.

[33] B. Martin and A. Salehian, "Continuum modeling of nonperiodic string-harnessed structures: Perturbation theory and experiments," *AIAA Journal*, vol. 57, no. 4, pp. 1736–1751, 2019.

[34] K. Yerrapragada and A. Salehian, "Coupled axial, in plane and out of plane bending vibrations of cable harnessed space structures," in *International Conference on Applied Mathematics, Modeling and Computational Science*, pp. 249–257, Springer, 2017.

[35] K. Yerrapragada and A. Salehian, "Coupled bending, torsion and axial vibrations of a cable-harnessed beam with periodic wrapping pattern," in *International Design Engineering Technical Conferences and Computers and Information in Engineering Conference*, vol. 51852, p. V008T10A030, American Society of Mechanical Engineers, 2018.

[36] K. Yerrapragada and A. Salehian, "Analytical study of coupling effects for vibrations of cable-harnessed beam structures," *Journal of Vibration and Acoustics*, vol. 141, no. 3, 2019.

[37] S. Cao, P. Agrawal, N. Qi, and A. Salehian, "Optimal geometry for cable wrapping to minimize dynamic impacts on cable-harnessed beam structures," *Journal of Vibration and Acoustics*, Submitted, Under Review, 2020.

[38] M. Remedia, G. S. Aglietti, and G. Richardson, "Modelling the effect of electrical harness on microvibration response of structures," *Acta Astronautica*, vol. 109, pp. 88–102, 2015.

[39] A. K. Noor, "Continuum modeling for repetitive lattice structures," *Applied Mechanics Reviews*, vol. 41, no. 7, pp. 285–296, 1988.

[40] D. L. Dean and C. P. Ugarte, "Field solutions for two-dimensional frameworks," *International Journal of Mechanical Sciences*, vol. 10, no. 4, pp. 315–339, 1968.

[41] J. Renton, "General properties of space grids," *International Journal of Mechanical Sciences*, vol. 12, no. 9, pp. 801–810, 1970.

[42] J. D. Renton, "The beam-like behavior of space trusses," *AIAA journal*, vol. 22, no. 2, pp. 273–280, 1984.

[43] P. Cartraud and T. Messager, "Computational homogenization of periodic beam-like structures," *International Journal of Solids and Structures*, vol. 43, no. 3-4, pp. 686–696, 2006.

[44] A. Kolpakov, "Calculation of the characteristics of thin elastic rods with a periodic structure," *Journal of Applied Mathematics and Mechanics*, vol. 55, no. 3, pp. 358–365, 1991.

[45] D. Manceau, "Small amplitude homogenization applied to models of non-periodic fibrous materials," *ESAIM: Mathematical Modelling and Numerical Analysis*, vol. 41, no. 6, pp. 1061–1087, 2007.

[46] A. Askar and A. Cakmak, "A structural model of a micropolar continuum," *International Journal of Engineering Science*, vol. 6, no. 10, pp. 583–589, 1968.

[47] C. Leech, "The modelling of net and cloth dynamics," *Journal of the Franklin Institute*, vol. 307, no. 6, pp. 361–378, 1979.

[48] C. Sun and T. Yang, "A continuum approach toward dynamics of gridworks," 1973.

[49] A. K. Noor, M. S. Anderson, and W. H. Greene, "Continuum models for beam-and platelike lattice structures," *Aiaa Journal*, vol. 16, no. 12, pp. 1219–1228, 1978.

[50] C. Sun and S. Liebbe, "Global-local approach to solving vibration of large truss structures," *AIAA journal*, vol. 28, no. 2, pp. 303–308, 1990.

[51] A. Salehian, E. M. Cliff, and D. J. Inman, "Continuum modeling of an innovative space-based radar antenna truss," *Journal of Aerospace Engineering*, vol. 19, no. 4, pp. 227–240, 2006.

[52] A. Salehian, T. M. Seigler, and D. J. Inman, "Dynamic effects of a radar panel mounted on a truss satellite," *AIAA journal*, vol. 45, no. 7, pp. 1642–1654, 2007.

[53] A. Salehian and D. J. Inman, "Dynamic analysis of a lattice structure by homogenization: Experimental validation," *Journal of Sound and Vibration*, vol. 316, no. 1-5, pp. 180–197, 2008.

[54] A. Salehian and D. Inman, "Micropolar continuous modeling and frequency response validation of a lattice structure," *Journal of Vibration and Acoustics*, vol. 132, no. 1, 2010.

[55] A. Salehian, "Effects of strain rates on kinetics of elements of repeated pattern structures: A continuous modeling approach," *Shock and Vibration*, vol. 19, no. 4, pp. 545–554, 2012.

[56] A. Salehian and Y. Chen, "On strain-rate dependence of kinetic energy in homogenization approach: theory and experiment," *AIAA journal*, vol. 50, no. 10, pp. 2029–2033, 2012.

[57] A. Salehian, M. Ibrahim, and T. Seigler, "Damping in periodic structures: a continuum modeling approach," *AIAA journal*, vol. 52, no. 3, pp. 569–590, 2014.

[58] R. Lord, "Theory of sound (two volumes)," 1877.

[59] S. Adhikari, *Damping models for structural vibration*. PhD thesis, University of Cambridge, 2001.

[60] H. T. Banks and D. Inman, "On damping mechanisms in beams," 1991.

[61] V. Gattulli and M. Lepidi, "Nonlinear interactions in the planar dynamics of cable-stayed beam," *International Journal of Solids and Structures*, vol. 40, no. 18, pp. 4729–4748, 2003.

[62] M.-Y. Liu, D. Zuo, and N. P. Jones, "Analytical and numerical study of deck-stay interaction in a cable-stayed bridge in the context of field observations," *Journal of Engineering Mechanics*, vol. 139, no. 11, pp. 1636–1652, 2013.

[63] Z. Kang, K. Xu, and Z. Luo, "A numerical study on nonlinear vibration of an inclined cable coupled with the deck in cable-stayed bridges," *Journal of Vibration and control*, vol. 18, no. 3, pp. 404–416, 2012.

[64] M. Lepidi and V. Gattulli, "Non-linear interactions in the flexible multi-body dynamics of cable-supported bridge cross-sections," *International Journal of Non-Linear Mechanics*, vol. 80, pp. 14–28, 2016.

[65] M. Wei, K. Lin, L. Jin, and D. Zou, "Nonlinear dynamics of a cable-stayed beam driven by sub-harmonic and principal parametric resonance," *International Journal of Mechanical Sciences*, vol. 110, pp. 78–93, 2016.

[66] S. Huang, "Stability analysis of the heave motion of marine cable-body systems," *Ocean Engineering*, vol. 26, no. 6, pp. 531–546, 1999.

[67] G. McClure and M. Lapointe, "Modeling the structural dynamic response of overhead transmission lines," *Computers & Structures*, vol. 81, no. 8-11, pp. 825–834, 2003.

[68] G. Cheng and J. W. Zu, "Dynamic analysis of an optical fiber coupler in telecommunications," *Journal of Sound and Vibration*, vol. 268, no. 1, pp. 15–31, 2003.

[69] J. S. Issa and W. F. Habchi, "Vibration suppression in a cantilever beam using a string-type vibration absorber," in *ASME International Mechanical Engineering Congress and Exposition*, vol. 44502, pp. 215–221, 2010.

[70] H. Rezaei DA, M. Kadkhodaei, and H. Nahvi, "Analysis of nonlinear free vibration and damping of a clamped–clamped beam with embedded prestrained shape memory alloy wires," *Journal of Intelligent Material Systems and Structures*, vol. 23, no. 10, pp. 1107–1117, 2012.

[71] D. More and S. Kumbhar, "An experimental study on shift in natural frequency of sandwich beam with elastomeric core embedded with sma wires," in *International Conference on Advanced Nanomaterials & Emerging Engineering Technologies*, pp. 592–596, IEEE, 2013.

[72] D. J. Inman and R. C. Singh, *Engineering vibration*, vol. 3. Prentice Hall Englewood Cliffs, NJ, 1994.

[73] N. Labonnote, A. Rønnquist, and K. A. Malo, "Modified hysteretic damping model applied to timoshenko timber beams," *Computers & Structures*, vol. 121, pp. 22–31, 2013.

[74] S. S. Rao, *Vibration of continuous systems*, vol. 464. Wiley Online Library, 2007.

[75] P. Agrawal and A. Salehian, "Damping mechanisms in cable-harnessed structures for space applications: Analytical modeling," *Journal of Vibration and Acoustics*, vol. 143, no. 2, 2020.

[76] T. Kocatürk and M. Şimşek, "Dynamic analysis of eccentrically prestressed viscoelastic timoshenko beams under a moving harmonic load," *Computers & structures*, vol. 84, no. 31-32, pp. 2113–2127, 2006.

[77] W.-R. Chen, "Bending vibration of axially loaded timoshenko beams with locally distributed kelvin–voigt damping," *Journal of Sound and Vibration*, vol. 330, no. 13, pp. 3040–3056, 2011.

[78] F. Cortés and M. J. Elejabarrieta, "Structural vibration of flexural beams with thick unconstrained layer damping," *International Journal of Solids and Structures*, vol. 45, no. 22-23, pp. 5805–5813, 2008.

[79] P. Warnitchai, Y. Fujino, and T. Susumpow, "A non-linear dynamic model for cables and its application to a cable-structure system," *Journal of Sound and Vibration*, vol. 187, no. 4, pp. 695–712, 1995.

[80] B. Yang and C. Tan, "Transfer functions of one-dimensional distributed parameter systems," 1992.

[81] B. Yang and H. Fang, "A transfer-function formulation for nonuniformly distributed parameter systems," 1994.

[82] G. D. Gounaris, E. Antonakakis, and C. A. Papadopoulos, "Hysteretic damping of structures vibrating at resonance: An iterative complex eigensolution method based on damping-stress relation," *Computers & structures*, vol. 85, no. 23-24, pp. 1858–1868, 2007.

[83] P. Agrawal and A. Salehian, "Damping mechanisms in cable-harnessed structures for space applications: Experimental validation," *Journal of Vibration and Acoustics*, vol. 143, no. 2, 2020.

[84] K. Menard, *Dynamic Mechanical Analysis*. CRC press, 2008.

[85] M. S. Corporation, *Model 831.50 x 1000Hz Elastomer Test System Features High Frequency Test Capability*, 2004 (accessed July 9, 2020).

[86] P. Agrawal and A. Salehian, "Vibration analysis of cable-harnessed plate structures," in *Proceedings of 26th International Congress of Sound and Vibration*, pp. 1–8, 2019.

[87] P. Agrawal and A. Salehian, "Vibrations analysis of cable-harnessed plates: Continuum modeling and experimental validation," *Journal of Vibration and Acoustics*, Accepted, 2020.

[88] J. N. Reddy, *Theory and analysis of elastic plates and shells*. CRC press, 1999.

[89] S. P. Timoshenko and S. Woinowsky-Krieger, *Theory of plates and shells*. McGraw-hill, 1959.

[90] J. N. Reddy, *Mechanics of laminated composite plates and shells: theory and analysis*. CRC press, 2003.

[91] B. Martin, "Continuum modelling and vibration analysis of string-harnessed structures," 2017.

[92] M. Pastor, M. Binda, and T. Harčarik, "Modal assurance criterion," *Procedia Engineering*, vol. 48, pp. 543–548, 2012.

[93] P. Agrawal and A. Salehian, "Continuum modeling and vibrations analysis of cable-harnessed plate structures of periodic patterns," *Journal of Vibration and Acoustics*, Submitted, Under Review, 2020.

[94] A. K. Noor and C. Andersen, "Analysis of beam-like lattice trusses," *Computer Methods in Applied Mechanics and Engineering*, vol. 20, no. 1, pp. 53–70, 1979.

[95] C. Xiang-sheng, "On buckling of cantilever rectangular plates under symmetrical edge loading," *Applied Mathematics and Mechanics*, vol. 11, no. 4, pp. 377–383, 1990.

[96] L. H. Donnell, *Stability of thin-walled tubes under torsion*. US Government Printing Office, 1933.

[97] K. M. Mushtari, "On the stability of cylindrical shells subjected to torsion," *Trudy Kazanskego aviatsionnugo inatituta*, vol. 2, 1938.

[98] A. E. H. Love, *A Treatise on the Mathematical Theory of Elasticity, by AEH Love*. The University Press, 1906.

[99] E. Reissner, "A new derivation of the equations for the deformation of elastic shells," *American Journal of Mathematics*, vol. 63, no. 1, pp. 177–184, 1941.

[100] P. Naghdi and J. Berry, "On the equations of motion of cylindrical shells," *Journal of Applied Mechanics*, vol. 21, no. 2, pp. 160–166, 1964.

[101] V. Vlasov, "Osnovnye differentsial'nye uravneniia obshchei teorii uprugikh obolochek [basic differential equations in the general theory of elastic shells]," *PMM*, vol. 8, no. 2, 1944.

[102] J. L. Sanders, *An improved first-approximation theory for thin shells*, vol. 24. US Government Printing Office, 1960.

[103] W. Flügge, *Stresses in shells*. Springer Science & Business Media, 2013.

[104] A. Goldenveizer, G. Herrmann, and P. Naghdi, "Theory of elastic thin shells," 1963.

[105] J. Witz and Z. Tan, "On the axial-torsional structural behaviour of flexible pipes, umbilicals and marine cables," *Marine Structures*, vol. 5, no. 2-3, pp. 205–227, 1992.

[106] A. Dall'Asta and G. Leoni, "Vibrations of beams prestressed by internal frictionless cables," *Journal of sound and vibration*, vol. 222, no. 1, pp. 1–18, 1999.

[107] P. Agrawal and A. Salehian, "Experimental validation of the vibration characteristics of cable-harnessed panels with wrapped cable geometry," *Journal of Vibration and Acoustics*, To be submitted, 2020.

[108] Z.-F. Fu and J. He, *Modal analysis*. Elsevier, 2001.

APPENDICES

Appendix A

Supplementary information on modeling of Cable-harnessed beam structures presented in Chapter 2

A.1 Calculation of the length and mass of the fundamental element

A.1.1 Zigzag pattern

The cable present within the fundamental element can be divided into four sections each on a different face of the beam. The total length of the cable wrapped around the beam within a fundamental element can be written as:

$$L^{(c)}_{e,zigzag} = \frac{2\bar{b}}{\sin\theta} + \frac{2\bar{h}}{\sin\theta} + \frac{2\bar{b}}{\sin\theta} + \frac{2\bar{h}}{\sin\theta} = \frac{4\left(\bar{b}+\bar{h}\right)}{\sin\theta} \tag{A.1}$$

Hence, the mass of cable within the fundamental element becomes

$$m^{(c)}_{e,zigzag} = \rho_c A_c \frac{4\left(\bar{b}+\bar{h}\right)}{\sin\theta} \tag{A.2}$$

Further, the length of the beam fundamental element can be expressed in terms of wrapping angle, and beam and cable parameters as

$$L_{e-zigzag} = \frac{2\bar{b}}{\tan\theta} + \frac{2\bar{h}}{\tan\theta} + \frac{2\bar{b}}{\tan\theta} + \frac{2\bar{h}}{\tan\theta} = \frac{4\left(\bar{b}+\bar{h}\right)}{\tan\theta} \tag{A.3}$$

Hence, the total mass of the fundamental element for the zigzag pattern is written by summing the mass of beam and cable as:

$$m_{e,zigzag} = \left(\rho_b A_b \frac{4\left(\bar{b}+\bar{h}\right)}{\tan\theta} + \rho_c A_c \frac{4\left(\bar{b}+\bar{h}\right)}{\sin\theta} \right) = \left(\rho_b A_b + \frac{\rho_c A_c}{\cos\theta} \right) \frac{4\left(\bar{b}+\bar{h}\right)}{\tan\theta} \tag{A.4}$$

A.1.2 Diagonal pattern

Similar to the previous case, for the diagonal pattern as well, the cable can be divided into four sections each on a different face of the beam. The total length of the cable within a fundamental element can be written as:

$$L^{(c)}_{e,diagonal} = \frac{2\bar{b}}{\sin\theta} + 2\bar{h} + 2\bar{b} + 2\bar{h} = 2\left(\frac{\bar{b}}{\sin\theta} + 2\bar{h} + \bar{b} \right) \tag{A.5}$$

Hence, the mass of cable within the fundamental element becomes

$$m^{(c)}_{e,diagonal} = 2\rho_c A_c \left(\frac{\bar{b}}{\sin\theta} + 2\bar{h} + \bar{b} \right) \tag{A.6}$$

The length of the beam fundamental element can be expressed in terms of wrapping angle, and beam and cable parameters as

$$L_{e-diagonal} = \frac{2\bar{b}}{\tan\theta} \tag{A.7}$$

Hence, the total mass of the fundamental element for the diagonal pattern is written as:

$$\begin{aligned} m_{e,zigzag} &= \left(\rho_b A_b \frac{2\bar{b}}{\tan\theta} + 2\rho_c A_c \left(\frac{\bar{b}}{\sin\theta} + 2\bar{h} + \bar{b} \right) \right) \\ &= \left(\rho_b A_b + \frac{\rho_c A_c \tan\theta}{\bar{b}} \left[\frac{\bar{b}}{\sin\theta} + 2\bar{h} + \bar{b} \right] \right) \frac{2\bar{b}}{\tan\theta} \end{aligned} \tag{A.8}$$

A.2 Calculation of strain energy

The strain energy of the beam part within an arbitrary fundamental element:

$$U_{e,beam} = \iiint_{V_b} \frac{1}{2} E_b \left(-\frac{T\cos(\theta)}{E_b A_b} - z\frac{\partial^2 w}{\partial \xi^2} + \frac{z^2}{2}\left(\frac{\partial^2 w}{\partial \xi^2} \right)^2 + \frac{1}{2}\left(\frac{\partial w}{\partial \xi} \right)^2 \right)^2 dA\, d\xi \tag{A.9}$$

$$U_{e,beam} = \iiint_{V_b} \frac{1}{2} E_b \Bigg[\frac{1}{4} \left(\frac{\partial w}{\partial \xi} \right)^4 - z \left(\frac{\partial w}{\partial \xi} \right)^2 \frac{\partial^2 w}{\partial \xi^2} + z^2 \left(\frac{\partial^2 w}{\partial \xi^2} \right)^2 + \frac{1}{2} z^2 \left(\frac{\partial w}{\partial \xi} \right)^2 \left(\frac{\partial^2 w}{\partial \xi^2} \right)^2 - z^3 \left(\frac{\partial^2 w}{\partial \xi^2} \right)^3 + \frac{z^4}{4} \left(\frac{\partial^2 w}{\partial \xi^2} \right)^4 - \frac{T cos(\theta)}{A_b E_b} \left(\frac{\partial w}{\partial \xi} \right)^2 + \frac{2Tz cos(\theta)}{A_b E_b} \frac{\partial^2 w}{\partial \xi^2} - \frac{Tz^2 cos(\theta)}{A_b E_b} \left(\frac{\partial^2 w}{\partial \xi^2} \right)^2 + \frac{T^2 \cos^2 \theta}{A_b^2 E_b^2} \Bigg] dA \; d\xi \quad \text{(A.10)}$$

$$U_{e,beam} \approx \iiint_{V_b} \frac{1}{2} E_b \Bigg[z^2 \left(\frac{\partial^2 w}{\partial \xi^2} \right)^2 - \frac{T cos(\theta)}{A_b E_b} \left(\frac{\partial w}{\partial \xi} \right)^2 + \frac{2Tz cos(\theta)}{A_b E_b} \frac{\partial^2 w}{\partial \xi^2} - \frac{Tz^2 cos(\theta)}{A_b E_b} \left(\frac{\partial^2 w}{\partial \xi^2} \right)^2 + \frac{T^2 \cos^2 \theta}{A_b^2 E_b^2} \Bigg] dA \; d\xi \quad \text{(A.11)}$$

On performing integration over the cross-section of the beam, we obtain

$$U_{e,beam} = \int_0^{L_e} \left\{ \frac{1}{2} \left(E_b I_b - \frac{T cos\,(\theta)\, I_b}{A_b} \right) \left(\frac{\partial^2 w}{\partial \xi^2} \right)^2 - \frac{1}{2} T \cos\theta \left(\frac{\partial w}{\partial \xi} \right)^2 + \frac{T^2 \cos^2 \theta}{2 A_b E_b} \right\} dx \quad \text{(A.12)}$$

The strain energy of the cable part within an arbitrary fundamental element can be written as:

$$U_{e,cable} = \int_0^{L_e} \int_{A_c} \frac{1}{2} E_c \left(\frac{T}{E_c A_c} + \left(-z_c \, \frac{\partial^2 w}{\partial \xi^2} + \frac{z_c^2}{2} \left(\frac{\partial^2 w}{\partial \xi^2} \right)^2 + \frac{1}{2} \left(\frac{\partial w}{\partial \xi} \right)^2 \right) \cos^2 \theta \right)^2 dA \left(\frac{d\xi}{\cos\theta} \right) \quad \text{(A.13)}$$

Expanding the square term results in

$$U_{e,cable} = \int_0^{L_e} \int_{A_c} \frac{1}{2} E_c \Bigg[\frac{1}{4} \left(\frac{\partial w}{\partial \xi} \right)^4 \cos^4(\theta) - z_c \left(\frac{\partial w}{\partial \xi} \right)^2 \frac{\partial^2 w}{\partial \xi^2} \cos^4(\theta) + z_c^2 \left(\frac{\partial^2 w}{\partial \xi^2} \right)^2 \cos^4(\theta) + \frac{1}{2} z_c^2 \left(\frac{\partial w}{\partial \xi} \right)^2 \left(\frac{\partial^2 w}{\partial \xi^2} \right)^2 \cos^4(\theta) - z_c^3 \left(\frac{\partial^2 w}{\partial \xi^2} \right)^3 \cos^4(\theta) + \frac{z_c^4}{4} \left(\frac{\partial^2 w}{\partial \xi^2} \right)^4 \cos^4(\theta) + \frac{T^2}{A_c^2 E_c^2} + \frac{T}{A_c E_c} \left(\frac{\partial w}{\partial \xi} \right)^2 \cos^2(\theta) - \frac{2Tz_c}{A_c E_c} \frac{\partial^2 w}{\partial \xi^2} \cos^2(\theta) + \frac{Tz_c^2}{A_c E_c} \left(\frac{\partial^2 w}{\partial \xi^2} \right)^2 \cos^2(\theta) \Bigg] dA \left(\frac{d\xi}{\cos\theta} \right) \quad \text{(A.14)}$$

On ignoring the terms higher than second order in displacement and its derivatives, the above expression is simplified as,

$$U_{e,cable} \approx \int_0^{L_e} \int_{A_c} \frac{1}{2} E_c \Bigg[z_c^2 \left(\frac{\partial^2 w}{\partial \xi^2} \right)^2 \cos^4(\theta) + \frac{T^2}{A_c^2 E_c^2} + \frac{T}{A_c E_c} \left(\frac{\partial w}{\partial \xi} \right)^2 \cos^2(\theta) - \frac{2T z_c}{A_c E_c} \frac{\partial^2 w}{\partial \xi^2} \cos^2(\theta) + \frac{T z_c^2}{A_c E_c} \left(\frac{\partial^2 w}{\partial \xi^2} \right)^2 \cos^2(\theta) \Bigg] dA \left(\frac{d\xi}{\cos\theta} \right) \quad \text{(A.15)}$$

Performing the integration over the cable's cross sectional area, we obtain

$$U_{e,cable} = \int_0^{L_e} \Bigg[\frac{1}{2} \left(E_c A_c z_c^2 \cos^3(\theta) + T z_c^2 \cos(\theta) \right) \left(\frac{\partial^2 w}{\partial \xi^2} \right)^2 - T z_c \cos\theta \, \frac{\partial^2 w}{\partial \xi^2} + \frac{1}{2} T \cos\theta \, \left(\frac{\partial w}{\partial \xi} \right)^2 + \frac{T^2}{2 A_c E_c \cos\theta} \Bigg] d\xi \quad \text{(A.16)}$$

The total strain energy within the fundamental element is a summation of strain energy in the beam and cable elements:

$$U_e = U_{e,beam} + U_{e,cable} \quad \text{(A.17)}$$

The total strain energy would be different for the fundamental element for both wrapping patterns. These energy expressions are calculated in the following sections:

A.2.1 Zigzag pattern

Using Fig. 2.1, the z_c coordinate values of the center of the cable are used to obtain the strain energy for the cable on each side, bottom and top sections for a zigzag element. They can be found as,

$$z_c(\xi) = \begin{cases} \bar{h} \, , & 0 \le \xi \le \frac{2\bar{b}}{\tan\theta} = L_1 \\ -\xi \tan\theta + 2\bar{b} + \bar{h} \, , & \frac{2\bar{b}}{\tan\theta} \le \xi \le \frac{2h+2\bar{b}}{\tan\theta} = L_2 \\ -\bar{h} \, , & \frac{2h+2\bar{b}}{\tan\theta} \le \xi \le \frac{4b+2\bar{h}}{\tan\theta} = L_3 \\ \xi \tan\theta - 4\bar{b} - 3\bar{h} \, , & \frac{4b+2\bar{h}}{\tan\theta} \le \xi \le \frac{4h+4\bar{b}}{\tan\theta} = L_e \end{cases} \quad \text{(A.18)}$$

The Taylors series expansion for the displacement within the fundamental element about the center of the fundamental element is given as:

$$w\left(\xi,t\right)=w\left(\frac{L_e}{2},t\right)+\left(\xi-\frac{L_e}{2}\right)\frac{\partial w}{\partial\xi}\left(\frac{L_e}{2},t\right)+\frac{1}{2}\left(\xi-\frac{L_e}{2}\right)^2\frac{\partial^2 w}{\partial\xi^2}\left(\frac{L_e}{2},t\right) \tag{A.19}$$

Clearly, the total strain energy of the zigzag pattern can be found by calculating the strain energy for each of the four sections as

$$U_{e-zigzag}=\int_0^{L_1}dU_e|_{z_c=\bar{h}}+\int_{L_1}^{L_2}dU_e|_{z_c=-\tan\theta\xi+2\bar{b}+\bar{h}}+\int_{L_2}^{L_3}dU_e|_{z_c=-\bar{h}} + \int_{L_3}^{L_e}dU_e|_{z_c=\tan\theta\xi-4\bar{b}-3\bar{h}} \tag{A.20}$$

Assume that the four integrals on the right hand side can be termed as U_1, U_2, U_3 and U_4, respectively. Using Eq. 2.16, these expressions can be simplified by integrating over their respective limits and written as (assuming $w\left(\xi,t\right)|_{\xi=\frac{L_e}{2}}=w^*\left(t\right)$):

$$U_1=\frac{1}{2}\left[E_bI_b(L_1)+(E_cA_c\cos^3\theta+T\cos\theta)(\bar{h}^2L_1)-\frac{T\cos\theta I_b}{A_b}\left(L_1\right)\right]\left(\frac{\partial^2 w^*}{\partial\xi^2}\right)^2 - T\bar{h}\cos\theta\frac{\partial^2 w^*}{\partial\xi^2}\left(L_1\right)+\frac{T^2\ \cos^2\theta}{2E_bA_b}(L_1)+\frac{T^2}{2E_cA_c\cos\theta}\ \left(L_1\right) \tag{A.21}$$

$$U_2=\frac{1}{2}\Bigg[E_bI_b(-L_1+L_2)+\left(E_cA_c\cos^3\theta+T\cos\theta\right)\Bigg(\left(4\bar{b}^2+4\bar{b}\bar{h}+\bar{h}^2\right)\left(-L_1+L_2\right) +\left(-\frac{L_1^3}{3}+\frac{L_2^3}{3}\right)\tan^2\theta+\left(-\frac{L_1^2}{2}+\frac{L_2^2}{2}\right)\left(-4\bar{b}\tan\theta-2\bar{h}\tan\theta\right)\Bigg)-\frac{T\cos\theta I_b}{A_b}\left(-L_1+L_2\right)\Bigg]\left(\frac{\partial^2 w^*}{\partial\xi^2}\right)^2 - T\cos\theta\left(-\tan\theta\left(-\frac{L_1^2}{2}+\frac{L_2^2}{2}\right)+\left(2\bar{b}+\bar{h}\right)\left(-L_1+L_2\right)\right)\frac{\partial^2 w^*}{\partial\xi^2}+\frac{T^2\ \cos^2\theta}{2E_bA_b}(-L_1+L_2) + \frac{T^2}{2E_cA_c\cos\theta}\ \left(-L_1+L_2\right) \tag{A.22}$$

$$U_3 = \frac{1}{2}\Bigg[E_b I_b(-L_2+L_3) + (E_c A_c \cos^3\theta + T\cos\theta)\bar{h}^2(-L_2+L_3) - \frac{T\cos\theta I_b}{A_b}(-L_2+L_3)\Bigg]\left(\frac{\partial^2 w^*}{\partial\xi^2}\right)^2 + T\bar{h}\cos\theta\frac{\partial^2 w^*}{\partial\xi^2}(-L_2+L_3) + \frac{T^2\cos^2\theta}{2E_b A_b}(-L_2+L_3) + \frac{T^2}{2E_c A_c\cos\theta}(-L_2+L_3) \quad \text{(A.23)}$$

$$U_4 = \frac{1}{2}\Bigg[E_b I_b(-L_3+L_e) + \left(E_c A_c\cos^3\theta + T\cos\theta\right)\Bigg(\left(16\bar{b}^2+24\bar{b}\bar{h}+9\bar{h}^2\right)(-L_3+L_e) + \left(-\frac{L_3^3}{3}+\frac{L_e^3}{3}\right)\tan^2\theta + \left(-\frac{L_3^2}{2}+\frac{L_e^2}{2}\right)\left(-8\bar{b}\tan\theta - 6\bar{h}\tan\theta\right)\Bigg) - \frac{T\cos\theta I_b}{A_b}(-L_3+L_e)\Bigg]\left(\frac{\partial^2 w^*}{\partial\xi^2}\right)^2 - T\cos\theta\left(\tan\theta\left(-\frac{L_3^2}{2}+\frac{L_e^2}{2}\right) - (4\bar{b}+3\bar{h})(-L_3+L_e)\right)\frac{\partial^2 w^*}{\partial\xi^2} + \frac{T^2\cos^2\theta}{2E_b A_b}(-L_3+L_e) + \frac{T^2}{2E_c A_c\cos\theta}(-L_3+L_e) \quad \text{(A.24)}$$

Upon summation of Eqs. A.21 —A.24 , we get the total strain energy within the fundamental element of zigzag pattern mentioned in Eq. 2.17.

A.2.2 Diagonal pattern

The cables on the side and bottom sections in the diagonal pattern do not contribute to the strain energy, as the cables for those sections will not strain during bending. This is because the width and the thickness of the beam are assumed to remain constant and do not deform during the bending vibrations.

For the diagonal wrapping pattern, the z_c coordinate values of the center of cable can be expressed as

$$z_c(\xi) = \bar{h}, \quad 0 \le \xi \le L_e \quad \text{(A.25)}$$

The strain energy for the fundamental element can be simply written using Eq. 2.16

as:

$$
\begin{aligned}
U_{e-diagonal} &= \int_0^{L_e} dU_e|_{z_c=\bar{h}} \\
&= \int_0^{L_e} \left[\frac{1}{2} \left[E_b I_b + E_c A_c \bar{h}^2 \cos^3\theta + T\bar{h}^2 \cos\theta - \frac{T\cos\theta I_b}{A_b} \right] \left(\frac{\partial^2 w^*}{\partial \xi^2} \right)^2 \right. \\
&\left. - T\bar{h}\cos\theta \frac{\partial^2 w^*}{\partial \xi^2} + \frac{T^2 \cos^2\theta}{2E_b A_b} + \frac{T^2}{2E_c A_c \cos\theta} \right] d\xi
\end{aligned} \tag{A.26}
$$

The simplification of Eq. A.26 results in the Eq. 2.18.

A.3 Rayleigh Dissipation function of the fundamental element

Expansion of the square term in Eq. 2.29 after calculating the time derivative results in

$$
\begin{aligned}
R_b = \int_0^{L_e} \int_{A_b} \frac{1}{2} C_b \left[z^2 \left(\frac{\partial^3 w}{\partial t\, \partial \xi^2} \right)^2 + z^4 \left(\frac{\partial^2 w}{\partial \xi^2} \right)^2 \left(\frac{\partial^3 w}{\partial t\, \partial \xi^2} \right)^2 + \left(\frac{\partial w}{\partial \xi} \right)^2 \left(\frac{\partial^2 w}{\partial t\, \partial \xi} \right)^2 \right. \\
- 2z^3 \left(\frac{\partial^2 w}{\partial \xi^2} \right) \left(\frac{\partial^3 w}{\partial t\, \partial \xi^2} \right)^2 + 2z^2 \left(\frac{\partial w}{\partial \xi} \right) \left(\frac{\partial^2 w}{\partial \xi^2} \right) \left(\frac{\partial^2 w}{\partial t\, \partial \xi} \right) \left(\frac{\partial^3 w}{\partial t\, \partial \xi^2} \right) \\
\left. - 2z \left(\frac{\partial w}{\partial \xi} \right) \left(\frac{\partial^3 w}{\partial t\, \partial \xi^2} \right) \left(\frac{\partial^2 w}{\partial t\, \partial \xi} \right) \right] dA d\xi
\end{aligned} \tag{A.27}
$$

In this expression, the higher order terms are neglected and the terms upto the second order of polynomial in $w(\xi, t)$ and its derivatives are kept. This truncation results in Eq. 2.30.

Similarly, Eq. 2.33 can be simplified as:

$$
\begin{aligned}
R_c = \int_0^{L_e} \int_{A_c} \frac{1}{2} C_c \left(z_c^2 \left(\frac{\partial^3 w}{\partial t\, \partial \xi^2} \right)^2 + z_c^4 \left(\frac{\partial^2 w}{\partial \xi^2} \right)^2 \left(\frac{\partial^3 w}{\partial t\, \partial \xi^2} \right)^2 + \left(\frac{\partial w}{\partial \xi} \right)^2 \left(\frac{\partial^2 w}{\partial t\, \partial \xi} \right)^2 \right. \\
- 2z_c^3 \left(\frac{\partial^2 w}{\partial \xi^2} \right) \left(\frac{\partial^3 w}{\partial t\, \partial \xi^2} \right)^2 + 2z_c^2 \left(\frac{\partial w}{\partial \xi} \right) \left(\frac{\partial^2 w}{\partial \xi^2} \right) \left(\frac{\partial^2 w}{\partial t\, \partial \xi} \right) \left(\frac{\partial^3 w}{\partial t\, \partial \xi^2} \right) \\
\left. - 2z_c \left(\frac{\partial w}{\partial \xi} \right) \left(\frac{\partial^3 w}{\partial t\, \partial \xi^2} \right) \left(\frac{\partial^2 w}{\partial t\, \partial \xi} \right) \right) \cos^3\theta\, dA d\xi
\end{aligned} \tag{A.28}
$$

An assumption similar to Eq. A.27 is taken while calculating the Rayleigh-dissipation function for the cable to obtain Eq. 2.34. Eqs. A.27 and A.28 upon integrating over respective cross section area, truncating higher order terms and summing together results in total Rayleigh dissipation function, R_e, presented in Eq. 2.35. Further, R_e is calculated over the entire length by expanding the Taylor's series for the velocity $\dot{w}(\xi,t)$ about the center of the fundamental element

$$\dot{w}(\xi,t) = \dot{w}\left(\frac{L_e}{2},t\right) + \left(\xi - \frac{L_e}{2}\right)\frac{\partial \dot{w}}{\partial \xi}\left(\frac{L_e}{2},t\right) + \frac{1}{2}\left(\xi - \frac{L_e}{2}\right)^2 \frac{\partial^2 \dot{w}}{\partial \xi^2}\left(\frac{L_e}{2},t\right) \tag{A.29}$$

A.3.1 Zigzag Pattern

Using Eq. A.18 , the total energy loss rate of the zigzag pattern can be found by calculating the Rayleigh dissipation function for each of the four sections as

$$R_{e-zigzag} = \int_0^{L_1} dR_e|_{z_c=\bar{h}} + \int_{L_1}^{L_2} dR_e|_{z_c=-\tan\theta\xi+2\bar{b}+\bar{h}} + \int_{L_2}^{L_3} dR_e|_{z_c=-\bar{h}} + \int_{L_3}^{L_e} dR_e|_{z_c=\tan\theta\xi-4\bar{b}-3\bar{h}} \tag{A.30}$$

Assume that the four integrals on the right hand side can be termed as R_1, R_2, R_3 and R_4, respectively. Using Eq. 2.35, R_1, R_2, R_3 and R_4 can be simplified by integrating over their respective limits and written as (assume $\dot{w}(\xi,t)|_{\xi=\frac{L_e}{2}} = \dot{w}^*(t)$):

$$R_1 = \frac{1}{2}\left[C_b I_b(L_1) + (C_c A_c \cos^3\theta)(\bar{h}^2 L_1)\right]\left(\frac{\partial^2 \dot{w}^*}{\partial \xi^2}\right)^2 \tag{A.31}$$

$$R_2 = \frac{1}{2}\Bigg[C_b I_b(-L_1+L_2) + \left(C_c A_c \cos^3\theta\right)\Bigg(\left(4\bar{b}^2 + 4\bar{b}\bar{h} + \bar{h}^2\right)(-L_1+L_2) + \left(-\frac{L_1^3}{3} + \frac{L_2^3}{3}\right)\tan^2\theta + \left(-\frac{L_1^2}{2} + \frac{L_2^2}{2}\right)\left(-4\bar{b}\tan\theta - 2\bar{h}\tan\theta\right)\Bigg)\Bigg]\left(\frac{\partial^2 \dot{w}^*}{\partial \xi^2}\right)^2 \tag{A.32}$$

$$R_3 = \frac{1}{2}\left[C_b I_b(-L_2+L_3) + (C_c A_c \cos^3\theta)\bar{h}^2(-L_2+L_3)\right]\left(\frac{\partial^2 \dot{w}^*}{\partial \xi^2}\right)^2 \tag{A.33}$$

$$R_4 = \frac{1}{2}\Bigg[C_b I_b(-L_3+L_e) + \left(C_c A_c \cos^3\theta\right)\Bigg(\left(16\bar{b}^2+24\bar{b}\bar{h}+9\bar{h}^2\right)(-L_3+L_e) + \left(-\frac{L_3^3}{3}+\frac{L_e^3}{3}\right)\tan^2\theta + \left(-\frac{L_3^2}{2}+\frac{L_e^2}{2}\right)\left(-8\bar{b}\tan\theta - 6\bar{h}\tan\theta\right)\Bigg)\Bigg]\left(\frac{\partial^2\ \dot{w}^*}{\partial\xi^2}\right)^2 \quad \text{(A.34)}$$

Upon summation of Eqs. A.31 —A.34, we get the total energy loss rate within the fundamental element of zigzag pattern mentioned in Eq. 2.36.

A.3.2 Diagonal Pattern

The cables on the side and bottom sections in the diagonal pattern do not contribute to the energy loss, as the cables for those sections will not strain during bending. Hence, the energy in the cable is assumed to be lost from the element on the top surface only.

For the diagonal wrapping pattern, the z_c coordinate values of the center of cable can be expressed as

$$z_c(\xi) = \bar{h}, \quad 0 \le \xi \le L_e \quad \text{(A.35)}$$

The energy dissipation rate for the fundamental element can be simply written as

$$\begin{aligned} R_{e-diagonal} &= \int_0^{L_e} dR_e|_{z_c=\bar{h}} \\ &= \int_0^{L_e}\left\{\frac{1}{2}\left[C_b I_b + C_c A_c \bar{h}^2\cos^3\theta\right]\left(\frac{\partial^2\ \dot{w}^*}{\partial\xi^2}\right)^2\right\}d\xi \end{aligned} \quad \text{(A.36)}$$

The simplification of A.36 results in Eq. 2.37.

A.4 Hamilton's principle

Eq. 2.50 can be written as:

$$\delta\int_{t_o}^{t_1}\left(\int_0^l \frac{1}{2}K_1(\dot{w})^2\,dx\right)dt - \delta\int_{t_o}^{t_1}\left(\int_0^l\left(\frac{1}{2}B_1\left(\frac{\partial^2 w}{\partial x^2}\right)^2 + B_2\frac{\partial^2 w}{\partial x^2} + B_3\right)dx\right)dt - \int_{t_o}^{t_1}\left(\int_0^l D_1\left(\frac{\partial^2\dot{w}}{\partial x^2}\right)\delta\left(\frac{\partial^2 w}{\partial x^2}\right)dx\right)dt = 0 \quad \text{(A.37)}$$

Here, the third term has been simplified using Eqs. 2.42 and 2.51. Eq. A.37 is evaluated using integration by parts as

$$-\int_{t_0}^{t_1}\left(\int_0^l K_1\ddot{w}\ \delta w\ dx\right)dt-\int_{t_0}^{t_1}\left(B_1\frac{\partial^2 w}{\partial x^2}\ \delta\left(\frac{\partial w}{\partial x}\right)\Big|_0^l-B_1\frac{\partial^3 w}{\partial x^3}\ (\delta w)|_0^l+\int_0^l B_1\frac{\partial^4 w}{\partial x^4}\delta w\ dx\right)dt-$$
$$\int_{t_0}^{t_1}\left(B_2\ \delta\left(\frac{\partial w}{\partial x}\right)\Big|_0^l\right)dt-\int_{t_0}^{t_1}\left(D_1\frac{\partial^2 \dot{w}}{\partial x^2}\ \delta\left(\frac{\partial w}{\partial x}\right)\Big|_0^l-D_1\frac{\partial^3 \dot{w}}{\partial x^3}\ (\delta w)|_0^l+\int_0^l D_1\frac{\partial^4 \dot{w}}{\partial x^4}\delta w\ dx\right)dt \tag{A.38}$$

The terms can be re-organized and written as:

$$\int_{t_0}^{t_1}\left\{\int_0^l\left[B_1\frac{\partial^4 w}{\partial x^4}-K_1\ddot{w}\ +\ D_1\frac{\partial^4 \dot{w}}{\partial x^4}\right]\delta w dx\right\}dt$$
$$+\int_{t_0}^{t_1}\left\{\int_0^l\left[-\left(B_1\frac{\partial^2 w}{\partial x^2}+D_1\frac{\partial^2 \dot{w}}{\partial x^2}-B_2\right)\delta\left(\frac{\partial w}{\partial x}\right)\Big|_0^l+\left(B_1\frac{\partial^3 w}{\partial x^3}+D_1\frac{\partial^3 \dot{w}}{\partial x^3}\right)(\delta w)|_0^l\right]dx\right\}dt \tag{A.39}$$

By setting the two expressions within the braces in each term of Eq. A.39 equal to zero, we obtain the PDE and the boundary conditions shown in Eq. 2.52 and 2.53, respectively.

A.5 Solution procedure for Kelvin-Voigt damped system

To evaluate the frequency response function of the homogenized cable-harnessed beam structure with Kelvin-Voigt damping, we assume an impulse excitation at $x = x_0$ at $t = 0$. The governing equation of motion shown in Eq. 2.52 becomes

$$K_1\ddot{w}+B_1w''''+D_1\dot{w}''''=f_0\ \delta(t)\ \delta(x-x_0) \tag{A.40}$$

Since Kelvin-Voigt damping is a proportionally damped system, the mode shapes remains identical to the undamped system. Also, the solution of the equation can be written in a variable separable form

$$w(x,t) = \sum_{n=1}^{\infty} \phi_n(x)\,\Gamma_n(t) \tag{A.41}$$

where $\phi_n(x)$ is the assumed mode shape function of the beam that varies with the boundary condition [72]. For example, the clamped-free beam mode shape can be written as

$$\phi_n(x) = A_n \left\{ \cos(\beta_n x) - \cosh(\beta_n x) - \frac{\cos(\beta_n l) + \cosh(\beta_n l)}{\sin(\beta_n l) + \sinh(\beta_n l)} \left[\sin(\beta_n x) - \sinh(\beta_n x) \right] \right\} \tag{A.42}$$

where A_n are the mass normalized coefficients of the homogenized cable-harnessed system such that the following orthogonality conditions hold:

$$\int_0^l K_1 \phi_k(x)\,\phi_n(x)\,dx = \delta_{kn} \tag{A.43a}$$

$$\int_0^l B_1 \phi_k(x)\,\phi_n''''(x)\,dx = \omega_k^2 \delta_{kn} \tag{A.43b}$$

Now, to solve the Eq. A.40, substitute the displacement from Eq. A.41, multiply with the kth mode shape and integrate over the domain of the homogenized beam to obtain:

$$\ddot{\Gamma}_k(t) + \frac{D_1 \omega_k^2}{B_1} \dot{\Gamma}_k(t) + \omega_k^2 \Gamma_k(t) = f_0 \left(\int_0^l \phi_k(x)\,\delta(x - x_0)dx \right) \delta(t) \tag{A.44}$$

Define the modal damping ratio of the system as

$$\zeta_k = \frac{D_1 \omega_k}{2B_1} \tag{A.45}$$

Simplifying Eq. A.44, we obtain

$$\ddot{\Gamma}_k(t) + 2\zeta_k \omega_k \dot{\Gamma}_k(t) + \omega_k^2 \Gamma_k(t) = f_0 \phi_k(x_0) \delta(t) \tag{A.46}$$

On applying the Laplace transform to this equation, we get

$$s^2\Gamma_k(s) + 2\zeta_k\omega_k s\Gamma_k(s) + \omega_k^2\Gamma_k(s) = f_0\phi_k(x_0) \tag{A.47}$$

The temporal variable can hence be written as

$$\Gamma_k(s) = \frac{f_0\phi_k(x_0)}{s^2 + 2\zeta_k\omega_k s + \omega_k^2} \tag{A.48}$$

In order to obtain the receptance FRF, substitute the above equation in the Laplace transform of Eq. A.41 to obtain

$$FRF(x, x_0, \omega) = \left| \sum_{n=1}^{\infty} \frac{\phi_n(x)\phi(x_0)}{-\omega^2 + j(2\zeta_n\omega_n\omega) + \omega_n^2} \right| \tag{A.49}$$

A.6 Solution procedure for hysteretically damped system

To evaluate the frequency response function of the homogenized cable-harnessed beam structure with hysteresis damping, we assume an external forcing function with an impulse excitation at $x = x_0$ at $t = 0$. The governing equation of motion shown in Eq. 2.54 becomes

$$K_1\ddot{w} + B_1^* w'''' = f_0\ \delta(t)\ \delta(x - x_0) \tag{A.50}$$

Since the hysteretic (structural) damping is also a proportionally damped system [108], the solution to the EOM can be written in a variable separable form as it was earlier written in Eq. A.41. Hence, on substitution of this solution in Eq. A.50, we obtain

$$K_1 \sum_{n=1}^{\infty} \phi_n(x)\,\ddot{\Gamma}_n(t) + B_1^* \sum_{n=1}^{\infty} \phi_n''''(x)\,\Gamma_n(t) = f_0\ \delta(t)\ \delta(x - x_0) \tag{A.51}$$

Following the similar procedure for the solution as shown in the previous section, the above equation is multiplied by $\phi_k(x)$ and integrated over the length of the homogenized beam. Using $B_1^* = B_1'(1 + j\eta_{CH})$, $B_1' = B_1$, and Eq. A.43, the previous equation is simplified as

$$\ddot{\Gamma}_k(t) + (1 + j\eta_{CH})\omega_k^2 \Gamma_k(t) = f_0 \phi_k(x_0)\delta(t) \tag{A.52}$$

On applying the Laplace transform, the temporal variable is obtained as

$$\Gamma_k(s) = \frac{f_0 \phi_k(x_0)}{s^2 + (1 + j\eta_{CH})\omega_k^2} \tag{A.53}$$

The receptance FRF for the hysteretically damped system is hence written as:

$$FRF(x, x_0, \omega) = \left| \sum_{n=1}^{\infty} \frac{\phi_n(x)\phi_n(x)}{-\omega^2 + (1 + \eta_{CH})\omega_n^2} \right| \tag{A.54}$$

Here, ω_n is the nth natural frequency of the undamped system.

A.7 Energy loss in one vibration cycle of a cable due to the two damping models

For a Kelvin-Voigt model, the energy dissipated over one vibration cycle of the cable (modeled as string) is calculated using:

$$W_{KV} = \eta_{kc} T \int_0^{T_1} \int_0^{l_C} \left(\frac{\partial^2 v}{\partial x \partial t} \right)^2 dx dt \tag{A.55}$$

Here, T_1 is the period of vibration and l_C is the length of cable under tension T. Also, $v(x,t)$ is the displacement of the cable.

Similarly, for a hysteretically damped model, the energy dissipation is found using:

$$W_H = (j\eta_{hc}) T \int_0^{T_1} \int_0^{l_C} \left(\frac{\partial v}{\partial x} \right) \left(\frac{\partial^2 v}{\partial x \partial t} \right) dx dt \tag{A.56}$$

Substituting the standing waveform of a cable $v(x,t) = A\cos(kx)\sin(\omega t)$ in both of these equations, we obtain Eq. 2.76 after simplification of integrals.

Appendix B

Supplementary information on modeling of cable-harnessed plate structures presented in Chapter 5

B.1 Coefficients in cable strain energy expressions

The following equations are the expansion of the coefficients defined for the cable's strain energy written in Eqs. 5.11, 5.16, 5.15, 5.18 and 5.19:

$$C_1 = \frac{T^2}{E_c^2 A_c^2} \tag{B.1}$$

$$C_2 = \frac{T z_c^2 \cos^2\theta}{E_c A_c} + z_c^2 \cos^4\theta \tag{B.2}$$

$$C_3 = \frac{T z_c^2 \sin^2\theta}{E_c A_c} + z_c^2 \sin^4\theta \tag{B.3}$$

$$C_3' = \frac{T z_c^2}{E_c A_c} + z_c^2 \tag{B.4}$$

$$C_4 = \frac{T z_c^2}{E_c A_c} + 4 z_c^2 \cos^2\theta \sin^2\theta \tag{B.5}$$

$$C_4' = \frac{T z_c^2}{A_c E_c} \tag{B.6}$$

$$C_5 = \frac{T \cos^2\theta}{E_c A_c} \tag{B.7}$$

$$C_6 = \frac{T \sin^2\theta}{E_c A_c} \tag{B.8}$$

$$C_6' = \frac{T}{E_c A_c} \tag{B.9}$$

$$C_7 = \frac{2T z_c \cos^2\theta}{E_c A_c} \tag{B.10}$$

$$C_8 = \frac{4T z_c \sin\theta \cos\theta}{E_c A_c} \tag{B.11}$$

$$C_9 = \frac{2T z_c \sin^2\theta}{E_c A_c} \tag{B.12}$$

$$C_9' = \frac{2T z_c}{A_c E_c} \tag{B.13}$$

$$C_{10} = \left(\frac{2T z_c^2 \cos\theta \sin\theta}{E_c A_c} + 4 z_c^2 \cos^3\theta \sin\theta \right) \tag{B.14}$$

$$C_{11} = \left(\frac{2T z_c^2 \cos\theta \sin\theta}{E_c A_c} + 4 z_c^2 \cos\theta \sin^3\theta \right) \tag{B.15}$$

$$C_{12} = \frac{2\ T \cos\theta \sin\theta}{E_c A_c} \tag{B.16}$$

$$C_{13} = 2 z_c^2 \cos^2\theta \sin^2\theta \tag{B.17}$$

B.2 Coefficients in total strain energy expression of a periodically wrapped cable-harnessed plate

In this following sub-sections, the coefficients shown in Eq. 5.33 are expanded in terms of the system parameters for both the periodically wrapped patterns in cable-harnessed plate system. As well, the coefficients in the governing equation of motion, Eq. 5.36, are also listed.

B.2.1 Zigzag pattern

$$H_1 = \frac{T^2}{E_c A_c L_2 \cos\theta} + \frac{1}{hE_p}\left(N_x^2 + N_y^2 - 2\nu N_x N_y + 2\left(1+\nu\right)N_{xy}^2\right) \tag{B.18}$$

$$H_2 = D + \frac{E_c A_c z_c^2 \cos^3\theta}{L_2} + \frac{T z_c^2 \cos\theta}{L_2} + \frac{N_x h^2}{24} \tag{B.19}$$

$$H_3 = D + \frac{E_c A_c z_c^2 \sin^4\theta}{L_2 \cos\theta} + \frac{T z_c^2 \sin^2\theta}{L_2 \cos\theta} + \frac{N_y h^2}{24} \tag{B.20}$$

$$H_4 = 2D\left(1-\nu\right) + \frac{4E_c A_c z_c^2 \cos\theta \sin^2\theta}{L_2} + \frac{T z_c^2}{L_2 \cos\theta} + \frac{N_x h^2}{24} + \frac{N_y h^2}{24} \tag{B.21}$$

$$H_5 = \frac{T\cos\theta}{L_2} + N_x = 0 \tag{B.22}$$

$$H_6 = \frac{T\sin^2\theta}{L_2\cos\theta} + N_y = 0 \tag{B.23}$$

$$H_7 = 0 \tag{B.24}$$

$$H_8 = 0 \tag{B.25}$$

$$H_9 = 0 \tag{B.26}$$

$$H_{10} = \frac{N_{xy} h^2}{6} = 0 \tag{B.27}$$

$$H_{11} = \frac{N_{xy} h^2}{6} = 0 \tag{B.28}$$

$$H_{12} = 2N_{xy} = 0 \tag{B.29}$$

$$H_{13} = 2\nu D + \frac{2E_c A_c z_c^2 \cos\theta \sin^2\theta}{L_2} \tag{B.30}$$

B.2.2 Diagonal pattern

$$H_1 = \frac{T^2}{E_c A_c\left(L_1 + L_2\cos\theta\right)} + \frac{1}{hE_p}\left(N_x^2 + N_y^2 - 2\nu N_x N_y + 2\left(1+\nu\right)N_{xy}^2\right) \tag{B.31}$$

$$H_2 = D + \frac{E_c A_c z_c^2 \cos^3\theta}{L_2} + \frac{T z_c^2 \cos\theta}{L_2} + \frac{N_x h^2}{24} \tag{B.32}$$

$$H_3 = D + E_c A_c \left\{ \frac{1}{L_2 \cos\theta} \left(\frac{T z_c^2 \sin\theta}{E_c A_c} + z_c^2 \sin^4\theta \right) + \frac{1}{L_1} \left(\frac{T z_c^2}{E_c A_c} + z_c^2 \right) \right\} + \frac{N_y h^2}{24} \quad \text{(B.33)}$$

$$H_4 = 2D\left(1-\nu\right) + \frac{4 E_c A_c z_c^2 \cos\theta \sin^2\theta}{L_2} + \frac{T z_c^2}{L_2 \cos\theta} + \frac{N_x h^2}{24} + \frac{N_y h^2}{24} \quad \text{(B.34)}$$

$$H_5 = \frac{T\cos\theta}{L_2} + N_x = 0 \quad \text{(B.35)}$$

$$H_6 = \frac{T\sin^2\theta}{L_2\cos\theta} + \frac{T}{L_1} + N_y = 0 \quad \text{(B.36)}$$

$$H_7 = \frac{2T z_c \cos\theta}{L_2} \quad \text{(B.37)}$$

$$H_8 = \frac{4T z_c \sin\theta}{L_2} \quad \text{(B.38)}$$

$$H_9 = -\frac{2T z_c \sin^2\theta}{L_2\cos\theta} + \frac{2T z_c}{L_1} \quad \text{(B.39)}$$

$$H_{10} = \frac{N_{xy} h^2}{6} + \frac{2T z_c^2 \sin\theta}{L_2} + \frac{4 E_c A_c z_c^2 \cos^2\theta \sin\theta}{L_2} \quad \text{(B.40)}$$

$$H_{11} = \frac{N_{xy} h^2}{6} + \frac{2T z_c^2 \sin\theta}{L_2} + \frac{4 E_c A_c z_c^2 \sin^3\theta}{L_2} \quad \text{(B.41)}$$

$$H_{12} = \frac{2T\sin\theta}{L_2} + 2N_{xy} = 0 \quad \text{(B.42)}$$

$$H_{13} = 2\nu D + \frac{2 E_c A_c z_c^2 \cos\theta \sin^2\theta}{L_2} \quad \text{(B.43)}$$